Seismic Load Path Effects in Reinforced Concrete Bridge Columns and Wall Piers

Volume 2: Out-of-plane buckling instability of Pier walls

(Ana Gabriela Haro – Constructed Facilities Laboratory - NCSU)
June 2017

Prepared By:
Ana Gabriela Haro Báez, Research Assistant (NCSU)
Dr. Mervyn J. Kowalsky, Principal Investigator (NCSU)
Dr. Y.H. Chai, Co-Principal Investigator (UC DAVIS)

Prepared For:
Alaska Department of Transportation & Public Facilities
Research, Development, and Technology Transfer
P.O. Box 112500
3132 Channel Drive
Juneau, Alaska 99811-2500

and

Federal Highway Administration
P.O. Box 21648
709 West 9th Street
Juneau, Alaska 99802-1648

REPORT DOCUMENTATION PAGE

Form approved OMB No.

Public reporting for this collection of information is estimated to average 1 hour per response, including the time for reviewing instructions, searching existing data sources, gathering and maintaining the data needed, and completing and reviewing the collection of information. Send comments regarding this burden estimate or any other aspect of this collection of information, including suggestion for reducing this burden to Washington Headquarters Services, Directorate for Information Operations and Reports, 1215 Jefferson Davis Highway, Suite 1204, Arlington, VA 22202-4302, and to the Office of Management and Budget, Paperwork Reduction Project (0704-1833), Washington, DC 20503

1. AGENCY USE ONLY (LEAVE BLANK)	2. REPORT DATE	3. REPORT TYPE AND DATES COVERED
4000(134)	June 30, 2017	Final Report / February 28, 2015 – June 30, 2017

4. TITLE AND SUBTITLE

Seismic Load Path Effects in Reinforced Concrete Bridge Columns and Wall Piers
Volume 2: Out-of-plane buckling instability of Pier walls

5. FUNDING NUMBERS

Federal# 4000(134)

IRIS# Z642030000

6. AUTHOR(S)
Ana Gabriela Haro Báez, Research Assistant (NCSU)
Dr. Mervyn J. Kowalsky, Principal Investigator (NCSU)
Dr. Y.H. Chai, Co-Principal Investigator (UC DAVIS)

7. PERFORMING ORGANIZATION NAME(S) AND ADDRESS(ES)

North Carolina State University
Raleigh, NC 27695

8. PERFORMING ORGANIZATION REPORT NUMBER

4000(134)

9. SPONSORING/MONITORING AGENCY NAME(S) AND ADDRESS(ES)

Alaska Department of Transportation and Public Facilities
Research, Development &Technology Transfer
3132 Channel Drive
Juneau, Alaska 99811-2500

10. SPONSORING/MONITORING AGENCY REPORT NUMBER

4000(134)

11. SUPPLEMENTARY NOTES

12a. DISTRIBUTION / AVAILABILITY STATEMENT

Copies available online at http://www.dot.alaska.gov/stwddes/research/search_lib.shtml

12b. DISTRIBUTION CODE

13. ABSTRACT (Maximum 200 words)
Buckling instability of reinforced concrete structural walls (RCSW) reported after the 2010 Chile and 2011 New Zealand earthquakes in addition to prior observations during laboratory tests have emphasized the importance of understanding this mode of structural response. Experimental tests on reinforced concrete prisms representative of boundary elements of prototype typical planar RC walls were conducted at the Constructed Facility Laboratory at North Carolina State University. The effects on out-of-plane instability due to a combination of selected longitudinal reinforcement ratios and various load paths were evaluated. As has been observed in past studies, when the buckled deformation is enough to cause instability, loss of vertical load carrying capacity occurred. The results of the study indicate that imposed out-of-plane displacements do not affect stability; however, in-plane loading history does impact the onset of the local buckling limit state.
In addition, a fiber-based computational model was developed and calibrated based on the response of the tested specimens. Subsequently, a parametric study was conducted, where formerly identified critical parameters were considered to create a new model to prevent out-of-plane buckling instability as a function of longitudinal tensile strains reached at the end regions of RC walls.

14. KEYWORDS:

Out-of-plane buckling stability, pier walls, structural walls, maximum tensile strain, minimum thickness, boundary elements

15. NUMBER OF PAGES
213

16. PRICE CODE
N/A

17. SECURITY CLASSIFICATION OF REPORT	18. SECURITY CLASSIFICATION OF THIS PAGE	19. SECURITY CLASSIFICATION OF ABSTRACT	20. LIMITATION OF ABSTRACT
Unclassified	Unclassified	Unclassified	None

Notice

This document is disseminated under the sponsorship of the U.S. Department of Transportation in the interest of information exchange. The U.S. Government assumes no liability for the use of the information contained in this document.

The U.S. Government does not endorse products or manufacturers. Trademarks or manufacturers' names appear in this report only because they are considered essential to the objective of the document.

Quality Assurance Statement

The Federal Highway Administration (FHWA) provides high-quality information to serve Government, industry, and the public in a manner that promotes public understanding. Standards and policies are used to ensure and maximize the quality, objectivity, utility, and integrity of its information. FHWA periodically reviews quality issues and adjusts its programs and processes to ensure continuous quality improvement.

Author's Disclaimer

Opinions and conclusions expressed or implied in the report are those of the author. They are not necessarily those of the Alaska DOT&PF or funding agencies.

SI* (MODERN METRIC) CONVERSION FACTORS

APPROXIMATE CONVERSIONS TO SI UNITS

Symbol	When You Know	Multiply By	To Find	Symbol
		LENGTH		
in	inches	25.4	millimeters	mm
ft	feet	0.305	meters	m
yd	yards	0.914	meters	m
mi	miles	1.61	kilometers	km
		AREA		
in^2	square inches	645.2	square millimeters	mm^2
ft^2	square feet	0.093	square meters	m^2
yd^2	square yard	0.836	square meters	m^2
ac	acres	0.405	hectares	ha
mi^2	square miles	2.59	square kilometers	km^2
		VOLUME		
fl oz	fluid ounces	29.57	milliliters	mL
gal	gallons	3.785	liters	L
ft^3	cubic feet	0.028	cubic meters	m^3
yd^3	cubic yards	0.765	cubic meters	m^3
	NOTE: volumes greater than 1000 L shall be shown in m^3			
		MASS		
oz	ounces	28.35	grams	g
lb	pounds	0.454	kilograms	kg
T	short tons (2000 lb)	0.907	megagrams (or "metric ton")	Mg (or "t")
		TEMPERATURE (exact degrees)		
^oF	Fahrenheit	5 (F-32)/9 or (F-32)/1.8	Celsius	^oC
		ILLUMINATION		
fc	foot-candles	10.76	lux	lx
fl	foot-Lamberts	3.426	candela/m^2	cd/m^2
		FORCE and PRESSURE or STRESS		
lbf	poundforce	4.45	newtons	N
lbf/in^2	poundforce per square inch	6.89	kilopascals	kPa

APPROXIMATE CONVERSIONS FROM SI UNITS

Symbol	When You Know	Multiply By	To Find	Symbol
		LENGTH		
mm	millimeters	0.039	inches	in
m	meters	3.28	feet	ft
m	meters	1.09	yards	yd
km	kilometers	0.621	miles	mi
		AREA		
mm^2	square millimeters	0.0016	square inches	in^2
m^2	square meters	10.764	square feet	ft^2
m^2	square meters	1.195	square yards	yd^2
ha	hectares	2.47	acres	ac
km^2	square kilometers	0.386	square miles	mi^2
		VOLUME		
mL	milliliters	0.034	fluid ounces	fl oz
L	liters	0.264	gallons	gal
m^3	cubic meters	35.314	cubic feet	ft^3
m^3	cubic meters	1.307	cubic yards	yd^3
		MASS		
g	grams	0.035	ounces	oz
kg	kilograms	2.202	pounds	lb
Mg (or "t")	megagrams (or "metric ton")	1.103	short tons (2000 lb)	T
		TEMPERATURE (exact degrees)		
^oC	Celsius	1.8C+32	Fahrenheit	^oF
		ILLUMINATION		
lx	lux	0.0929	foot-candles	fc
cd/m^2	candela/m^2	0.2919	foot-Lamberts	fl
		FORCE and PRESSURE or STRESS		
N	newtons	0.225	poundforce	lbf
kPa	kilopascals	0.145	poundforce per square inch	lbf/in^2

*SI is the symbol for the International System of Units. Appropriate rounding should be made to comply with Section 4 of ASTM E380.
(Revised March 2003)

TABLE OF CONTENTS

TABLE OF CONTENTS ..... **v**

TABLE OF FIGURES ..... **ix**

LIST OF TABLES ..... **xvi**

ACKNOWLEDGEMENTS **1**

EXECUTIVE SUMMARY **2**

CHAPTER I: INTRODUCTION **3**

1.1 Motivation 3

1.2 Objective 4

1.3 Layout 5

CHAPTER 2: LITERATURE REVIEW **6**

2.1 Structural performance of RC walls observed in historical earthquakes 6

2.2 Structural performance of RC walls observed in laboratory tests 8

2.2.1 Laboratory studies in rectangular walls 8

2.2.2 Laboratory studies in boundary elements – prisms 24

2.3 State of the art in out-of-plane instability prediction 36

2.3.1 Phenomenological models 36

2.3.2 Code requirements 40

2.4 Local buckling prediction assessment 42

CHAPTER 3: STUDY PLAN **46**

3.1 Research Gap 46

3.2 Research Objectives 46

CHAPTER 4: METHOD **47**

4.1 Experimental program 47

4.1.1 Tests conceptualization 47

4.1.2 Specimens detailing 48

4.1.3 Specimens construction 49

4.1.4 Material properties 51

4.1.5 Test setup and instrumentation 54
4.1.6 Loading protocols 57
4.1.7 Data source 61
4.2 Analytical Predictions 62
CHAPTER 5: EXPERIMENTAL RESULTS 64
5.1 Experimental Observations 64
5.1.1 Test 1 64
5.1.2 Test 2 69
5.1.3 Test 3 74
5.1.4 Test 4 79
5.1.5 Test 5 84
5.1.6 Test 6 90
5.1.7 Test 7 95
5.1.8 Test 8 100
5.1.9 Test 9 105
5.1.10 Test 10 110
5.1.11 Test 11 116
5.1.12 Test 12 121
5.2 Trends of the experimental results 126
5.2.1 Out-of-plane displacements vs. maximum tensile strains 126
5.2.2 Influence of out-of-plane displacement on boundary elements stability 129
5.2.3 Out-of-plane deformations vs. stability criteria 131
5.2.4 Longitudinal reinforcement ratio vs. maximum tensile demands 133
5.2.5 Curvature distribution 134
5.2.6 Hysteretic response of longitudinal reinforcement 135
5.2.7 Crushing limit state 137
5.2.8 Axial loading paths 138
5.2.9 ACI 318-14 transverse reinforcement spacing for boundary elements 139
5.2.10 Experimental program: Concluding remarks 139

CHAPTER 6: ANALYTICAL STUDY 141

6.1 Numerical model 141

6.1.1 Reinforcing steel model 142

6.1.2 Concrete model 143

6.1.3 Performance criteria 144

6.2 Validation: experimental results vs. numerical model 144

6.2.1 Hysteretic response 145

6.2.2 Structural performance 148

6.2.3 Out-of-plane deformations 149

6.2.4 Numerical model validation: Concluding remarks 152

6.3 Parametric study 153

6.3.1 Material properties 153

6.3.2 Geometric and reinforcement detailing parameters 154

6.3.3 Loading protocol 155

6.3.4 Results of the parametric study 155

6.3.5 Parametric study: Concluding remarks 164

CHAPTER 7: NEW MODEL TO PREVENT OUT-OF-PLANE BUCKLING INSTABILITY OF RCSW 166

7.1 HKC model 166

7.1.1 Strain components 166

7.1.2 Validation of the HKC model 168

7.2 Axial strain gradient effects 172

7.2.1 Buckled region length 173

7.3 Applications of the HKC model: Direct Displacement-Based Design 176

7.3.1 Maximum Tensile Strains 176

7.3.2 Minimum Wall Thickness 180

7.4 Preliminary estimation of the minimum structural wall thickness 182

7.4.1 Case Study: 18-story RC building in Santiago, Chile 183

7.5 Summary: HKC model for structural walls 184

CHAPTER 8: DESIGN RECOMMENDATIONS FOR PIER WALLS.....185

8.1 Applications of the HKC model: Direct Displacement-Based Design 185

8.1.1 Example: Bridge Pier Wall.....185

8.1.2 Example: Bridge Pier Wall.....187

8.2 Preliminary estimation of the minimum pier wall thickness.....188

8.2.1 Case Study: Alaska DOT Bridge 539.....189

8.3 Summary: HKC model for pier walls.....191

CHAPTER 9: DISCUSSION AND FUTURE WORK.....192

9.1 Discussion 192

9.2 Future Work 193

REFERENCES.....195

TABLE OF FIGURES

Figure 2-1. RC 18-story building in Santiago: (a) Overall view of the building; (b) wall local buckling failure (Wallace & Moehle, 2012) 7
Figure 2-2. RC 7-story building in Christchurch: (a) Overall view of the building; (b) wall local buckling failure (Sri Sritharan, 2011) 8
Figure 2-3. Cross section dimensions of the thin walls tested by Oesterle et al. (1976) 10
Figure 2-4. Local buckling of wall R2 tested by Oesterle et al. (1976) 10
Figure 2-5. Dimensions and details of the rectangular walls tested by Vallenas et al. (1979) 11
Figure 2-6. Typical rectangular wall tested by Goodsir (1985) 12
Figure 2-7. T-section wall tested by Goodsir (1985) 13
Figure 2-8. Wall T3 at the end of the test. Views: west face, east end. (Goodsir, 1985) 13
Figure 2-9. Geometry and reinforcement of the walls tested by Thiele et al. (2000) 14
Figure 2-10. South side of the wall WPH2 after failure. Buckled zone. 15
Figure 2-11. Reinforcing details for the rectangular walls tested by Thomsen & Wallace (2004) 15
Figure 2-12. Reinforcing details of the T-shaped walls tested by Thomsen & Wallace (2004) (a) TW1, (b) TW2. 16
Figure 2-13. Walls (a) RW1 damage—2% drift; (b) RW2 damage— 2.5% drift; (c) TW1 damage—1.25% drift; and (d) TW2 damage—2.5% drift 16
Figure 2-14. NTW1 detailing. Section and elevation views. 17
Figure 2-15. NTW2 detailing. Section and elevation views. 17
Figure 2-16. North flange tip of the NTW2 wall tested by Brueggen (2009) 18
Figure 2-17. Reinforcement details of the three walls (RWN, RWC, and RWS) tested by Aaleti et al. (2013) 19
Figure 2-18. Buckling of the boundary element. Specimen RWC 19
Figure 2-19. Reinforcement detailing of walls tested by Alarcon (2013) 20
Figure 2-20. Observed behavior of three walls tested by Alarcon (2013) 21
Figure 2-21. Reinforcement detailing for the walls tested by Marihuén (2014) 22
Figure 2-22. Observed damage of specimen M5 tested by Marihuén (2014) 22
Figure 2-23. Geometry and detailing of walls TW1 and TW4 tested by Rosso et al. (2015) 23
Figure 2-24. Deformed shapes: (a) Wall TW1 at 0% in-plane drift; (b) Wall TW1 at the end of the test; (c) Wall TW4 at the end of the test. (Rosso et al., 2015) 24
Figure 2-25. Reinforcement details and test set-up of a typical prisms considered by Goodsir (1985) 26
Figure 2-26. Final state of four prisms tested by Goodsir (1985) 27
Figure 2-27. Cross area and reinforcement details of prisms tested by Chai & Elayer (1999) 28

Figure 2-28. Samples of buckled shapes for prisms tested by Chai & Elayer (1999).....28
Figure 2-29. Geometry of specimens tested by Creagh et al. (2010).....29
Figure 2-30. Damage stages of specimens tested by Creagh et al. (2010).....30
Figure 2-31. Geometry details of the specimens tested by Chrysanidis & Tegos (2012b).....31
Figure 2-32. Failure mechanism of the five specimens tested by Chrysanidis & Tegos (2012b).....31
Figure 2-33. Failure mechanism of the eleven specimens tested by Chrysanidis & Tegos (2012a)...32
Figure 2-34. Cross-section and detailing of the eight prisms tested by Shea et al. (2013) & Flintrop et al. (2013).....33
Figure 2-35. Strain history covered in the 2013 NEES@UCLA project.....33
Figure 2-36. State of prisms reported by Shea (2013) and Flintrop (2013).....34
Figure 2-37. Cross-sections and detailing of the selected specimens tested by Welt (2015).....35
Figure 2-38. Final states of prisms CS1 and CS2 tested by Welt (2015); a) without, and b) with tensile pre-strain. 36
Figure 2-39. Deformation and strain patterns in a plastic hinge region. (Goodsir, 1985).....37
Figure 2-40. Idealized nominal axial strain vs. axial force response (Chai & Elayer, 1999).....39
Figure 2-41. Design provisions of boundary element for special RCSW. [Fig. R18.10.6.4.2 ACI 318 (2014)].....41
Figure 2-42. Wall experimental displacements normalized to PPBM and CEBM displacements. (Herrick & Kowalsky, 2016).....43
Figure 2-43. Experimental prism strains normalized to PPBM and CEBM strains. (Herrick & Kowalsky, 2016).....44
Figure 4-1. Conceptualization of the specimens.....48
Figure 4-2. Specimens - Cross Sections.....49
Figure 4-3. Specimens - Reinforcement Detailing.....49
Figure 4-4. Construction of specimens: (a) prism reinforcement cage; (b) formwork assembly; (c) formwork and rebar cage for specimens (d) needle gun used to clear voids.....50
Figure 4-5. Initial and final stages from tensile tests conducted on bars #3.....52
Figure 4-6. Stress-strain curve from a longitudinal rebar #5 – Phase 1.....52
Figure 4-7. Stress-strain curve from a longitudinal rebar #4 – Phase 2.....53
Figure 4-8. Stress-strain curve from a longitudinal rebar #3 – Phase 3.....53
Figure 4-9. Stress-strain curve from a transverse rebar #3 – Phase 1.....54
Figure 4-10. Test setup sketch.....55
Figure 4-11. Test setup in the CFL at NC State.....56
Figure 4-12. Optotrak LEDs distribution on right face of a specimen and spatial coordinate output.57
Figure 4-13. Prism Constituents.....62
Figure 5-1. Prism 1: Out-of-Plane Lateral Displacement History.....65

Figure 5-2. Prism 1: Deformed shape at 10in. (254mm) lateral displacement.....65
Figure 5-3. Prism 1: Buckling instability at the end of the axial cycle 66
Figure 5-4. Prism 1: Axial Strain vs. Axial Force established 4in. (102mm) below midheight on a) south face and b) north face 67
Figure 5-5. Prism 1: Out-of-plane deformation captured upon compressive loading at the end of the test 67
Figure 5-6. Axial Strain History applied to Prism 2.....70
Figure 5-7. Prism 2: Stable out-of-plane buckling mechanism during $12\varepsilon_y(2)$, second cycle: a) Onset of buckling – cracks opened, b) Stable buckling – cracks partially closed, c) End of buckling - cracks closed.....71
Figure 5-8. Prism 2: Instable out-of-plane buckling mechanism during $12\varepsilon_y(3)$, third cycle 71
Figure 5-9. Prism 2: Axial Strain vs. Axial Force established at midheight on a) south face and b) north face 72
Figure 5-10. Prism 2: Evolution of out-of-plane deformations captured upon compressive loading at different stages 72
Figure 5-11. Axial Strain History applied to Prism 3.....75
Figure 5-12. Prism 3: Stable out-of-plane buckling mechanism during $12\varepsilon_y(3)$, third cycle: a) Onset of buckling – cracks opened, b) Stable buckling – cracks partially closed, c) End of buckling - cracks closed.....76
Figure 5-13. Prism 3: Instable out-of-plane buckling mechanism during 14εy(1), first cycle.....76
Figure 5-14. Prism 3: Axial Strain vs. Axial Force established 2in. (51mm) above midheight a) south face and b) north face 77
Figure 5-15. Prism 3: Evolution of out-of-plane deformations captured upon compressive loading at different stages 77
Figure 5-16. Axial Strain History applied to Prism 4.....80
Figure 5-17. Prism 4: Stable out-of-plane buckling mechanism during 10εy(3), third cycle: a) Onset of buckling – cracks opened, b) Stable buckling – cracks partially closed, c) End of buckling - cracks closed.....81
Figure 5-18. Prism 4: Deformed shape at the end of 12εy(1), first cycle 81
Figure 5-19. Prism 4: Instable out-of-plane buckling mechanism during 12εy(2), second cycle 82
Figure 5-20. Prims 4: Axial Strain vs. Axial Force established 2in. (51mm) below midheight a) south face and b) north face 82
Figure 5-21. Prism 4: Evolution of out-of-plane deformations captured upon compressive loading at different stages 83
Figure 5-22. Lateral Displacement History applied to Prism 5.....84
Figure 5-23. Axial Strain History applied to Prism 5.....85

Figure 5-24. Prism 5: Stable out-of-plane buckling mechanism during 10εy(3), third cycle: a) Onset of buckling – cracks opened, b) Stable buckling – cracks partially closed, c) End of buckling - cracks closed.....87
Figure 5-25. Prism 5: Instable out-of-plane buckling mechanism during 12εy(1), first cycle.....87
Figure 5-26. Prism 5: Axial Strain vs. Axial Force at 4 in (102mm) above midheight a) south face and b) north face 88
Figure 5-27. Prism 5: Evolution of out-of-plane deformations captured upon compressive loading at different stages 88
Figure 5-28. Axial Strain History applied to Prism 6.....91
Figure 5-29. Prism 6: Stable out-of-plane buckling mechanism at the end of: a) 12εy(2) second cycle and b) 12εy(3) third cycle 92
Figure 5-30. Prism 6: Instable out-of-plane buckling mechanism during 14εy(1), first cycle.....93
Figure 5-31. Prism 6: Axial Strain vs. Axial Force established 16 in. (406mm) below midheight on a) south face and b) north face 93
Figure 5-32. Prism 6: Evolution of out-of-plane deformations captured upon compressive loading at different stages 94
Figure 5-33. Axial Strain History applied to Prism 7.....96
Figure 5-34. Prism 7: Stable out-of-plane buckling mechanism during 12εy(3), third cycle: a) Onset of buckling – cracks opened, b) Stable buckling – cracks partially closed, c) End of buckling - cracks closed.....97
Figure 5-35. Prism 7: Instable out-of-plane buckling mechanism during 14εy(1), first cycle.....97
Figure 5-36. Prism 7: Axial Strain vs. Axial Force established 4in. (102mm) above midheight on a) south face and b) north face 98
Figure 5-37. Prism 7: Evolution of out-of-plane deformations captured upon compressive loading at different stages 98
Figure 5-38. Axial Strain History applied to Prism 8.....101
Figure 5-39. Prism 8: Stable out-of-plane buckling mechanism during 12εy(3), third cycle: a) Onset of buckling – cracks opened, b) Stable buckling – cracks partially closed, c) End of buckling - cracks closed.....102
Figure 5-40. Prism 8: Instable out-of-plane buckling mechanism during 14εy(1), first cycle.....102
Figure 5-41. Prism 8: Axial Strain vs. Axial Force established at midheight on a) south face and b) north face.....103
Figure 5-42. Prism 8: Evolution of out-of-plane deformations captured upon compressive loading at different stages 104
Figure 5-43. Axial Strain History applied to Prism 9.....106

Figure 5-44. Prism 9: Stable out-of-plane buckling mechanism during 14εy(1), first input data: a) Onset of buckling – cracks opened, b) Stable buckling – cracks partially closed, c) End of buckling - cracks closed. 107
Figure 5-45. Prism 9: Stable out-of-plane buckling mechanism during 16εy(1), second input data: a) Onset of buckling – cracks opened, b) Stable buckling – cracks partially closed, c) End of buckling - cracks closed 107
Figure 5-46. Prism 9: Instable out-of-plane buckling mechanism during 16εy(2), third input data .108
Figure 5-47. Prism 9: Axial Strain vs. Axial Force established 4in. (102mm) below midheight on a) south face and b) north face 108
Figure 5-48. Prism 9: Evolution of out-of-plane deformations captured upon compressive loading at different stages 109
Figure 5-49. Axial Strain History applied to Prism 10.....111
Figure 5-50. Prism 10: Stable out-of-plane buckling mechanism during 14εy(3), third cycle: a) Onset of buckling – cracks opened, b) Stable buckling – cracks partially closed, c) End of buckling - cracks closed.....112
Figure 5-51. Prism 10: Final state 112
Figure 5-52. Prism 10: Axial Strain vs. Axial Force from established from the region where bar fracture was captured on a) south face and b) north face 113
Figure 5-53. Prism 10: Strain history response of two gages adjacent to the location where the bar fractured: (a) upper gage and (b) lower gage 114
Figure 5-54. Prism 10: Evolution of out-of-plane deformations captured upon compressive loading at different stages 114
Figure 5-55. Axial Strain History applied to Prism 11.....117
Figure 5-56. Prism 11: Stable out-of-plane buckling mechanism during the 16εy cycle: a) Onset of buckling – cracks opened, b) Stable buckling – cracks partially closed, c) End of buckling - cracks closed.....118
Figure 5-57. Prism 11: Instable out-of-plane buckling mechanism during the 22εy cycle.....119
Figure 5-58. Prism 11: Axial Strain vs. Axial Force from established at midheight on a) south face and b) north face 119
Figure 5-59. Prism 11: Evolution of out-of-plane deformations captured upon compressive loading at different stages 120
Figure 5-60. Axial Strain History applied to Prism 12.....122
Figure 5-61. Prism 12: Stable out-of-plane buckling mechanism during the 18εy(1) first cycle: a) Onset of buckling – cracks opened, b) Stable buckling – cracks partially closed, c) End of buckling - cracks closed.....123
Figure 5-62. Prism 12: Instable out-of-plane buckling mechanism during the last cycle 123

Figure 5-63. Prism 12: Axial Strain vs. Axial Force established 4in. (102mm) above midheight on a) south face and b) north face 124
Figure 5-64. Prism 12: Evolution of out-of-plane deformations captured upon compressive loading at different stages 124
Figure 5-65. Phase 1: Peak tensile strains 127
Figure 5-66. Phase 2: Peak tensile strains 128
Figure 5-67. Phase 3: Peak tensile strains 129
Figure 5-68. Buckled shape of Prism 2 during the $10\varepsilon_y(3)$ third cycle 130
Figure 5-69. Phase 1: Maximum out-of-plane deformations captured at midheight 131
Figure 5-70. Phase 2: Maximum out-of-plane deformations captured at midheight 132
Figure 5-71. Phase 3: Maximum out-of-plane deformations captured at midheight 133
Figure 5-72. Maximum tensile strains influenced by longitudinal reinforcement ratios 134
Figure 5-73. Axial Strain vs. Axial Load in Prism 2: a) south face and b) north face 136
Figure 6-1. Discretization of a typical RC cross-section. (Seismosoft Ltd., 2014) 141
Figure 6-2. Menegotto-Pinto Steel Model. (Yu, 2006) 142
Figure 6-3. Definition of the curvature parameter $R(\xi)$ in Menegotto-Pinto Steel Model. (Yu, 2006) 143
Figure 6-4. Stress-Strain model for monotonic loading of confined and unconfined concrete. (Mander et al., 1988) 143
Figure 6-5. Reference data points to calculate axial deformations from the tested prisms 144
Figure 6-6. Numerical model: Typical cross section 145
Figure 6-7. Phase 1: Experimental and Numerical Hysteretic Curves 146
Figure 6-8. Phase 2: Experimental and Numerical Hysteretic Curves 147
Figure 6-9. Phase 3: Experimental and Numerical Hysteretic Curves 148
Figure 6-10. Stages captured from the SeismoStruct interface 149
Figure 6-11. Phase 1: Experimental vs. Computed out-of-plane deformations; (a) Prism 2, (b) Prism 3, (c) Prism 4, (d) Prism 5, (e) Prism 6 150
Figure 6-12. Phase 2: Experimental vs. Computed out-of-plane deformations; (a) Prism 7, (b) Prism 8, (c) Prism 9 151
Figure 6-13. Phase 3: Experimental vs. Computed out-of-plane deformations; (a) Prism 10, (b) Prism 11, (c) Prism 12 152
Figure 6-14. Parametric study: Typical axial strain protocol 155
Figure 6-15. Parametric study-Phase 1: Influence of critical parameters 156
Figure 6-16. Parametric study-Phase 2: Influence of critical parameters 157
Figure 6-17. Parametric study-Phase 3: Influence of critical parameters 157
Figure 6-18. Parametric study-Phase 1 ($h_s/16$): Influence of boundary element length, l_{be} 158

Figure 6-19. Parametric study-Phase 1 ($h_s/10$): Influence of boundary element length, l_{be} 158
Figure 6-20. Parametric study-Phase 2 ($h_s/16$): Influence of boundary element length, l_{be} 159
Figure 6-21. Parametric study-Phase 2 ($h_s/10$): Influence of boundary element length, l_{be} 159
Figure 6-22. Parametric study-Phase 3 ($h_s/16$): Influence of boundary element length, l_{be} 160
Figure 6-23. Parametric study-Phase 3 ($h_s/10$): Influence of boundary element length, l_{be} 160
Figure 6-24. Parametric study - $h_s/16$: Influence of interstory height, h_s 161
Figure 6-25. Parametric study - $h_s/10$: Influence of interstory height, h_s 161
Figure 6-26. Phase 1: Strain components, (a) $h_s/16$, (b) $h_s/10$.....162
Figure 6-27. Phase 2: Strain components, (a) $h_s/16$, (b) $h_s/10$.....162
Figure 6-28. Phase 3: Strain components, (a) $h_s/16$, (b) $h_s/10$.....163
Figure 7-1. Axial Response of Prism 2 - Stages: a) south face and b) north face 167
Figure 7-2. Validation of the HKC model: Parametric Study Phase 1.....169
Figure 7-3. Validation of the HKC model: Parametric Study Phase 2.....169
Figure 7-4. Validation of the HKC model: Parametric Study Phase 3.....170
Figure 7-5. Validation of the HKC model: Experimental Phase 1.....171
Figure 7-6. Validation of the HKC model: Experimental Phase 2.....171
Figure 7-7. Validation of the HKC model: Experimental Phase 3.....172
Figure 7-8. End region idealization of a building RC wall (Chai & Elayer, 1999).....173
Figure 7-9. Normalized web edge out-of-plane deformations along the height of the of wall TW1 (Rosso et al., 2015).....174
Figure 7-10. Out-of-plane deformations along the edge height of wall R2 (Parra, 2015). 174
Figure 7-11. Deformed shape of an RC prism that considers strain gradient 175
Figure 7-12. Structural response of a boundary element; a) Normalized out-of-plane deformations, b) Axial strain gradient, c) Axial force gradient.....176
Figure 7-13. Approximate flexural compression depth. (Moehle et al., 2012) 178
Figure 7-14. Strain profile of an RCSW section 178
Figure 7-15. Approximate minimum wall thickness for structural walls.....182
Figure 7-16. Case study: Approximate estimation of the minimum wall thickness.....183
Figure 8-1. Approximate minimum wall thickness for pier walls.....188
Figure 8-2. HKC model predications of a pier wall with h_w=12m (39.4ft) as a function of: a) aspect ratio, b) normalized maximum tensile strain, c) curvature ductility, d) in-plane drift percentage...189
Figure 8-3. Case study: Approximate assessment of the minimum pier wall thickness 190

LIST OF TABLES

Table 1-1. Alaska DOT pier walls constructed since 1960s 4
Table 2-1. Historical earthquakes with reported damage in RCSW 6
Table 2-2. Parametric Study: Experimental programs that reported out-of-plane buckling in RCSW . 9
Table 2-3. Parametric Study: Prisms 24
Table 4-1. Experimental Phases Matrix 47
Table 4-2. Concrete mechanical properties 51
Table 4-3. Steel reinforcement mechanical properties 54
Table 4-4. Experimental test matrix of Phase 1 58
Table 4-5. Experimental test matrix of Phase 2 59
Table 4-6. Experimental test matrix of Phase 3 60
Table 4-7. Exponential Coefficients to Obtain Cycle Amplitudes (Bazaez and Dusicka 2016) 60
Table 4-8. Proposed Loading Protocols Using the Prepeak Approach (Bazaez and Dusicka 2016) .. 61
Table 4-9. Maximum Tensile Predicted Strains 63
Table 5-1. Prism 1: Specifications 64
Table 5-2. Prism 2: Specifications 69
Table 5-3. Prism 3: Specifications 74
Table 5-4. Prism 4: Specifications 79
Table 5-5. Prism 5: Specifications 84
Table 5-6. Prism 6: Specifications 90
Table 5-7. Prism 7: Specifications 95
Table 5-8. Prism 8: Specifications 100
Table 5-9. Prism 9: Specifications 105
Table 5-10. Prism 10: Specifications 110
Table 5-11. Prism 11: Specifications 116
Table 5-12. Prism 12: Specifications 121
Table 5-13. Tensile strain components 137
Table 5-14. Concrete cover strain 138
Table 6-1. Reinforcement steel: Material model parameters 142
Table 6-2. Numerical model: Material mechanical properties 145
Table 6-3. Phase 1: Maximum normalized tensile strains captured before buckling instability 146
Table 6-4. Phase 3: Maximum normalized tensile strains captured before buckling instability 147
Table 6-5. Phase 3: Maximum normalized tensile strains captured before buckling instability 148
Table 6-6. Parametric study: Concrete model parameters 153
Table 6-7. Parametric study: Reinforcement steel parameters 154

Table 6-8. Parametric study: Geometry and longitudinal reinforcement detailing 154
Table 6-9. Fitting functions for the strain components ε_e and ε_r 163
Table 8-1. Alaska DOT pier wall 190

ACKNOWLEDGEMENTS

The authors wish to thank the Alaska Department of Transportation and Public Facilities for providing funding for the conduct of this research. In particular, we would like to thank Mr. Elmer Marx for his involvement in the work. We would also like to thank the entire technical staff of the Constructed Facilities Laboratory, with a special mention to Dr. Greg Lucier who provided extensive assistance during the experimental portion of this work. It could not have been completed without his efforts. Lastly, we wish to thank the NC State Department of Civil Engineering and SENESCYT – IECE from Ecuador for providing additional financial support for PhD student Gabriela Haro to conduct this work.

EXECUTIVE SUMMARY

Pier walls are occasionally used by Alaska DOT because of their in-plane lateral rigidity. The height-to-thickness ratios found in building applications can also be found in piers walls, increasing the possibility of buckling instability. Unexpected nonlinear behavior in rectangular reinforced concrete structural walls, reported during the 2010 Chile and 2011 New Zealand earthquakes, highlighted the significance of out-of-plane stability, which had been observed in laboratory tests many years prior. The local buckling mechanism of reinforced concrete structural walls (RCSW) was defined first in the 1980s. In-plane lateral loading causes large inelastic tensile strains in one of the boundary elements, accompanied by cracking at the level of the plastic hinge region. Under load reversals, out-of-plane deformations can be generated in the compression zone as a result of residual crack widths and eccentricity in the compression force at the wall toes. If the lateral deformation is sufficient, instability can occur followed by the loss of lateral and vertical load carrying capacity of the wall.

Analytical models created in the 1990s correlate in-plane tensile strains to out-of-plane buckling wall deformations resulting in instability. The models comprise a respective curvature distribution along the plastic hinge region, mechanical properties of the materials, and geometry of the compression zone. Past studies on prisms subjected to axial tensile and compressive cycles have demonstrated how promising the existing models are. However, these models do not consider the potential impact of different loading paths on the buckling mechanism of RCSW, suggesting further investigation.

Prisms representative of the boundary elements of prototype typical pier walls from Alaska DOT and structural walls from Chile and New Zealand were built and physical tests were conducted in the Constructed Facility Laboratory at the North Carolina State University. The aim of the tests was to evaluate the effect of different longitudinal reinforcement ratios in combination with different load paths on the onset of out-of-plane instability of planar special RCSW. Subsequently, a fiber-based computational model was developed and calibrated based on the response of the tested specimens. Later, a parametric study was conducted, where formerly identified critical parameters were considered in order to establish an out-of-plane buckling stability limit state as a function of longitudinal tensile strains reached at the end regions of RCSW.

The principal outcomes of the experimental program and the details the fiber-based computational model are discussed in this report, along with the results of the parametric study which indicated that imposed out-of-plane displacements do not impact stability, however, in-plane loading history and longitudinal reinforcement ratio do impact the onset of the local buckling limit state. Finally, a new approach is proposed to prevent buckling instability of RCSW based on previous models, as it confirmed to be less conservative for design purposes.

CHAPTER I: INTRODUCTION

Chapter 1 first presents the incentive of the current research project, which highlights the importance of further research associated with buckling instability of reinforced concrete structural walls. Next, the main objective of the research, which includes experimental and analytical studies, is stated. Finally, this chapter describes the themes covered along the final report.

1.1 Motivation

Reinforced concrete structural walls (RCSW) are recognized as effective seismic protective systems if the capacity based design philosophy is applied and special reinforcement detailing is provided in the regions where energy is expected to dissipate. Experimental programs involving different geometries and material properties have been executed all around the world resulting in improved design processes. Generally, the preferences regarding the wall geometry depend on the building configuration, however, in recent years thinner walls have become more prevalent due to growing engineering costs and higher compressive strengths for concrete (Wallace, 2012).

Since poor structural performance was observed in recent earthquakes, more reliable procedures are required to identify the non-linear behavior of RCSW. There is still a gap between actual failure modes produced in the boundary elements of thin RCSW and simulations through numerical models. This fact was recognized from reported damage after the occurrence of strong ground motions during the 2010 Chile and 2011 New Zealand earthquakes, which highlighted the importance of out-of-plane stability of reinforced concrete structural walls due to in-plane loading.

Alaska DOT occasionally employs pier walls because of their in-plane lateral stiffness. While these walls are usually thicker than the walls typically found in building applications, their clear heights are also larger, giving rise to height-to-thickness ratios that may be larger than those of buildings and consequently, may be prone to buckle. The New Zealand 2011 earthquake showed that even walls with height-to-thickness ratios equal to ten, could lead to out-of-plane buckling instability. Table 1-1 shows pier walls built by Alaska DOT since 1960s where height-to-thickness ratios close to ten were used in three of them.

Noticing the concentration of damage in the boundary elements of rectangular reinforced concrete structural walls due to higher stress and strain demands, some past investigations by others have been carried out on prisms, which was found to be an economical way to study the inelastic instability of structural walls. In general, the main objective of these tests focuses on subjecting specimens to cyclic tension and compression actions to simulate vertical components of actual seismic loading on structural walls.

While past tests on prisms have shown that the existing models developed by Paulay & Priestley (1993), and Chai & Elayer (1999) are promising (Herrick & Kowalsky, 2016), missing from

the models is the interaction with out-of-plane loading. These existing models correlate tensile strain from in-plane loading to out-of-plane deformation, assuming a prescribed curvature distribution. If loading also occurs in the out-of-plane direction, the relationship between tensile strain and out-of-plane deformations should be adjusted to reflect this.

Table 1-1. Alaska DOT pier walls constructed since 1960s

Pier Wall Id.		539	670	671	1149	1243
Year		1973	1966	2004	1972	1973
l_w	[ft]	26	12	72	40	50
h_w	[ft]	41	19	32.5	46	36
b_w	[ft]	4.33	3	4	4.33	3
reinf. (l)	[-]	14	11	11	14	11
reinf. (t)	[-]	s#6@12"+4t#4@12"	s#4@12"+5t#4@24"	s#6@6"+55t#5@14"	s#6@12"+10t#4@24"	s#5@12"+6t#4@24"
ρ (l)	[-]	0.0092	0.0286	0.0089	0.0095	0.0129
h_w/t_w	[ft/ft]	9.5	6.3	8.1	10.6	12.0
h_w/l_w	[ft/ft]	1.6	1.6	0.5	1.2	0.7
Shape			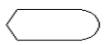			

A total of twelve (12) half-scale reinforced concrete rectangular prisms were designed and built simulating boundary elements from prototype walls. Later the specimens were experimentally tested in the Constructed Facilities Laboratory (CFL) at North Carolina State University. Two critical parameters associated with lateral instability of reinforced concrete walls were considered during this experimental program: a) loading protocols, and b) longitudinal reinforcement ratios. In addition to the results obtained from the experimental program, this report includes the analytical modeling and design recommendations for boundary elements of planar RC structural walls / pier walls. The proposed approach is based on the experimental results and the parametric study conducted using a fiber-based computational model.

1.2 Objective

This research project focus on capturing the buckling instability of RC structural walls / pier walls due to in-plane loading considering the effect of out-of-plane loading through analytical and experimental studies. Based on previous methods (Paulay & Priestley, 1993) (Chai & Elayer, 1999), a new model is suggested to comprise not only the material properties and geometry of boundary elements, but also the effect of out-of-plane lateral displacements.

The specific objectives are detailed in Chapter 3, where the study plan to address the aim of the current research is addressed.

1.3 Layout

Chapter 2 presents the description of the out-of-plane buckling mechanism and the different studies conducted on reinforced concrete structural walls and prisms. In addition, Chapter 2 includes details about the existing phenomenological models and code recommendations addressing buckling instability of walls. Chapter 3 includes the study plan where the research gap and the specific objectives are described. The experimental program and its results are detailed in Chapter 4 and Chapter 5, respectively. Chapter 5 also describes the influence of identified critical parameters affecting the onset of instability, which constitutes the base of the analytical study that includes the parametric study, presented in Chapter 6. Based on the key findings noticed from the experimental results and the parametric study, a proposed model to prevent out-of-plane instability on RCSW due to in-plane loading and its corresponding validation is presented in Chapter 7. Direct displacement-based seismic approaches for design and assessment purposes, focused on buckling instability of structural walls, are also discussed in Chapter 7. Chapter 8 covers similar practical procedures for bridge pier walls. Chapter 9 summarizes the concluding remarks of this project and identifies possible future work areas.

CHAPTER 2: LITERATURE REVIEW

Reinforced concrete structural walls are utilized in seismic design of multistory buildings as systems that exhibit high levels of strength and ductility under ultimate loads (Chai and Elayer, 1999). However, a behavior related to inelastic lateral instability, which only had been observed in laboratory tests, was reproduced in recent earthquakes generating significant damage to buildings that included rectangular or flanged wall geometries. This chapter focuses on observed damage in the Chile (2010) and New Zealand (2011) earthquakes. In addition, experimental programs for thin RCSW where out-of-plane buckling was captured or studied are also described. Finally, the last section of this chapter, details the state-of-the-art of the out-of-plane buckling mechanism of structural walls.

2.1 Structural performance of RC walls observed in historical earthquakes

Structural wall systems and dual systems, the latter known as wall-frame structures (Paulay & Priestley, 1992), have been utilized since the 1960s for medium to high-rise buildings located in urban areas (Moroni M. O., 2002). Reports originated after important seismic events have provided valuable information about the performance of RCSW buildings. Table 2-1 shows the details of selected historical earthquakes and the number of damaged RCSW buildings affected during each event.

Table 2-1. Historical earthquakes with reported damage in RCSW

Earthquake	Date	M	PHGA (g)	Depth [km]	# of RCSW	Sources
Alaska (USA), 1964	03-27-1964	9.2	0.18	25	10	(Christensen, 2002) (Committee on the Alaska Earthquake of the Division of Earth Sciences. National Research Council, 1973)
San Fernando (USA), 1971	02-09-1971	6.6	0.3; 1.25*	8.4	7	(Strong Motion Center, 2014) (Rutenberg, Jennings, & Housner, 1980)
Vrancea (Romania), 1977	03-04-1977	7.5	0.20	109	100	(Berg, Bolt, Sozen, & Christopher, 1980) (Lungu, 2008)
Chile, 1985	03-03-1985	7.8	0.67	33	3	(U. S. Geological Survey, 1985)
Mexico, 1985	09-19-1985	8.1	0.22	18	4	(EEFIT, 1986)
Loma Prieta (USA), 1989	10-17-1989	6.9	0.64	18	3	(EEFIT, 1993)
Northridge (USA), 1994	01-17-1994	6.8	1.0; 1.82*	18.5	6	(EEFIT, 1994)
Kobe (Japan), 1995	01-17-1995	6.9	0.80	22	12	(EEFIT, 1997)
Kocaeli (Turkey), 1999	08-17-1999	7.4	0.41	15.9	10	(EEFIT, 2003)(PEER, 2000)
Chi Chi (Taiwan) 1999	09-21-1999	7.3	1.1	8	1	(Su, 2001)
Maule (Chile), 2010	02-27-2010	8.8	0.65	35	14	(Elnashai et al., 2010)
Christchurch (New Zealand), 2011	02-22-2011	6.3	0.7; 1.6*	5	47	(Kam & Pampanin, 2011)

* First value corresponds to the peak horizontal ground acceleration PHGA recorded in populated areas and the second value constitutes an exceptional case.

Historically, diagonal cracking, web crushing, compressive boundary element damage, horizontal failure plane and collapse have been the dominant types of damage identified for buildings

where partial or full replacement of walls was required (Birely, 2011). However, out-of-plane buckling instability was only noticed in the 2010 Chile and 2011 Christchurch earthquakes.

On February 27, 2010, an 8.8 magnitude earthquake struck Chilean regions for about three minutes producing substantial losses. The maximum recorded peak ground acceleration was 0.65g. Structural walls of mid-to high-rise RC buildings in Santiago presented damage in the lower stories. Figure 2-1(a) shows the overall view of a new 20-story building that experienced buckling instability. Figure 2-2(b) shows the damage in one of the slender walls located at the parking level. It was the first time where the out-of-plane instability phenomenon was captured in a real structure. The average thickness of the walls was 8in. (200mm) and the height-to-width ratio was close to eighteen (18), maximum value recommended by the Chile concrete design standard (NCh 433 1996) (Saatcioglu et al., 2013). The failure was attributed to the slenderness of the boundary zones prone to buckle under compressive loading.

(a) (b)

Figure 2-1. RC 18-story building in Santiago: (a) Overall view of the building; (b) wall local buckling failure (Wallace & Moehle, 2012)

New Zealand registered a 6.3 magnitude earthquake on February 22, 2011, where Christchurch was severely damaged since the hypocenter was located below the city. Peak accelerations of 2.2g and 1.7g were recorded in the vertical and horizontal directions, respectively. The Mw 7.1, Darfield earthquake on September 4, 2010, preceded the Christchurch earthquake. According to many seismologists, the Christchurch earthquake was considered an aftershock of the Darfield event.

Figure 2-2(a) and (b) shows the overall view and the structural performance of a wall in the Pacific Brands House (PBH), respectively. The PBH was a 7-story RC building constructed in 1984

which included two L-shaped walls of about 300 mm thick. The boundary element of the north wall in the lower level developed an out-of-plane buckling failure including significant concrete damage on its surrounding areas. The cyclic combination of compressive strains preceded by large tensile strains were assumed to be the cause of this phenomenon (Sritharan et al., 2014). Contrary to what was exposed for the 2010 Chile Earthquake, the PBH building included thicker RC walls but a lower ratio of these structural elements against the total plan area.

(a) (b)

Figure 2-2. RC 7-story building in Christchurch: (a) Overall view of the building; (b) wall local buckling failure (Sri Sritharan, 2011)

2.2 Structural performance of RC walls observed in laboratory tests

A significant number of experimental programs have been performed to examine the behavior of RCSW with different characteristics. Considering that the aim of this study is to assess the out-of-plane buckling failure mode, tests where this phenomenon was observed or studied is presented, followed by the results of tests carried on prisms replicated as boundary elements of planar RCSW.

2.2.1 Laboratory studies in rectangular walls

Table 2-2 summarizes the parametric study of tests carried on thin RC walls, where out-of-plane buckling was captured. In this table, b_w, h_w, and l_w are the thickness, the total height, and the length of the RC walls, respectively, ρ_b is the longitudinal reinforcement ratio of the boundaries elements, ρ_h is the transverse reinforcement ratio of the wall web, ρ_l is the distributed longitudinal web reinforcement ratio, and ALR is the maximum axial load ratio applied to each specimen. The detailed transverse reinforcement only corresponds to the web regions. The names of the walls refer to those established during the corresponding experimental programs.

Table 2-2. Parametric Study: Experimental programs that reported out-of-plane buckling in RCSW

Test	Walls	Material Properties		Geometry			Reinforcement web			ALR [-]	Lateral Load Pattern
							B.E.	Web			
		f'c [MPa]	fy [MPa]	b_w [mm]	l_w [mm]	h_w [mm]	ρb [%]	ρl [%]	ρh [%]		
(Oesterle et al., 1976)	F1	38.2	442	102	1905	4570	3.89	0.30	0.71	0	cyclic
	F2	45.3	428				4.35	0.31	0.63	0.14	cyclic
	R1	44.5	509				1.47	0.25	0.31	0	cyclic
	R2*	46.2	448				4.00	0.25	0.31	0	cyclic
(Vallenas, Bertero, & Popov, 1979)	**R1***	27.5	482	114	2412	3.085	5.57	0.54	0.54	0	monotonic
	R2*										cyclic
(Goodsir, 1985)	**R1***	28.6	450	100	1500	2400	4.71	0.94	0.71	0.26	cyclic
	R2*	25.3	450		1500		4.71	0.94		0.15	cyclic
	T3*	33.8	400		1300		3.93	0.76		0.12	cyclic
	R4*	36.5	345		1500		4.71	0.94		0.15	cyclic
(Thiele, Wenk, & Bachmann, 2000)	**WPH2***	30.0	470	100	1000	4000	3.5	0.4	0.42	0.15	cyclic
	WPH3						3.5	0.4	0.42	0.04	cyclic
	WPH4*						1.6	0.4	0.42	0.15	cyclic
(Thomsen & Wallace, 2004)	RW1	27.4	414	102	1219	3658	2.93	0.33	0.46-0.49	0.1	cyclic
	RW2						2.93	0.33	0.69-0.37	0.07	cyclic
	TW1						2.93	0.33	0.46-0.49	0.09	cyclic
	TW2*						0.70	0.44	0.92-0.53	0.075	cyclic
(Brueggen, 2009)	NTW1	50.1	414	152	2286	7315	3.78	0.59	0.26	0.05	cyclic
	NTW2*	45.3				3658	2.16	2.16	0.41	0.05	cyclic
(Aaleti, Brueggen, Johnson, French, & Sritharan, 2013)	**RWN***	34.5	414	150	2280	6400	3.8-9.0	0.37	0.68-0.85	0	cyclic
	RWC*										cyclic
	RWS										cyclic
(Alarcón, 2013)	**M1***	27.4	420	100	700	1600	0.45	0.72	0.44	0.15	cyclic
	M2*									0.25	cyclic
	M3*									0.35	cyclic
(Marihuén, 2014)	**W1***	27.4	420	100	700	1600	0.49	0.67	0.46	0.15	cyclic
	W7*			100		1600	0.45	0.72	0.44		cyclic
	M8			100		1600	0.45	0.72	0.64		cyclic
	M9*			100		1600	0.45	0.72	0.56		cyclic
(Rosso, Almeida, & Beyer, 2015)	**TW1**	28.8	565	80	2700	2000	3.14	0.64	0.18	0.05	cyclic
	TW4	31.2	515								cyclic

* Buckled specimen; ALR – Axial Load Ratio

2.2.1.1 Oesterle et al., 1976

A total of two rectangular walls, ten barbell walls, and two flanged walls were tested under monotonic and incrementally increasing reversed loading. Two of the barbell walls were repaired and tested once more. Figure 2-3 illustrates the nominal cross sections of the rectangular and flanged walls with a height of 4,570 mm. The objectives of the study were to determine ductility levels, load-deformation characteristics, energy dissipation capacity and strength of the walls.

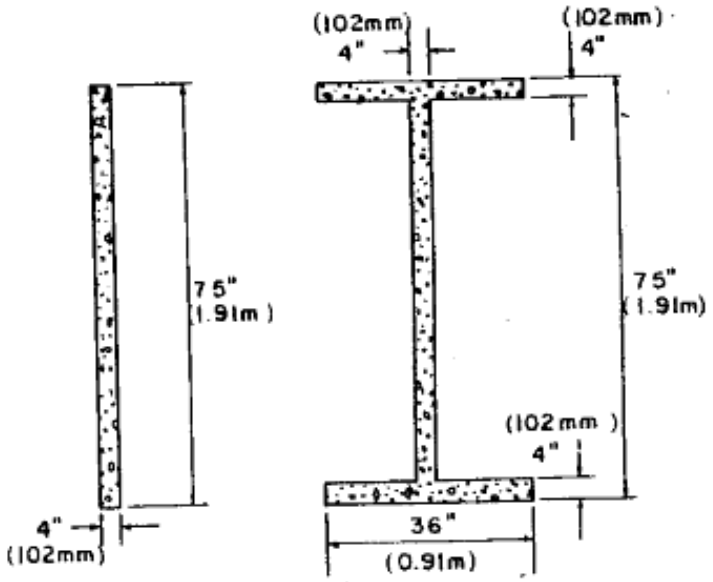

Figure 2-3. Cross section dimensions of the thin walls tested by Oesterle et al. (1976)

Wall R2 was the only one that reported out-of-plane buckling of the compression zone. It was caused by "alternate tensile yielding" of the flexural reinforcement in the boundary elements. The load-carrying capacity of the wall was reduced by the large out-of-plane deformation developed in the lower 910mm (3ft) after several load reversals. Rebar buckling and fracture were captured for the remaining three walls. Figure 2-4 shows the appearance of R2 wall at the end of the test.

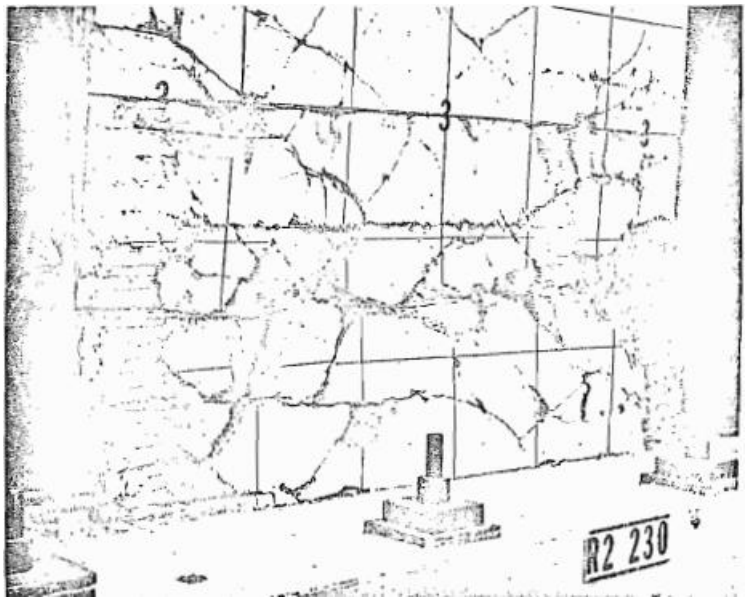

Figure 2-4. Local buckling of wall R2 tested by Oesterle et al. (1976)

2.2.1.2 Vallenas et al. (1979)

With the purpose of accomplishing a better understanding of the behavior of RCSW subjected to high shear seismic loading, Vallenas et al. (1979) simulated eight earthquake tests on three-story 1:3 scaled RC walls from prototypes of ten and seven story buildings designed in accordance with in progress code requirements.

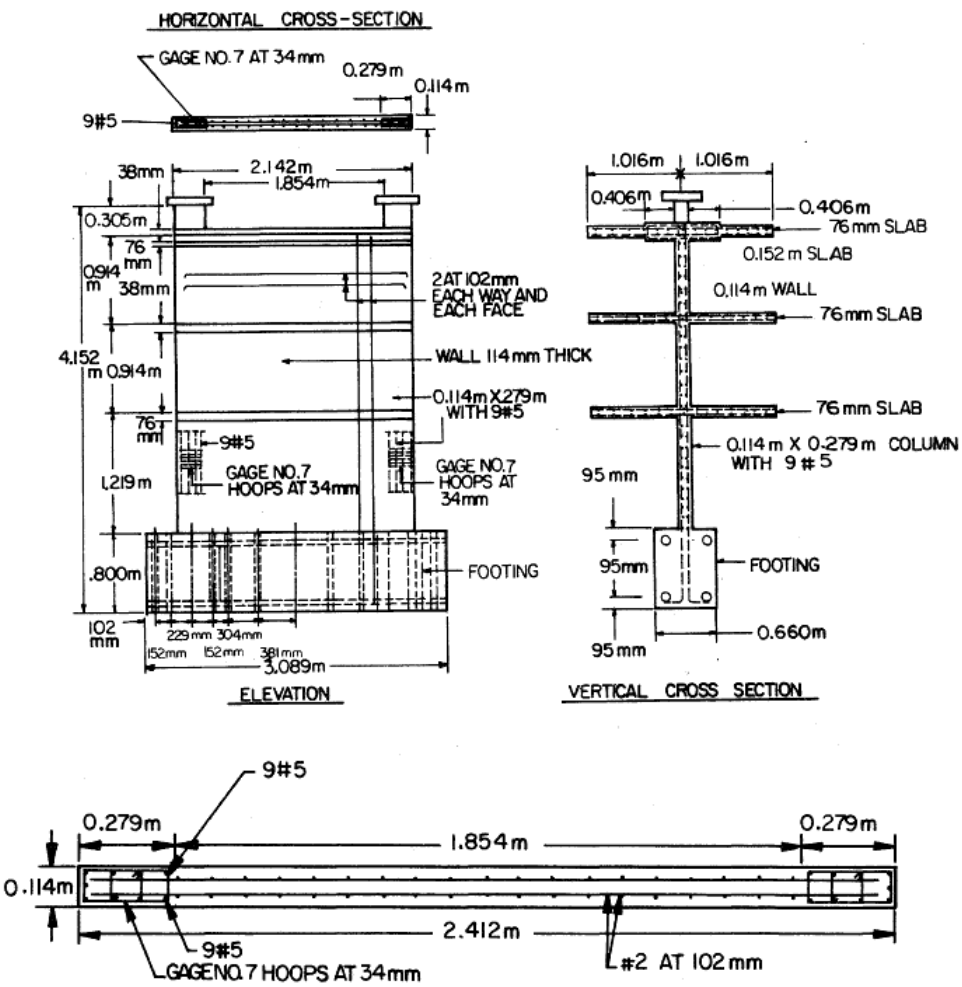

Figure 2-5. Dimensions and details of the rectangular walls tested by Vallenas et al. (1979)

This research involved the study of the influence of parameters like, type of confinement in the boundary elements, wall cross-section, moment-to-shear ratios, monotonic and cyclic load patterns, and repair procedures. Two barbell walls and two rectangular walls were considered in the study. After subjecting the specimens to the established loading conditions, they were repaired and tested again. Figure 2-5 presents the geometry and reinforcement of the original rectangular walls that reported problems associated with out-of-plane buckling instability. Steel tensile strains reached in the

boundary elements and the corresponding crack widths and spacing were identified as determining parameters to cause local buckling instability under load reversals.

2.2.1.3 Goodsir (1985)

The aim of this research was to study the capacity-based design approach established in existing code provisions, especially regarding the confinement in critical sections subjected to large compression strains. Cyclic lateral loading conditions in combination with different axial load ratios (ARL) were applied to a set of three rectangular walls and one T-section wall. Figure 2-6 and Figure 2-7 show the geometry and reinforcement of the walls considered in this experimental program.

The four specimens exhibited out-of-plane deformations especially concentrated in the boundary elements. The failure modes detected for walls R1 and R4 suggested material failure instead of lateral instability. The full east end of the R2 wall buckled before returning to the original straight position during the last cycles until out-of-plane stability was observed. The web of T3 wall also experienced lateral instability. Figure 2-8 shows the final state of T3. The slenderness of the specimens was considered one of the main reasons to provoke large out-of-plane deformations in combination with residual tensile strains captured in the longitudinal bars when they were resisting compressive loads.

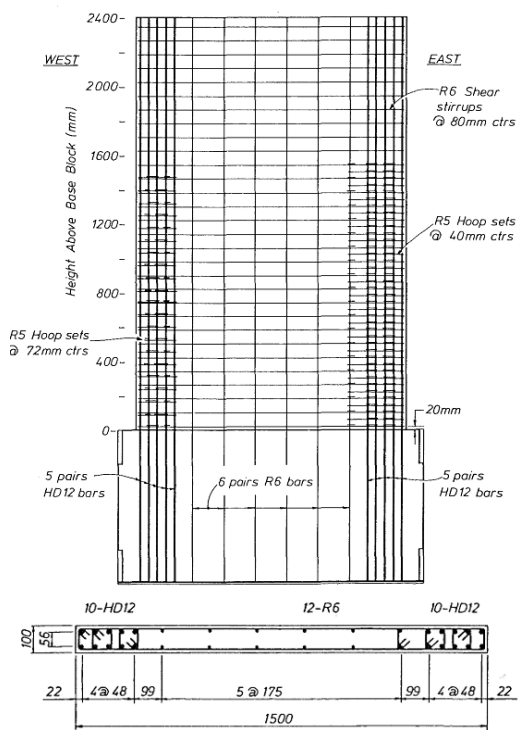

Figure 2-6. Typical rectangular wall tested by Goodsir (1985)

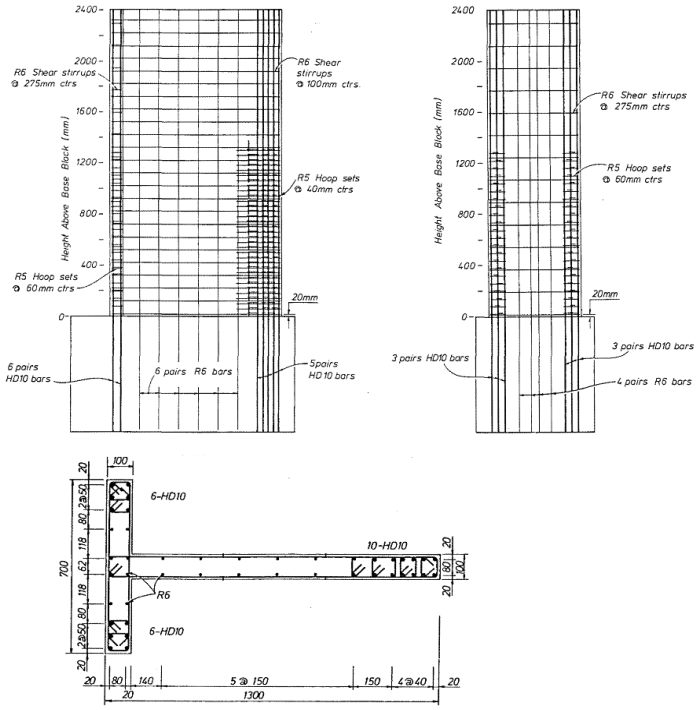

Figure 2-7. T-section wall tested by Goodsir (1985)

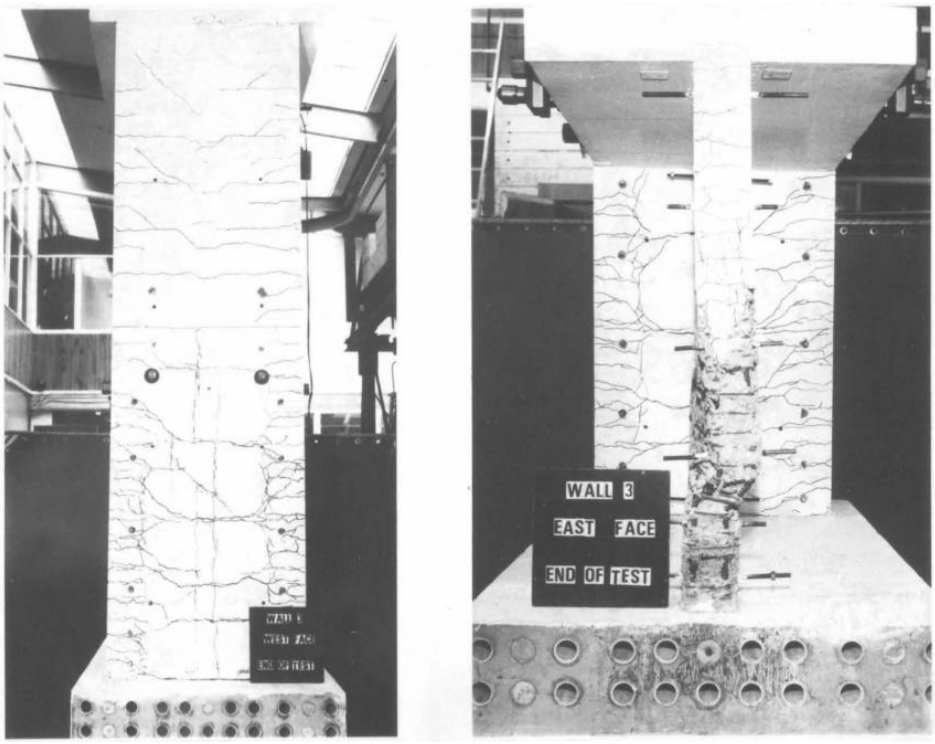

Figure 2-8. Wall T3 at the end of the test. Views: west face, east end. (Goodsir, 1985)

2.2.1.4 Thiele et al. (2000)

Three 1:3 scaled rectangular walls were tested by Thiele et al. (2000), where extreme pseudo-dynamic loads were applied. The influence of the reinforcement content and the axial force were investigated. Figure 2-9 illustrates the configuration of the walls considered in this study.

The results reported local buckling for walls WPH2 and WPH4 at 400% and 300% of an artificially generated earthquake, respectively. Wall WPH3 did not present out-of-plane buckling behavior. Figure 2-10 shows the end of the test conducted for WPH2. The most significant conclusions from the tests were: a) the effect of low and moderate earthquakes combined with high axial load ratios could be advantageous since the stiffness is not severely affected at small plastic elongations; and, b) under strong earthquakes, walls with high axial load ratios could fail prematurely since low levels of energy dissipation are achieved.

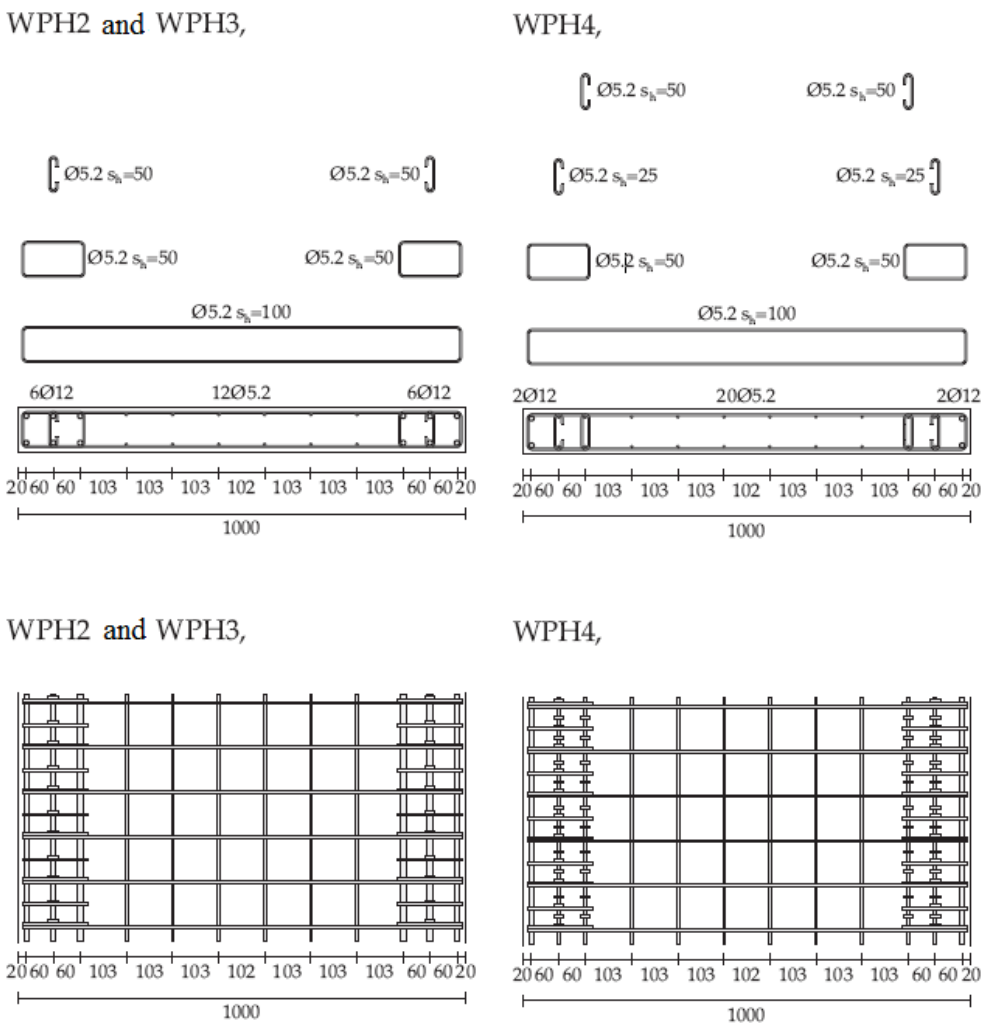

Figure 2-9. Geometry and reinforcement of the walls tested by Thiele et al. (2000)

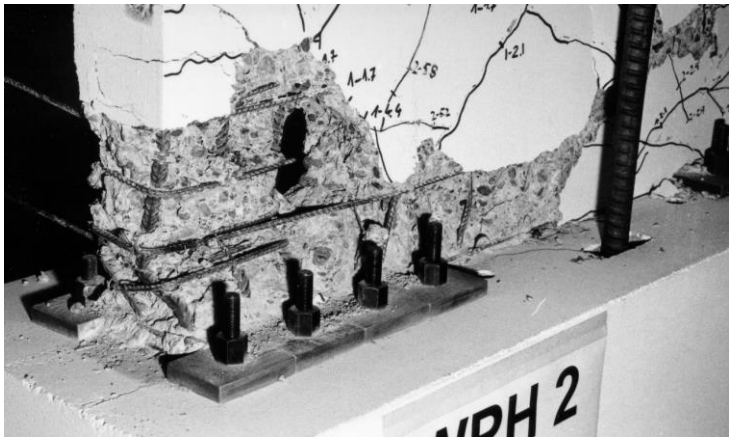

Figure 2-10. South side of the wall WPH2 after failure. Buckled zone.

2.2.1.5 Thomsen & Wallace (2004)

Six quarter-scale wall specimens were tested under the experimental verification carried out by Thomsen & Wallace (2004), but because of the scope of this research, only the results of two solid rectangular (RW1, RW2) and two T-shaped (TW1, TW2) walls cross sections are presented. Figure 2-11 and Figure 2-12 show the reinforcing details of the four specimens which were subjected to cyclic lateral displacements in combination with axial loads of approximately $0.10A_g f'_c$.

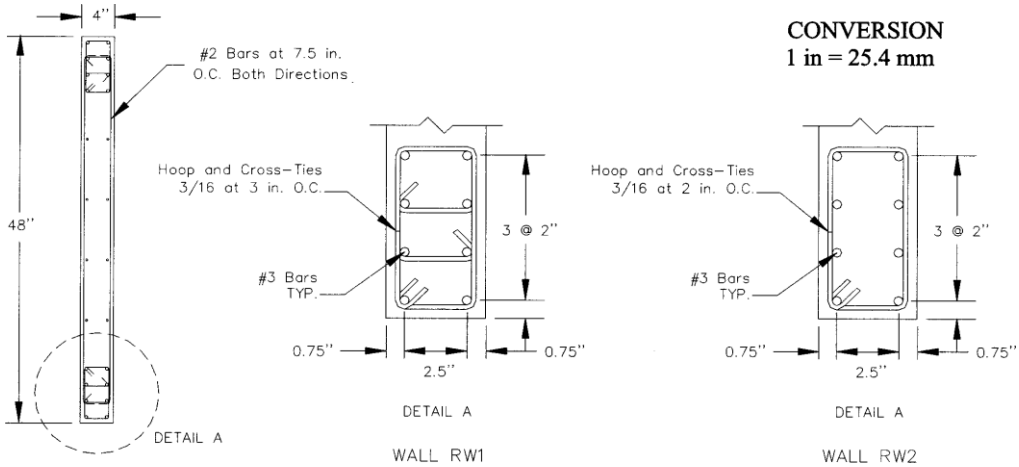

Figure 2-11. Reinforcing details for the rectangular walls tested by Thomsen & Wallace (2004)

Specimen RW1 reported significant loss in lateral load capacity when buckling of the longitudinal reinforcement was produced at 2.5% drift. RW2 behaved similarly but because of the closer spacing of the hoops at the boundary elements, the lateral load capacity was maintained longer. Specimen TW1 experienced brittle failure for a drift of 1.25% where buckling of the bars located along the boundary element and the web was observed. Even though the lateral load capacity for the specimen TW2 exceeded the response from TW1, it was the only one affected by out-of-plane

buckling deformations primarily caused by a very narrow confined core. Figure 2-13 reveals the damage at the end of the tests for the four specimens.

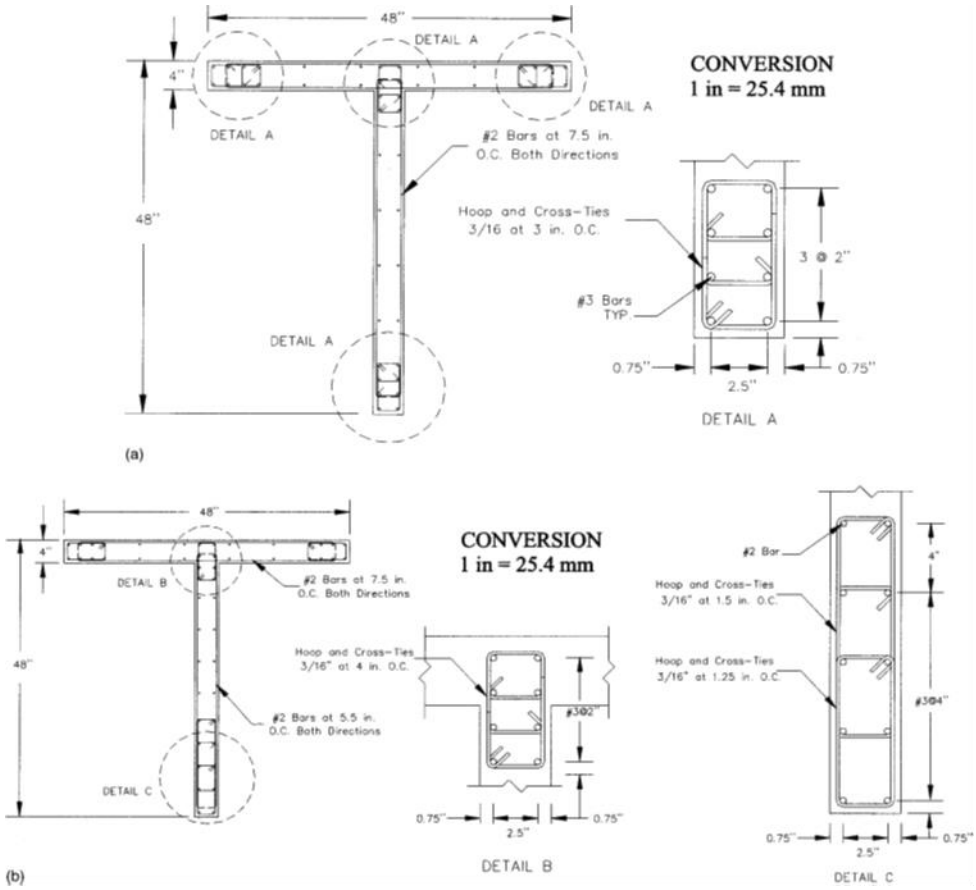

Figure 2-12. Reinforcing details of the T-shaped walls tested by Thomsen & Wallace (2004) (a) TW1, (b) TW2.

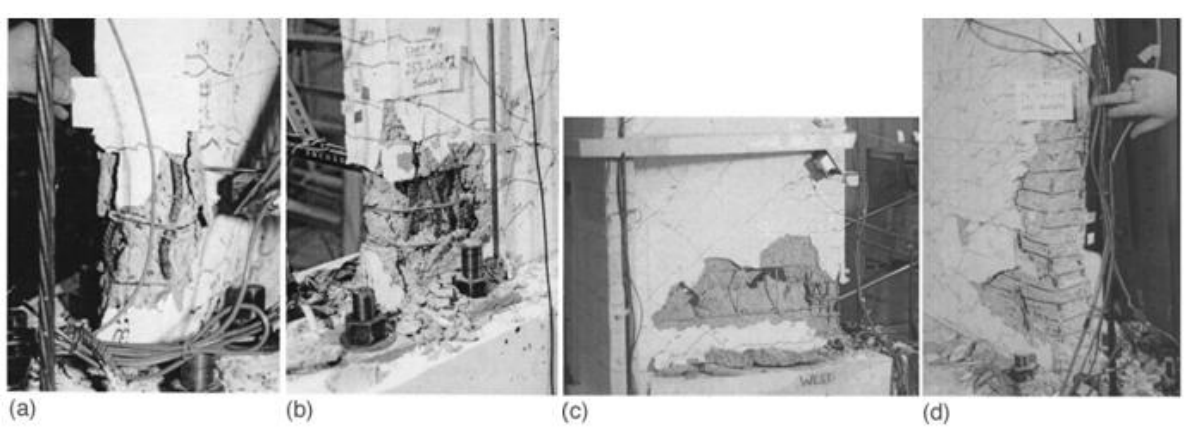

Figure 2-13. Walls (a) RW1 damage—2% drift; (b) RW2 damage— 2.5% drift; (c) TW1 damage—1.25% drift; and (d) TW2 damage—2.5% drift

2.2.1.6 Brueggen (2009)

Two T-shaped RCSW were subjected to multidirectional cyclic loading as part of a research program focused on developing a simplified modeling approach to predict the response of structural walls under the philosophy of performance-based design. The reinforcing detailing of the two specimens NTW1 and NTW2 is shown in Figure 2-14 and Figure 2-15.

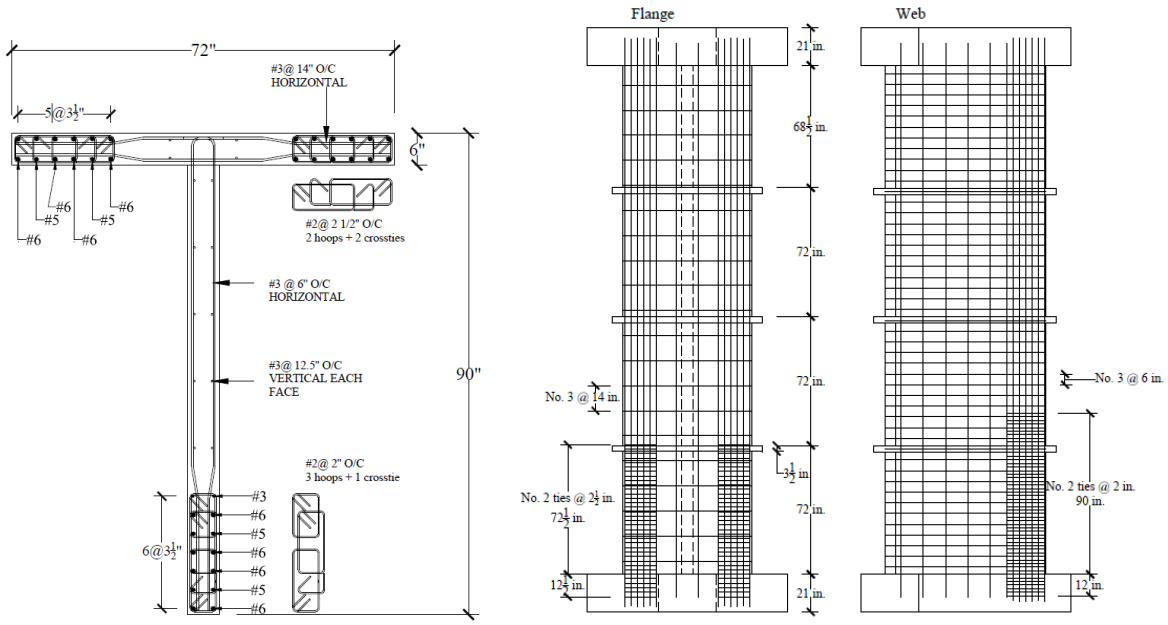

Figure 2-14. NTW1 detailing. Section and elevation views.

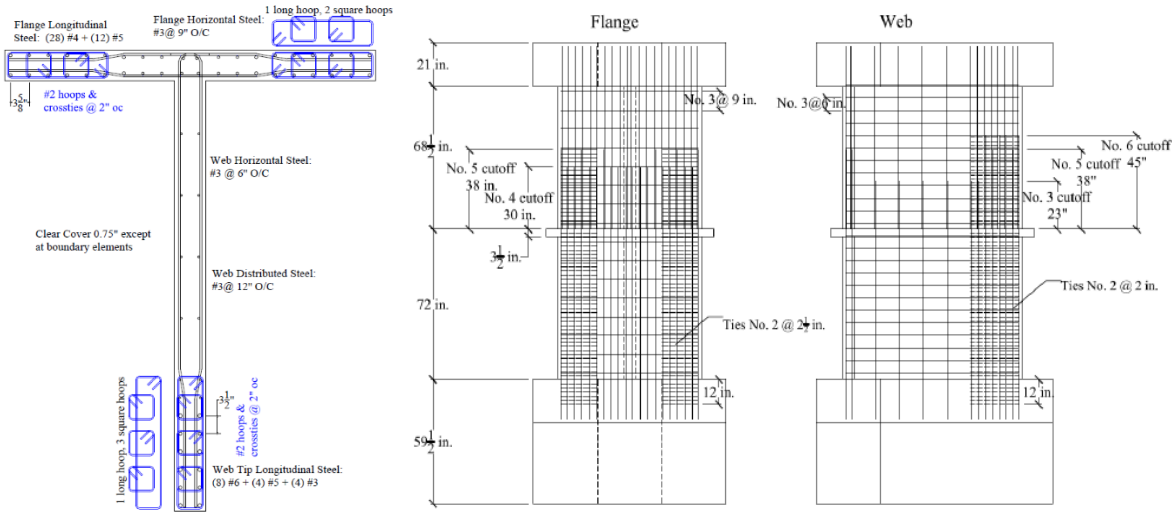

Figure 2-15. NTW2 detailing. Section and elevation views.

The damage during the flange-in-tension direction of the wall NTW1 was caused by the failure of the confinement in the boundary element of the web; consequently, concrete core crushed and the longitudinal reinforcing buckled. This behavior was associated with unwinding of the confining hoops

close to the base of the web tip. Based on the structural performance of NTW1, when constructing the wall NTW2, the open corner of the hoops was relocated out of the extreme compression reinforcement and additionally the confined region was extended. The modifications led to a failure caused by fracture of the confining reinforcement.

The study concluded that increasing the length of the boundary elements produced an irrelevant effect on the general structural behavior of the latter specimen whose north flange experienced out-of-plane buckling as illustrated in Figure 2-16. The results also demonstrated that the skew-direction loading did not increment significantly the maximum compression strains in comparison to the orthogonal loading at the same drift level, nor it did generate larger compression strains in the unconfined regions of the specimens which would provoke early web failure.

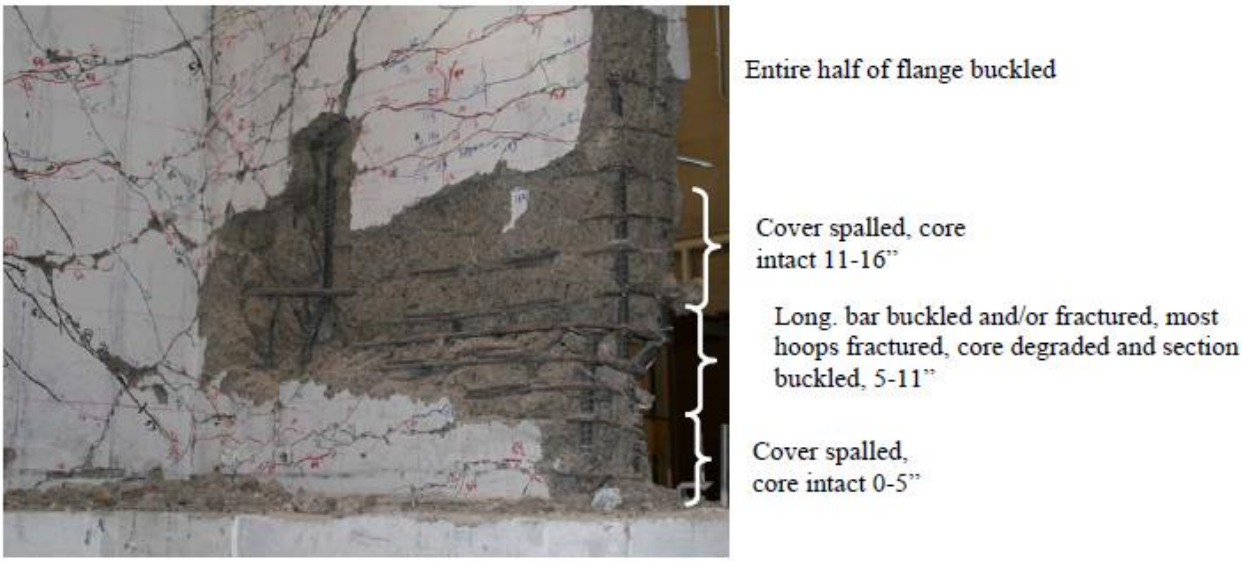

Figure 2-16. North flange tip of the NTW2 wall tested by Brueggen (2009)

2.2.1.7 Aaleti et al. (2013)

In order to investigate the consequences of considering continuous reinforcement (N), lap splices (S), and mechanical couplers (C) in the plastic hinge region, three identical rectangular RCSW were built and tested under cyclic reversal loadings. Two different boundary elements were included in the design with the purpose of accounting for a flange. Figure 2-17 shows the cross section and elevation views of the specimens.

Specimens RWN and RWC experienced lateral instability in the left boundary elements by the time a 2.0% drift was reached. Figure 2-18 shows the local buckling behavior of the specimen RWC. The cause of the failure was attributed to the combination of large compressive forces, large tensile strains developed in previous cycles, large in-plane displacements, and the lack of out-of-plane

supports at the level of the floor diaphragms. Specimen RWS, with twice the longitudinal reinforcement, did not exhibited out-of-plane buckling instability.

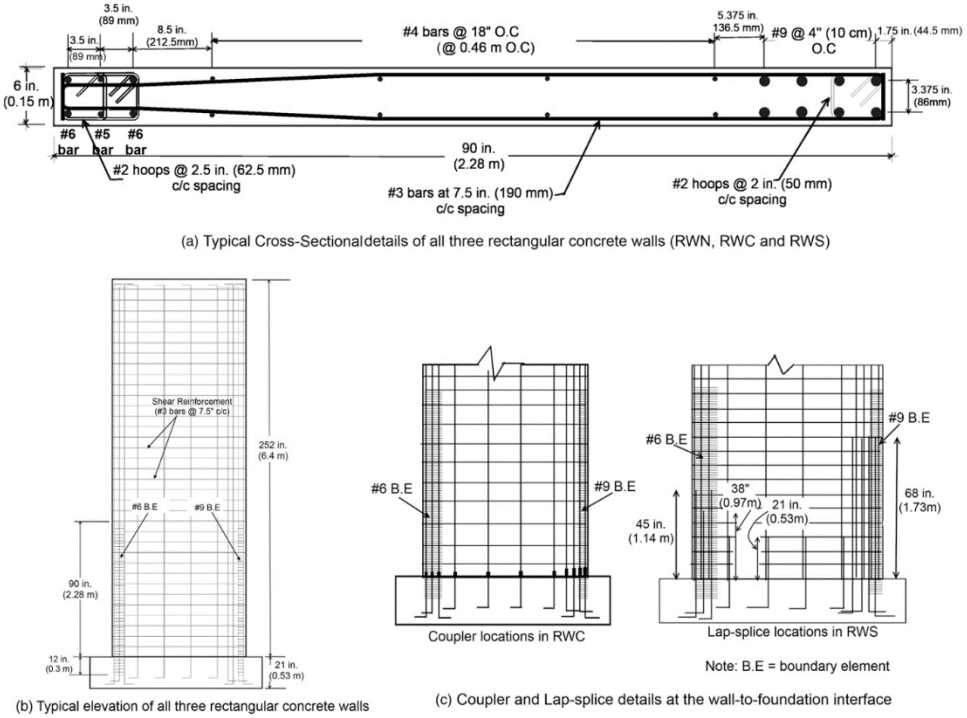

Figure 2-17. Reinforcement details of the three walls (RWN, RWC, and RWS) tested by Aaleti et al. (2013)

Figure 2-18. Buckling of the boundary element. Specimen RWC

2.2.1.8 Alarcon (2013)

After the 2010 Chile earthquake, some experimental programs have been conducted in that region in order to reproduce the different observed failure modes in RCSW. In particular, Alarcon (2013), captured the influence of the axial load ratios in the seismic structural performance of thin rectangular RC walls without seismic detailing. A prototype RC wall was established as a function of a survey of walls damaged in the mentioned earthquake. This project involved the construction of three identical 1:2 scaled RC wall specimens subjected to in-plane double-cycle increasing displacements following the application of axial loads. Constant ALRs of 0.15, 0.25, and 0.35 were considered for each specimen. Figure 2-19 presents the geometry and reinforcement of the three specimens. A cross section of 700mm length, 100mm thick, and 1600mm height was utilized. The average concrete strength was 27.4 MPa. Steel yielding strengths of 420 MPa and 500 MPa were employed for the longitudinal and transverse reinforcement, respectively.

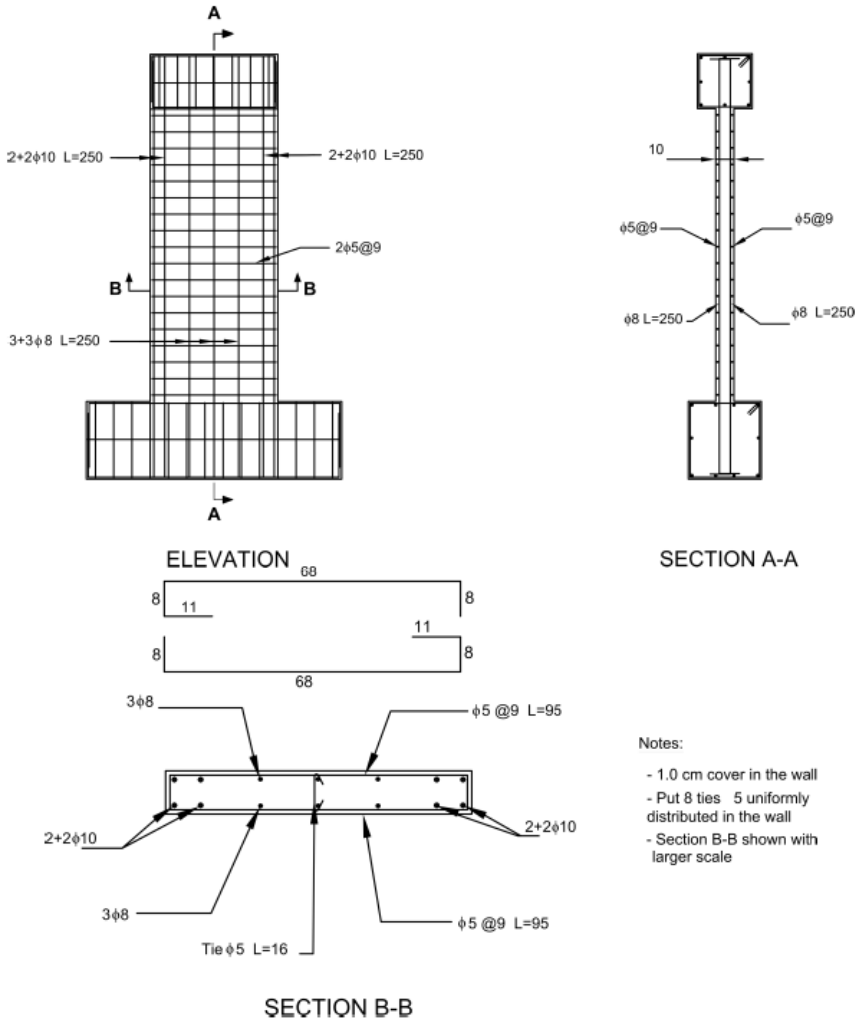

Figure 2-19. Reinforcement detailing of walls tested by Alarcon (2013)

The failure mode detected in the three walls was controlled by axial-flexure interaction associated with a relatively high *M/V*lw* ratio of 2.5 (*M*:moment; *V*:shear). The sequence of the observed structural behavior for the three walls was, flexural cracking, yielding of reinforcement, vertical cracking, concrete spalling and reinforcement buckling accompanied with opening of horizontal reinforcement, concrete crushing failure, and wall buckling. Out-of-plane buckling was developed as a consequence of compressive failure and small wall thickness (Figure 2-20). The results indicated that high ARLs induce a substantial decrease in the ultimate curvature, displacement capacity, and ductility.

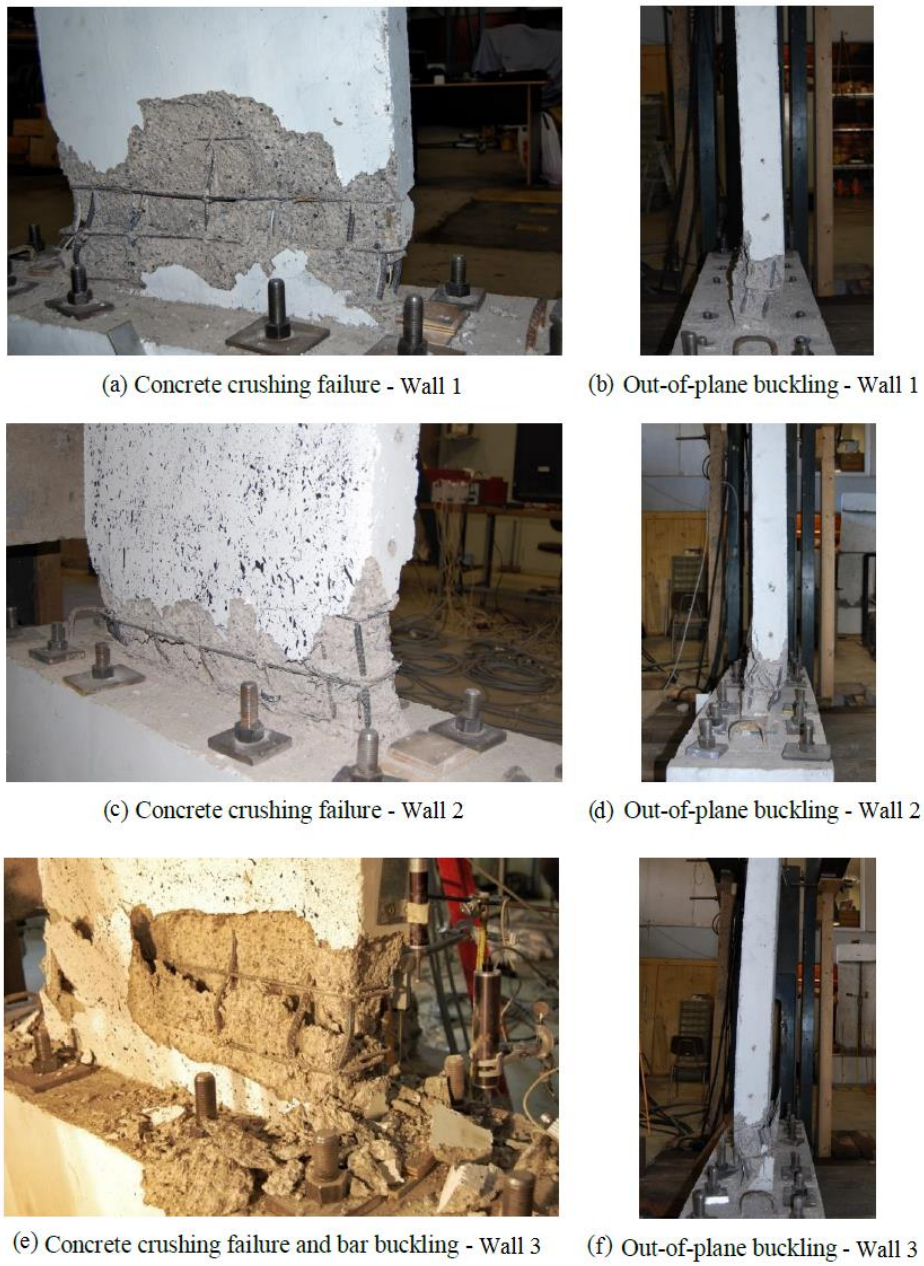

(a) Concrete crushing failure - Wall 1 (b) Out-of-plane buckling - Wall 1

(c) Concrete crushing failure - Wall 2 (d) Out-of-plane buckling - Wall 2

(e) Concrete crushing failure and bar buckling - Wall 3 (f) Out-of-plane buckling - Wall 3

Figure 2-20. Observed behavior of three walls tested by Alarcon (2013)

2.2.1.9 Marihuén (2014)

This study was part of a large experimental program where Alarcon (2013) was involved. Marihuén (2014) tested six walls in total with a length l_w equal to 700mm. Figure 2-21 presents the different reinforcement detailing considered for each specimen. The material mechanical properties were similar to the values specified in the latter case study.

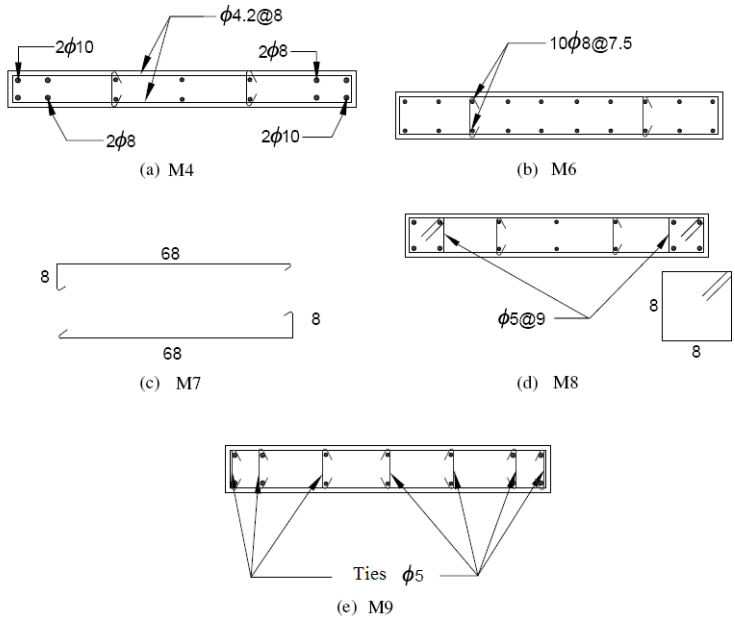

Figure 2-21. Reinforcement detailing for the walls tested by Marihuén (2014)

Figure 2-22. Observed damage of specimen M5 tested by Marihuén (2014)

In general, five specimens suffered out-of-plane buckling deformations after crushing was observed at the bottom regions of the walls, Figure 2-22. Only wall M8 behaved differently, which failed due to flexural-compression effects without exhibiting out-of-plane buckling after crushing. The difference can be attributed to the transverse reinforcement distribution that consisted of locating the closed stirrups in the space between the principal horizontal reinforcement and not at the same level.

2.2.1.10 Rosso et al. (2015)

Five thin flanged reinforced concrete walls were tested at EPFL under different in-plane and out-of-plane loading protocols. The response of walls TW1 and TW4 are detailed by Rosso et al. (2015), where significant damage was observed at the end of the tests. These two full scaled walls were geometrically identical and only considered a single layer of longitudinal and transverse reinforcement. The web was 2,000mm tall, 80mm thick, and 2,620mm long. The flange was 80mm thick and 440mm long. Figure 2-23 shows the geometry and reinforcement detailing of the specimens.

Mainly, the test results showed that premature in-plane failure of thin walls including only a single layer of reinforcement could be caused by large out-of-plane deformations. Additionally, it was demonstrated that out-of-plane deformations larger than half of the wall thickness did not necessarily lead to inelastic buckling failure of a wall contrary to what was suggested by Paulay and Priestley (1993). Figure 2-24 captures the deformed shapes of TW1 and TW4.

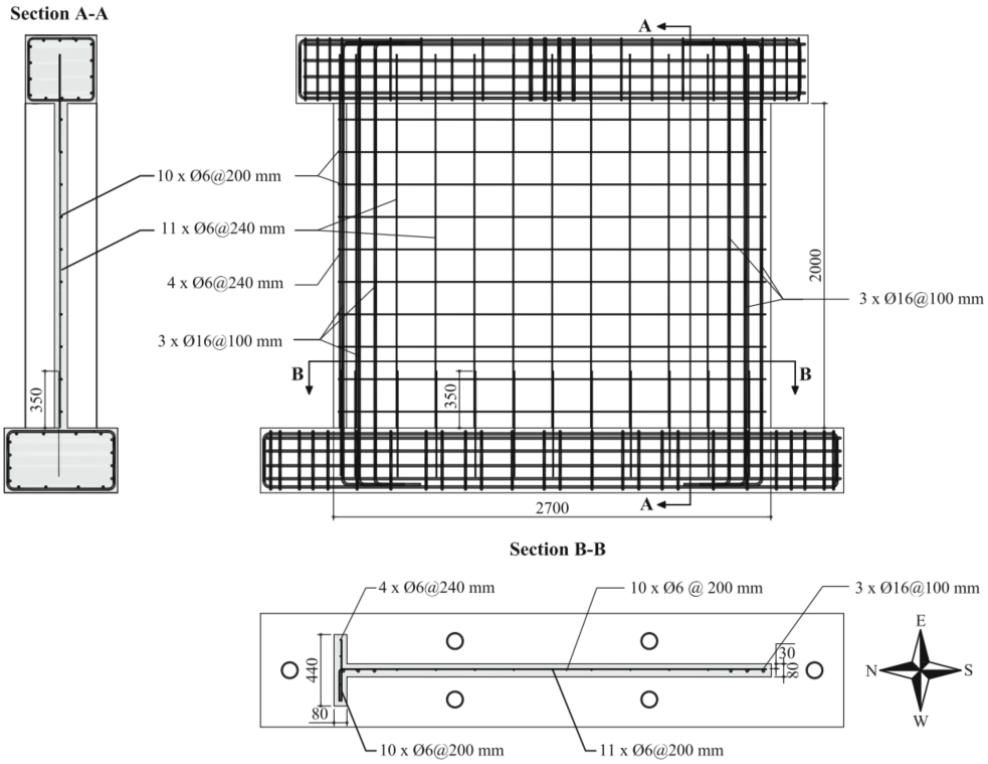

Figure 2-23. Geometry and detailing of walls TW1 and TW4 tested by Rosso et al. (2015)

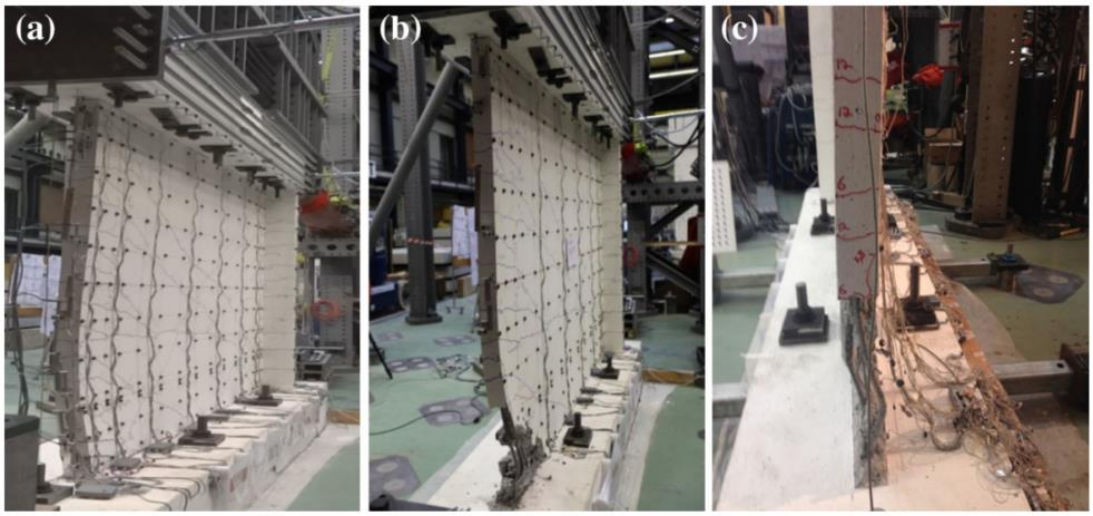

Figure 2-24. Deformed shapes: (a) Wall TW1 at 0% in-plane drift; (b) Wall TW1 at the end of the test; (c) Wall TW4 at the end of the test. (Rosso et al., 2015)

2.2.2 Laboratory studies in boundary elements – prisms

Noticing the concentration of damage in the boundary elements of planar RCSW due to higher stress and strain demands, some investigations have been carried on prisms, which constitutes an economical procedure to study the influence of critical parameters associated with out-of-plane instability of RCSW. In general, the prisms are subjected to axial tensile and compressive actions to simulate vertical seismic components developed in the boundary elements of RCSW. Table 2-3 summarizes the principal parameters that varied in the experimental programs reviewed in this section.

Table 2-3. Parametric Study: Prisms

Test Name	# of prisms	Material Properties		Geometry			Reinforcement		Max. Tensile Strains [%]	Axial Load Type, T-Tension C-Compression
		f'c [MPa]	fy [MPa]	Cross Section [mm²]	Clear Cover [mm]	Height [mm]	Long. [%]	Trans. dt@sh [mm]		
(Goodsir, 1985)	1	24.1	442	160x480	12.5	970	3.14	5@64	-	cyclic T - C
	2	24.1	442			970		6@64	-	cyclic T - C
	3	24.1	442			970		6@96	N/A	C
	4	24.1	290			970		5@64	2.3	cyclic T - C
	5	29.0	290			970		5@64	-	cyclic T - C
	6	29.0	290			730		5@64	-	cyclic T - C
	7	29.0	350			730		5@64	-	cyclic T - C
	8	29.0	350			490		5@64	2.5	cyclic T - C
	9	29.0	350			490		5@64	-	cyclic T - C
(Chai & Elayer, 1999)	1	34.1	375	102x203	6	1199	2.1	6@57	2.55	cyclic T - C
	2		455			1199	3.8	6@76	1.85	
	3,4,5		375			1505	2.1	6@57	1.61	
	6,7,8		455			1505	3.8	6@76	1.43	
	9,10,11		375			1811	2.1	6@57	1.39	
	12,13,14		455			1811	3.8	6@76	1.17	

Table 2-3. Continued

Test Name	# of prisms	Material Properties		Geometry			Reinforcement		Max. Tensile Strains [%]	Axial Load Type, T-Tension C-Compression
		f'c [MPa]	fy [MPa]	Cross Section [mm^2]	Clear Cover [mm]	Height [mm]	Long. [%]	Trans. dt@sh [mm]		
(Creagh et al., 2010)	1	30	460	152x305	19	915	3.7	9.5@50	4.0	1 cycle T - C
	2								N/A	C
(Chrysanidis & Tegos, 2012b)	1	24.89	604	75x150	8	900	2.68	4.2@33	0.0	1 cycle T - C
	2								1.0	
	3								2.0	
	4								3.0	
	5								5.0	
(Chrysanidis & Tegos, 2012a)	1	23.33	604	75x150	8	900	1.79	4.2@33	3.0	1 cycle T - C
	2	22.22					2.68			
	3	22.82					3.18			
	4	22.82					3.68			
	5	23.26					4.02			
	6	23.26					4.19			
	7	23.26					5.47			
	8	23.26					6.03			
	9	23.26					7.15			
	10	23.26					8.21			
	11	23.26					10.72			
(Shea et al., 2013) & (Flintrop et al., 2013)	1	28	414	152x381	25	762	2.9	9.5@203	4.5	cyclic T - C
	2							9.5@203	3.0	
	3							9.5@152	4.5	
	4							9.5@152	4.5	
	5							9.5@203	4.5	
	6							9.5@152	4.5	
	7							9.5@114	4.5	
	8							9.5@114	4.2	
(Welt, 2015)	CS14	26	576	381x203	16	1016	2.6	9.5@64	1.09	cyclic T - C
	CS10	26	576					9.5@64	2.0	cyclic T - C
	CS16	32	553					9.5@64	2.4	cyclic T - C
	CS17	32	553					9.5@64	2.47	cyclic T - C
	CS8	27	576					9.5@128	1.35	cyclic T - C
	CS1	27	576					9.5@64	2.0	cyclic T - C
	CS4	27	576					9.5@64	2.1	cyclic T - C
	CS6	27	576					9.5@64	2.25	cyclic T - C
	CS2	27	576					9.5@64	5.0	Pre-strain + cyclic

2.2.2.1 Goodsir (1985)

Nine prisms were tested as part of the experimental program described previously. Once Goodsir (1985) completed the tests on the RCSW, the potential of out-of-plane instability developed in the boundary elements when the walls were subjected to reversal lateral loads was detected. Figure 2-25 shows the details of a typical prism considered in this study including the testing assembly. Aspect ratios of 7, 5.5, and 4 were utilized.

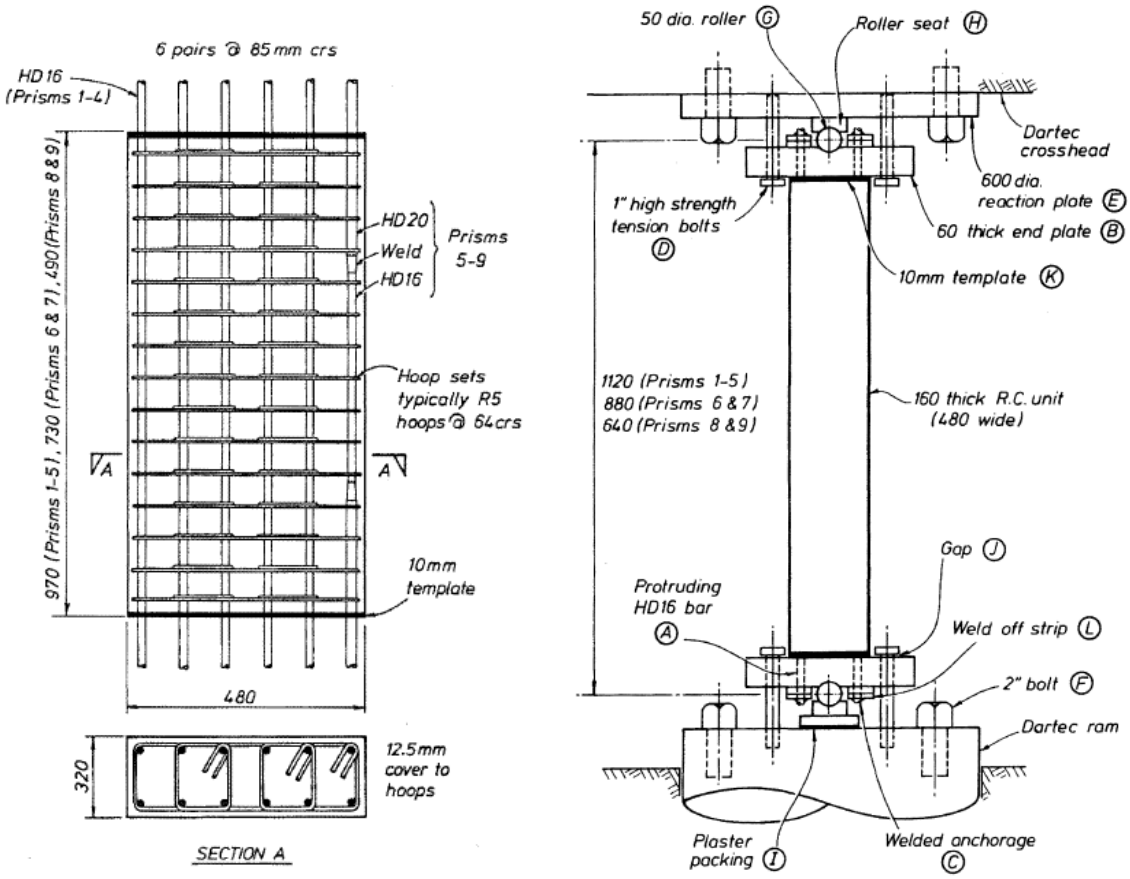

Figure 2-25. Reinforcement details and test set-up of a typical prisms considered by Goodsir (1985)

Axial displacements were imposed to reach the set of strains in tension and compression. Only unit #3 was imposed a monotonic load and it performed well. The specimens with the two highest aspect ratios developed buckling failure. The two units with aspect ratio of 4 reported a failure associated with concrete crushing although out-of-plane deformations were also recorded. Degradation of bond between the longitudinal reinforcement and the concrete was identified to be more critical at higher strains for cyclic loading in comparison to monotonic loading. Figure 2-26 presents the final state of four of the prisms tested in this program.

The Euler buckling theory was used as an attempt to predict the out-of-plane deformations on the prisms, however the results fell apart from what was expected. This research highlighted the fact that buckling instability is prone to happen with increasing aspect ratios and high tensile strain levels. In fact, Goodsir (1985) defined this mechanism as the effect of large inelastic tensile strains accompanied by cracking of the boundary elements at the level of the plastic hinge region. Under load reversals, out-of-plane deformations can be generated in the compression zone as a consequence of two possible scenarios: remaining horizontal open cracks, and exceedance of limit tensile strains.

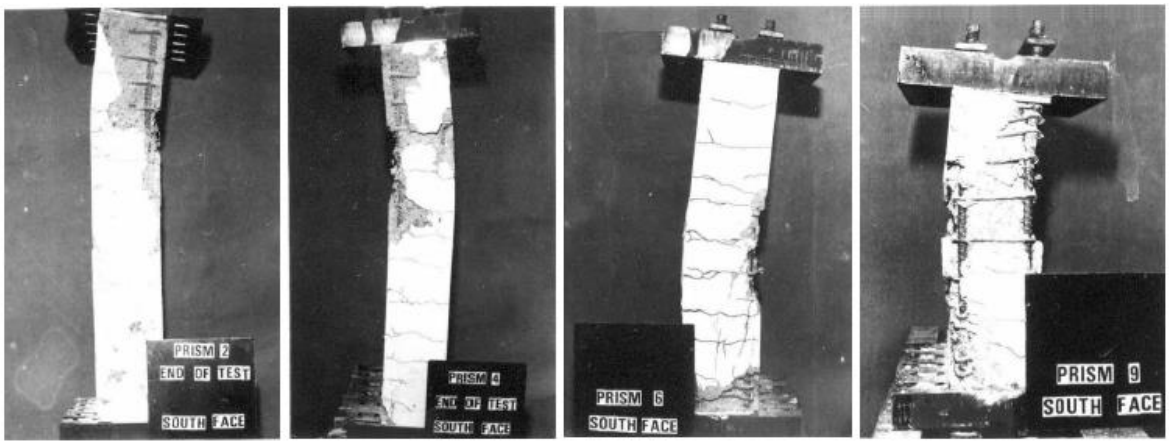

(a) Prism #2 (b) Prism #4 (c) Prism #6 (d) Prism #9

Figure 2-26. Final state of four prisms tested by Goodsir (1985)

2.2.2.2 Chai & Elayer (1999)

Fourteen prisms were tested to establish the maximum tensile strain that a ductile prism could sustain under quasi-static axial forces. The axial reversed cyclic loading comprised an initial half-cycle of axial tensile strain followed by a compression half cycle. The target compressive strain for twelve prisms consisted of 1/7 of the axial tensile strain and 1/5 for the other two specimens. Aspect ratios (Lo/b_w = *height/thickness*) of 11.75, 14.75, and 17.75 were used in a combination with two longitudinal reinforcement ratios of 2.1% (6 bars 9.525mm) and 3.8% (6 bars 12.7mm). Transverse ties of 6.4mm diameter spaced at 57mm and 76mm were adopted as a function of the longitudinal rebar diameter, respectively. Figure 2-27 shows the geometry and reinforcing details for the specimens considered in the experimental program.

In general, the prisms with 2.1% longitudinal steel ratio exhibited out-of-plane instability upon compressive loading after approaching larger tensile strains compared with the prisms with 3.8% reinforcement content. In addition, the cases with the largest Lo/b_w ratio reported lower tensile strains before the onset of inelastic buckling was captured upon compression. These findings suggest that the longitudinal reinforcement ratio and the height-to-thickness ratio play an important role on the lateral stability of walls.

A kinematic relation between the axial strain and the out-of-plane displacement had been proposed previously by Paulay & Priestley (1993) once the tensile strains imposed on a RCSW was recognized as a critical parameter that governs its lateral stability. Chai & Elayer (1999) proposed an improved phenomenological model based on the same concept. When the maximum tensile strain values predicted from the two mentioned formulations were compared to the tests results of this experimental program, both methods showed to be conservative. Figure 2-28 shows samples of two buckled shapes for prisms with aspect ratios equal to 14.75 and 17.75, respectively.

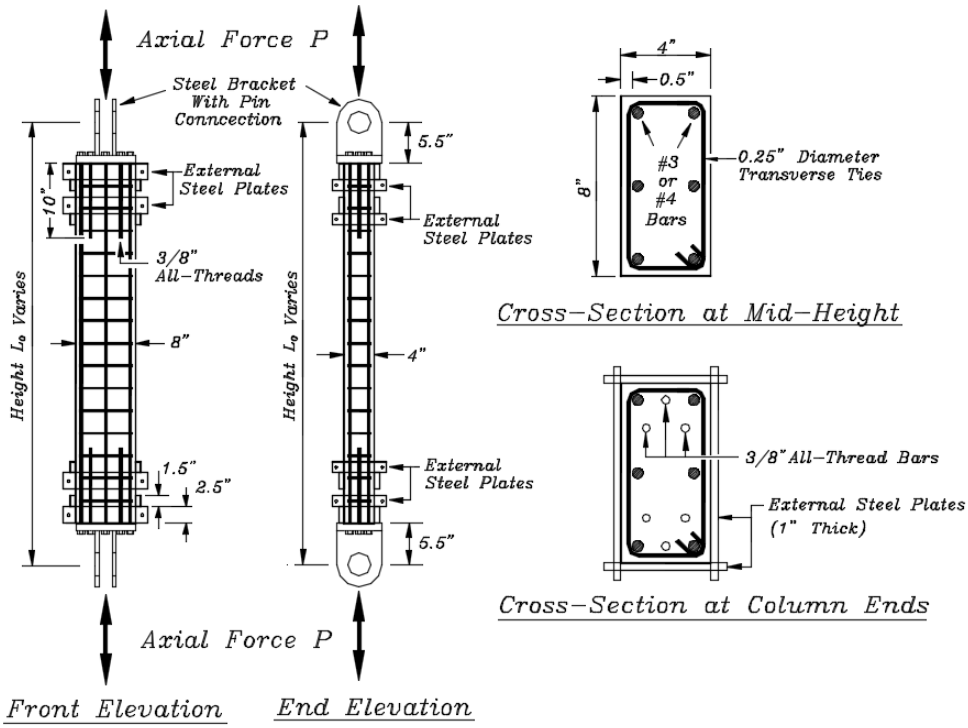

Figure 2-27. Cross area and reinforcement details of prisms tested by Chai & Elayer (1999)

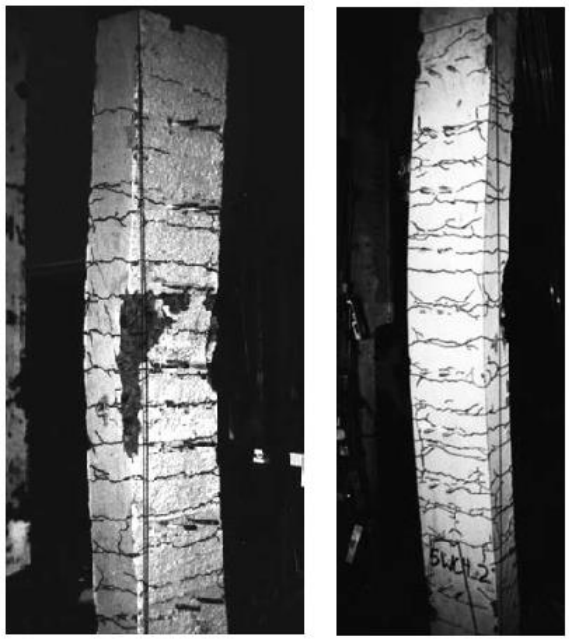

(a) Lo/b = *14.75* (b) Lo/b = *17.75*

Figure 2-28. Samples of buckled shapes for prisms tested by Chai & Elayer (1999)

2.2.2.3 Creagh et al. (2010)

Two prisms were tested by Creagh et al. (2010) to demonstrate how tensile strains reached in special boundary elements affect the load bearing capacity and incite a buckling failure mode. The specimens were constructed as showed in Figure 2-29. The first prism was tensioned until yielding and then it was subjected to sequential tensile strains of 1.5, 2.0, 3.0, and 4.0%; the later followed by a single compressive action until failure. The second prism was directly subjected only to compression.

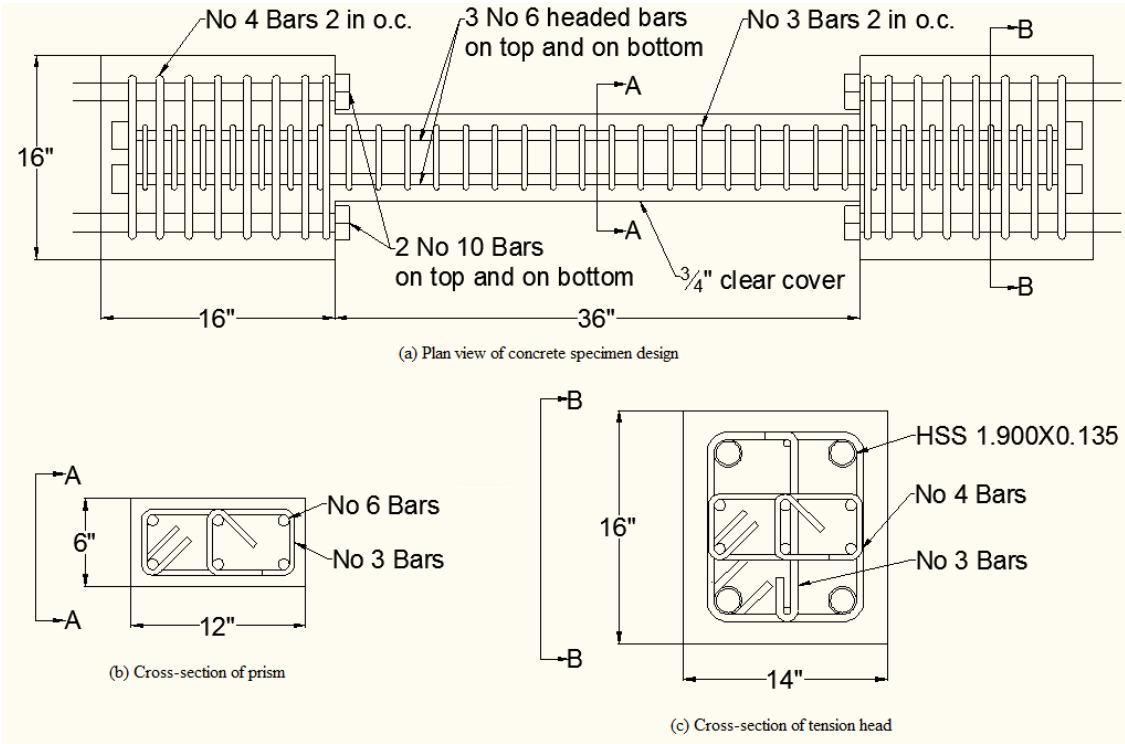

Figure 2-29. Geometry of specimens tested by Creagh et al. (2010)

The damage of the specimens at the end of each test is presented in Figure 2-30. Two different failure mechanisms were observed: prism #1 evidenced buckling instability; and, prism #2 suffered a brittle failure due to concrete crushing in the upper zone. The final compression capacity of prism #1 resulted a third of the one exhibited by prism #2. Further research was suggested on the conditions that make the boundary elements more vulnerable to excessive tensile strains. Still, a method to prevent out-of-plane buckling was not proposed.

(a) Specimen 1. Final state

(b) Specimen 2. Final state

Figure 2-30. Damage stages of specimens tested by Creagh et al. (2010)

2.2.2.4 Chrysanidis & Tegos (2012b)

In order to study the effect of high tensile strains reached in boundary edges of thin RCSW, with respect to the ultimate bearing capacity as a function of a decrease in the effective rigidity, five identical 1:3 scaled specimens were experimentally tested by Chrysanidis & Tegos (2012b). The geometry and reinforcement details of the prisms are shown in Figure 2-31.

The specimens were subjected to five elongation levels with values of 0.0, 10.0, 20.0, 30.0, and 50.0‰, respectively. A uniaxial tensile load followed by a concentric compression load constituted the load pattern for the tests. Different structural behaviors were detected in the process. The three first specimens reported failure modes related to crushing of the compression zone. The last two specimens with elongations levels of 30.0‰ and 50.0‰ experienced compressive capacity reductions in the order of 38% and 26%, respectively. The failure mechanism recounted for these latter specimens was associated with out-of-plane buckling.

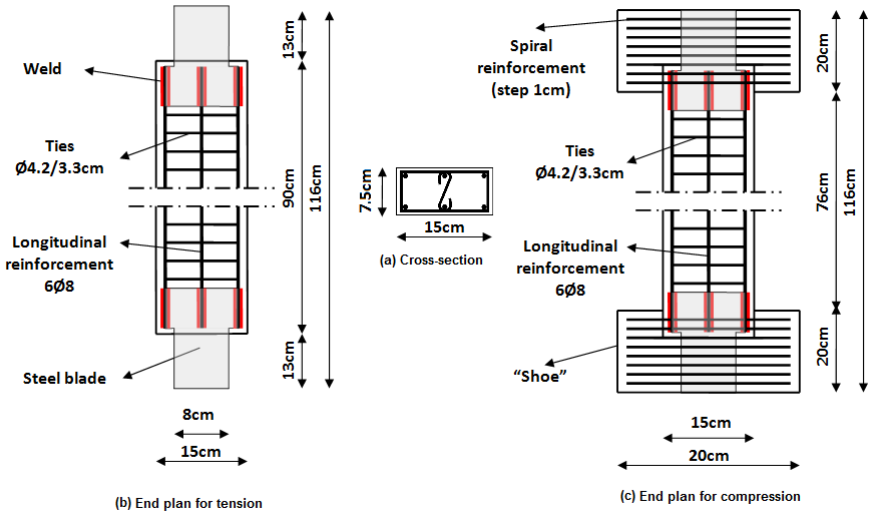

Figure 2-31. Geometry details of the specimens tested by Chrysanidis & Tegos (2012b)

Figure 2-32. Failure mechanism of the five specimens tested by Chrysanidis & Tegos (2012b)

The stated results corroborate the close relationship between the levels of tensile strains and the performance of boundary ends of thin RCSW. Additionally, this study identified the lateral instability as a complex phenomenon that requires further examination since it does not only depend on aspect ratios as previously suggested by some design codes. Figure 2-32 illustrates the final state of the specimens at the end of the tests. The legend below each case describes the rebar distribution,

the longitudinal reinforcement ratio multiplied by 100, the degree of elongation (‰), and the number of the specimen.

2.2.2.5 Chrysanidis & Tegos (2012a)

With the aim of completing the previous research, another eleven specimens with similar geometries but different longitudinal reinforcement ratios, between 1.79 and 10.72%, and different concrete strengths were tested. All specimens were subjected to a single tensile strain degree of 30.0‰ before exposing them to a compression load to complete the cycle. As result, two important outcomes are specified: first, an increment in longitudinal reinforcement ratio does not reduce the chance of instability because out-of-plane buckling was reported for all cases; and second, the mentioned increment does not always lead to a buckling failure load rise but it seems to depend on the rebar distribution. Figure 2-33 shows the failure modes of the eleven specimens considered in this phase. A procedure to predict the local buckling behavior was not suggested as part of this experimental program.

Figure 2-33. Failure mechanism of the eleven specimens tested by Chrysanidis & Tegos (2012a)

2.2.2.6 Shea et al. (2013) & Flintrop et al. (2013)

Eight reinforced concrete prisms were subjected to cyclic loading as part of the 2013 NEES@UCLA project. The longitudinal reinforcement ratio and the prism height (762 mm) were identical for all eight specimens but hoop spacing varied. The cross-area and detailing of the prisms are exhibited in Figure 2-34. Regarding the material properties, 28 MPa and 414 MPa were the values for the concrete strength and the steel yielding stress, respectively.

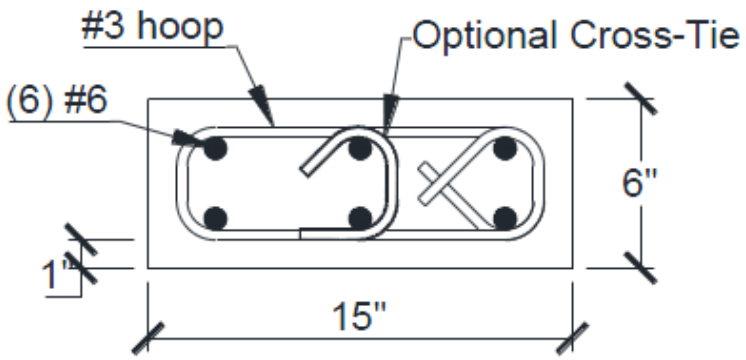

Figure 2-34. Cross-section and detailing of the eight prisms tested by Shea et al. (2013) & Flintrop et al. (2013)

The tests consisted of inputs of diverse magnitudes for maximum compression strains between 0.2% and 0.6%, and maximum tension strains of 2.0% and 4.5%, as can be noticed in Figure 2-35. Prisms #1, #2, and #4 evidenced rebar buckling as a failure mode. Prism #3 reported out-of-plane buckling similar from what prisms #5 and #6 revealed at the end of the tests (Flintrop et al., 2013). Prisms #7 and #8 failed do to out-of-plane buckling and concrete crushing, respectively (Shea et al., 2013). Figure 2-36 shows the failure modes of the last four specimens considered in this experimental program.

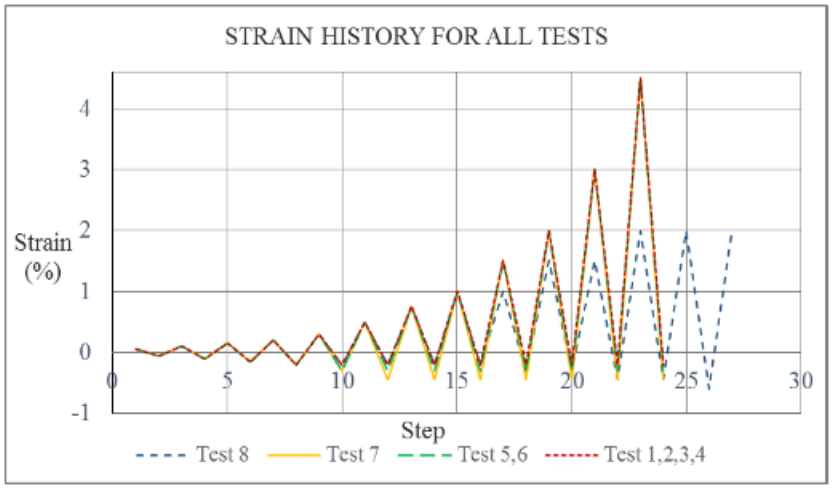

Figure 2-35. Strain history covered in the 2013 NEES@UCLA project

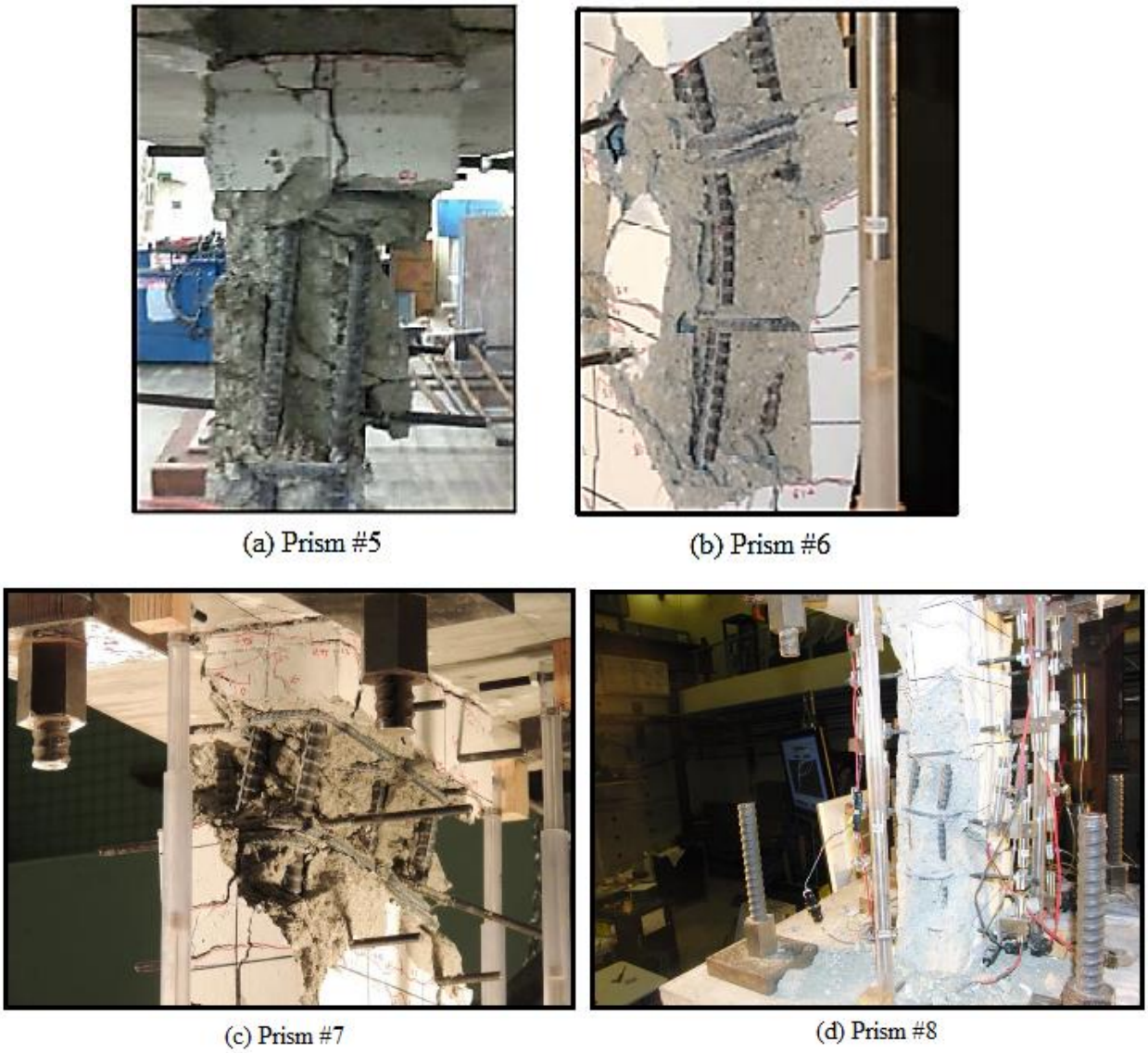

Figure 2-36. State of prisms reported by Shea (2013) and Flintrop (2013)

The more significant conclusions of this project are first, a limit for the concrete cover should be provided to guarantee the stability in the core; and second, a limit for the wall thickness must be required when large tension and compression strains are expected, which has been considered for various design codes previously. As it has been stated in other studies, more research is suggested to establish a ductile compressive failure of RCSW.

2.2.2.7 Welt (2015)

Nineteen 2:3 scaled prisms representative of modern boundary elements of RCSW were tested by Welt (2015) to determine the influence of different parameters on the strength and strain capacity

of compression members. The studied parameters were transverse reinforcement detailing, longitudinal reinforcement ratios, loading protocol, and debonding of longitudinal reinforcement. Only the specimens subjected to cyclic axial compressive and tensile strains are detailed in this section. Figure 2-37 presents the cross-sections of these selected specimens. Prism CS12 was also subjected to cyclic loading, however, since bar bonding conditions were varied for this case, then its results are excluded from this review.

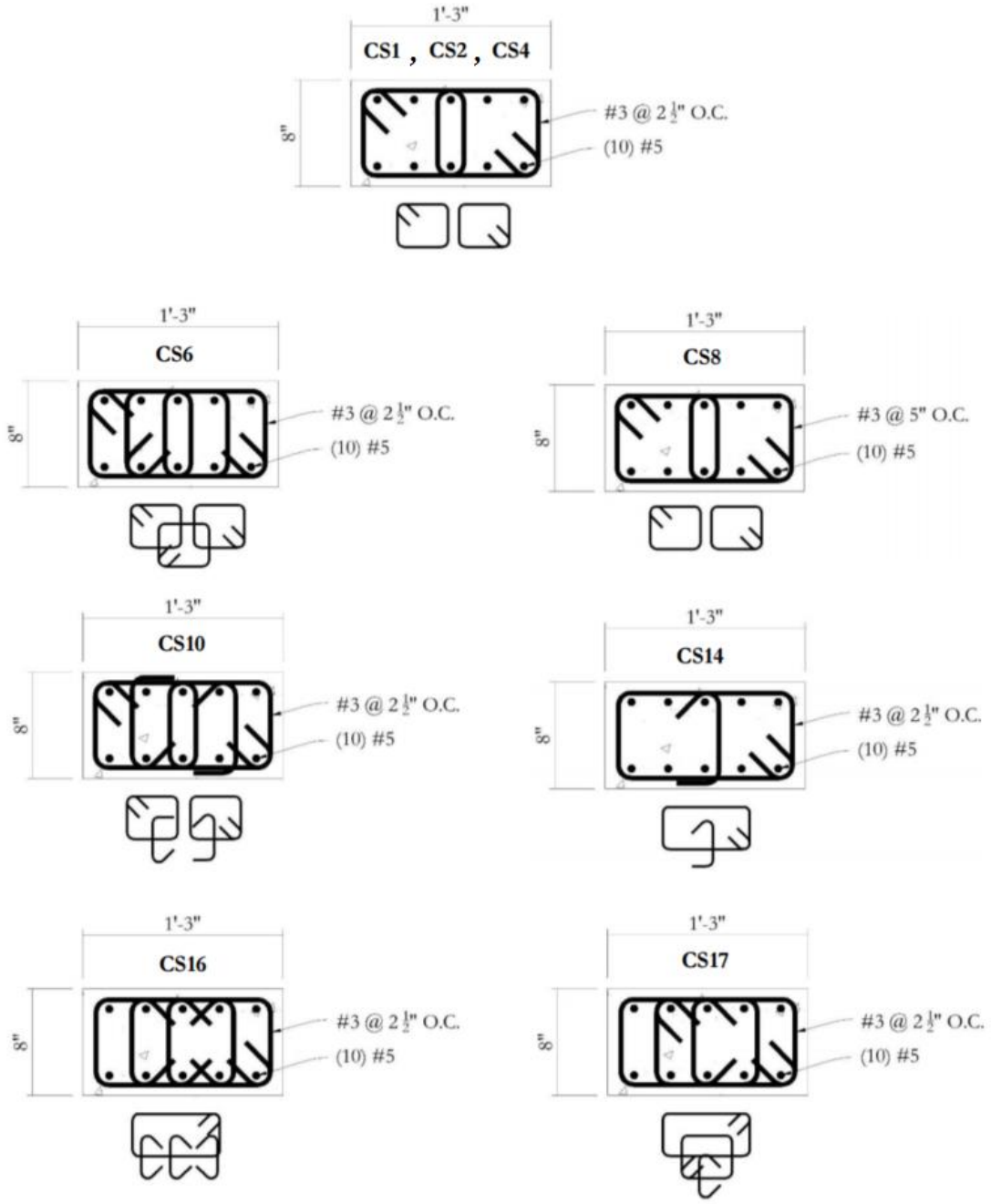

Figure 2-37. Cross-sections and detailing of the selected specimens tested by Welt (2015)

Only prisms CS1 and CS2 were conceived to study the influence of tensile pre-strains prior compressive loading on the strength capacity of boundary elements. Figure 2-38 exhibits the damage states at the end of the tests for prisms CS1 which did not include a tensile pre-strain and CS2 which considered a 5% tensile pre-strain. Both prisms were subjected to reversed-axial cyclic loading. The damage propagation in prism CS2 was not uniform across its thickness, showing the presence of P-δ effects, which were evident at the time the prism returned to a neutral displacement position after experiencing the 5% tensile pre-strain and before continuing with the reversed-cyclic loading. Welt (2015) noticed that the higher tensile pre-strains caused a compressive strength reduction close to 50%. Regarding the remaining parameters analyzed for the other specimens, the test results indicated that crossties do not provide enough restraint to prevent bar buckling; and, additionally, it was observed that only closed hoops around every bar increase the strain compressive capacity of the specimens.

(a) CS1 – No Pre-Strain (b) CS2 – 5.0% Pre-Strain

Figure 2-38. Final states of prisms CS1 and CS2 tested by Welt (2015); a) without, and b) with tensile pre-strain.

2.3 State of the art in out-of-plane instability prediction

The following subsections describe the fundamentals of the phenomenological models created in the 1990s to prevent out-of-plane buckling instability. Because of their simplicity and efficiency, these models have been suggested to be implemented in existing design procedures to limit wall thicknesses of ductile RCSW.

2.3.1 Phenomenological models

Goodsir (1985) defined the out-of-plane instability as a mechanism that develops during different stages when walls are subjected to in-plane cyclic reversal loading. At high in-plane

displacements in one direction, large tensile strains and wide horizontal cracks appear in the boundary element subjected to tension along the plastic hinge region. While unloading through the opposite direction, compression strains, originated from the axial load and the moment caused by its eccentricity tend to balance the remaining tensile strains. During this stage as the in-plane lateral load increases, out-of-plane deformations could develop. The described behavior is presented in Figure 2-39, which shows the deformations and strain patterns in the plastic hinge region of RCSW.

Figure 2-39 illustrates two possible scenarios. First, if the horizontal cracks close before reaching a critical state, explained below, the out-of-plane deformations are small and the compressive force is sustained without exhibiting instability. On the contrary, if the horizontal cracks remain open, large out-of-plane deformations develop and consequently instability is evidenced by a reduction in the strength of the wall.

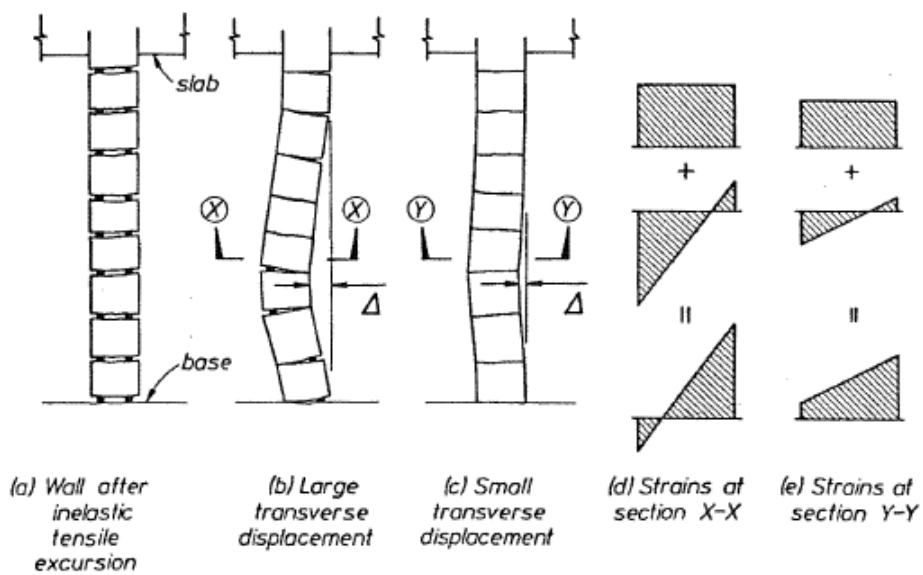

Figure 2-39. Deformation and strain patterns in a plastic hinge region. (Goodsir, 1985)

In order to capture the mentioned critical stage, Paulay & Priestley (1993) created a model that involves the relationship between tensile strains reached under in-plane loading and out-of-plane deformations manifested simultaneously under reversal loading; additionally, the model suggests an out-of-plane deformation limit to prevent wall local buckling.

In this context, Equation (2-1) restrains the maximum tensile strain value to ensure lateral stability of structural walls.

$$\varepsilon_{sm} \leq 8\beta \left(\frac{b_w}{L_o} \right)^2 \xi_c \tag{2-1}$$

where $\beta = d/b_w$ is a parameter defining the position of the longitudinal reinforcement; b_w and d are the thickness and the transverse effective depth of the wall section, respectively. The buckled length of

the wall L_o, can be taken equal to the plastic hinge length L_p of a wall as established by Paulay & Priestley (1992). However, as noted by Johnson (2010) and Rosso et al. (2015), this consideration may lead to poor predictions. Consequently, the buckled length developed between the contraflexure points should be considered instead.

The stability criterion is defined as:

$$\xi \leq \xi_c = 0.5\left(1 + 2.35m - \sqrt{5.53m^2 + 4.70m}\right) \tag{2-2}$$

$$m = \rho_{end}\,\frac{f_y}{f_c^{'}} \tag{2-3}$$

where m is the mechanical reinforcement ratio, ρ_{end} is the longitudinal reinforcement ratio of the compression region of the wall, f_y is the yield strength of the longitudinal reinforcement, and f'_c is the uniaxial compressive strength of the concrete.

Based on this approach, Chai & Elayer (1999) carried out the previously described experiment program on prisms and proposed a phenomenological Equation (2-4) to evaluate maximum axial tensile strains developed in the compression zone of RCSW to prevent buckling instability when exposed to in-plane reversal loading.

$$\varepsilon_{sm} \leq \frac{1}{2c}\left(\frac{b_w}{L_o}\right)^2 \xi_c + 3\varepsilon_y \tag{2-4}$$

where ε_y is the yielding strain of the longitudinal reinforcement and c is a coefficient that reflects the variation of the curvature along the buckled zone.

Chai & Elayer (1999) assumed sinusoidal curvature distribution, $c = 1/\pi^2$. Paulay & Priestley (1993) considered a constant curvature distribution, which had been suggested earlier by Goodsir (1985), then $c = 1/8$. The main difference between these two formulations is determined by the second term of Equation (2-4), which considers the hysteretic response of the longitudinal bars located in the idealized compressive region. According to Chai & Elayer (1999), the maximum tensile strain consists of three components:

$$\varepsilon_{sm} = \varepsilon_a^* + \varepsilon_e + \varepsilon_r \tag{2-5}$$

where ε_a* is the axial strain at first closure of cracks, ε_e is the strain required to yield the reinforcement in compression, and ε_r accounts for the effect of strains elastically recovered during unloading. The two last components can be expressed as proportions of ε_y, i.e., $\varepsilon_e = 1\varepsilon_y$ and $\varepsilon_r = 2\varepsilon_y$. Figure 2-40 shows the idealized response of a prism in terms of nominal axial strain and axial force from a last cycle where inelastic buckling was captured. The three mentioned strains components are identified in the graph. The experimental results showed that coefficient η_1 is close to 1.5 and coefficient η_2 varies in the range of 3 to 5. For design purposes, these coefficients were assumed to be *1* and *2*, respectively.

From Chai & Elayer (1999) study, Equations (2-1) and (2-4) resulted to be conservative, but because of their simplicity they can be easily applied in design procedures to limit the wall thickness of planar RCSW as proposed in (Chai & Kunnath, 2005).

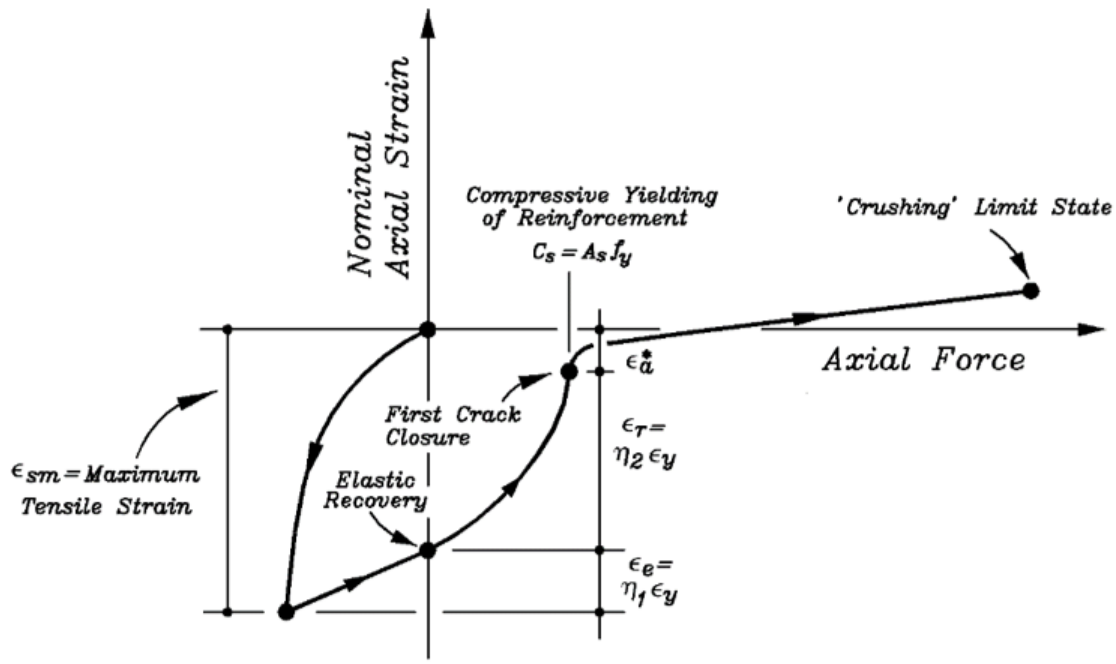

Figure 2-40. Idealized nominal axial strain vs. axial force response (Chai & Elayer, 1999)

The phenomenological models described in the previous section consider a constant or close to constant axial load over the height of the boundary region. A similar assumption was involved in the Parra & Moehle (2014) approach, presented in Equation (2-6), which is based on the modeling concepts proposed by Paulay & Priestley (1993).

$$\varepsilon_{sm} = \left(\frac{b_{cr}}{0.7kh_u} \right)^2 + 0.005 \tag{2-6}$$

where b_{cr} is the critical width of the wall, kh_u is the effective length equal to $0.5h_u$ assuming fixed ends, and h_u is the clear interstory height. Equation (2-6) was derived for preliminary design of walls with two curtains of reinforcement. The effects of the longitudinal steel content is omitted from the Parra & Moehle (2014) approach since the stability criterion was simplified by a practical value of 0.25. However, tests on prisms suggest that one of the most influential parameters on the onset of lateral instability is the longitudinal reinforcement ratio and consequently this approach would need further improvements.

In addition, Parra (2015) studied the effect of strain gradients along the height and length of a wall on the onset of buckling instability through FE numerical simulations. The results showed that the gradient of the axial force along the boundary element height is more consequential than the strain

gradient along the wall length. In order to account for the effects of a non-uniform distribution of the axial load, Parra (2015) suggested a correction factor for Equation (2-6), which was derived from the results of the FE modeling. The new approach estimates the maximum tensile strains as

$$\varepsilon_{sm} = (5 - 4\alpha)\left(\left(\frac{b_{cr}}{0.7kh_u}\right)^2 + 0.005\right) \tag{2-7}$$

where α is the parameter that represents the axial force profile, considered as 0.2 for practical solutions. According to Parra (2015), Equation (2-6) would overestimate the wall thickness required to prevent instability and consequently Equation (2-7) would report a more reasonable estimation.

2.3.2 Code requirements

The following subsections compile the approaches implemented in common codes to limit the minimum wall thickness that could prevent buckling instability of planar RCSW.

2.3.2.1 ACI 318 (2014)

Observed damage in recent earthquakes and laboratory studies on RCSW and prisms replicated as boundary elements suggest that slim end regions can be prone to local inelastic buckling under in-plane cyclic load reversals. Considering this fact, the ACI 318 (2014) Chapter 18 establishes limits on slenderness for special structural walls or pier walls when special boundary elements are required in accordance with sections 18.10.6.2 or 18.10.6.3. A minimum wall thickness $b_w \geq h_u/16$ is recommended by section 18.10.6.4 (b); h_u, is the laterally unsupported height at extreme compression fiber of a wall or pier wall.

In the case where $h_w/l_w \geq 2.0$ and $c/l_w \geq 3/8$, section 18.10.6.4 (c) suggests a minimum wall thickness of 300 mm to prevent lateral instability of the compression zone once the concrete cover is lost. In the expressions, h_w, is the total height of the wall; l_w, is the length of the wall; and, c is the largest neutral axis depth associated with the factored axial load P_u, and the nominal moment strength, consistent with the design displacement δ_u. Figure 2-40 summarizes the design provisions of boundary element for special RCSW [Fig. R18.10.6.4.2 ACI 318 (2014)]. The aspect ratio h_w/l_w defines two cases to consider. In addition, depending on the extreme fiber compressive stress and the longitudinal reinforcement ratio, three vertical regions are established.

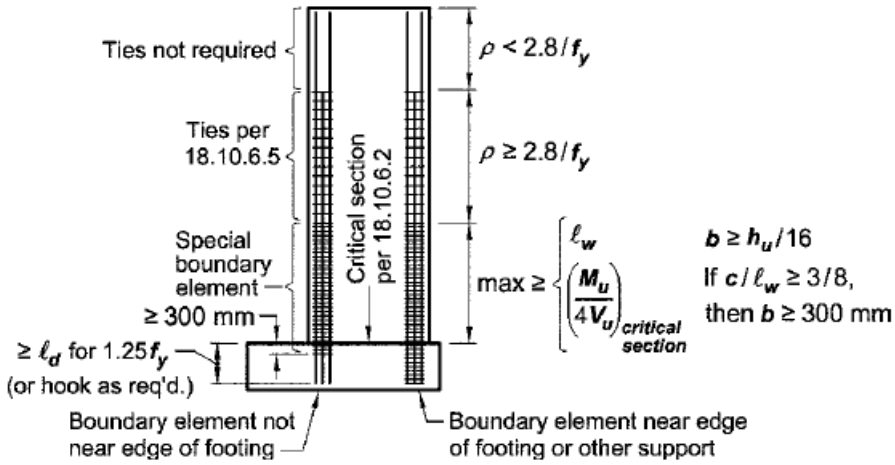

(a) Wall with $h_w/\ell_w \geq 2.0$ and a single critical section controlled by flexure and axial load designed using 18.10.6.2, 18.10.6.4, and 18.10.6.5

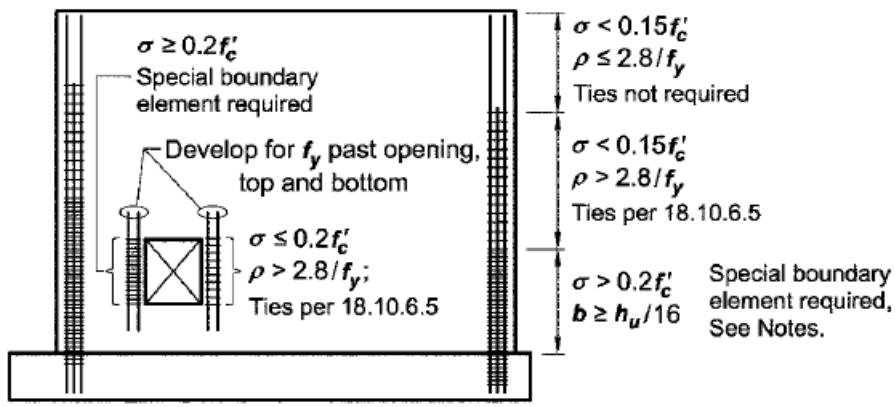

Notes: Requirement for special boundary element is triggered if maximum extreme fiber compressive stress $\sigma \geq 0.2f'_c$. Once triggered, the special boundary element extends until $\sigma < 0.15f'_c$. Since $h_w/\ell_w \leq 2.0$, 18.10.6.4(c) does not apply.

(b) Wall and wall pier designed using 18.10.6.3, 18.10.6.4, and 18.10.6.5

Figure 2-41. Design provisions of boundary element for special RCSW. [Fig. R18.10.6.4.2 ACI 318 (2014)]

2.3.2.2 AASHTO LRFD Bridge Design Specifications (2010)

In accordance with Section 5.5.4.3 from the AASHTO LRFD Bridge Design Specifications (2010), the structure as a whole and its components shall be designed to resist buckling. The seismic design provisions for wall-type piers conforming to Article 5.10.11.4.2 do not explicitly include a criterion to avoid the onset of out-of-plane instability.

2.3.2.3 AASHTO Guide Specifications for LRFD Seismic Bridge Design (2011)

The pier wall thickness is determined so the nominal shear capacity (V_n) satisfies the upper limit in Equation 8.6.9-2 from Section 8.6.9 (AASHTO, 2011), as follows:

$$V_n = (0.13\sqrt{f_c^{'}} + \rho_h f_{yh}) \leq 0.25\sqrt{f_c^{'}} A_e \rightarrow (kips) \tag{2-8}$$

where $\rho_h = A_v / (b.s)$, A_v is cross-section area of shear reinforcement in direction of loading (in^2), b is the section width (in), s is tie reinforcement spacing (in), f'_c is concrete compressive strength (ksi), f_{yh} is tie reinforcement yielding stress (ksi), $A_e = 0.8A_g$, and A_g is the gross cross section area.

Neither aspect ratios nor other formulations to prevent out-of-plane instability of pier walls are included in the AASHTO Guide Specifications for LRFD Seismic Bridge Design (2011).

2.3.2.4 Caltrans Seismic Design Criteria (2013)

Minimum thickness requirements are established as a function of the shear capacity of pier walls in accordance with Section 3.6.6 (Caltrans, 2013). The thickness is determined so the shear stress satisfies Equation 3.6.6.2-2:

$$\frac{V_n^{pw}}{0.8A_g} < 8\sqrt{f_c^{'}} \rightarrow (psi)\,; \qquad \frac{V_n^{pw}}{0.8A_g} < 0.67\sqrt{f_c^{'}} \rightarrow (MPa) \tag{2-9}$$

where V_n^{pw} is the nominal shear strength of a pier wall in the strong direction, f'_c is concrete compressive strength, and A_g is the gross cross section area.

The Caltrans Seismic Design Criteria (2013) does not contain any method to control the out-of-plane buckling failure mode of pier walls.

2.3.2.5 Canadian Standards Association (2004)

In accordance with section 21.6.3 (Canadian Standards Association, 2004), ductile walls with a ductility-related force modification factor R_d of 3.5 or 4 and $h_w/l_w>2$, require a wall thickness equivalent to $l_u/10$ in the zone where a plastic hinge is expected; l_u is the clear span or unsupported length between floors or other effective horizontal lines of lateral.

2.4 Local buckling prediction assessment

Herrick & Kowalsky (2016) compared the predictions from the Paulay and Priestley buckling model (PPBM) and the Chai and Elayer buckling model (CEBM) for selected RCSW tested by others in the past. Figure 2-42 shows normalized in-plane displacements captured before out-of-plane buckling occurred for walls subjected to cyclic loads from the Herrick (2014)'s database. Some walls from this database were not tested with the purpose of capturing inelastic buckling. The in-plane displacements were normalized against the displacements calculated from the PPBM and CEBM associated with the maximum vertical tensile strains sustained prior to buckling. A moment curvature sectional analysis program, CumbiaWall, was used for this purpose. Note that the prediction of the CEBM agrees better than the PPBM.

A complementary analysis was conducted in the same study. Considering the PPBM and CEBM, Herrick & Kowalsky (2016) established a limit state related to the maximum tensile strains captured before out-of-plane instability was observed during selected experimental programs where RC prisms were tested under cyclic and monotonic axial loads. Once the experimental tensile strains were identified for each case, they were compared with the predicted values demonstrating that the PPBM shows more discrepancy than the CCBM, which can be perceived from Figure 2-43.

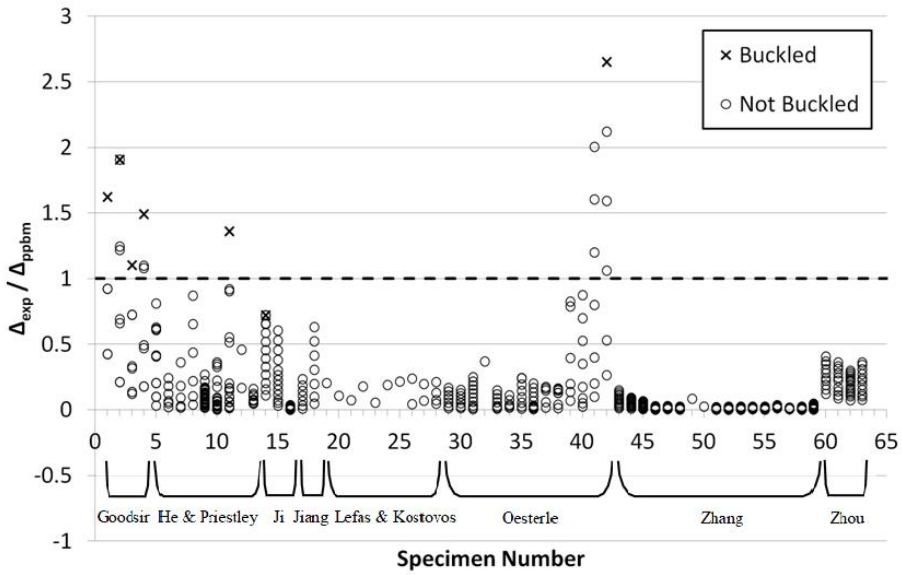

(a) Normalized to PPBM displacements

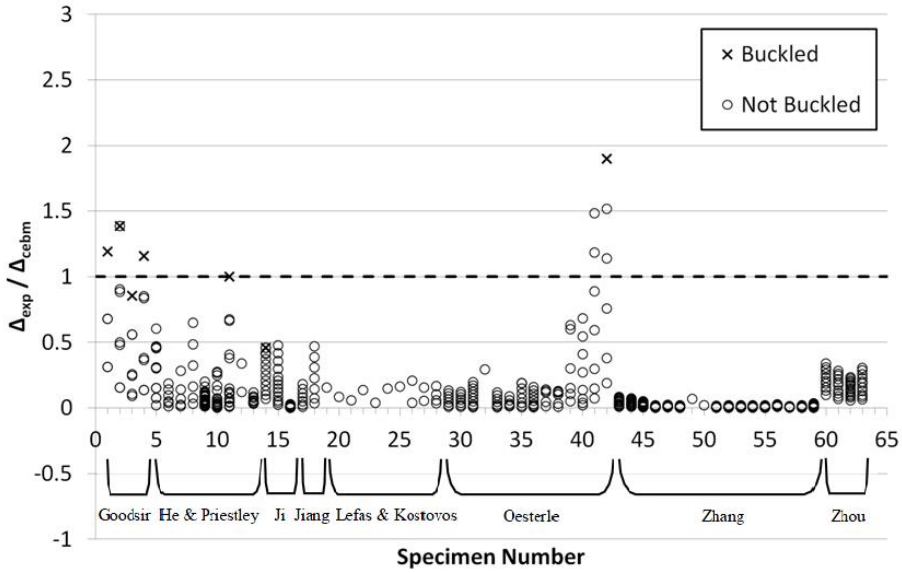

(b) Normalized to CEBM displacements

Figure 2-42. Wall experimental displacements normalized to PPBM and CEBM displacements. (Herrick & Kowalsky, 2016)

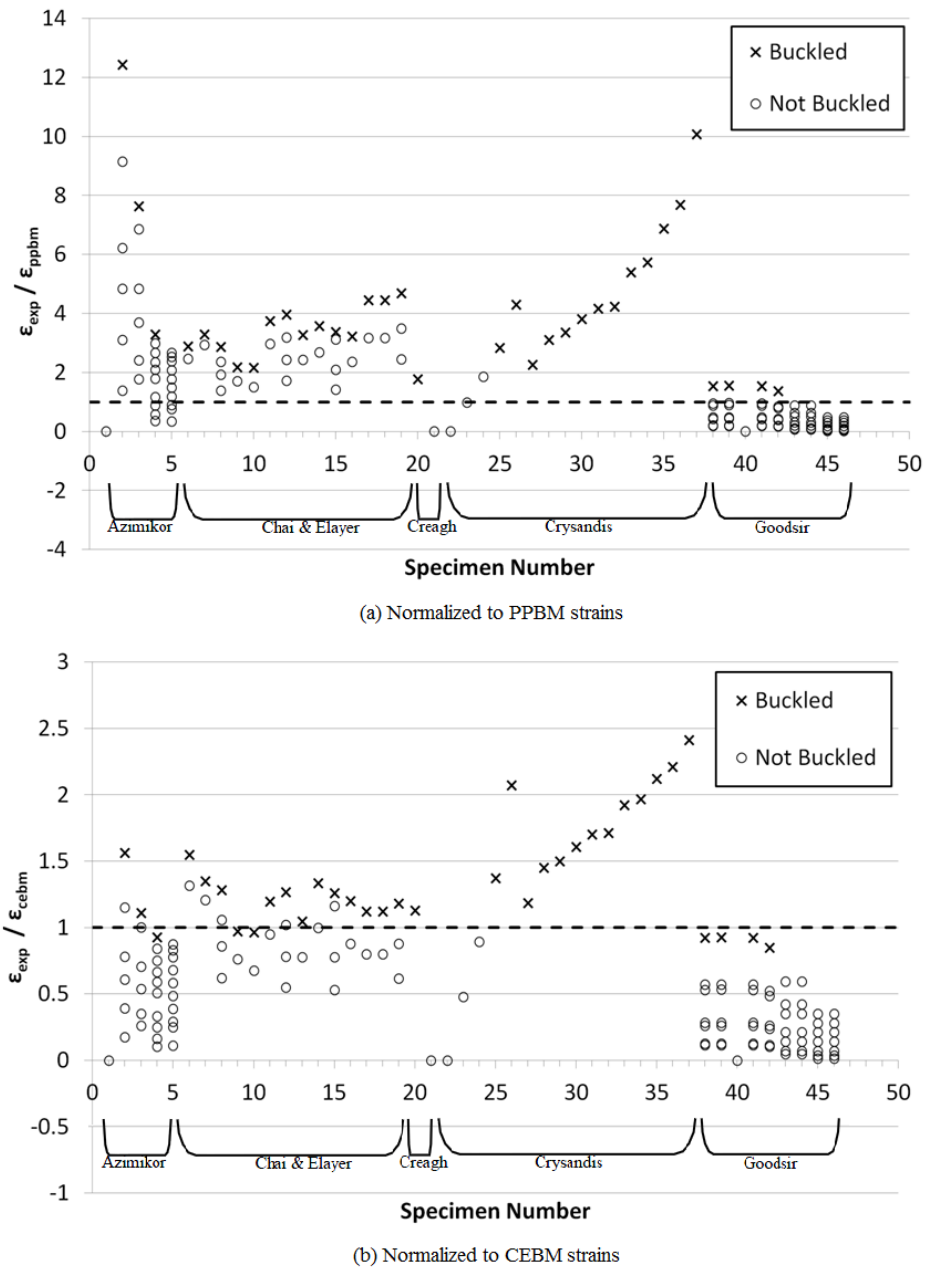

Figure 2-43. Experimental prism strains normalized to PPBM and CEBM strains. (Herrick & Kowalsky, 2016)

Note that monotonic loading cases were set as "zero" in both examinations, for walls and prisms. The symbol 'x' represents cycles where buckling instability was detected, and 'o' denotes the cycles where buckling was not captured. The specimens were assumed to experience a buckling failure mode after detecting moderate loss of strength, in the range between 10% and 30%, accompanied by visible out-of-plane deformations. In conclusion, the two models are promising at predicting out-of-

plane buckling of prisms; however, when applied to walls, the predictions tend to be conservative, especially for the PPBM.

A parametric study was also conducted by Herrick & Kowalsky (2016) where variables most likely to be important for stability were identified. These include wall geometry, reinforcement details, single versus double-layers reinforcement, plastic hinge length, and material properties. The results revealed that out-of-plane instability is primarily influenced by geometric properties: height, length, and thickness. This implies that wall aspect ratios should be limited to prevent local plastic buckling failure modes.

CHAPTER 3: STUDY PLAN

Chapter 3 covers the research gap identified through Chapter 2 and the research objectives to be addressed during the experimental program and the analytical study.

3.1 Research Gap

From Herrick & Kowalsky (2016) study, further analytical and experimental investigations are suggested to detect the effect of missing parameters and the actual influence of some variables deemed to be significant for stability. Consequently, the main concern of the project described throughout this document is to capture the impact of one of those missing parameters because no examination has been done to evaluate the influence of out-of-plane loading on prisms and wall boundary elements. Even though a few initiatives were developed to study local buckling failure in T-shape cross sections walls subjected to biaxial loading, the results suggest that additional research is warranted (Wallace, 2012).

The existing models correlate tensile strain from in plane loading to out-of-plane deformation, assuming a prescribed curvature distribution. If loading occurs in the out-of-plane direction, the relationship between tensile strain and out-of-plane deformations should be adjusted to reflect this. In its simplest form, this would be an addition of an out-of-plane displacement to the existing equation. However, out-of-plane displacement may influence the distribution of curvature with height, thus requiring additional adjustments to the models.

3.2 Research Objectives

The main objective of this study is to develop a model capable of capturing the local buckling failure mode of RC structural walls / pier walls due to in-plane loading considering the effect of out-of-plane loading throughout analytical and experimental studies.

The specific objectives for this research are:

1) Examine the effects of historic earthquakes in RCSW and establish the possible reasons that caused failure due to out-of-plane buckling;
2) Analyze worldwide test results and provide insights about inelastic stability of RCSW;
3) Assess analysis methods to predict local buckling behavior and establish an improved model to capture the failure mode associated with this phenomenon considering the effect of out-of-plane loading;
4) Validate the proposed formulation through an experimental program on prisms simulated as wall boundary elements; and,
5) Develop a parametric analysis and consequently propose design guidelines for planar and flanged walls to prevent local buckling.

CHAPTER 4: METHOD

Reinforced Concrete Prisms (RCP) representative of compression zones of prototype walls have been recognized as suitable elements to study the influence of critical parameters affecting the stability of RCSW. Considering this fact, the experimental component of the current research contemplates the construction of twelve RCP. The aim of the tests is to evaluate the effect of different longitudinal reinforcement ratios in combination with different load paths on the onset of out-of-plane instability of planar special RCSW. The analytical component of this project considers the creation and validation of a new phenomenological model and in addition a parametric study on prisms, both using a fiber-based model calibrated based on the experimental results. This section describes the constituents of the experimental program that supported the findings of the project. The analytical studies will be described in Chapter 5.

4.1 Experimental program

Twelve half scaled RCP were experimentally tested in the Constructed Facilities Laboratory (CFL) during this project. The support conditions for the RCP are conceived as fixed-fixed. Three phases were considered during the experimental program. The first testing phase involved controlled load paths where the specimens were subjected to axial tension/compression cycles combined with lateral loading to mimic the effects of out-of-plane displacements. In the second and third phases, longitudinal reinforcement ratios varied and additional loading protocols were followed. In general, the three phases include reinforcement ratios of typical values used in RC buildings and employed by the Alaska DOT for pier walls. The details associated with the three phases are presented in Table 4-1.

Table 4-1. Experimental Phases Matrix

Phase	Configuration	As Built Geometry b_w x l_{be} x h_w	Detailing		Reinforcement ratio as built	
			Longitudinal	Transverse	Longitudinal ρ_l	Transverse ρ_{tx} / ρ_{ty}
1	1	5”x12”x60”	6 #5	1s#3+1t#3 @ 2in.	0.031	0.0138 / 0.022
2	2	5”x12”x60”	6 #4	1s#3+1t#3 @ 2in.	0.020	0.0138 / 0.022
3	3	5”x12”x60”	6 #3	1s#3+1t#3 @ 2in.	0.011	0.0138 / 0.022

4.1.1 Tests conceptualization

When a planar wall section is exposed to the combination of compression strains preceded by large tensile strains due to in-plane loading, out-of-plane buckling instability could develop causing significant damage especially in the boundary elements. As previously implied, in order to evaluate critical parameters controlling this failure mode, the construction of RCP simulating boundary elements of RCSW has resulted more convenient than the construction of wall specimens. Axial tensile

and compressive loads applied to RCP mimic the axial demands in boundary elements due to in-plane loading, which constitutes a practical approximation. In addition, if the RCP are subjected to out-of-plane loads, then this combination simulates a real case scenario when seismic loads strike a wall. Figure 4-1 shows a special planar RCSW with two boundary elements resisting in-plane and out-of-plane demands. The green regions represent the boundary elements considered for the construction of the RCP contemplated in the current study.

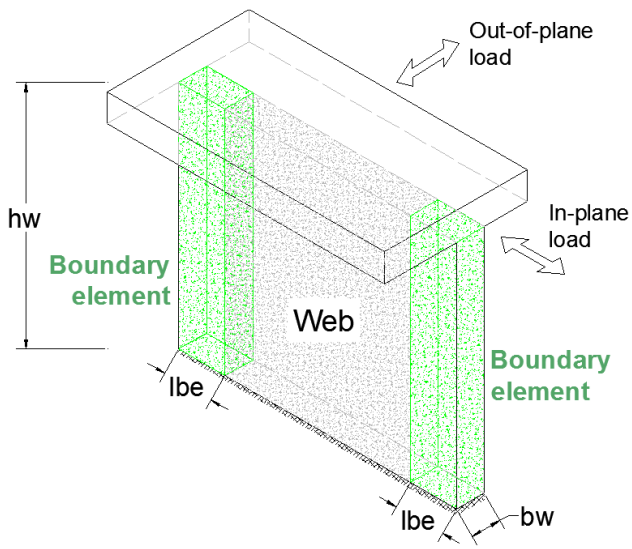

Figure 4-1. Conceptualization of the specimens

4.1.2 Specimens detailing

The experimental program comprises a total of twelve RCP built according to the recommendations of the ACI 318-14, chapter 18. The first phase consists of testing six 1/2-scale identical specimens. The thickness of the prisms is 5 inches (127mm) since the cover was excluded from the construction. The geometry used is 5”x12”x60” (127mm x 305mm x 1,524mm), corresponding to an aspect ratio (h_w/b_w = *height/thickness*) of 10 (including the missing cover). The longitudinal reinforcement ratio is 3.1% (6 bars #5). Transverse reinforcement includes #3 diameter rebar spaced at 2 inches (51mm).

The geometry of the specimens built for phases 2 and 3 was the same as the one adopted during the first phase. The three specimens related to phase 2 included 6 #4 longitudinal bars and the three specimens related to phase 3 consist of 6 bars #3, corresponding to reinforcement ratios of 2.0% and 1.1%, respectively. The distribution of transverse reinforcement is similar to the one used for the first phase. Figure 4-2 and Figure 4-3 show the reinforcement detailing of the specimens built for the three described phases.

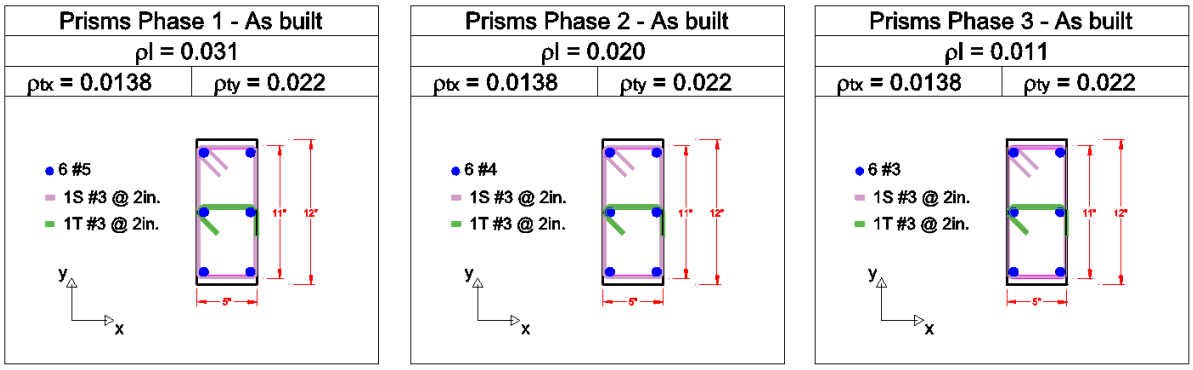

Figure 4-2. Specimens - Cross Sections

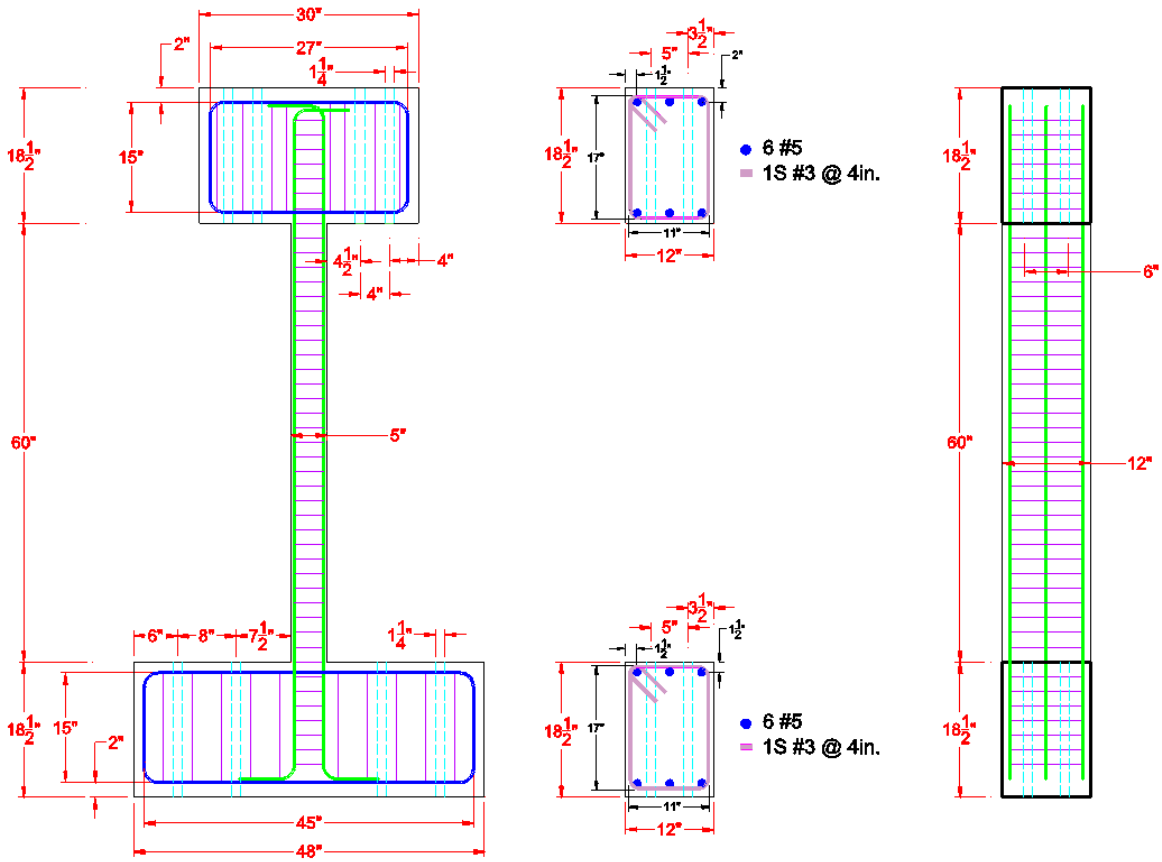

Figure 4-3. Specimens - Reinforcement Detailing

4.1.3 Specimens construction

The reinforced concrete elements, including the twelve specimens, the support block and the transfer block, were constructed at the CFL on the North Carolina State University's Centennial Campus. The RC elements were built considering three phases, which coincides with the number of

experimental phases contemplated in the project. The dimensions of each element were guaranteed to properly connect each component of the test setup through threaded rods and PT bars.

Rebar cages were assembled for the concrete blocks and then placed in the Steel-Ply formwork. Because of the geometry of the specimens, wooden formwork was fabricated at the CFL using plywood and dimensional lumber. Separately, the longitudinal and transverse reinforcement of the specimens, including their footing and cap beams were assembled using wooden templates. Before placing together the reinforcement skeleton and the wooden formwork, and in order to create voids in the prisms to connect the infrared LEDs sensors to the reinforcement before the tests, small pieces of foam were attached. PVC tubes were embedded in the footing and cap beams to later connect the specimens to the transfer block and the loading beam, respectively.

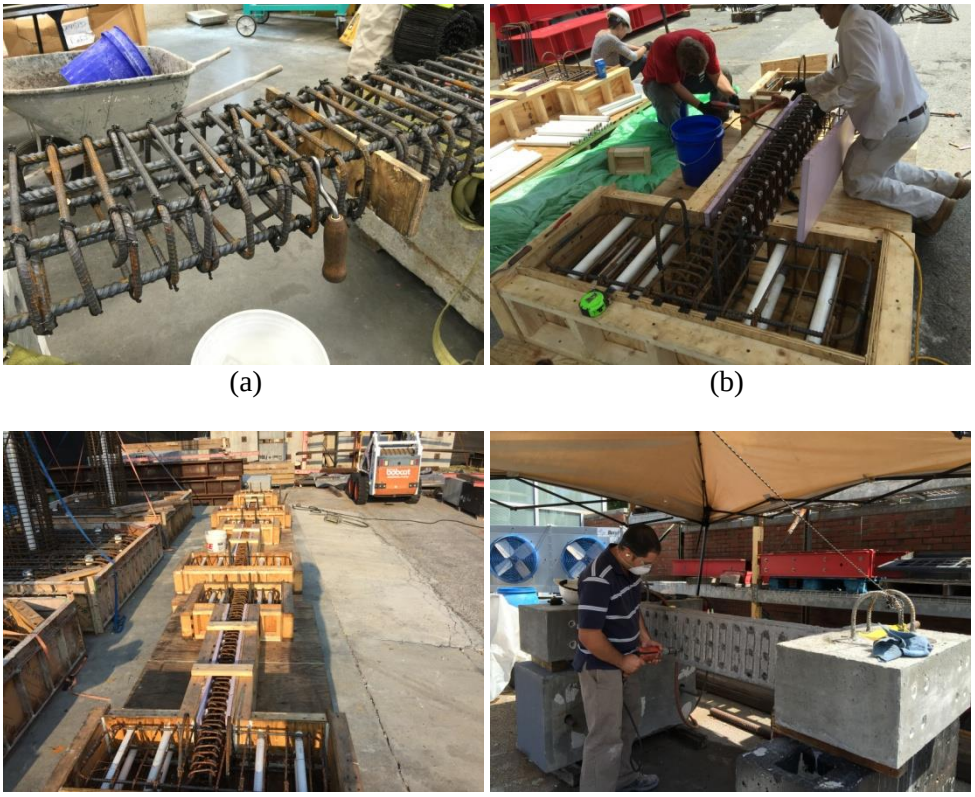

(a) (b)

(c) (d)

Figure 4-4. Construction of specimens: (a) prism reinforcement cage; (b) formwork assembly; (c) formwork and rebar cage for specimens (d) needle gun used to clear voids

Figure 4-4 shows pictures of the specimens under construction before and after casting. Once the formwork was released after 7 days, a needle gun was used to clear the voids and subsequently the specimens were cleaned and painted. Before each test, plastic caps used as devices to fix the infrared LED sensors to the reinforcement, were attached following a prescribed procedure to clean the bars and immediately glue the plastic caps.

4.1.4 Material properties

4.1.4.1 Concrete

The specified concrete compressive strength for the three phases was 5,000 psi (35 MPa). Each concrete mix was produced by a local company and included retarding admixtures. A water-based concrete curing and sealing compound was used on the freshly placed concrete and subsequently, the specimens were covered with plastic sheeting during the consecutive 7 days. A total of 72 test cylinders (4-inch-diameter by 8-inch-height) were cast to verify the required compressive strength at 7 days, 28 days, and on each specimen test day, according to ASTM C39-15 (2015). The average mechanical properties corresponding to the different phases and specimens are detailed in Table 4-2.

Table 4-2. Concrete mechanical properties

Specimen	f'_c (28 days)		f'_c (Test day)		E_c		f_r	
	[Ksi]	[Mpa]	[Ksi]	[Mpa]	[Ksi]	[Mpa]	[Ksi]	[Mpa]
P1-P1	6.10	42.10	7.70	53.10	5.00	34.50	0.53	3.70
P1-P2			7.60	52.40	5.00	34.50	0.52	3.60
P1-P3			7.40	51.00	4.90	33.80	0.52	3.60
P1-P4			7.20	49.60	4.80	33.10	0.51	3.50
P1-P5			7.10	49.00	4.80	33.10	0.51	3.50
P1-P6			7.70	53.10	5.00	34.50	0.53	3.70
P2-P7	6.60	45.50	7.00	48.30	4.80	33.10	0.50	3.40
P2-P8			7.60	52.40	5.00	34.50	0.52	3.60
P2-P9			7.50	51.70	4.90	33.80	0.52	3.60
P3-P10	5.80	40.00	6.50	44.80	4.60	31.70	0.48	3.30
P3-P11			6.30	43.40	4.50	31.00	0.48	3.30
P3-P12			6.50	44.80	4.60	31.70	0.48	3.30

The modulus of elasticity (E_c) and the modulus of rupture (f_r), were determined from the following equations:

$$E_c = 57\sqrt{f_c^{'}} \quad [psi]; \quad f_c^{'} \rightarrow [psi] \tag{4-1}$$

$$f_r = 6\sqrt{f_c^{'}} \quad [psi]; \quad f_c^{'} \rightarrow [psi] \tag{4-2}$$

4.1.4.2 Steel Reinforcement

The longitudinal and transverse reinforcement for all test specimens was ASTM A706, Grade 60 (420 MPa) black steel. Gerdau – Raleigh Reinforcing Steel provided the longitudinal and transverse reinforcement for the first phase of this project. Gerdau – Charlotte Reinforcing Steel produced the longitudinal reinforcement for the second phase and the transverse steel for the

second and third phases. Nucor Steel Seattle, Inc. provided the longitudinal reinforcement for the third phase. Batches of reinforcement were required for each diameter and phase. Subsequently, tension tests were conducted based on ASTM A370-14 (2014) using the MTS Material Test System at the CFL and a 2 in. (51mm) extensometer mounted at mid-height of each bar coupon. Rates of 0.5 in/min and 1.0 in/min were applied up to and beyond the yielding point, respectively. Figure 4-5 presents the initial and final stages from tensile tests conducted on bars #3. Figure 4-6 through Figure 4-8 show representative stress-strain curves from the three different bar sizes utilized as longitudinal reinforcement on each phase of the project. The stress-strain curves from the #3 stirrups utilized in phase 1 do not exhibit yielding plateau, as shown through a representative sample in Figure 4-9.

Figure 4-5. Initial and final stages from tensile tests conducted on bars #3

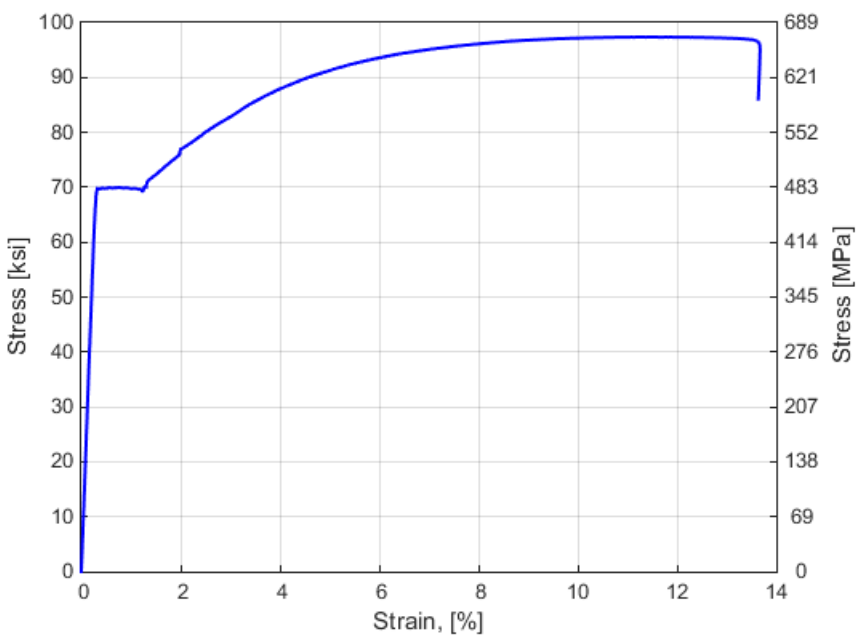

Figure 4-6. Stress-strain curve from a longitudinal rebar #5 – Phase 1

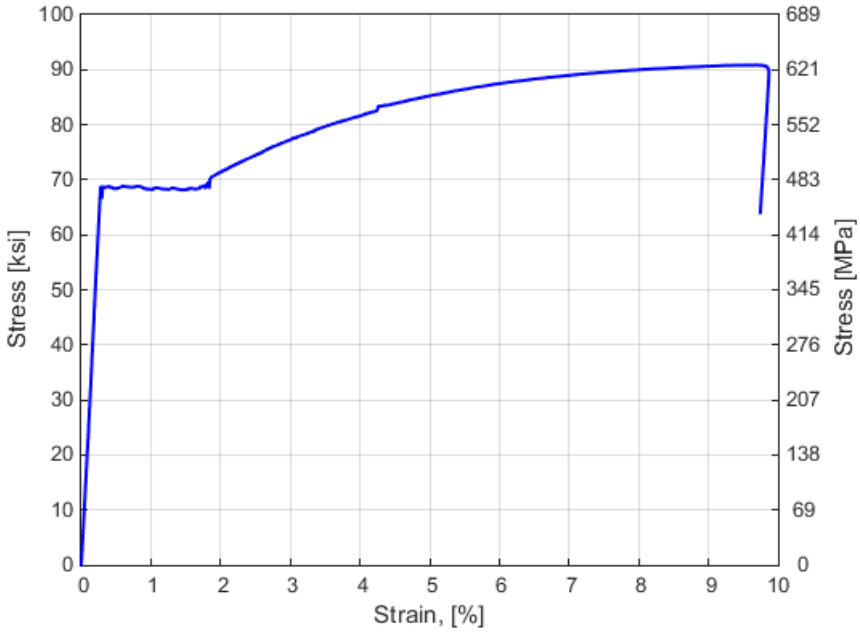

Figure 4-7. Stress-strain curve from a longitudinal rebar #4 – Phase 2

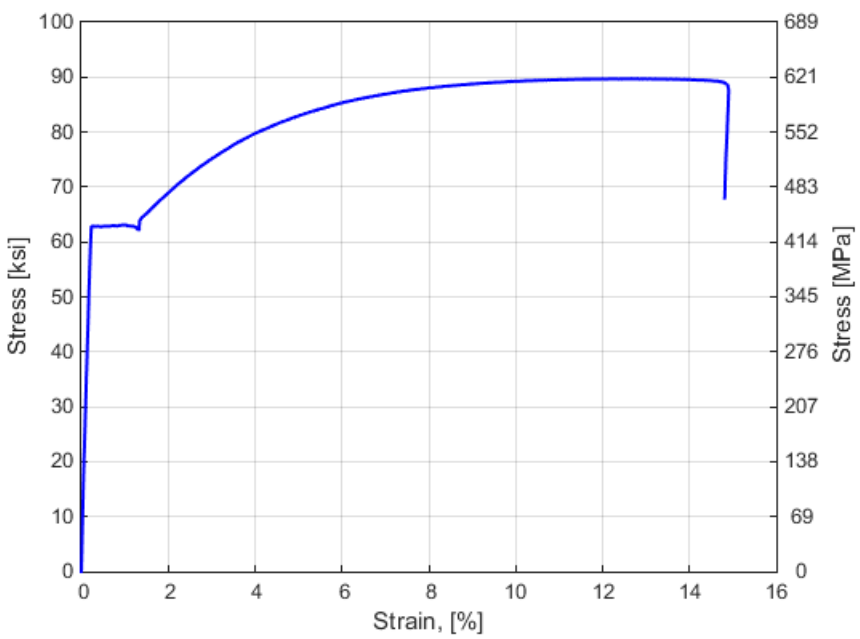

Figure 4-8. Stress-strain curve from a longitudinal rebar #3 – Phase 3

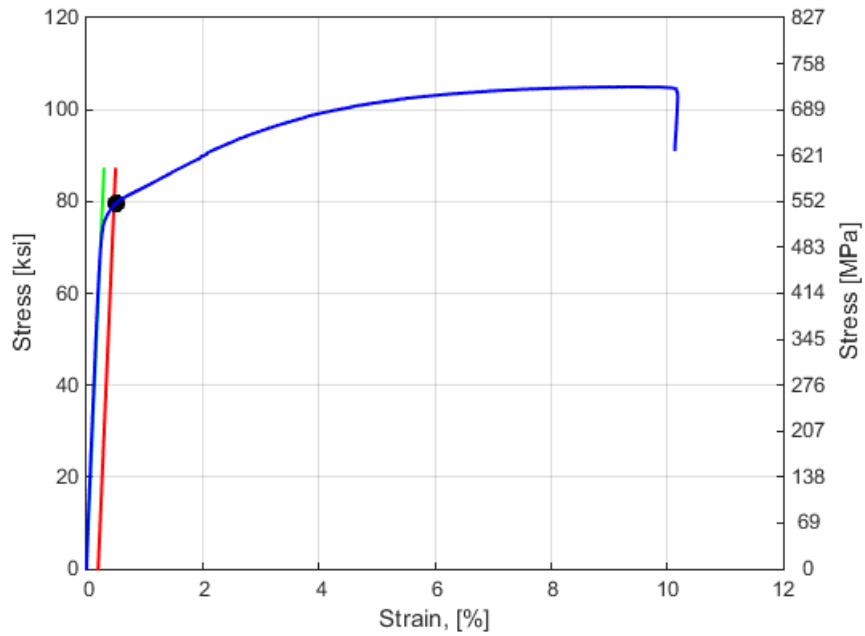

Figure 4-9. Stress-strain curve from a transverse rebar #3 – Phase 1

The averages of the steel reinforcement material properties are summarized in Table 4-3, where *fy* is the yielding stress; ε*y* is obtained dividing the yielding stress by the modulus of elasticity (*E*s) equal to 29,000 ksi; *fu* is the ultimate stress determined as the maximum tensile stress. The ultimate strain (ε*u*) is captured at the point where the ultimate stress occurs.

Table 4-3. Steel reinforcement mechanical properties

Phase	Bar Size	Reinforcement	f_y		$\varepsilon_y = f_y/E_s$	f_u		ε_u
	#	Type	[ksi]	[MPa]	[%]	[ksi]	[MPa]	[%]
1	3	Transverse	76.70	528.80	0.2644	103.10	710.80	8.5641
	5	Longitudinal	69.30	477.80	0.2389	97.00	668.80	11.3190
2	3	Transverse	69.80	481.30	0.2407	100.70	694.30	9.4064
	4	Longitudinal	69.10	476.40	0.2381	91.80	632.90	10.6915
3	3	Transverse	69.80	481.30	0.2407	100.70	694.30	9.4064
	3	Longitudinal	62.90	433.70	0.2171	89.90	619.80	12.2084

4.1.5 Test setup and instrumentation

The test setup was located in the CFL and it consisted of one concrete support block attached to the strong floor and connected to a second transfer concrete block, which was connected to the base of the specimens. The geometry of these concrete blocks was determined as a function of the required height to reach the effective length of the 440kips (1957kN) capacity actuators. A 14ft (4.27m) long

steel loading beam placed on the top of the specimen was connected to three actuators. The two 440kips (1957kN) capacity actuators in charge of inducing axial loads/displacements to the specimens were attached to the strong floor throughout steel floor plates. A third 55kips (245kN) capacity actuator used to apply out-of-plane displacements was horizontally connected to the strong floor throughout a steel wall plate and a steel bracket built specially for these tests.

Two steel frames were used to restrain torsion in the loading beam, and they were connected to each other using steel elements to guarantee global stability of the system. Figure 4-10 displays the test setup drawings and Figure 4-11 shows a picture of the area where the components of the project are placed in CFL.

The horizontal actuator was controlled by displacements. The vertically inclined actuator located at the left hand side of the specimen was controlled by rotations captured throughout an inclinometer attached to the center of the loading beam. The actuator placed at the right hand of the specimen was controlled by a combination of forces and displacements depending on the yielding point for each test. Loads and strokes in the actuators were measured through integrated LVDTs and loads cells.

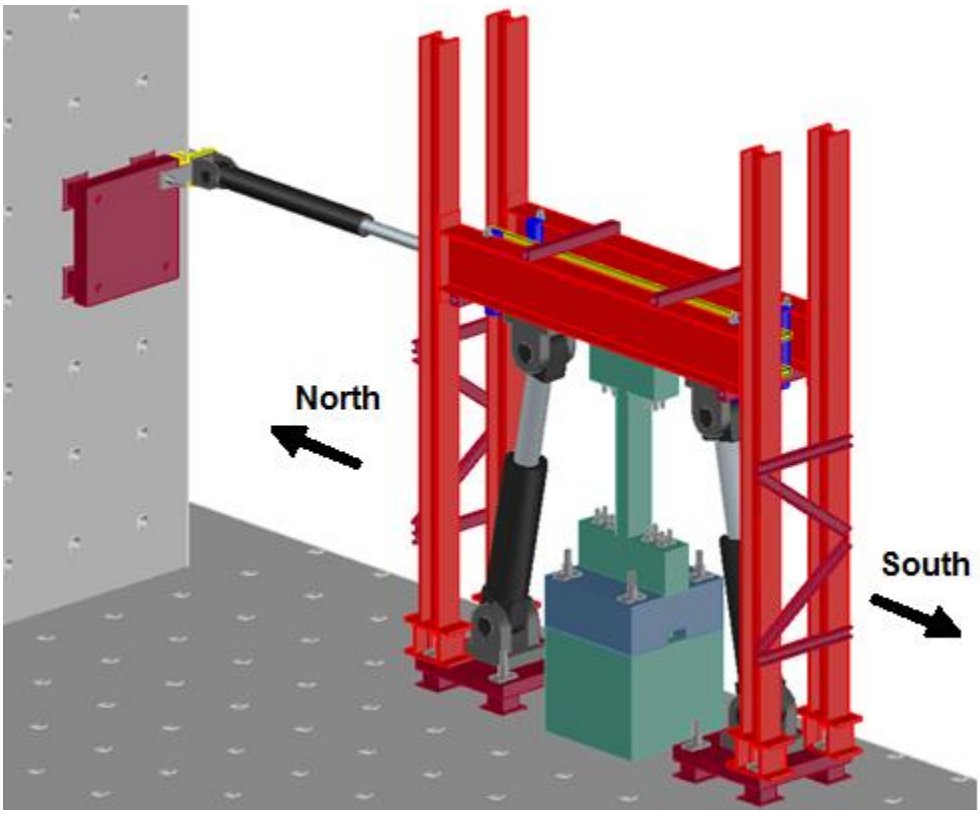

Figure 4-10. Test setup sketch

Figure 4-11. Test setup in the CFL at NC State

Relative displacements resulting from the interaction between the specimen and the transfer concrete block, and between the specimen and the loading beam were obtained using two linear potentiometers, respectively. Axial deformations of the prism were registered by four string potentiometers. In addition to the LVDT of the horizontal actuator, a string potentiometer attached to the strong wall and the loading beam was used to check the lateral out-of-plane displacement induced to the specimens.

A total of 110 infrared LEDs from the optical tracking system Optotrak Certus developed by Northern Digital Inc. were placed directly on the steel reinforcement of each prism. The two Optotrak cameras were strategically located to capture the data on both sides of the prisms. During the tests strains in the longitudinal and transverse reinforcement were determined in real time using the MATLAB code “REALSTRAIN”, created specifically for this project. In addition, this code was able to capture real time displacements from one of the four additional infrared LEDs that were positioned on the front face of the prism cap as a plane of reference. Figure 4-12 shows the distribution of the LEDs on the right face of one of the tested prisms and the overall allocation of the markers obtained from the Optotrak spatial coordinate output.

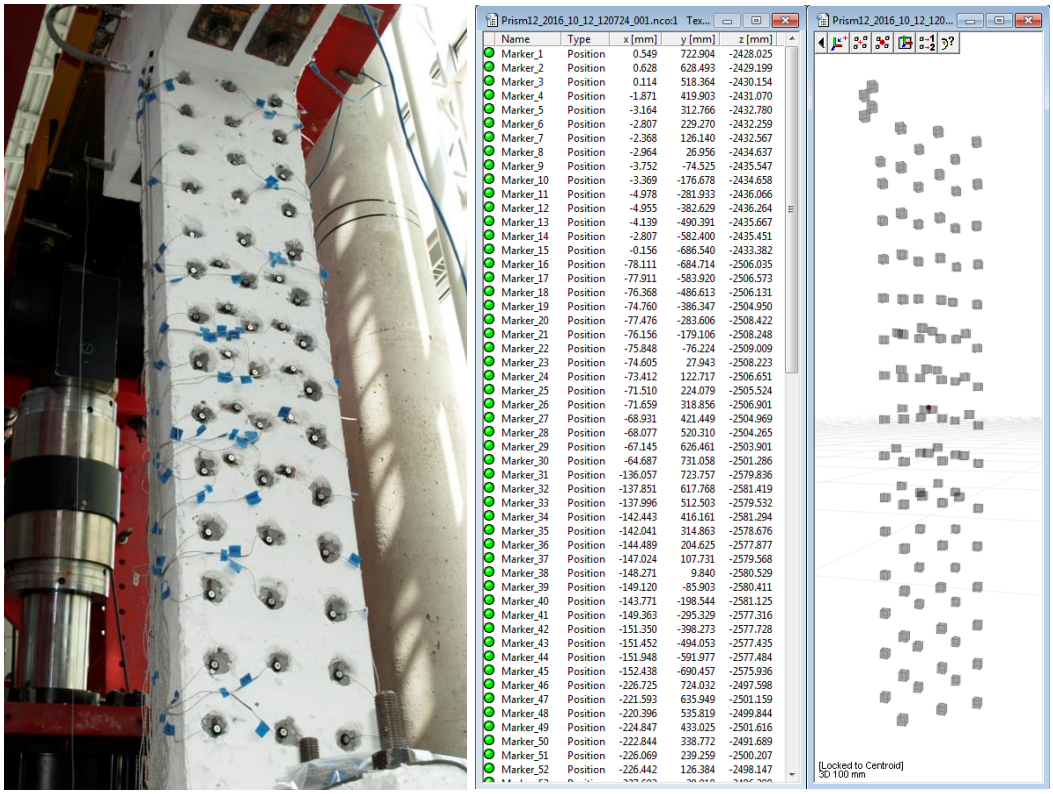

Figure 4-12. Optotrak LEDs distribution on right face of a specimen and spatial coordinate output

4.1.6 Loading protocols

The first and second experimental phases involved controlled load paths where the specimens were subjected to axial tensile and compressive loads in addition to lateral displacements. When out-of-plane displacements were applied, the compressive loads included P-Δ effects. The third phase only considered axial cycles for reasons explained later. Regarding the material properties, an unconfined concrete strength of 5 *ksi* and a reinforcement yielding strength of 60 *ksi* were considered as design values to define the experimental load history in compression. Actual material properties were used to calculate tensile demands.

4.1.6.1 Experimental Phase 1

Table 4-4 summarizes the maximum target axial and lateral loads/displacements contemplated for the six specimens included in Phase 1. The design axial compression capacity (*Po*) of the prisms contemplated on this phase is equal to 358 *kips* (1592 *kN*), calculated from:

$$P_o = 0.85 \cdot [f_c^{'}(A_g - A_s)] + f_y A_s \tag{4-3}$$

$$P_o = 0.85[5ksi * (5in * 12in - 0.31in^2 * 6)] + 60ksi * 0.31in^2 * 6$$

Table 4-4. Experimental test matrix of Phase 1

Specimen	Config.	Load protocol				
		Lateral		Axial		
		Displacement	Type	Max. Tension	Max. Compression	Type
Prism 1	1	17% drift	Monotonic	3%	0.5 in.	1 Cycle
Prism 2	1	0% drift	-	12 ε_y	Po = 358 kips	Cyclic
Prism 3	1	1% drift	Monotonic	14 ε_y	$P_{1\%}$ = 319 kips	Cyclic
Prism 4	1	4% drift	Monotonic	12 ε_y	$P_{4\%}$ = 241 kips	Cyclic
Prism 5	1	4% drift	Cyclic	12 ε_y	$P_{4\%}$ = 241 kips	Cyclic
Prism 6	1	8% drift	Monotonic	12 ε_y	$P_{8\%}$ = 182 kips	Cyclic

Unsymmetrical cycles that included compressive loads and tensile displacements were induced to the tests. The unique compressive target was selected based on *Po* and the corresponding P-Δ effects when the tests also contemplated permanent lateral displacements, determined as a function of drift percentages. The constant compressive targets were selected based on *Po* and the corresponding P-Δ effects when the tests also contemplated permanent lateral displacements, determined as a function of drift percentages. P-Δ effects were established through the linear interaction from the following equation:

$$P_{\%} = P_o - (P_o - P_b)\frac{M_{\%}}{M_b} \tag{4-4}$$

where, P_b = 164 kips and M_b = 475 kip.in are the axial force and bending moment at balanced stage, respectively. The flexural moment at an out-of-plane drift ratio is $M_{\%} = P_{\%}(\%drift*60in.)/2$. Substituting this expression in the previous equation and solving for $P_{\%}$, the compressive load is obtained.

The targets in tension were chosen as fractions of the yielding displacement determined from: $0.25\varepsilon_y$, $0.50\varepsilon_y$, and $0.75\varepsilon_y$ and $1.0\varepsilon_y$. Subsequently, three identical cycles at different axial tensile displacement ductility levels continued until buckling was captured upon compressive loading. Further explanation regarding the characteristics of the loading protocols followed during each test are found in Chapter 5 and APPENDIX A.

4.1.6.2 Experimental Phase 2

Table 4-5 shows the experimental test matrix corresponding to the three specimens tested during Phase 2, where the maximum target values reached in the different applied load/displacement directions are summarized. The design axial compression capacity (*Po*) of the prisms contemplated on this phase is equal to 322 *kips* (1432 *kN*), calculated as follows:

$$P_o = 0.85[5ksi*(5in*12in - 0.20in^2*6)] + 60ksi*0.20in^2*6$$

Table 4-5. Experimental test matrix of Phase 2

Specimen	Config.	Load protocol				
		Lateral		Axial		
		Displacement	Type	Max. Tension	Max. Compression	Type
Prism 7	2	0% drift	-	14 ε_y	Po = 322 kips	Cyclic
Prism 8	2	4% drift	Monotonic	14 ε_y	$P_{4\%}$ = 222 kips	Cyclic
Prism 9	2	2.5% drift	Monotonic	16 ε_y	$P_{2.5\%}$ = 251 kips	EQ-Sylmar Station ('94)

Unsymmetrical cycles that included compressive loads and tensile displacements were induced to the specimens. The constant compressive targets were selected based on *Po* and the corresponding P-Δ effects when the tests also contemplated permanent lateral displacements, determined as a function of drift percentages. P-Δ effects were included through the linear interaction from Equation (4-3), where P_b = 165 kips and M_b = 418 kip.in are the axial force and bending moment at balanced stage, respectively.

The targets in tension were established as fractions of the yielding displacement referred as $60\varepsilon_y$, where 60 represents the height of the prisms. During Phase 1 it was noticed that the elastic cycles did not influence the onset of instability, and consequently they were eliminated from Phase 2. Beyond the yielding stage and depending on the loading type, different tensile targets continued until out-of-plane instability was captured upon compressive loading.

In order to consider the effects of near-field records that contain long duration pulses, Test 9 included a seismic axial displacement history based on the structural response of a prototype RC wall subjected to an actual in-plane horizontal earthquake record. The 1994 Northridge earthquake (Sylmar station) was selected since it is characterized for a long duration pulse.

Further explanation regarding the characteristics of the loading protocols followed during each test are found in Chapter 5 and APPENDIX A.

4.1.6.3 Experimental Phase 3

The experimental test matrix detailed in Table 4-6, summarizes the maximum target axial and lateral loads/displacements contemplated for the three specimens considered in Phase 3. The design axial compression capacity (*Po*) of the prisms contemplated on this phase is equal to 292 *kips* (1299 *kN*), calculated as follows:

$$P_o = 0.85[5ksi*(5in*12in - 0.11in^2*6)] + 60ksi*0.11in^2*6$$

Table 4-6. Experimental test matrix of Phase 3

Specimen	Config.	Load protocol				
		Lateral		Axial		
		Displacement	Type	Max. Tension	Max. Compression	Type
Prism 10	3	0% drift	-	16 ε_y	P_o = 294 kips	Cyclic
Prism 11	3	0% drift	-	24 ε_y	P_o = 294 kips	EQ-Megathrust
Prism 12	3	0% drift	-	18 ε_y	P_o = 294 kips	EQ-Sylmar Station ('94)

Phase 3 considered three different axial loading history: cyclic, megathrust-type earthquake, and high pulse-type earthquake. The targets in tension were established as fractions of the yielding displacement referred as $60\varepsilon_y$, where 60 represents the height of the prisms in inches. Noticing the lack of influence of out-of-plane displacements on the onset of instability during Phase 1 and Phase 2, they were suppressed from Phase 3. Beyond the yielding stage and depending on the loading type, different tensile targets continued until failure due to bar buckling, bar fracture, or out-of-plane instability was captured.

Prism 11 was subjected to inelastic cycles based on subduction megathrust earthquakes generated from a loading protocol created according to Bazaez and Dusicka (2016), that requires the calculation of equivalent yielding displacements (δy). For this purpose, Moment-Curvature analyses of four prototype RCSW were conducted. Once the cyclic displacement responses of the walls were obtained from Equation (4-5), strains developed at each stage were used to establish the tensile axial displacements as a function of $60\varepsilon_y$. Table 4-7 and Table 4-8 define the exponential coefficients (*a*, *b*, *c*, *d*) to obtain the cycle amplitudes and the proposed loading protocols using the prepeak approach, respectively (Bazaez and Dusicka 2016).

$$f(N) = \left(a \cdot e^{bN} + c \cdot e^{dN}\right)\delta_y \tag{4-5}$$

where *N*, is the number of the inelastic cycle.

Table 4-7. Exponential Coefficients to Obtain Cycle Amplitudes (Bazaez and Dusicka 2016)

	$\mu = 2$			$\mu = 4$			$\mu = 8$		
	T	*T*	*T*	*T*	*T*	*T*	*T*	*T*	*T*
Coefficient	0.5 s	1.0 s	2.0 s	0.5 s	1.0s	2.0s	0.5 s	1.0 s	2.0 s
				Prepeak excursions					
a	0.9934	0.9934	0.5215	0.9653	0.9557	0.9638	0.8695	0.9014	0.9869
b	0.0221	0.0221	−0.3778	0.0281	0.0439	0.0543	0.0336	0.0415	0.0444
c	0.0137	0.0137	0.5674	1.15E-4	8.91E-4	2.72E-3	1.913E-7	2.83E-5	1.09E-3
d	0.4511	0.4511	0.2066	0.4284	0.4853	0.5570	0.4252	0.417	0.4282
				All excursions					
a	Same as prepeak excursions			0.9505	0.9335	0.936	0.8356	0.8659	0.8931
b				0.0245	0.0357	0.0485	0.0224	0.0314	0.0433
c				1.18E-5	3.14E-5	5.57E-5	1.84E-8	3.45E-7	3.4E-6
d				0.3875	0.478	0.613	0.3167	0.3816	0.4398

Table 4-8. Proposed Loading Protocols Using the Prepeak Approach (Bazaez and Dusicka 2016)

	Number of inelastic cycles (trailing cycles shown in parentheses)								
	Ductility ($\mu = 2$)			Ductility ($\mu = 4$)			Ductility ($\mu = 8$)		
Cycle amplitude $\times \delta_{yield}$	$T = 0.5$ s	$T = 1.0$ s	$T = 2.0$ s	$T = 0.5$ s	$T = 1.0$ s	$T = 2.0$ s	$T = 0.5$ s	$T = 1.0$ s	$T = 2.0$ s
1.0	1	1	1	3	2	2	3	3	2
1.1	2	2	1	3	2	1	3	3	2
1.2	2	2	1	3	2	1	3	3	1
1.3	1	1	—	2	1	1	3	2	1
1.4	—	—	1	2	1	1	3	1	1
1.5	1	1	—	1	1	1	3	1	1
1.6	—	—	—	1	1	—	3	1	1
1.7	1	1	1	1	1	1	2	1	1
1.8	—	—	—	1	—	—	2	1	1
1.9	—	—	—	1	1	—	2	1	1
2.0	1	1	1	1	1	1	1	1	1
2.1				—	—	—	—	1	—
2.2				1	—	1	1	1	1
2.4				—	—	—	1	1	—
2.6				1	1	—	1	1	1
2.8				—	—	—	1	1	—
3.0				(+5)	1(+4)	1(+3)	1	1	1
3.2				1	—	—	1	—	—
3.5				—	—	—	1	1	1
4.0				1	1	1	1	1	—
4.5							1	—	1
5.0							(+8)	1(+6)	(+5)
5.5							1	—	—
6.0							—	1	1
6.5							1	—	—
8.0							1	1	1

The effects of near-field records that contain long duration pulses were considered for Test 12. The 1994 Northridge earthquake (Sylmar station) was selected for this purpose and consequently the seismic axial displacement history was determined based on the structural response of a prototype RC wall subjected to in-plane horizontal accelerations.

The constant compressive targets were selected based on *Po* and the corresponding P-Δ effects when the tests also contemplated permanent lateral displacements, determined as a function of drift percentages. P-Δ effects were established through the linear interaction from Equation (4-3), where $P_b = 165\ kips$ and $M_b = 342\ kip.in$ are the axial force and bending moment at balanced stage, respectively.

Further explanation regarding the characteristics of the loading protocols followed during each test are found in Chapter 5 and APPENDIX A.

4.1.7 Data source

Eleven specimens included 14 gages on each longitudinal bar along the 60 in. (1,524mm) height. Prism 3 only included 13 gages on each longitudinal reinforcement bar since the location of the cavities allowed a different distribution for the infrared LEDs. In addition, since the central region of the prisms was the main area under study and with the aim of determining the influence of the transverse reinforcement on the onset of instability, ten gages were contemplated for the stirrups along

the central 20in. (508mm). Five gages were located on the north face and five on the south face of the prisms. The gage length was 4in. (101mm) for the longitudinal and transverse reinforcement. Strain profiles were determined for each longitudinal reinforcement line, which were six in total, three for the north face and three for the south face. In order to control the tensile strains demands in real time during the tests, the average of the central longitudinal reinforcement lines was the governing input. Figure 4-13 shows the regions and reinforcement lines described above that can be considered as reference for next sections where the test results are presented.

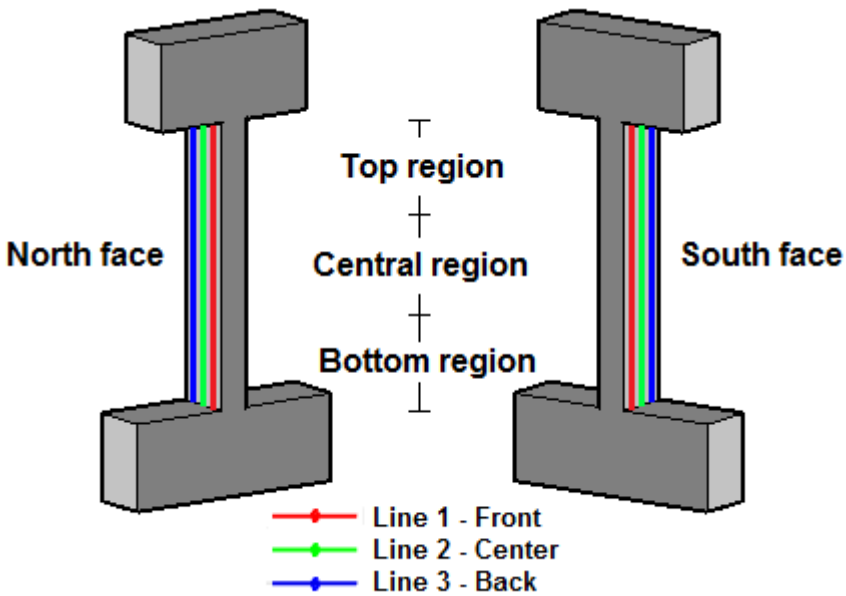

Figure 4-13. Prism Constituents

4.2 Analytical Predictions

Tensile strains calculated from Paulay and Priestley (1993) and Chai and Elayer (1999) models, already described in Chapter 2, were considered to determine the limit of stable cycles for the different experimental phases. Since the Parra & Moehle (2014) model neglects the effects of different longitudinal reinforcement ratios, its usage would result unsuitable considering the essence of the current experimental program. However, for comparison purposes the predictions are also included in Table 4-9. The values presented in the table for Phase 1 were established from a scaled prototype wall with total height h_w = 420in (10.6m), length l_w = 80in (2.0m), and effective height h_e = 280in (7.1m). The buckled length of the wall L_o was calculated from Equation (4-6), expression suggested by Priestley et al. (2007) to determine the plastic hinge length of structural walls.

$$L_p = k \cdot h_e + 0.1 l_w + L_{SP} \tag{4-6}$$

where, $k = 0.2(f_u/f_y - 1) \leq 0.08$ and $L_{SP} = 0.022\, f_y\, d_{bl}$ (f_y in MPa). The largest diameter of the longitudinal reinforcement placed in the compression region is defined by d_{bl}.

Table 4-9. Maximum Tensile Predicted Strains

Experimental Phase	Paulay and Priestley (1993)		Chai and Elayer (1999)		Parra & Moehle (2014)	
	$\varepsilon_{sm}/\varepsilon_y$	ε_{sm}	$\varepsilon_{sm}/\varepsilon_y$	ε_{sm}	$\varepsilon_{sm}/\varepsilon_y$	ε_{sm}
1	8.6	0.0206	9.2	0.0219	25.9	0.062
2	12.8	0.0304	11.9	0.0285	26.0	0.062
3	19.7	0.0427	16.5	0.0359	28.6	0.062

The results from Phase 1 suggested that the buckled length of the prisms was close to *60%* of their height, and consequently the predicted values for Phase 2 and Phase 3, presented in Table 4-9, where accordingly adjusted. Phase 1 also demonstrated that the maximum tensile strains captured before buckling instability was observed upon compressive loading were considerably lower than the values predicted from the Parra & Moehle (2014) model. Consequently, this model was omitted from the analyses developed in the following chapters.

CHAPTER 5: EXPERIMENTAL RESULTS

This chapter presents a summary of the experimental results of twelve prisms representative of boundary elements of prototype typical walls that were built and tested in the Constructed Facility Laboratory at the North Carolina State University. The aim of the tests is to evaluate the effect of different longitudinal reinforcement ratios in combination with different load paths on the onset of out-of-plane instability of planar special RCSW.

5.1 Experimental Observations

5.1.1 Test 1

Test 1 was conducted at the Constructed Facilities Laboratory on Thursday, February 18, 2016, as part of the experimental phase of this project. A monotonic lateral load and later one axial cycle load were applied to the specimen to capture its structural performance and to determine preliminary critical parameters associated with lateral instability of RC walls. Table 5-1 includes the principal properties of Prism 1, where ρ_l is the longitudinal reinforcement ratio, d_{bl} is the diameter of the bar, and s_h is the transverse reinforcement spacing.

Table 5-1. Prism 1: Specifications

Prism	Dimensions	Longitudinal Reinforcement Layout	ρ_l	s_h/d_{bl}	ε_y
1	5”x12”x60” (127mm x 305mm x 1,524mm)	(6) #5 (15.9mm)	0.031	3.2	0.00239

5.1.1.1 Test 1 Summary

Prism 1 was first subjected to a 10in. (254mm) monotonic increasing out-of-plane displacements, equivalent to 16.7% drift. The purpose of this part of the test was to confirm that the boundary element could sustain this level of drift in the absence of axial load. Figure 5-1 shows lateral displacements applied to Prism 1. During the 0.5in. (13mm) displacement, cracks appeared on the bottom north (BN) and top south (TS) regions of the prism. Experimental first yielding was expected at 0.7in. (18mm). Upon loading to 0.75in. (19mm), more small cracks formed and extended to the moment connections. After stage 3, the cracks became wider and more numerous. Concrete flaking occurred at 2in. (51mm) on the top north (TN) region. By the time the 3in. (76mm) displacement was completed, concrete flaking was observed on the bottom south (BS) region. Crack widths close to 3/32in. (2.4mm) were measured on the bottom north region. When the specimen deformed 5in. (127mm), slight concrete crushing on both compression regions was captured. In addition, concrete spalling was observed on the bottom south region. For the next displacements damage continued

propagating and more cracks appeared on the joints. The tensile strains reached at 10in. (254mm) were close to 5.6% obtained from the farthest gages located on bottom north and top south regions. The deformed during this stage is presented in Figure 5-2. Only minor loss on the lateral capacity of the prism was detected at the end of this stage.

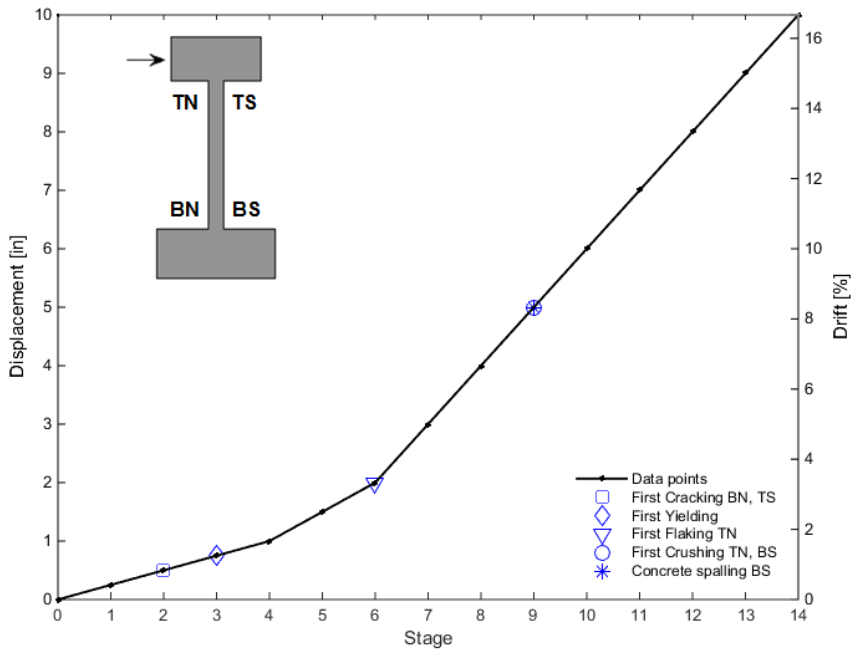

Figure 5-1. Prism 1: Out-of-Plane Lateral Displacement History

Figure 5-2. Prism 1: Deformed shape at 10in. (254mm) lateral displacement

Once the lateral monotonic loading was concluded, the specimen was returned to a zero lateral displacement position and subsequently was subjected to axial an axial tension/compression cycle. The tensile strain target was 3% and the compressive target displacement was 0.0in. (0.0mm). Upon compressive loading, and before reaching the compressive target, out-of-plane buckling instability was captured as shown in Figure 5-3. Concrete cover crushing and spalling were observed in the central part of the buckled region. The load captured at the time the prism started to buckle was 96kips (427kN), equivalent to 27% of the compression design capacity of the prism, *Po* = 358 kips (1,592kN).

Figure 5-3. Prism 1: Buckling instability at the end of the axial cycle

Figure 5-4 depicts axial strains plotted against axial loads captured where the out-of-plane deformation reached a maximum value at the end of the test. Notice a stable response of the prism at low levels of axial tensile strains. An axial stiffness reduction is evident by the time the axial compressive load approaches the compressive yielding strength. The specimen was still extended at this stage. This point was associated with the out-of-plane buckling mechanism. Then, instability was captured since the prism was not able to recover its strength. The maximum applied load at this stage was -236 kips, equivalent to 66% of the axial design compressive force, *Po*. Figure 5-4 also shows the corrected predictions according to Paulay & Priestley (1993) "P&P" and Chai & Elayer (1999) "Ch&E" models once the actual buckled length was determined. In addition, tensile and compressive yielding strengths, *Asfy*, are similarly plotted, where *As* is the area of the longitudinal reinforcement.

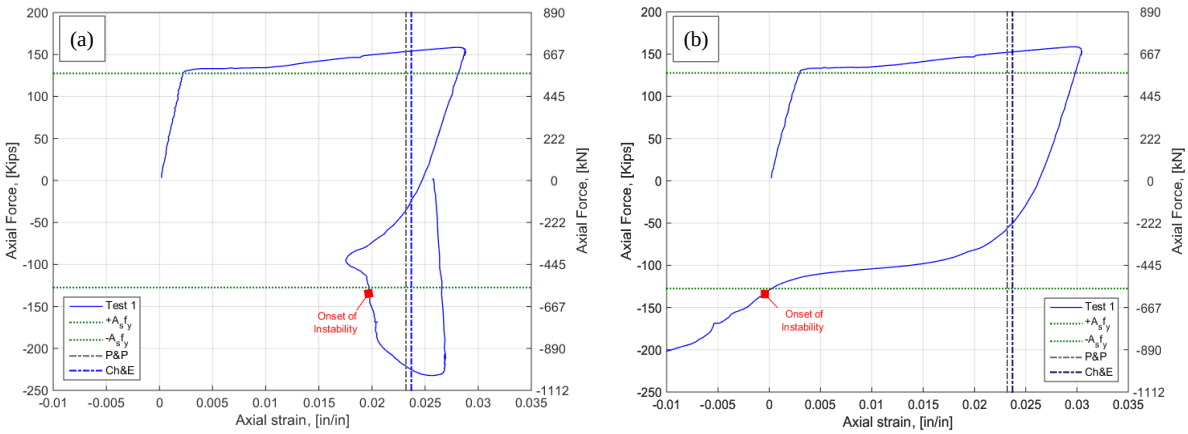

Figure 5-4. Prism 1: Axial Strain vs. Axial Force established 4in. (102mm) below midheight on a) south face and b) north face

Figure 5-5 shows the of out-of-plane deformations captured at the end of the test. The stability criterion from Paulay & Priestley (1993) model calculated as out-of-plane deformation and denoted as stability limit, is included in Figure 5-10 to show that instability was expected beyond this limit. During this cycle, the maximum out-of-plane deformation was δm = 2.7in. (69mm) located 4in. (102mm) below midheight, which exceeded 50% of the prism thickness.

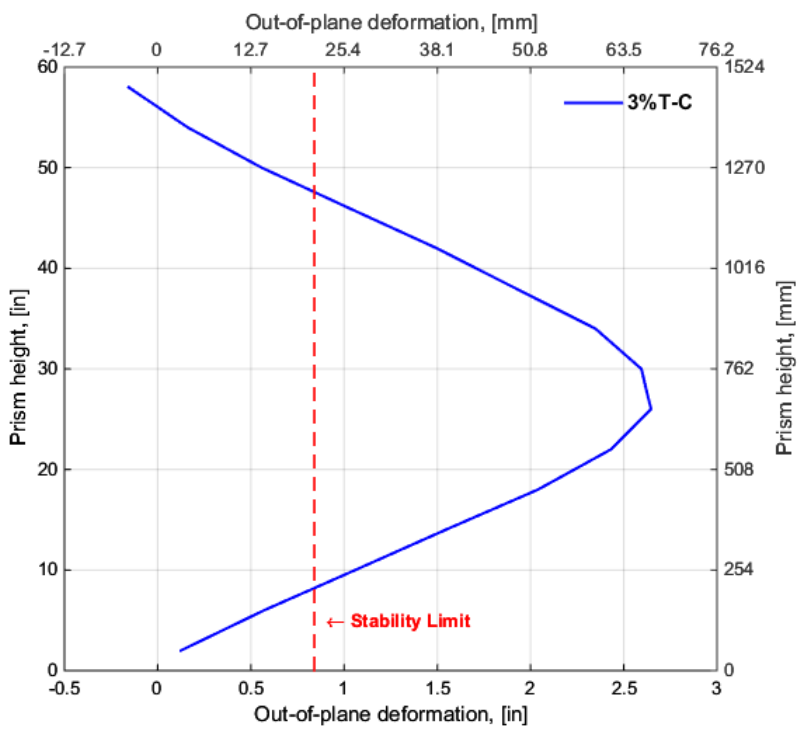

Figure 5-5. Prism 1: Out-of-plane deformation captured upon compressive loading at the end of the test

5.1.1.2 Test 1 Conclusions

Prism 1 was tested during 4 hours where different loading patterns were applied. The first part of the test showed that the prism reached the 10in. (254mm) displacement with minor loss of capacity. Initial signs of concrete crushing and concrete spalling were noticed at 5in. (127mm). Maximum strain values of 5.6% were computed on the bottom north and top south regions by the end of the final stage related to the lateral monotonic loading.

In the second part of the test, axial tensile displacements equivalent to 3% strain were induced. Values close to the target were observed in the central region of the prism. However, the bottom north and top south showed higher values, demonstrating the influence of the previous loading pattern. The onset of buckling was captured by the time the prism was still elongated. An out-of-plane deformation greater than 50% of the prism thickness was determined for a compressive load equivalent to 66% of the compressive design capacity of the prism. Neither bar buckling nor bar fracture were detected during or after the test. The stirrups remained as originally constructed.

5.1.2 Test 2

Test 2 was conducted at the Constructed Facilities Laboratory on Thursday, March 22, 2016, as part of the load path project. An axial compression load followed by cyclic axial tensile displacements and compressive loads were applied to the specimen to capture its structural performance and to determine additional critical parameters associated with lateral instability of RC walls. Table 5-2 includes the principal properties of Prism 2, where ρ_l is the longitudinal reinforcement ratio, d_{bl} is the diameter of the bar, and s_h is the transverse reinforcement spacing.

Table 5-2. Prism 2: Specifications

Prism	Dimensions	Longitudinal Reinforcement Layout	ρ_l	s_h/d_{bl}	ε_y
2	5”x12”x60” (127mm x 305mm x 1,524mm)	(6) #5 (15.9mm)	0.031	3.2	0.00239

5.1.2.1 Test 2 Summary

Prism 2 first was subjected to an axial load equivalent to the design axial compression capacity of the prism, *Po* = -358 kips. The purpose of this part of the test was to confirm that the boundary element of the wall could sustain this level of compressive load in the absence of lateral displacements. Strain profiles captured at this stage showed that the average compressive strain in both faces of the prism was close to -0.15%, which is less than the yielding compressive strain -0.239%.

Subsequently, the axial cyclic displacements/forces were applied starting with elastic single targets. The tensile values were chosen as fractions of the yielding displacement referred as: $0.25\varepsilon_y$, $0.50\varepsilon_y$, $0.75\varepsilon_y$, and ε_y. After yielding, three identical cycles at different axial tensile displacement ductility levels continued until buckling was captured upon compressive loading. The unique compressive target was established from the first part of the experiment corresponding to *Po*, which was applied on each cycle during the whole test. Figure 5-6 shows the axial strain history applied to Prism 2.

First cracks developed at the footing-prism interface on the right face and along the height of the prism during $0.50\varepsilon_y$. Upon loading to $2\varepsilon_y$, more small cracks formed and extended to the joints. Crack widths close to 1/16in. were captured at $4\varepsilon_y$. During the following cycle the cracks became wider and the number of new cracks decreased. In addition, it was observed that the spacing of the horizontal cracks were governed by the spacing of the transverse reinforcement since they fairly corresponded to each other. Signs of concrete flaking on the footing-prism interface appeared in the first cycle corresponding to $6\varepsilon_y$. At the end of the third cycle, concrete cover fell down on the back

face of the prism and the transverse reinforcement was exposed within a length of 34in. In the cycles associated with an $8\varepsilon_y$ tensile demand, cracks became wider and the concrete cover continued falling apart in the same region described before. At the end of the third cycle, the transverse reinforcement was uncovered within a height of 54in. All through these cycles, the specimen remained visibly straight.

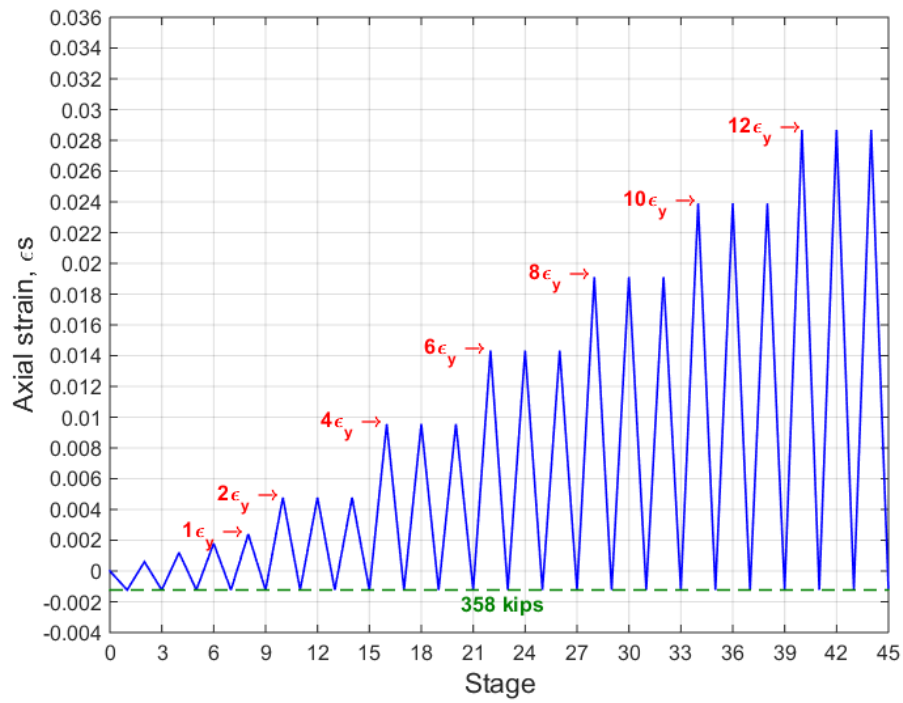

Figure 5-6. Axial Strain History applied to Prism 2

As tensile demands increased during the cycles related to $10\varepsilon_y$, the out-of-plane buckling mechanism was visually captured upon compressive loading. In this scenario, where the out-of-plane deformation is relatively small, the compression force developed to resist the overturning moment, can be fully reached as cracks close and consequently, the prism returns to a fairly straight and stable position. This phenomenon was similarly observed during the first two cycles corresponding to a tensile demand of $12\varepsilon_y$. Figure 5-7 shows the evolution of out-of-plane deformations when a stable buckling mechanism occurred upon compressive loads during the second cycle associated with $12\varepsilon_y$. In the third cycle upon compressive loading, a different scenario developed since instability occurred as illustrated in Figure 5-8. A well confined concrete core was noticed at this stage.

Figure 5-9 depicts axial strains plotted against axial loads captured where the out-of-plane deformation reached a maximum value at the end of the test. Notice a stable response of the prism at low levels of axial tensile strains. In the last six cycles, an axial stiffness reduction is evident by the time the axial compressive load approaches the compressive yielding strength. At these stages, the

specimen was still extended. These points were associated with the out-of-plane buckling mechanism. In the last cycle, instability occurred since the prism was not able to recover its strength. The maximum applied load at this stage was -232 kips, equivalent to 65% of the axial design compressive force, *Po*.

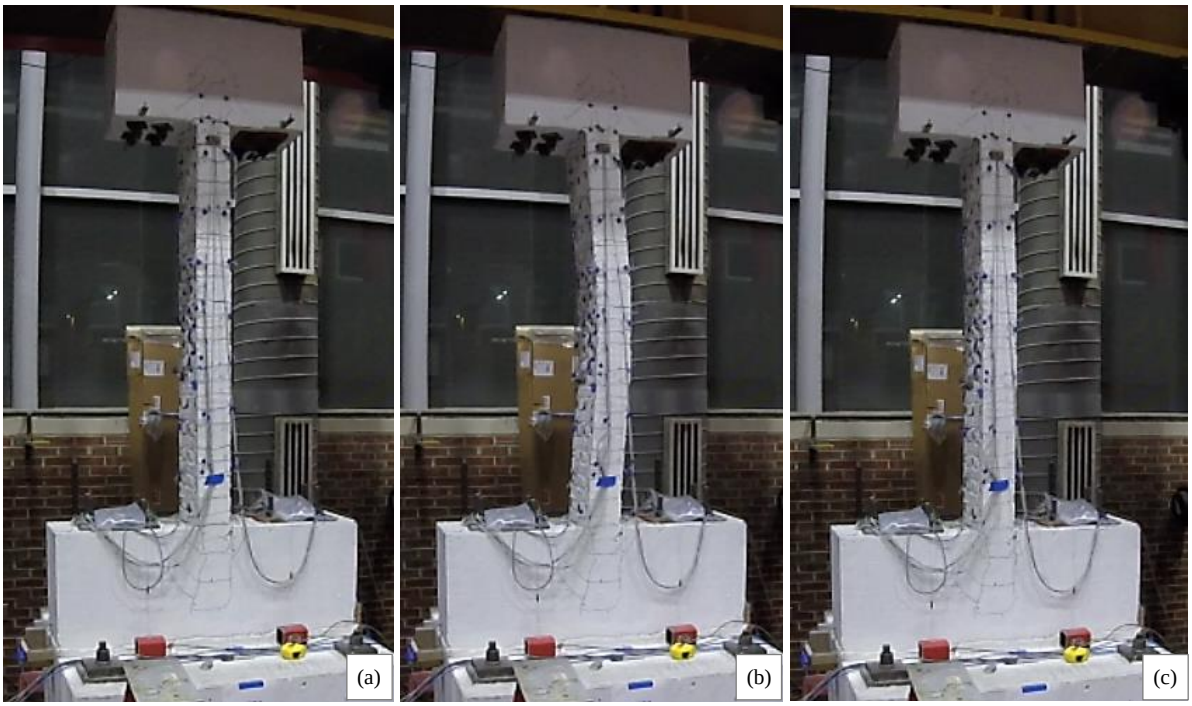

Figure 5-7. Prism 2: Stable out-of-plane buckling mechanism during $12\varepsilon_y(2)$, second cycle: a) Onset of buckling – cracks opened, b) Stable buckling – cracks partially closed, c) End of buckling - cracks closed.

Figure 5-8. Prism 2: Instable out-of-plane buckling mechanism during $12\varepsilon_y(3)$, third cycle

Figure 5-9 also shows the corrected predictions according to Paulay & Priestley (1993) "P&P" and Chai & Elayer (1999) "Ch&E" models once the actual buckled length was determined. In addition, tensile and compressive yielding strengths, *Asfy*, are similarly plotted, where *As* is the area of the longitudinal reinforcement.

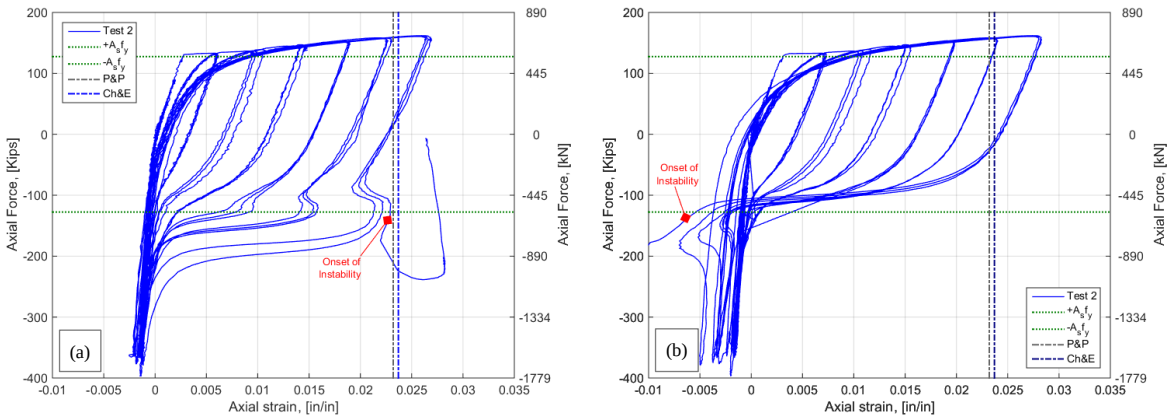

Figure 5-9. Prism 2: Axial Strain vs. Axial Force established at midheight on a) south face and b) north face

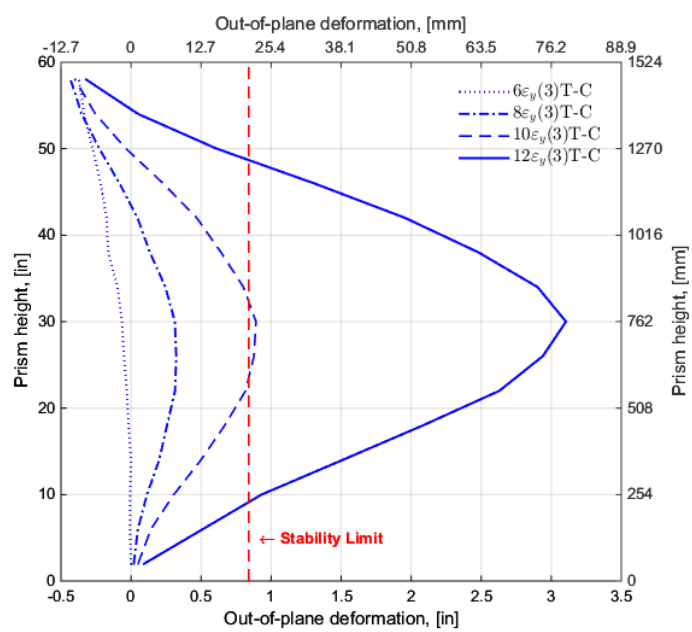

Figure 5-10. Prism 2: Evolution of out-of-plane deformations captured upon compressive loading at different stages

Out-of-plane deformations increased upon compressive loading during the first cycle associated with $8\varepsilon_y$. Figure 5-10 shows the evolution of out-of-plane deformations at different stages. Throughout the first cycle of $12\varepsilon_y$, the specimen suffered from a permanent out-of-plane deformation.

A sudden increment on this deformation took place when the load slightly exceeded the yielding compressive strength. The stability criterion from Paulay & Priestley (1993) model calculated as out-of-plane deformation and denoted as stability limit, is included in Figure 5-10 to show that instability was expected beyond this limit. During the final cycle, the maximum out-of-plane deformation was δm = 3.1in. (79mm) located at midheight, which exceeded 50% of the prism thickness.

Notice that the out-of-plane top displacement is close to 0.35in. (9mm) instead of 0in., which is attributed to the complexity of the technic implemented to control the three actuators at once. However, the axial response of the prism is indifferent to this minor input.

5.1.2.2 Test 2 Conclusions

The first part of the test indicates the prism reached the maximum axial design compressive load with zero loss of capacity. The average compressive strain in both faces was close to -0.0015, less than the yielding strain. In the second part of the test, progressive cyclic axial loads/strains were applied to the specimen reaching maximum values close to the axial design compressive force, Po = -358 kips and $12\varepsilon_y$, in compression and tension, respectively. The specimen presented a stable response at low levels of axial tensile demands. Out-of-plane deformations were not noticed during the cycles before $8\varepsilon_y$. Beyond the first cycle of $8\varepsilon_y$, a gradual increase in the out-of-plane deformations were captured until instability developed during the last cycle of $12\varepsilon_y$. The large buckling displacement led to concrete crushing and spalling in the central region. The axial force at this stage was 65% of the target compressive load. Neither bar buckling nor bar fracture were detected during or after the test. The stirrups remained as originally constructed.

5.1.3 Test 3

Test 3 was conducted at the Constructed Facilities Laboratory on Thursday, March 27, 2016, as part of the load path project. A monotonic and constant lateral displacement equivalent to 1% drift was applied first to the specimen followed by cyclic axial compressive loads and tensile displacements. Table 5-3 includes the principal properties of Prism 3, where ρ_l is the longitudinal reinforcement ratio, d_{bl} is the diameter of the bar, and s_h is the transverse reinforcement spacing.

Table 5-3. Prism 3: Specifications

Prism	Dimensions	Longitudinal Reinforcement Layout	ρ_l	s_h/d_{bl}	ε_y
3	5”x12”x60” (127mm x 305mm x 1,524mm)	(6) #5 (15.9mm)	0.031	3.2	0.00239

5.1.3.1 Test 3 Summary

A 0.6in. out-of-plane top displacement, equivalent to 1% drift, was first induced to Prism 3. The purpose was to keep this displacement constant during the entire test. First cracks appeared on the bottom and top regions of the prism at the end of this stage. The strains were close to 0.15%, less than the yielding strain. Subsequently, the axial displacement history started with elastic single cycles. The targets in tension were chosen as fractions of the yielding displacement referred as: $0.25\varepsilon_y$, $0.50\varepsilon_y$, and $0.75\varepsilon_y$. Including the axial yielding point, ε_y, three identical cycles at different axial tensile displacement ductility levels continued until buckling was captured upon compressive loading. The unique compressive target load, $P_{1\%}$ = -319 kips, was established considering P-Δ effects, representing 89% of the maximum axial design compressive load, Po = -358 kips. Figure 5-11 shows the axial strain history applied to Prism 3.

During the application of the first compressive load, a small vertical crack appeared in the concrete cover of the east face of the prism. Horizontal cracks became more numerous upon yielding tensile demands while small cracks formed and extended to the joints. During the application of compressive loads, the cracks tended to close as expected. Crack widths close to 1/32 in. were captured at $2\varepsilon_y$. During the following cycles the cracks became wider and the number of new cracks decreased. It was noticed that the spacing of the horizontal cracks were governed by the spacing of the transverse reinforcement. Signs of concrete spalling on the east face of the prism were observed in the first cycle at $4\varepsilon_y$. Crack widths close to 0.05 in. and 0.075 in. were captured at $6\varepsilon_y$ and $8\varepsilon_y$, respectively. Cracks became wider than 0.10 in. for the $10\varepsilon_y$ and $12\varepsilon_y$ cycles. During tensile demands at $14\varepsilon_y$, concrete

cover fell down on the east face of the prism and transverse reinforcement was exposed in different regions.

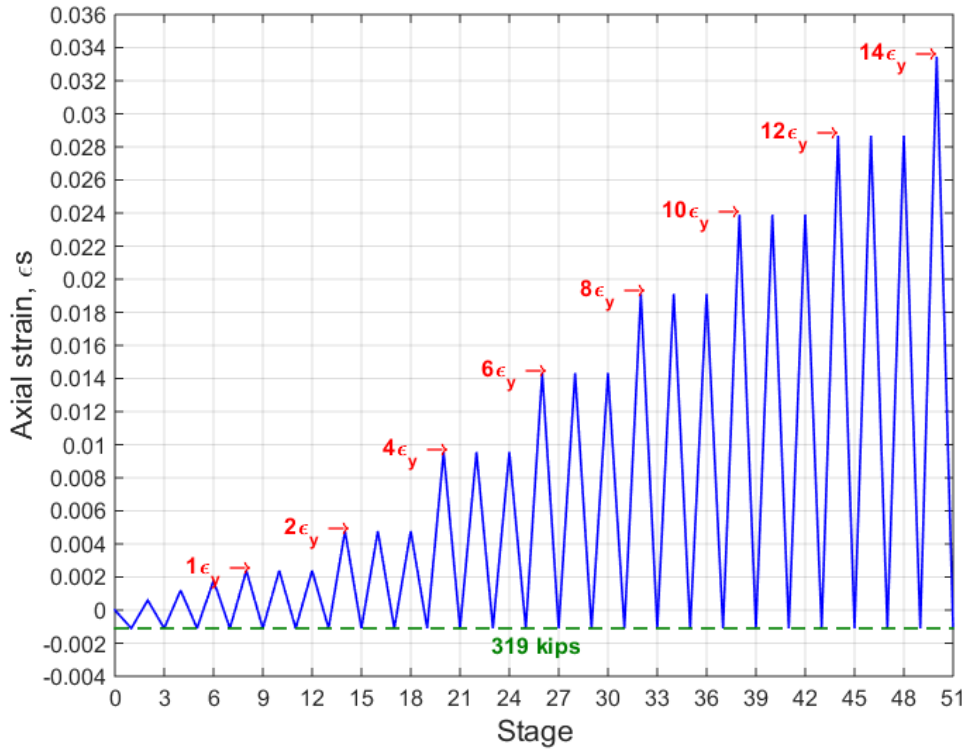

Figure 5-11. Axial Strain History applied to Prism 3

Throughout the first cycle related to $8\varepsilon_y$, a stable out-of-plane buckling mechanism was observed upon compressive loading. This scenario, where the out-of-plane deformations were relatively small, was captured during the three cycles corresponding to $8\varepsilon_y$, $10\varepsilon_y$, and $12\varepsilon_y$. After experimenting these out-of-plane deformations, the prism returned to a fairly straight position when the cracks closed and consequently it was able to resist the intrinsic forces associated with compressive forces developed to sustain overturning moments. Figure 5-12 shows the evolution of out-of-plane deformations when a stable buckling mechanism occurred upon compressive loads during the third cycle associated with $12\varepsilon_y$. During the first cycle related to $14\varepsilon_y$ and upon compressive loading, a different scenario was captured where instability occurred as illustrated in Figure 5-13.

Figure 5-14 depicts axial strains plotted against axial loads captured where the out-of-plane deformation reached a maximum value at the end of the test. Notice a stable response of the prism at low levels of axial tensile strains. In the last ten cycles an axial stiffness reduction is evident by the time the axial compressive load approaches the compressive yielding strength. At this stage, the specimen was still extended. These points were associated with the out-of-plane buckling mechanism. In the last cycle, instability was captured since the prism was not able to recover its strength. The

maximum applied load at this stage was -210 kips, equivalent to 66% of the axial target load, $P_{1\%}$ = -*319 kips*.

Figure 5-12. Prism 3: Stable out-of-plane buckling mechanism during 12ε_y(3), third cycle: a) Onset of buckling – cracks opened, b) Stable buckling – cracks partially closed, c) End of buckling - cracks closed.

Figure 5-13. Prism 3: Instable out-of-plane buckling mechanism during 14εy(1), first cycle

Figure 5-14 also shows the corrected predictions according to Paulay & Priestley (1993) "P&P" and Chai & Elayer (1999) "Ch&E" models once the actual buckled length was determined. In addition, tensile and compressive yielding strengths, *Asfy*, are similarly plotted, where *As* is the area of the longitudinal reinforcement.

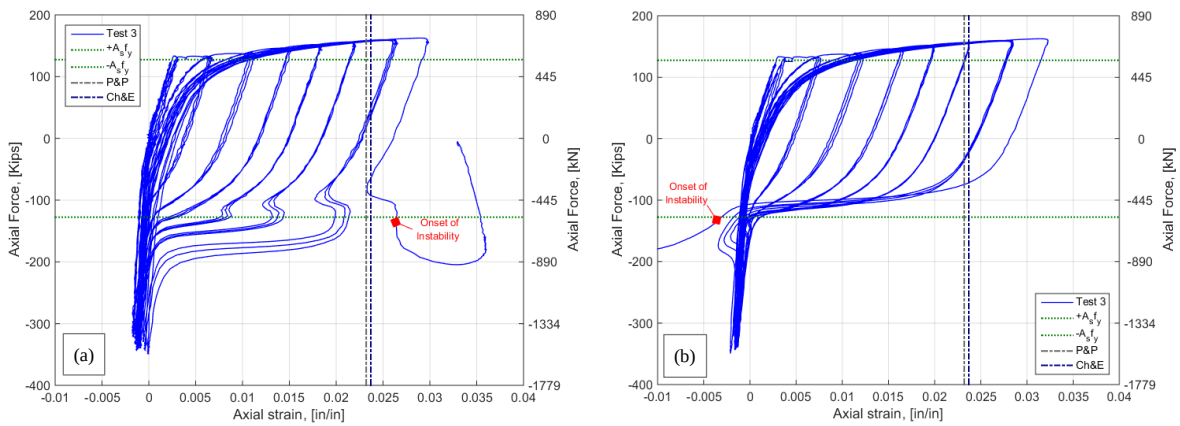

Figure 5-14. Prism 3: Axial Strain vs. Axial Force established 2in. (51mm) above midheight a) south face and b) north face

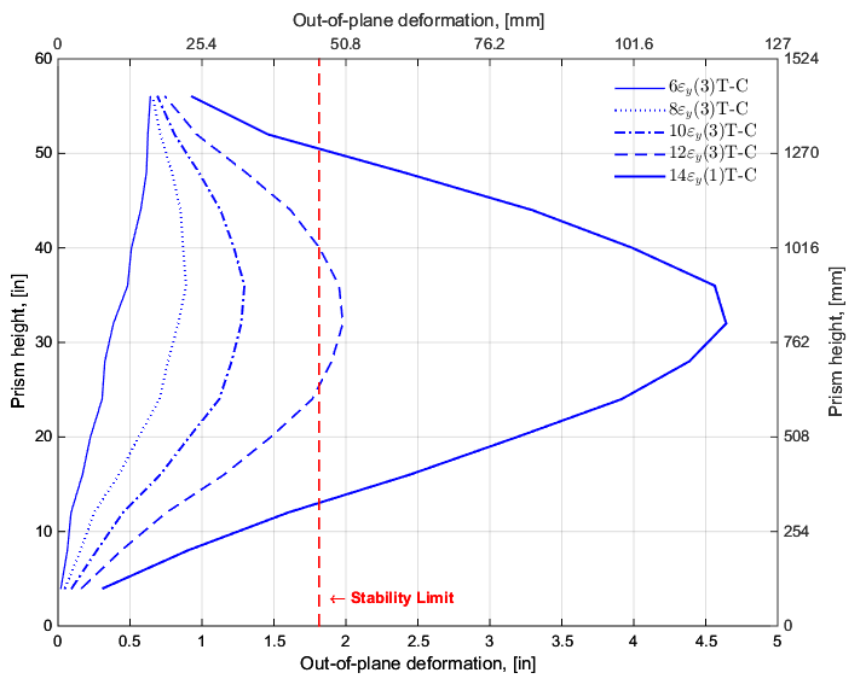

Figure 5-15. Prism 3: Evolution of out-of-plane deformations captured upon compressive loading at different stages

Out-of-plane deformations increased upon compressive loading during the first cycle associated with $8\varepsilon_y$. Figure 5-15 shows the evolution of out-of-plane deformations at different stages. During the third cycle of $12\varepsilon_y$, the specimen suffered from a permanent out-of-plane deformation. A

sudden increment on this deformation took place when the load slightly exceeded the yielding compressive strength. The stability criterion from Paulay & Priestley (1993) model calculated as out-of-plane deformation and denoted as stability limit, is included in Figure 5-15 to show that instability was expected beyond this limit. During the final cycle, the maximum out-of-plane deformation was δm = 4.6in. (177mm), located 2in. (51mm) above midheight, which exceeded 50% of the prism thickness.

5.1.3.2 Test 3 Conclusions

Prism 3 was tested during five hours where combined load patterns were applied. A lateral out-of-plane displacement equivalent to 1% drift was sustained during the entire test to analyze its influence on the stability of RC walls. The maximum tensile strain in bottom and top tensile regions of the prism during this first stage, where axial loads were not induced, was close to 0.0015. Subsequently, progressive cyclic axial loads/strains were applied to the specimen reaching maximum values fairly close to the targets $P_{1\%}$ = -319 kips and $14\varepsilon_y$, in compression and tension, respectively. The specimen presented a stable response at low levels of axial tensile demands. Out-of-plane deformations were not noticed during the cycles before $8\varepsilon_y$. Beyond the first cycle of $8\varepsilon_y$, a gradual increment in the out-of-plane deformations were captured until instability developed during the first cycle of $14\varepsilon_y$. The large buckling displacement led to concrete crushing and spalling in the central region. The axial force at this stage was 66% of the target compressive force. Neither bar buckling nor bar fracture were detected during or after the test. The stirrups remained as originally constructed.

5.1.4 Test 4

Test 4 was conducted at the Constructed Facilities Laboratory on Thursday, April 12, 2016, as part of the load path project. A monotonic and constant lateral displacement equivalent to 4% drift was applied first to the specimen followed by cyclic axial compressive loads and tensile displacements to capture its structural performance and to determine additional critical parameters associated with lateral instability of RC walls. Table 5-4 includes the principal properties of Prism 4, where ρ_l is the longitudinal reinforcement ratio, d_{bl} is the diameter of the bar, and s_h is the transverse reinforcement spacing.

Table 5-4. Prism 4: Specifications

Prism	Dimensions	Longitudinal Reinforcement Layout	ρ_l	s_h/d_{bl}	ε_y
4	5”x12”x60” (127mm x 305mm x 1,524mm)	(6) #5 (15.9mm)	0.031	3.2	0.00239

5.1.4.1 Test 4 Summary

An out-of-plane displacement of 2.4 in., equivalent to 4% drift, was induced to Prism 4. The purpose was to keep this displacement constant during the entire test. First cracks appeared on the bottom north and top south regions of the prism at the end of this stage. Concrete spalling was also observed in the same regions where the strains were close to 0.4%, greater than the yielding strain. Subsequently, the axial displacement history started with elastic single cycles. The targets in tension were chosen as fractions of the yielding displacement referred as: $0.25\varepsilon_y$, $0.50\varepsilon_y$, and $0.75\varepsilon_y$ and $1.0\varepsilon_y$. Subsequently, three identical cycles at different axial tensile displacement ductility levels continued until buckling was captured upon compressive loading. The unique compressive target load, $P_{4\%}$ = -241 kips, was established considering P-Δ effects, representing 67% of the axial design compressive load, Po = -358 kips. Figure 5-16 shows the axial strain history applied to Prism 4.

Through the first compressive load, vertical cracks appeared in the concrete cover on top north (TN) and bottom south (BS) regions accompanied by concrete spalling. Upon yielding tensile demands, horizontal cracks became more numerous and small cracks formed and extended to the joints. During the application of compressive loads, the cracks tended to close only in the central region of the prism. Once again, it was noticed that the spacing of the transverse reinforcement induced the spacing of the horizontal cracks. Crack widths between 1/32 in. and 3/64 in. were captured close to the joints at $1\varepsilon_y$. Concrete spalling became more severe at TN and BS regions where the damage was concentrated. In the following cycles the number of new cracks decreased. Through tensile demands at $6\varepsilon_y$, concrete flacking and concrete spalling propagated approximately 8 in. at TN and BS regions, which became more severe during the next cycles. Upon the $8\varepsilon_y$ first cycle, crack widths close to 0.10

in. were measured in the central region. Concrete cover continued to fall down on the TN and BS regions and consequently transverse reinforcement was exposed on the corners. The cracks became visibly wider than previous cycles and close to 1/8 in. beyond the $10\varepsilon_y$ cycles.

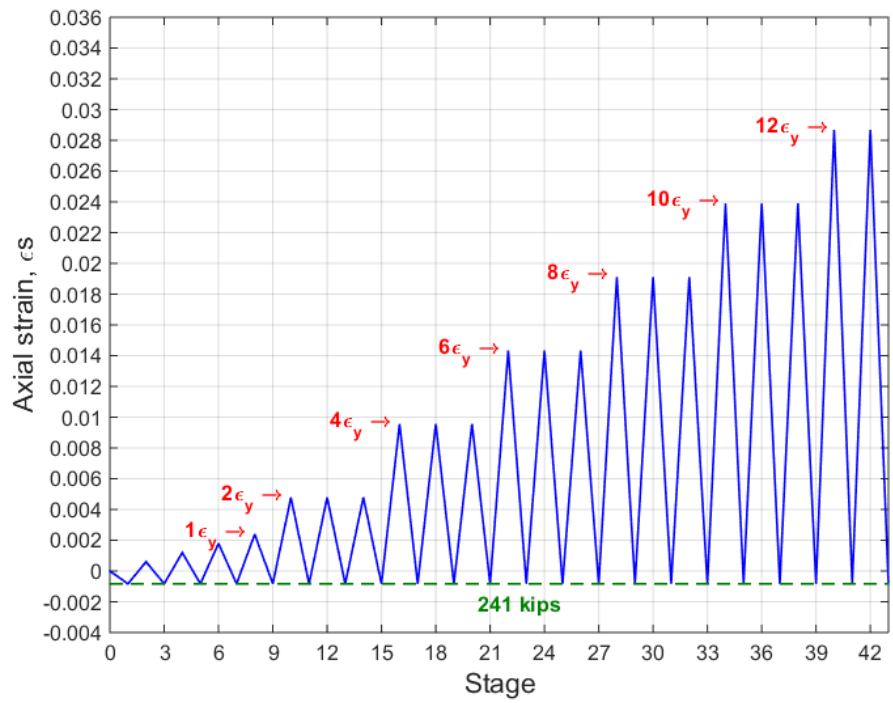

Figure 5-16. Axial Strain History applied to Prism 4

During the three cycles related to $10\varepsilon_y$, out-of-plane buckling was visually captured upon compressive loading. After experiencing these small out-of-plane deformations, the prism returned to a straight position when the cracks closed in the central region, and consequently the prism was able to resist the intrinsic forces associated with compressive forces developed to sustain overturning moments. Figure 5-17 shows the evolution of out-of-plane deformations when a stable buckling mechanism occurred upon compressive loads during the third cycle associated with $10\varepsilon_y$. In the first cycle associated with $12\varepsilon_y$ upon compressive loading, a different scenario was captured. Even though the prism was able to carry the same level of compressive loads achieved in previous cycles, it preserved a deformed but stable shape as shown in Figure 5-18. It was during the second cycle where instability occurred as illustrated in Figure 5-19.

Figure 5-20 depicts axial strains plotted against axial loads captured where the out-of-plane deformation reached a maximum value at the end of the test. Notice a stable response of the prism at low levels of axial tensile strains. In the last five cycles, an axial stiffness reduction is evident by the time the axial compressive load approaches the compressive yielding strength. At this stage, the specimen was still extended. These points were associated with the out-of-plane buckling mechanism.

In the last cycle, instability occurred since the prism was not able to recover its strength. The maximum applied load at this stage was -208 kips, equivalent to 86% of the axial target load, $P_{4\%} = -241$ *kips*. Figure 5-20 also shows the corrected predictions according to Paulay & Priestley (1993) "P&P" and Chai & Elayer (1999) "Ch&E" models once the actual buckled length was determined. In addition, tensile and compressive yielding strengths, *Asfy*, are similarly plotted, where *As* is the area of the longitudinal reinforcement.

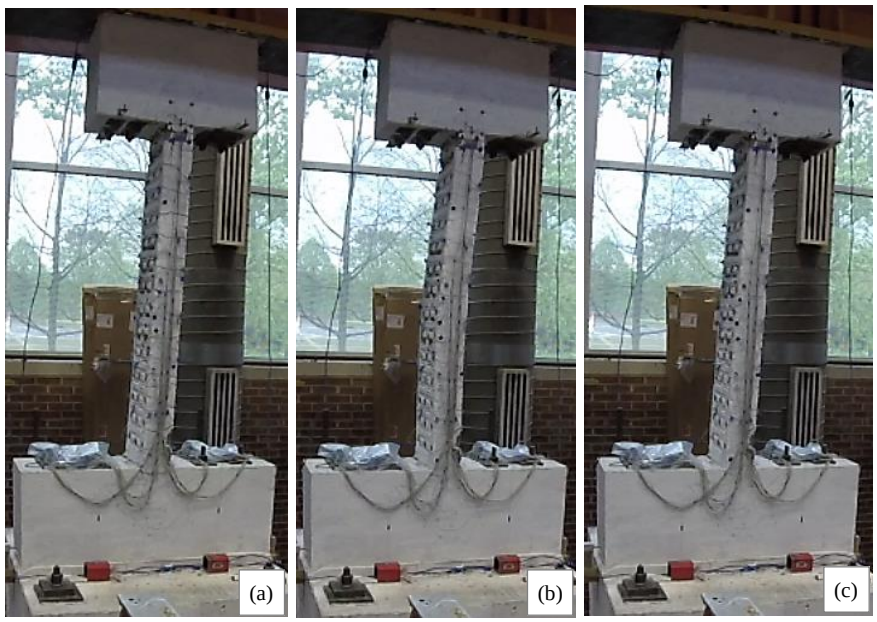

Figure 5-17. Prism 4: Stable out-of-plane buckling mechanism during 10εy(3), third cycle: a) Onset of buckling – cracks opened, b) Stable buckling – cracks partially closed, c) End of buckling - cracks closed.

Figure 5-18. Prism 4: Deformed shape at the end of 12εy(1), first cycle

Figure 5-19. Prism 4: Instable out-of-plane buckling mechanism during 12εy(2), second cycle

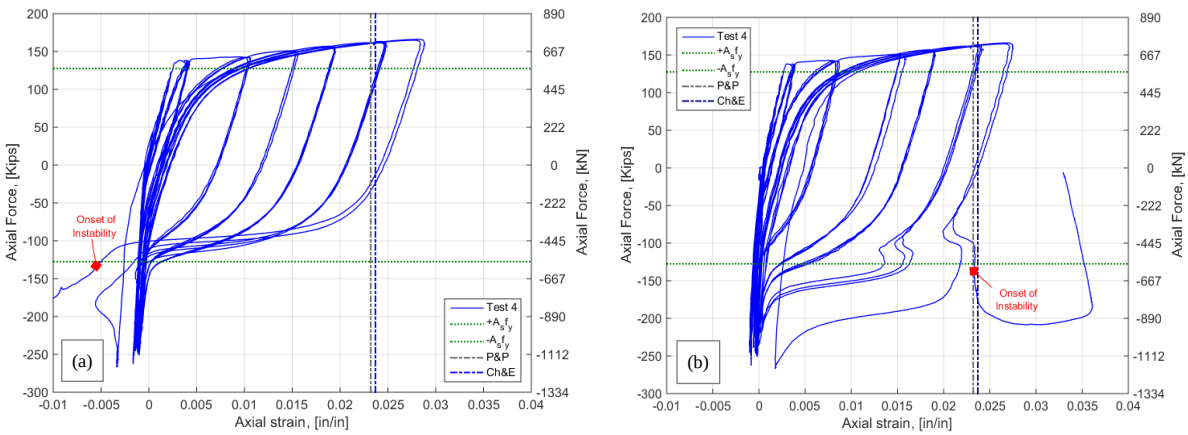

Figure 5-20. Prims 4: Axial Strain vs. Axial Force established 2in. (51mm) below midheight a) south face and b) north face

Out-of-plane deformations increased upon compressive loading during the first cycle associated with $10\varepsilon_y$. Figure 5-21 shows the evolution of out-of-plane deformations at different stages. During the first cycle of $12\varepsilon_y$, the specimen suffered from a permanent out-of-plane deformation. A sudden increment on this deformation took place when the load slightly exceeded the yielding compressive strength. The stability criterion from Paulay & Priestley (1993) model calculated as out-of-plane deformation and denoted as stability limit, is included in Figure 5-21 to show that instability was expected beyond this limit. During the final cycle, the maximum out-of-plane deformation was δm = 4.0in. (102mm), located 2in. (51mm) below midheight, which exceeded 50% of the prism thickness.

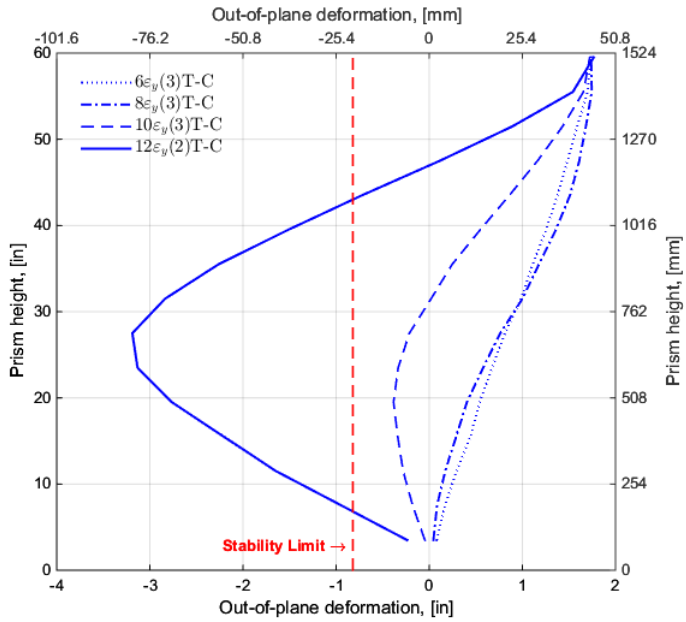

Figure 5-21. Prism 4: Evolution of out-of-plane deformations captured upon compressive loading at different stages

5.1.4.2 Test 4 Conclusions

Prism 4 was tested during five hours where combined load patterns were applied. A lateral out-of-plane displacement equivalent to 4% drift was sustained during the entire test. Tensile strains close to 0.4% were measured close to the interface between the prism and the joints before initiating the axial cycles. Subsequently, progressive cyclic axial loads/strains were applied to the specimen reaching maximum values fairly close to the targets $P_{4\%}$ = -241 kips and $12\varepsilon_y$, in compression and tension, respectively. The specimen presented a stable response at low levels of axial tensile demands. Out-of-plane deformations were not noticed during the cycles before $10\varepsilon_y$. Beyond the first cycle of $10\varepsilon_y$, a gradual increment in the out-of-plane deformations were captured until instability developed during the second cycle of $12\varepsilon_y$. The large buckling displacement led to cover concrete crushing and spalling specially in the central region. The axial force at this stage was 86% of the target compressive load. Neither bar buckling nor bar fracture were detected during or after the test. The stirrups remained as originally constructed and a well confined concrete core was notice at the end of the test.

5.1.5 Test 5

Test 5 was conducted at the Constructed Facilities Laboratory on Thursday, June 7, 2016, as part of the load path project. A combination of cyclic lateral displacements and cyclic axial compressive loads and tensile displacements were applied to the specimen to capture its structural performance and to determine additional critical parameters associated with lateral instability of RC walls. Table 5-5 includes the principal properties of Prism 5, where ρ_l is the longitudinal reinforcement ratio, d_{bl} is the diameter of the bar, and s_h is the transverse reinforcement spacing.

Table 5-5. Prism 5: Specifications

Prism	Dimensions	Longitudinal Reinforcement Layout	ρ_l	s_h/d_{bl}	ε_y
5	5”x12”x60” (127mm x 305mm x 1,524mm)	(6) #5 (15.9mm)	0.031	3.2	0.00239

5.1.5.1 Test 5 Summary

Prism 5 was subjected to cyclic out-of-plane displacements combined with cyclic axial tensile displacements and compressive loads. The axial displacement history started with single elastic cycles analytically predicted. Subsequently, three identical cycles at different drift levels continued until instability developed due to the axial protocol. The targets regarding the out-of-plane displacements were established as ratios of a maximum 4% drift and are shown in Figure 5-22.

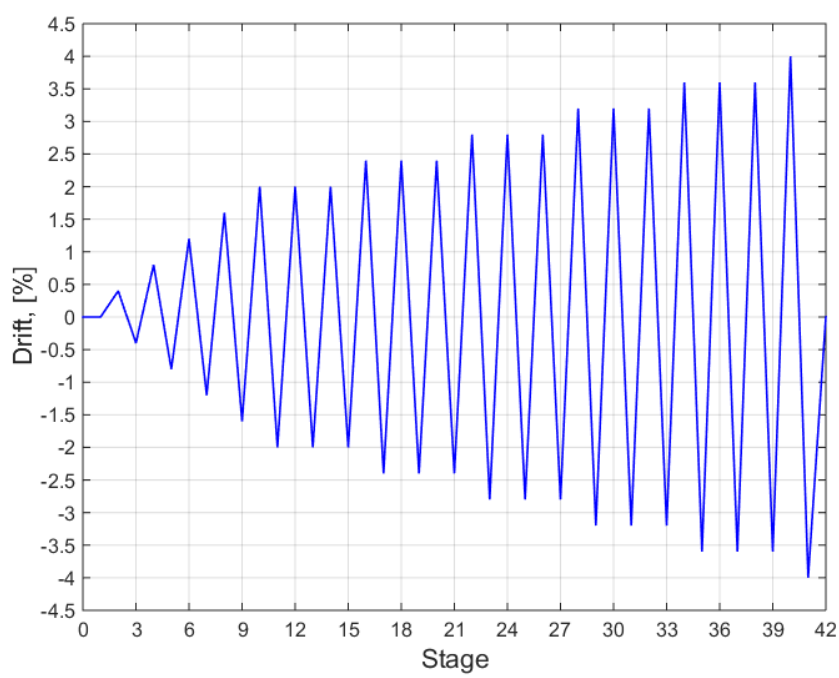

Figure 5-22. Lateral Displacement History applied to Prism 5

Regarding the axial demands, the peak values in tension were chosen as fractions of the yielding strain referred as: $0.25\varepsilon_y$, $0.50\varepsilon_y$, and $0.75\varepsilon_y$ and $1.0\varepsilon_y$. Subsequently, three identical cycles at different axial tensile displacement ductility levels continued until buckling was captured upon compressive loading. The compressive target loads, $P_{\%}$, were established considering P-Δ effects, representing different percentages of the maximum axial design compressive load, Po = -358 kips. The compressive loads varied from 341 kips to 241 kips, corresponding to the small and the largest out-of-plane displacements applied to the top of the specimen, respectively. Figure 5-23 shows the axial strain history applied to Prism 5.

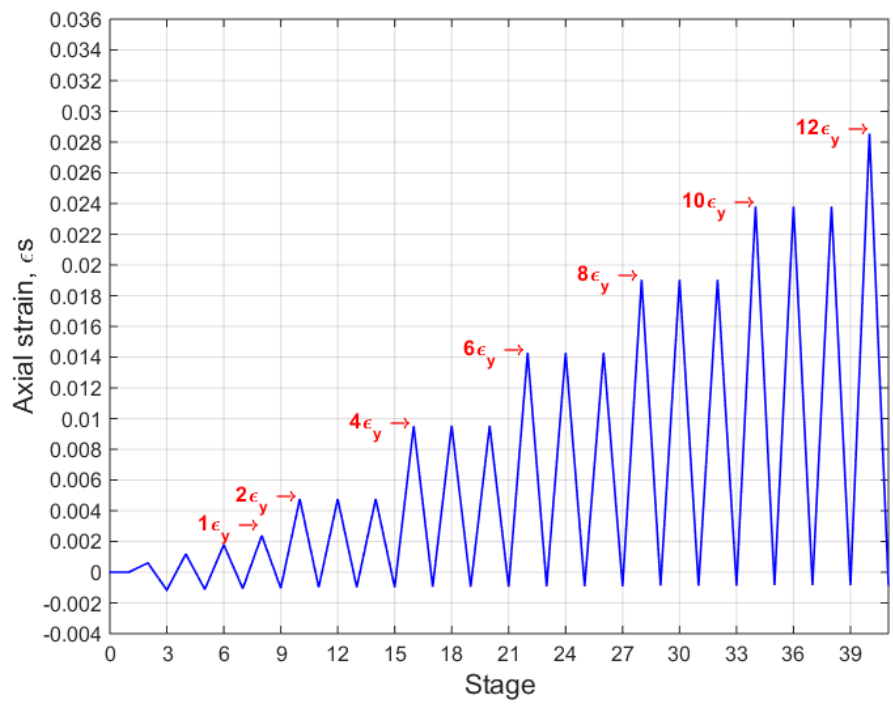

Figure 5-23. Axial Strain History applied to Prism 5

During the elastic cycles regarding the tensile demands and up to +1.6% drift, cracks propagated along the height of the prism and the joints. Tensile strains close to 0.3% were observed in the bottom north and top south regions. Concrete flacking was also detected on the interface between the prism and the joints. Upon yielding tensile demands, horizontal cracks became more numerous and wider. During the application of compressive loads, the cracks tended to close in the central region of the prism. The spacing of the transverse reinforcement induced the development of horizontal cracks. Crack widths bigger than 5/64 in. were captured at the footing-prism interface during the first cycle at $2\varepsilon_y$ and +2% drift. In the stage when the specimen was subjected to an axial compressive force of 288 kips (1,281 kN) and -2% drift, vertical cracks appeared in the concrete cover at bottom north

and top south regions accompanied by concrete flacking. Through the consecutive two cycles, concrete cover fell down on the south bottom region and consequently transverse reinforcement was exposed on the corners. During the first cycle associated with $4\varepsilon_y$, cracks widths close to 3/32 in. were observed close to the joints and few new cracks formed in the prism. Concrete flacking and concrete spalling propagated upon a 278 kips (1,237 kN) compressive load and a -2.4% drift. This damage was captured along 10in. (254mm) height approximately in the end regions, which extended during the following cycles. Concrete spalling propagated through the cycles related to $6\varepsilon_y$ and +2.8% drift. Upon $8\varepsilon_y$ and +3.2% drift, crack widths greater than 5/64 in. were measured in the central region of the prism. Concrete cover continued falling down on end regions and more stirrups were exposed on the corners. In the interface between the prism and joints, the cracks became visibly wider than previous cycles and close to 1/4 in. beyond the $10\varepsilon_y$ cycles.

Throughout the first cycle related to $10\varepsilon_y$, out-of-plane buckling was visually captured upon compressive loading. This scenario, where the out-of-plane deformations were relatively small, was observed during the three cycles corresponding to $10\varepsilon_y$. After experiencing these out-of-plane deformations, the prism returned to a straight position when the cracks closed in the central region and consequently, the prism was able to resist the intrinsic forces associated with compressive forces developed to withstand overturning moments. Figure 5-24 shows the evolution of out-of-plane deformations when a stable buckling mechanism occurred upon compressive loads during the third cycle associated with $10\varepsilon_y$. During the first cycle associated with 12εy and upon compressive loading, a different scenario was captured when instability occurred as presented in Figure 5-25**.** Regarding the state of the stirrups, it was noticed that they remained as originally constructed.

Figure 5-26 shows axial strains plotted against axial loads captured where the out-of-plane deformation reached a maximum value at the end of the test. Notice a stable response of the prism at low levels of axial tensile strains. In the last seven cycles, an axial stiffness reduction is evident by the time the axial compressive load approaches the compressive yielding strength. At this stage, the specimen was still extended. These points were associated with the out-of-plane buckling mechanism. In the last cycle, instability was captured since the prism was not able to recover its strength. The maximum applied load at this stage was -210 kips (934kN), equivalent to 87% of the axial target load, $P_{4\%} = -241$ *kips* (1,072kN). Figure 5-26 also shows the corrected predictions according to Paulay & Priestley (1993) "P&P" and Chai & Elayer (1999) "Ch&E" models once the actual buckled length was determined. In addition, tensile and compressive yielding strengths, *Asfy*, are similarly plotted, where *As* is the area of the longitudinal reinforcement.

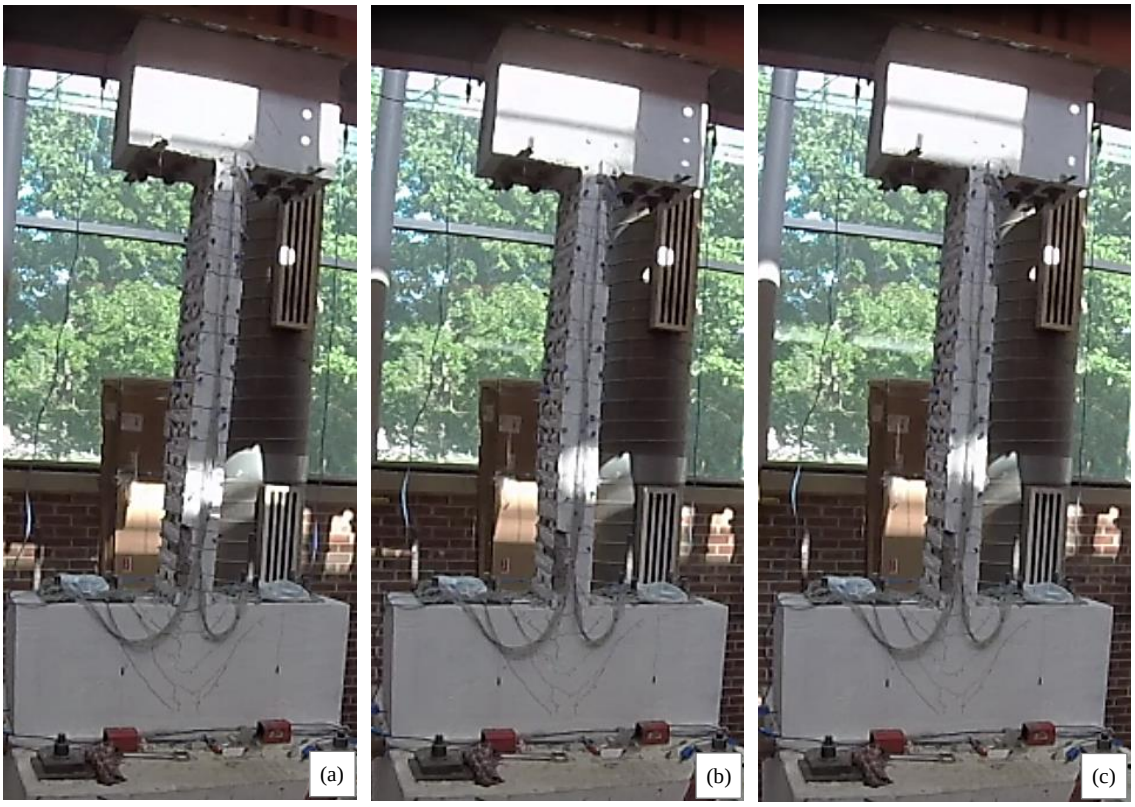

Figure 5-24. Prism 5: Stable out-of-plane buckling mechanism during 10εy(3), third cycle: a) Onset of buckling – cracks opened, b) Stable buckling – cracks partially closed, c) End of buckling - cracks closed.

Figure 5-25. Prism 5: Instable out-of-plane buckling mechanism during 12εy(1), first cycle

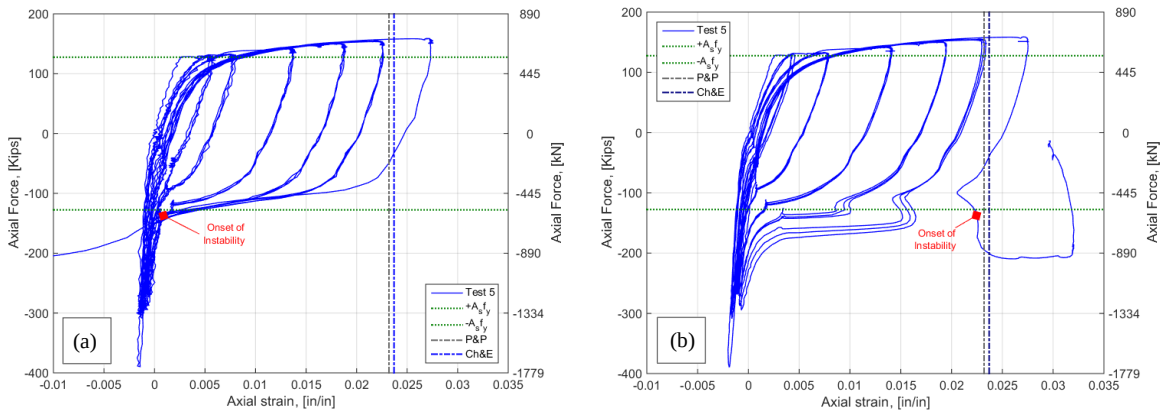

Figure 5-26. Prism 5: Axial Strain vs. Axial Force at 4 in (102mm) above midheight a) south face and b) north face

Out-of-plane deformations increased upon compressive loading during the first cycle associated with $8\varepsilon_y$. Figure 5-27 shows the evolution of out-of-plane deformations at different stages. A sudden increment on this deformation took place when the load slightly exceeded the yielding compressive strength. The stability criterion from Paulay & Priestley (1993) model calculated as out-of-plane deformation and denoted as stability limit, is included in Figure 5-27 to show that instability was expected beyond this limit. During the final cycle, the maximum out-of-plane deformation was δm = 4.1in. (104mm), located 4in. (51mm) above midheight, which exceeded 50% of the prism thickness.

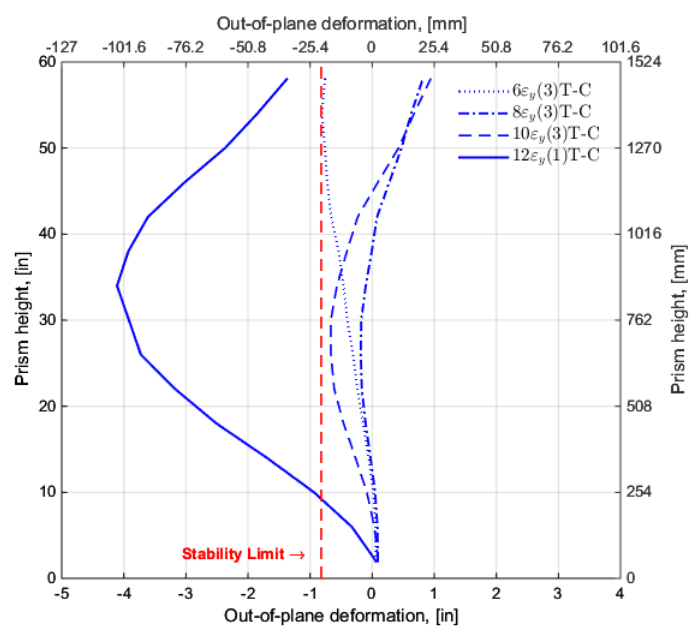

Figure 5-27. Prism 5: Evolution of out-of-plane deformations captured upon compressive loading at different stages

5.1.5.2 Test 5 Conclusions

Prism 5 was tested during six hours where combined and progressive cyclic out-of-plane lateral displacements and cyclic axial loads were applied. P-Δ effects were included to establish the different target loads in compression, which were associated with their corresponding lateral displacement. The tensile strain demands beyond yielding were controlled and adjusted in real time according to the readings reported by the MATLAB code "REALSTRAIN".

Regarding the stability of the specimen, it presented a stable response at early cycles. Indeed, out-of-plane deformations were not visibly noticed during the cycles before $10\varepsilon_y$. Beyond the first cycle of $10\varepsilon_y$, a gradual increment in the out-of-plane deformations were captured until instability developed during the first cycle of $12\varepsilon_y$. The large buckling displacement led to cover concrete crushing and spalling in the central, bottom and top regions. The axial force at this stage was 87% of the target load. Neither bar buckling nor bar fracture were detected during or after the test. The stirrups remained as originally constructed.

5.1.6 Test 6

Test 6 was conducted at the Constructed Facilities Laboratory on Thursday, June 14, 2016, as part of this project. A monotonic and constant lateral displacement equivalent to 8% drift was applied first to the specimen followed by cyclic axial compressive loads and tensile displacements to capture its structural performance and to determine additional critical parameters associated with lateral instability of RC walls. Table 5-6 includes the principal properties of Prism 6, where ρ_l is the longitudinal reinforcement ratio, d_{bl} is the diameter of the bar, and s_h is the transverse reinforcement spacing.

Table 5-6. Prism 6: Specifications

Prism	Dimensions	Longitudinal Reinforcement Layout	ρ_l	s_h/d_{bl}	ε_y
6	5”x12”x60” (127mm x 305mm x 1,524mm)	(6) #5 (15.9mm)	0.031	3.2	0.00239

5.1.6.1 Test 6 Summary

An out-of-plane displacement of 4.8 in., equivalent to 8% drift, was induced first to Prism 6, which was constant during the entire test. Flexural crack widths close to 0.10 in. were measured in the bottom north and top south regions of the prism. Concrete spalling was observed on top left top north and bottom south regions. Maximum tensile strains close to 2.0% and 3.0% were captured on the bottom north and top south regions, respectively.

Subsequently, the prism was subjected to unsymmetrical cyclic axial compressive loads and tensile displacements. The axial displacement history started with elastic single cycles analytically predicted. The targets in tension were chosen as fractions of the yielding displacement referred as: $0.25\varepsilon_y$, $0.50\varepsilon_y$, and $0.75\varepsilon_y$ and $1.0\varepsilon_y$. Subsequently, three identical cycles at different axial tensile displacement ductility levels continued until buckling was captured upon compressive loading. The unique compressive target load, $P_{8\%}$ = -182 kips (810kN), was established considering P-Δ effects, representing 51% of the maximum axial design compressive load, Po = -358 kips (1,592kN). Figure 5-28 shows the axial strain history applied to Prism 6.

Through the first tensile displacement related to 0.25εy, horizontal cracks appeared and became more numerous in following cycles where shear cracks formed and extended to the joints. The transverse reinforcement induced the spacing of the horizontal cracks. During the application of compressive loads, the horizontal cracks tended to close only in the central region of the prism. Vertical cracks appeared in the concrete cover at top north and bottom south regions after the first compressive load, which generated concrete spalling in the subsequent cycles.

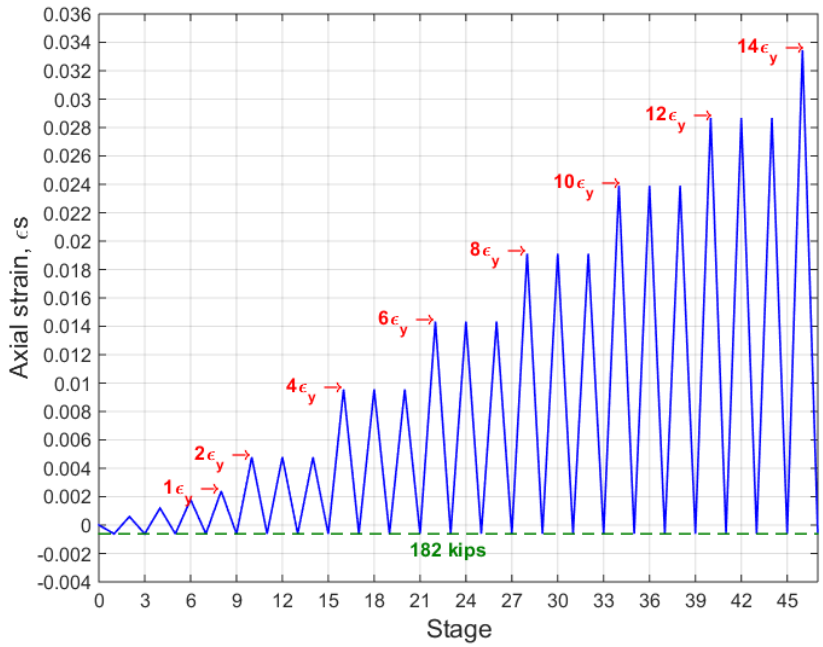

Figure 5-28. Axial Strain History applied to Prism 6

Crack widths around 3/16in. (4.8mm) were measured close to the joints at $2\varepsilon_y$. Concrete spalling became more severe at top north and bottom south regions where the damage was concentrated. On the central region, crack widths close to 1/64in. were captured at $2\varepsilon_y$. During the first cycle associated with $6\varepsilon_y$ new cracks formed on the central region. In the following cycles the number of new cracks decreased. Through tensile demands at $8\varepsilon_y$, crack widths close to 0.075in. (1.9mm) were measured on the central region. Concrete spalling propagated approximately 8in. (203mm) and 10in. (254mm) on top north and bottom south regions, respectively, and consequently transverse reinforcement was exposed on the corners. Upon $10\varepsilon_y$ first cycle concrete cover continued detaching on the top north and bottom south regions. During the cycles associated with $12\varepsilon_y$ cracks became visibly wider than previous cycles and severe damage was observed in the interface between the prism and the footing.

In the first cycle related to $10\varepsilon_y$, out-of-plane buckling was visually captured upon compressive loading. This scenario, where the out-of-plane deformations were relatively small, was observed during the three cycles corresponding to $10\varepsilon_y$ and the first cycle associated with $12\varepsilon_y$. After experimenting these out-of-plane deformations, the prism returned to a fairly straight position when the cracks closed in the middle region and consequently it was able to resist the intrinsic forces associated with compressive forces developed to sustain overturning moments.

At the end of the second and third cycles related to $12\varepsilon_y$ a stable buckled shape was captured as shown in Figure 5-29. The compressive loads at these stages were similar to the loads achieved in previous cycles. Signs of concrete cover crushing were observed in the middle and end regions during the third cycle, which suggested that out-of-plane instability already developed at this stage. An additional $14\varepsilon_y$ cycle was induced to the specimen since it was still able to sustain the compressive target. It was noticed that the prism conserved an out-of-plane deformation upon $14\varepsilon_y$ tensile strains, which confirmed that the prism experienced buckling instability in a previous cycle. Upon compressive loading, the compressive capacity of the specimen significantly decreased due to the combination of out-of-plane buckling instability and shear failure. The final state of the prism exhibited severe damage located in the bottom region of the prism as presented in Figure 5-30.

Figure 5-31 shows axial strains plotted against axial loads captured where the out-of-plane deformation reached a maximum value at the end of the test. Notice that the prism remained buckled at the end of each cycle corresponding to $12\varepsilon_y$, but it still was able to sustain the target compressive loads. In the last cycle, the prism was not able to recover its strength. The maximum applied load at this stage was -100 kips (445kN), equivalent to 55% of the axial target load, $P_{8\%} = -182$ *kips* (810kN).

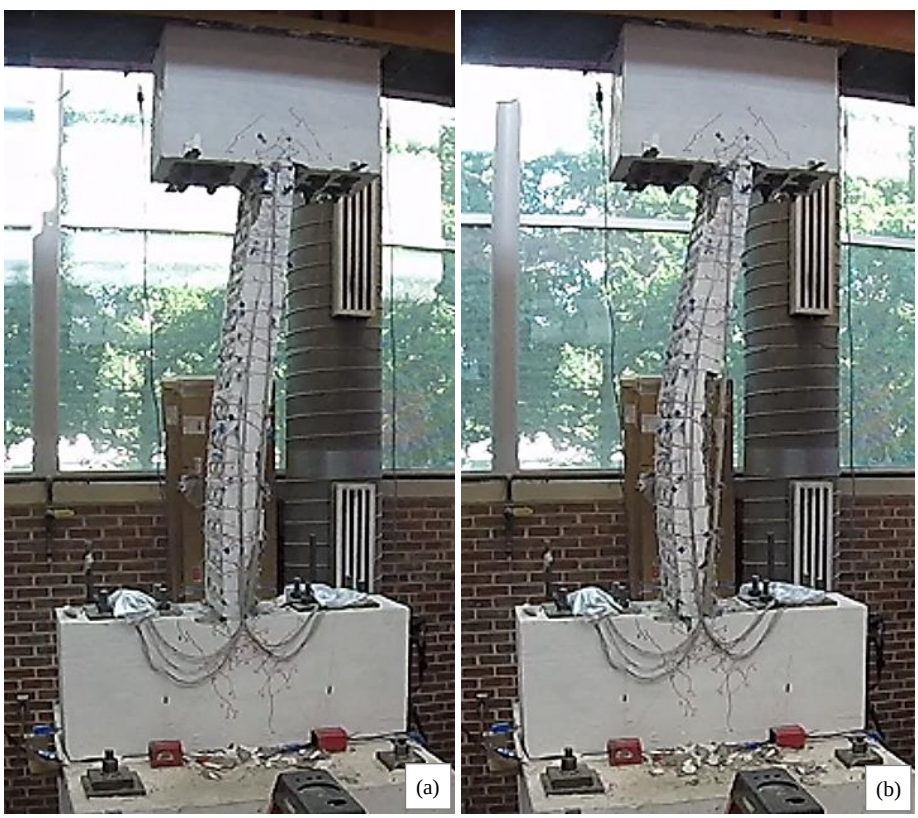

Figure 5-29. Prism 6: Stable out-of-plane buckling mechanism at the end of: a) 12εy(2) second cycle and b) 12εy(3) third cycle

Figure 5-30. Prism 6: Instable out-of-plane buckling mechanism during 14εy(1), first cycle

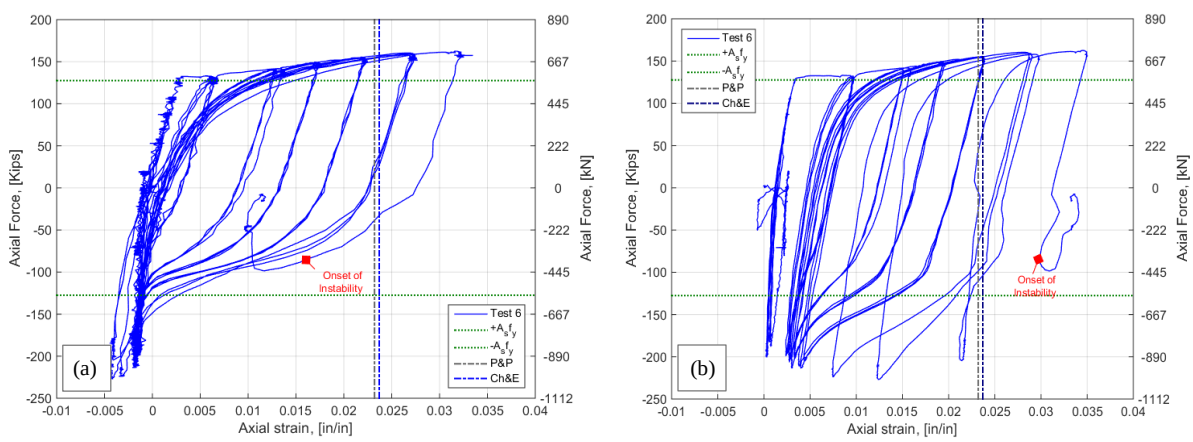

Figure 5-31. Prism 6: Axial Strain vs. Axial Force established 16 in. (406mm) below midheight on a) south face and b) north face

Figure 5-31 also shows the corrected predictions according to Paulay & Priestley (1993) "P&P" and Chai & Elayer (1999) "Ch&E" models once the actual buckled length was determined. In addition, tensile and compressive yielding strengths, *Asfy*, are similarly plotted, where *As* is the area of the longitudinal reinforcement.

Out-of-plane deformations increased upon compressive loading during the first cycle associated with $10\varepsilon_y$. Figure 5-32 shows the evolution of out-of-plane deformations at different stages. The stability criterion from Paulay & Priestley (1993) model calculated as out-of-plane deformation

and denoted as stability limit, is included in Figure 5-32 to show that instability was expected beyond this limit. During the final cycle, the maximum out-of-plane deformation was δm = 3.3in. (84mm), located 16in. (406mm) below midheight, which exceeded 50% of the prism thickness.

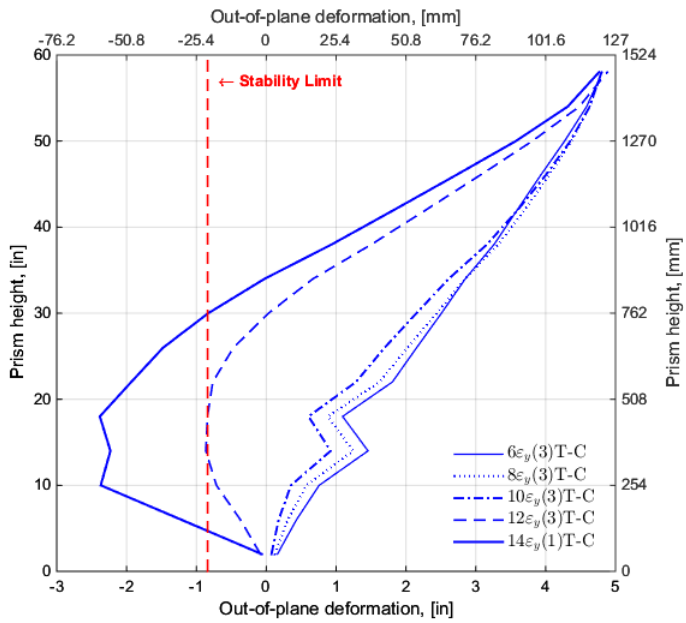

Figure 5-32. Prism 6: Evolution of out-of-plane deformations captured upon compressive loading at different stages

5.1.6.2 Test 6 Conclusions

Prism 6 was tested during six hours where combined load patterns were applied. A lateral out-of-plane displacement equivalent to 8% drift was sustained during the entire test to analyze its influence on the stability of RC walls. Tensile strains close to 2% and 3% were captured at this stage in the bottom north and top south regions, respectively.

Subsequently, progressive cyclic axial loads/strains were applied to the specimen reaching maximum values fairly close to the targets $P_{8\%}$ = -182 kips and 14ε_y, in compression and tension, respectively. The specimen presented a stable response at low levels of axial tensile demands. Out-of-plane deformations were not noticed during the cycles before 10ε_y. Beyond the first cycle of 10ε_y, a gradual increment in the out-of-plane deformations were captured until the test ended. The actual onset of instability occurred during the third cycle for 12ε_y. The large out-of-plane buckling displacement in the last cycle corresponding to 12ε_y, led to concrete cover crushing and spalling in the bottom region. The failure mode captured in the 14ε_y cycle under compressive loads was a combination of buckling instability and shear failure. The axial force at this stage was 55% of the compressive target load. Bar fracture was not detected during or after the test. The closed stirrups remained as originally constructed, however the 90 degrees hook of the ties opened where the severe damage was concentrated.

5.1.7 Test 7

Test 7 was conducted at the Constructed Facilities Laboratory on Thursday, July 21, 2016, as part of the second phase related to this project. An axial compression load followed by cyclic axial tensile displacements and compressive loads were applied to the specimen to determine the influence of additional critical parameters associated with lateral instability of RC walls. Table 5-7 includes the principal properties of Prism 7, where ρ_l is the longitudinal reinforcement ratio, d_{bl} is the diameter of the bar, and s_h is the transverse reinforcement spacing.

Table 5-7. Prism 7: Specifications

Prism	Dimensions	Longitudinal Reinforcement Layout	ρ_l	s_h/d_{bl}	ε_y
7	5”x12”x60” (127mm x 305mm x 1,524mm)	(6) #4 (12.7mm)	0.02	4	0.00238

5.1.7.1 Test 7 Summary

Specimen 7 was subjected first to an axial load equivalent to the design axial compression capacity of the prism, *Po = -322 kips* (1,432kN). The purpose of this part of the test was to confirm that the boundary element of the wall could sustain this level of compressive load in the absence of lateral displacements. Subsequently, cyclic axial strains started with an elastic single cycle. After yielding, three identical cycles at different axial tensile displacement ductility levels continued until buckling was captured upon compressive loading. The unique compressive target was established from the first part of the experiment, corresponding to *Po* = -322 kips. Figure 5-33 shows the axial strain history applied to Prism 7.

Small horizontal cracks appeared all along the prism and slightly extended to the moment connections at $1\varepsilon_y$ tensile strain. This time, the cavities created to include the infrared LEDs governed the horizontal cracks spacing. Upon compressive loads cracks uniformly closed as expected. This phenomenon was observed during the following cycles until instability was captured. In the course of the cycles corresponding to $2\varepsilon_y$, more small cracks formed and the old ones propagated. Crack widths close to 0.035in. (0.9mm) and 0.05in. (1.3mm) were captured in the middle region at $4\varepsilon_y$ and $6\varepsilon_y$ tensile strain targets, respectively. In the following cycles, the cracks became wider and the number of new cracks decreased. Crack widths close to 0.075in. (1.9mm) were measured in the middle region during the $8\varepsilon_y$ cycles. Signs of concrete flaking on the footing-prism interface were observed in the first cycle at $10\varepsilon_y$. Vertical and diagonal cracks were also observed during this cycle. Upon tensile strains during the last cycle related to $12\varepsilon_y$, concrete cover fell down on the east face of the prism and

the transverse reinforcement was exposed within a length of 14in. (356mm). Upon compressive loads, more concrete cover fell down in the same region exposing the transverse reinforcement within a length of 26in. (660mm), approximately.

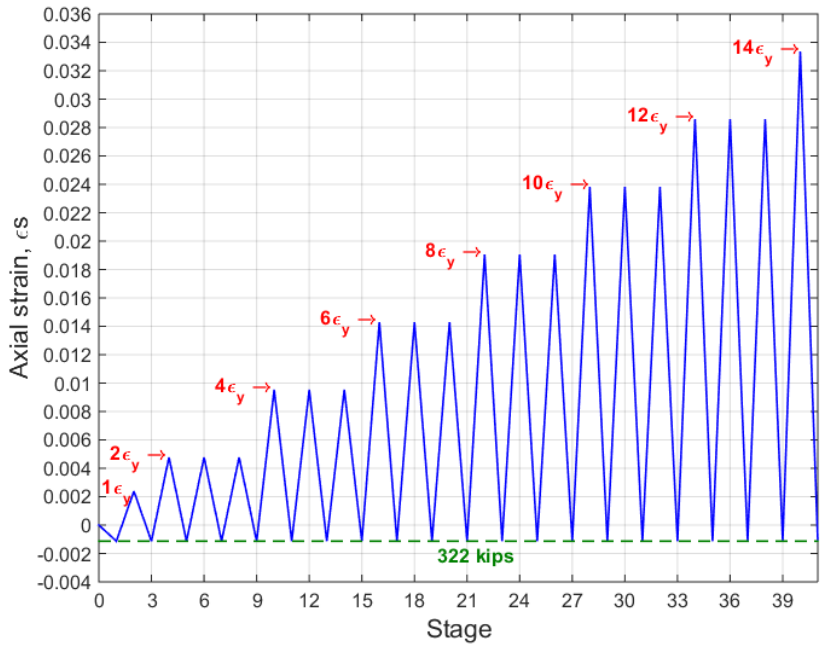

Figure 5-33. Axial Strain History applied to Prism 7

As tensile demands increased during the cycles related to $10\varepsilon_y$ and $12\varepsilon_y$ the out-of-plane buckling mechanism was visually captured upon compressive loading. In this scenario, where the out-of-plane deformation was relatively small, the compression force developed to resist the overturning moment can be fully reached as cracks close and consequently, the prism returned to a fairly straight and stable position. Figure 5-34 shows the evolution of out-of-plane deformations when a stable buckling mechanism occurred upon compressive loads during the third cycle associated with $12\varepsilon_y$. During the first cycle at $14\varepsilon_y$, cracks widths close to 3/16 in. (4.8mm) were measured at midheight and upon compressive loading, instability occurred as presented in Figure 5-35. The end of the test showed concrete cover crushing in the central, top north and bottom north regions.

Figure 5-36 shows axial strains plotted against axial loads captured where the out-of-plane deformation reached a maximum value at the end of the test. Notice a stable response of the prism at low levels of axial tensile strains. In the last ten cycles, an axial stiffness reduction is evident by the time the axial compressive load approaches the compressive yielding strength. At this stage, the specimen was still extended. These points were associated with the out-of-plane buckling mechanism. In the last cycle, instability was captured since the prism was not able to recover its strength. The

maximum applied load at this stage was -154 kips (685kN), equivalent to 48% of the axial target load, *Po = -322 kips* (1,432kN).

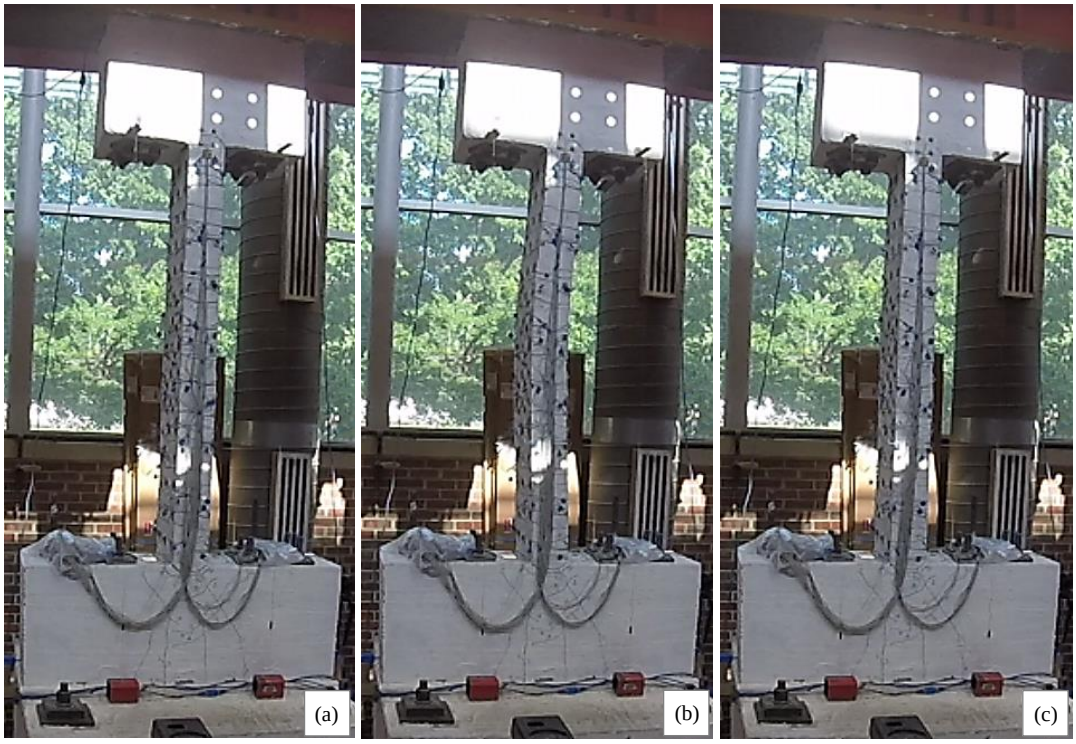

Figure 5-34. Prism 7: Stable out-of-plane buckling mechanism during 12εy(3), third cycle: a) Onset of buckling – cracks opened, b) Stable buckling – cracks partially closed, c) End of buckling - cracks closed.

Figure 5-35. Prism 7: Instable out-of-plane buckling mechanism during 14εy(1), first cycle

Figure 5-36 also shows the corrected predictions according to Paulay & Priestley (1993) "P&P" and Chai & Elayer (1999) "Ch&E" models once the actual buckled length was determined. In addition, tensile and compressive yielding strengths, *Asfy*, are similarly plotted, where *As* is the area of the longitudinal reinforcement.

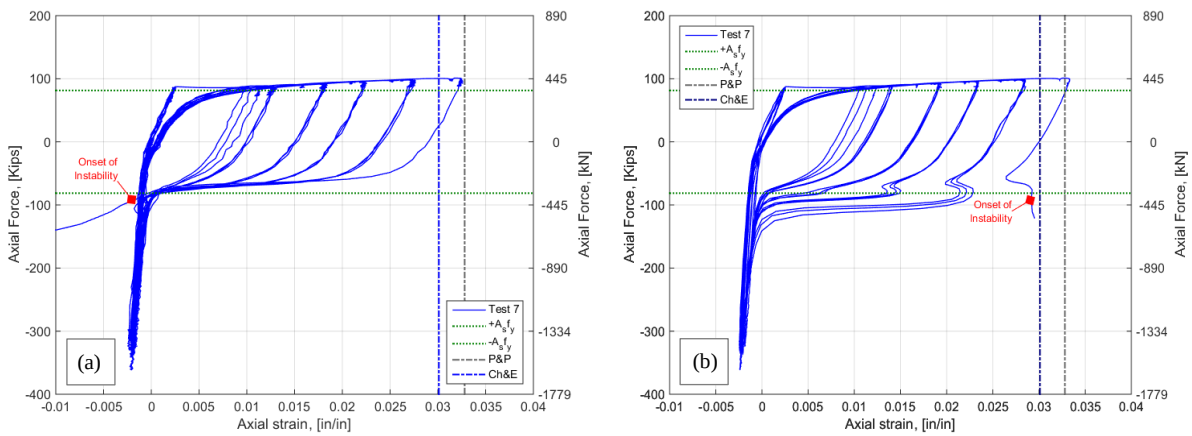

Figure 5-36. Prism 7: Axial Strain vs. Axial Force established 4in. (102mm) above midheight on a) south face and b) north face

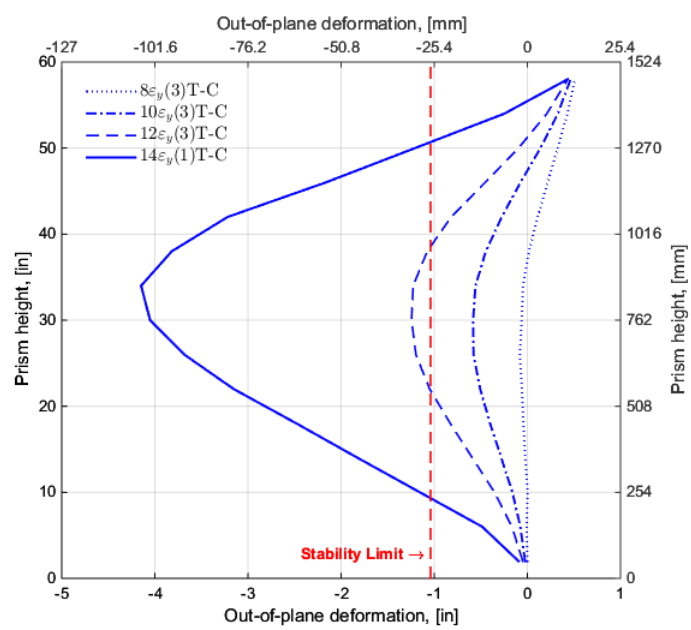

Figure 5-37. Prism 7: Evolution of out-of-plane deformations captured upon compressive loading at different stages

Out-of-plane deformations increased upon compressive loading during the first cycle associated with $8\varepsilon_y$. Figure 5-37 shows the evolution of out-of-plane deformations at different stages. The stability criterion from Paulay & Priestley (1993) model calculated as out-of-plane deformation and denoted as stability limit, is included in Figure 5-37 to show that instability was expected beyond

this limit. During the final cycle, the maximum out-of-plane deformation was δm = 4.2in. (107mm), located 4in. (102mm) above midheight, which exceeded 50% of the prism thickness.

Notice that the out-of-plane top displacement is close to 0.4in. (10mm) instead of 0in., which is attributed to the complexity of the technic implemented to control the three actuators at once. However, the axial response of the prism is indifferent to this minor input.

5.1.7.2 Test 7 Conclusions

Prism 7 was tested during four hours where two loading patterns were applied. The first part of the test indicated that the prism reached the maximum axial design compressive load with zero loss capacity. In the second part of the test, progressive cyclic axial loads/strains were applied to the specimen reaching maximum values close to the axial design compressive force, Po = -322 kips (1,432kN) and $14\varepsilon_y$, in compression and tension, respectively. The specimen presented a stable response at low levels of axial tensile demands. Out-of-plane deformations were not noticed during the cycles before $8\varepsilon_y$. Beyond the first cycle of $8\varepsilon_y$, a gradual increase in the out-of-plane deformations were captured until instability developed upon compressive loading during the first cycle of $14\varepsilon_y$. The large buckling deformation led to concrete cover crushing and spalling in the central region. The axial force at this stage was 48% of the compressive target load. Neither bar buckling nor bar fracture were detected during or after the test. The stirrups remained as originally constructed.

5.1.8 Test 8

Test 8 was conducted at the Constructed Facilities Laboratory on Wednesday, August 17, 2016, as part of the second phase related to this research project. A monotonic and constant lateral displacement equivalent to 4% drift was applied first to the specimen followed by cyclic axial tensile displacements and compressive loads. The purpose of this test was to capture the influence of additional critical parameters associated with lateral instability of RC walls. Table 5-8 includes the principal properties of Prism 8, where ρ_l is the longitudinal reinforcement ratio, d_{bl} is the diameter of the bar, and s_h is the transverse reinforcement spacing.

Table 5-8. Prism 8: Specifications

Prism	Dimensions	Longitudinal Reinforcement Layout	ρ_l	s_h/d_{bl}	ε_y
8	5”x12”x60” (127mm x 305mm x 1,524mm)	(6) #4 (12.7mm)	0.02	4	0.00238

5.1.8.1 Test 8 Summary

First, a 2.4in. (61mm) out-of-plane displacement, equivalent to 4% drift, was induced to Prism 8. Concrete flacking was observed on top north and bottom south regions and tensile strains close to 0.5% were determined in the bottom north and top south regions. Subsequently, axial cycles were applied to the specimen. Beyond yielding, three identical cycles at different axial tensile displacement ductility levels continued until buckling was captured upon compressive loading. The unique compressive target load, $P_{4\%}$ = -222 kips (988kN), was established considering P-Δ effects, representing 69% of the maximum axial design compressive load, Po = -322 kips (1,432kN). Figure 5-38 shows the axial strain history applied to Prism 8.

During the first applied compressive load, vertical cracks appeared in the concrete cover on top north and bottom right regions accompanied by concrete spalling. At $1\varepsilon_y$ small horizontal cracks appeared all along the prism and slightly extended to the moment connections. Crack widths of about 1/4in. (6mm) were captured at the interface between the prism and the footing. Upon compressive loads cracks uniformly closed in the central region as expected. This phenomenon was observed during the following cycles until instability was captured. Along the $2\varepsilon_y$ cycles, new cracks appeared. Beyond this tensile demand, cracks became wider and the number of new cracks decreased. The horizontal cracks developed where the stirrups are located. Concrete spalling became more severe during the $4\varepsilon_y$ and $6\varepsilon_y$ cycles. Through the cycles associated with $8\varepsilon_y$, crack widths close to 3/16in. (4.8mm) and 0.075 in. (1.9mm) were measured on the prism-footing interface and midheight, respectively.

Propagation of concrete spalling on the top north region was observed in the first cycle at $10\varepsilon_y$. Diagonal cracks were also captured during this cycle and horizontal crack widths of about 1/8in. (3.2mm) were measured at midheight. During the first cycle at $12\varepsilon_y$, cracks widths reached 1/4in. (6.1mm) on the prism-footing interface. At the end of the cycles associated with $12\varepsilon_y$, the transverse reinforcement was exposed within a length of 12in. (305mm) on the top north and bottom south regions.

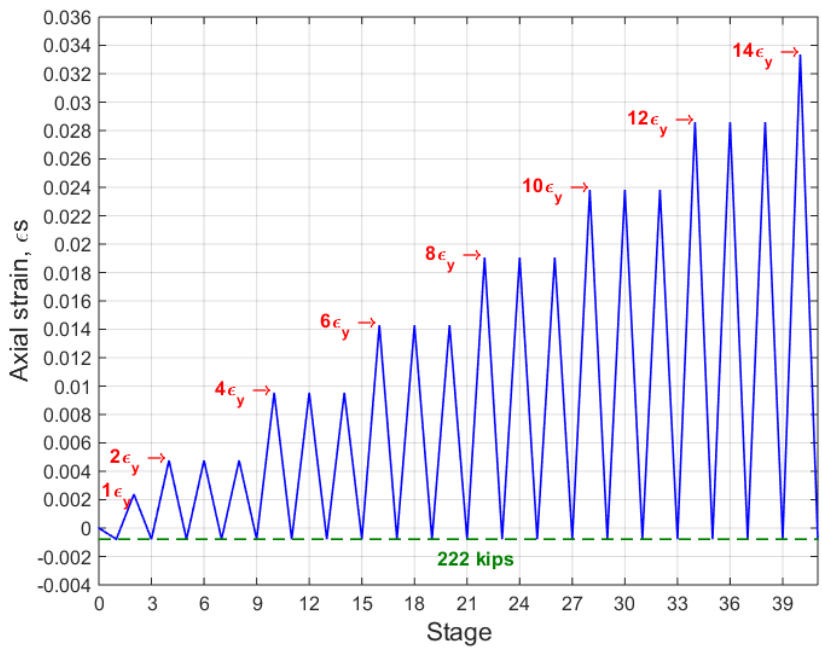

Figure 5-38. Axial Strain History applied to Prism 8

As tensile demands increased during the cycles related to $10\varepsilon_y$ and $12\varepsilon_y$ the out-of-plane buckling mechanism was visually captured upon compressive loading. In this scenario, where the out-of-plane deformation is relatively small, the compression force developed to resist the overturning moment, is fully reached as cracks close and consequently, the prism returns to a fairly straight and stable position. Figure 5-39 shows the evolution of out-of-plane deformations when a stable buckling mechanism occurred upon compressive loads during the third cycle associated with $12\varepsilon_y$. During the first cycle at $14\varepsilon_y$, cracks widths close to 5/32in. (4mm) were measured at midheight and upon compressive loading, instability occurred as presented in Figure 5-40. The end of the test showed concrete cover crushing in the central, top north and bottom north regions.

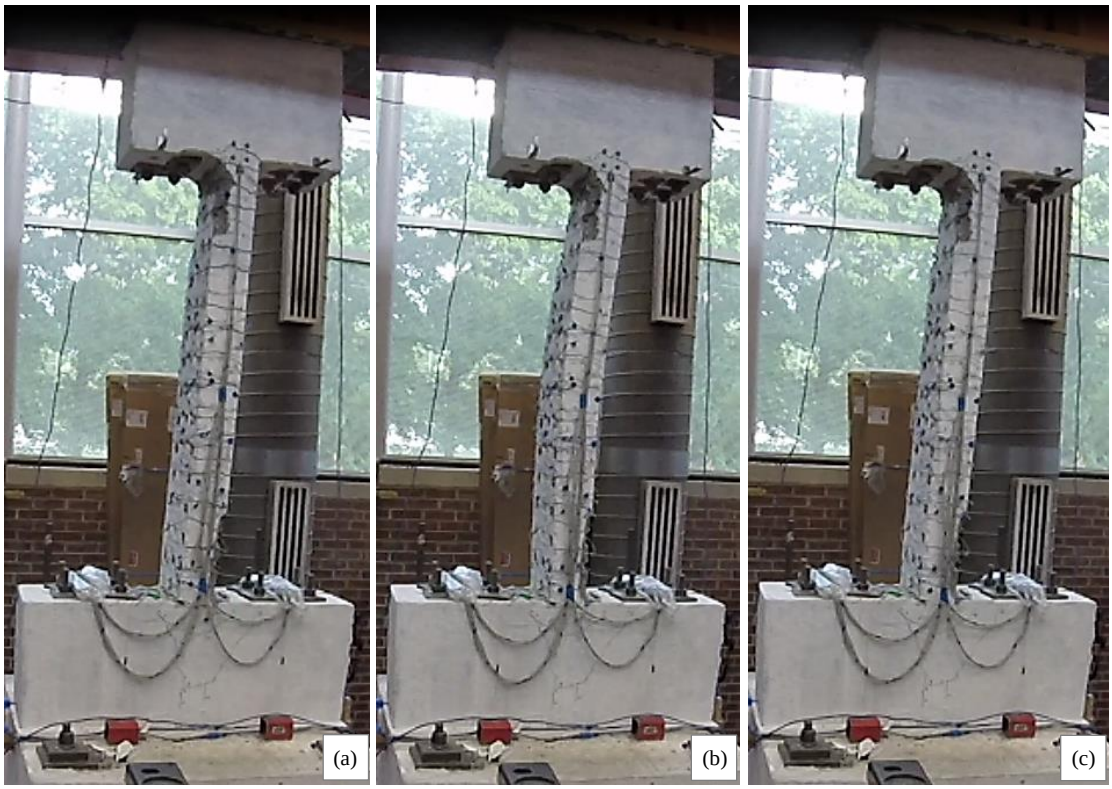

Figure 5-39. Prism 8: Stable out-of-plane buckling mechanism during 12εy(3), third cycle: a) Onset of buckling – cracks opened, b) Stable buckling – cracks partially closed, c) End of buckling - cracks closed.

Figure 5-40. Prism 8: Instable out-of-plane buckling mechanism during 14εy(1), first cycle

Figure 5-41 shows axial strains plotted against axial loads captured where the out-of-plane deformation reached a maximum value at the end of the test. Notice a stable response of the prism at low levels of axial tensile strains. During the last cycles, an axial stiffness reduction is evident by the time the axial load approaches the compressive yielding strength. At this stage, the specimen was still extended. These points were associated with the out-of-plane buckling mechanism. In the last cycle, instability was captured since the prism was not able to recover its strength. The maximum applied load at this stage was -189 kips (841kN), equivalent to 85% of the axial target load, $P_{4\%}$ = -222 kips (988kN).

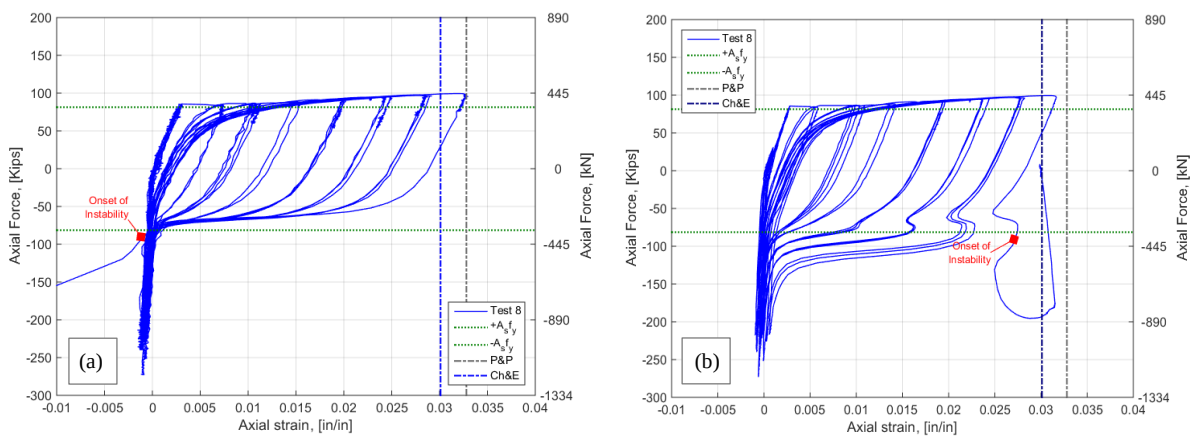

Figure 5-41. Prism 8: Axial Strain vs. Axial Force established at midheight on a) south face and b) north face

Figure 5-41 also shows the corrected predictions according to Paulay & Priestley (1993) "P&P" and Chai & Elayer (1999) "Ch&E" models once the actual buckled length was determined. In addition, tensile and compressive yielding strengths, *Asfy*, are similarly plotted, where *As* is the area of the longitudinal reinforcement.

Out-of-plane deformations increased upon compressive loading during the first cycle associated with $8\varepsilon_y$. Figure 5-42 shows the evolution of out-of-plane deformations at different stages. The stability criterion from Paulay & Priestley (1993) model calculated as out-of-plane deformation and denoted as stability limit, is included in Figure 5-42 to show that instability was expected beyond this limit. During the final cycle, the maximum out-of-plane deformation was δm = 2.8in. (71mm), at midheight, which exceeded 50% of the prism thickness.

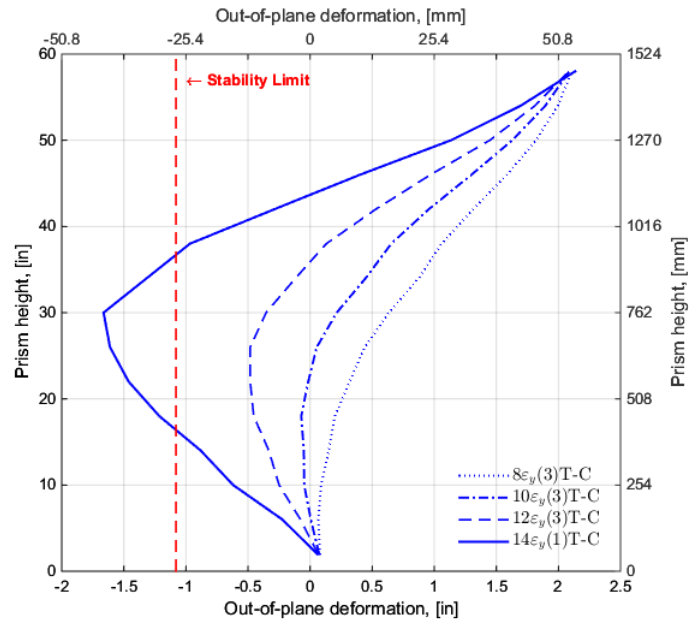

Figure 5-42. Prism 8: Evolution of out-of-plane deformations captured upon compressive loading at different stages

5.1.8.2 Test 8 Conclusions

Prims 8 was tested during five hours where two loading patterns were applied. During the first part, a monotonic out-of-plane displacement was induced until reaching a target of 2.4in. (61mm) equivalent to 4% drift. Tensile strains close to 0.5% were determined on the bottom north and top south regions, exceeding the yielding strain.

In the second part of the test, progressive cyclic axial loads/strains were applied to the specimen reaching maximum values close to the axial compressive force including P-Δ effects, $P_{4\%}$ = 222 kips and 14ε_y, in compression and tension, respectively. The specimen presented a stable response upon compressive loading through low levels of axial tensile demands. Out-of-plane deformations were not noticed during the cycles before 8ε_y. Beyond the first 8ε_y cycle, a gradual increase in the out-of-plane deformations were captured until instability occurred during the first 14ε_y cycle. The large buckling deformation led to concrete crushing and spalling in the central region of the prism. The axial force at this stage was 85% of the compressive target force applied in previous cycles. Neither bar buckling nor bar fracture were detected during or after the test. The stirrups remained as originally constructed.

5.1.9 Test 9

Test 9 was conducted at the Constructed Facilities Laboratory on Wednesday, August 31, 2016, as part of the second phase related to this research project. A monotonic and constant lateral displacement equivalent to 2.5% drift was applied first to the specimen followed by an axial seismic historic record from 1994 Northridge earthquake (Sylmar station). The purpose of this test was to capture the structural performance of the specimen #9 and to determine additional critical parameters associated with lateral instability of RC walls. Table 5-9 includes the principal properties of Prism 9, where ρ_l is the longitudinal reinforcement ratio, d_{bl} is the diameter of the bar, and s_h is the transverse reinforcement spacing.

Table 5-9. Prism 9: Specifications

Prism	Dimensions	Longitudinal Reinforcement Layout	ρ_l	s_h/d_{bl}	ε_y
9	5”x12”x60” (127mm x 305mm x 1,524mm)	(6) #4 (12.7mm)	0.02	4	0.00238

5.1.9.1 Test 9 Summary

First, a monotonic and constant 1.5in. (38mm) out-of-plane displacement, equivalent to 2.5% drift, was induced to Prism 9. Tensile strains close to 0.3% were determined in the bottom north region. In the top south region, tensile strains were close to 1.0%. The yielding strain was exceeded in both cases. Subsequently, Prism 9 was subjected to an axial seismic axial displacement history based on the structural response of a prototype RC wall exposed to an actual in-plane horizontal earthquake record. The seismic record selected for this analysis was the 1994 Northridge earthquake (Sylmar station). The main purpose of subjecting the specimen to this kind of demand was to consider the effects of near-field records that contain long duration pulses.

The strain response of a bar located at the base of the boundary elements of a the prototype wall was determined through SeismoStruct V7.0, a finite element package for structural analysis capable of predicting the behavior of space frames under static or dynamic loadings, considering both geometric nonlinearities and material inelasticity (Seismosoft Ltd., 2014). For the first input data, the maximum tensile strain was scaled to $14\varepsilon_y$ since inelastic buckling was captured upon compressive loading after reaching this strain level based on the test results from Prism 7 and Prism 8. A second input data scaled to $16\varepsilon_y$ was also created in case the prism survived the first input data, which actually happened during the test. The unique compressive load, $P_{2.5\%}$ = -251kips (1,117kN), was established considering P-Δ effects, representing 78% of the axial design compressive capacity of the prism, Po = -322 kips (1,432kN). Figure 5-43 shows the axial strain history applied to Prism 9.

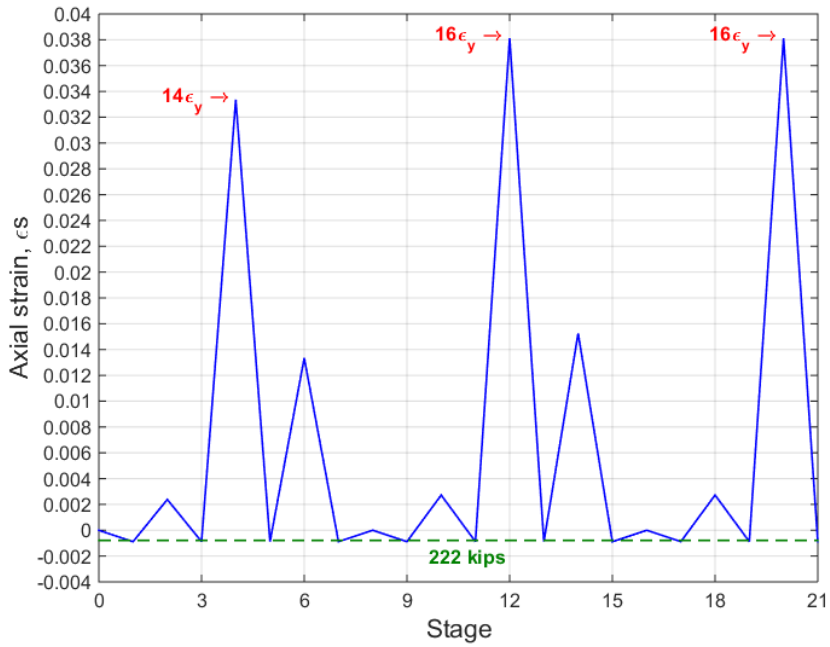

Figure 5-43. Axial Strain History applied to Prism 9

Crack widths close to 1/8in. (3.2mm) were captured at midheight when the prism was tensioned at $14\varepsilon_y$. The distribution of cracks was nearly uniform along the height of the prism. A stable out-of-plane buckling mechanism was visually captured upon compressive loading. Since the out-of-plane deformation was relatively small, the compression force developed to resist the overturning moment, was fully reached as cracks closed and consequently, the prism returned to a fairly straight and stable position. Figure 5-44 shows the evolution of out-of-plane deformations captured during the cycle associated with $14\varepsilon_y$. Next, the stages related to 16εy were applied and concrete cover spalling propagated in the top north and bottom south regions. The out-of-plane buckling mechanism developed upon compressive loading, but the prism returned to a straight and stable position as shown in Figure 5-45. Consequently, a second $16\varepsilon_y$ axial strain history was applied, and this time instability occurred upon compressive loading after reaching the maximum tensile demand at $16\varepsilon_y$ as presented in Figure 5-46. The end of the test exhibited concrete cover crushing at midheight.

Figure 5-47 shows axial strains plotted against axial loads captured where the out-of-plane deformation reached a maximum value at the end of the test. During the cycles related to the maximum tensile demands, an axial stiffness reduction is evident by the time the axial load approaches the compressive yielding strength. At this stage, the specimen was still extended. These points were associated with the out-of-plane buckling mechanism. In the last cycle, instability was captured since the prism was not able to recover its strength. The maximum applied load at this stage was -156 kips (694kN), equivalent to 62% of the axial target load, $P_{2.5\%}$ = -251 kips (1,117kN).

Figure 5-44. Prism 9: Stable out-of-plane buckling mechanism during 14εy(1), first input data: a) Onset of buckling – cracks opened, b) Stable buckling – cracks partially closed, c) End of buckling - cracks closed.

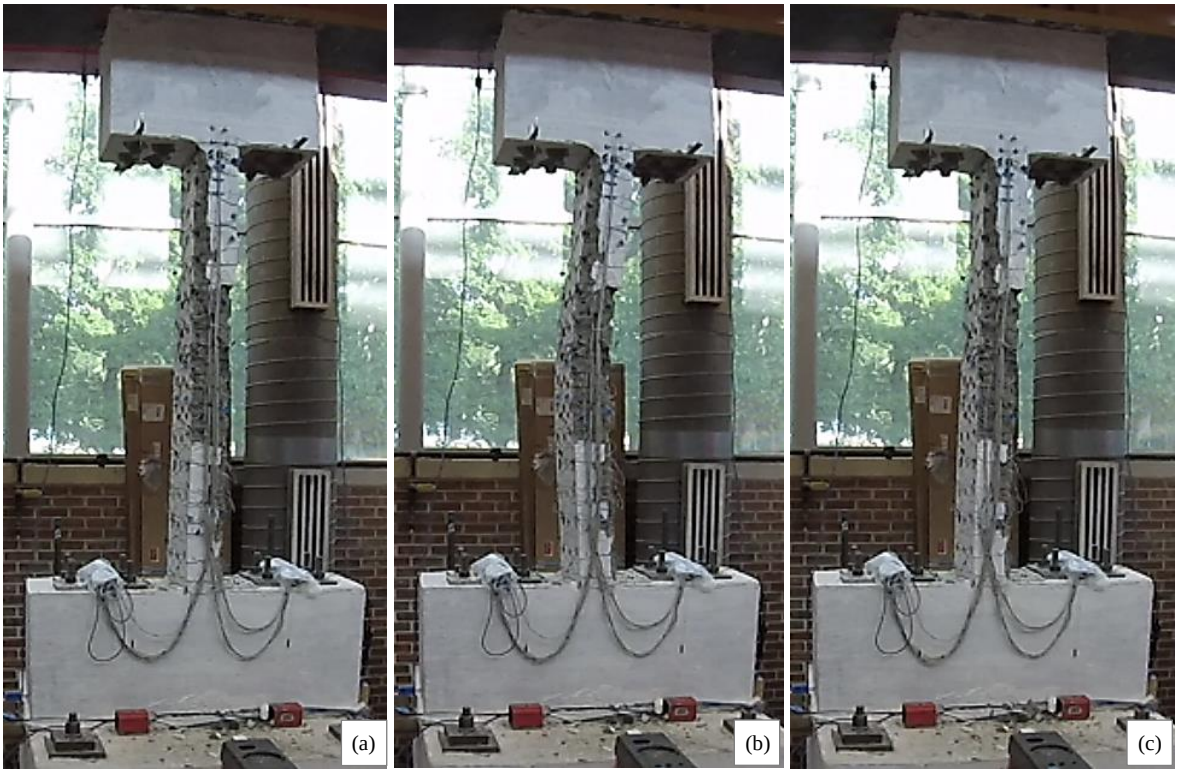

Figure 5-45. Prism 9: Stable out-of-plane buckling mechanism during 16εy(1), second input data: a) Onset of buckling – cracks opened, b) Stable buckling – cracks partially closed, c) End of buckling - cracks closed

Figure 5-46. Prism 9: Instable out-of-plane buckling mechanism during 16εy(2), third input data

Figure 5-47 also shows the corrected predictions according to Paulay & Priestley (1993) "P&P" and Chai & Elayer (1999) "Ch&E" models once the actual buckled length was determined. In addition, tensile and compressive yielding strengths, *Asfy*, are similarly plotted, where *As* is the area of the longitudinal reinforcement.

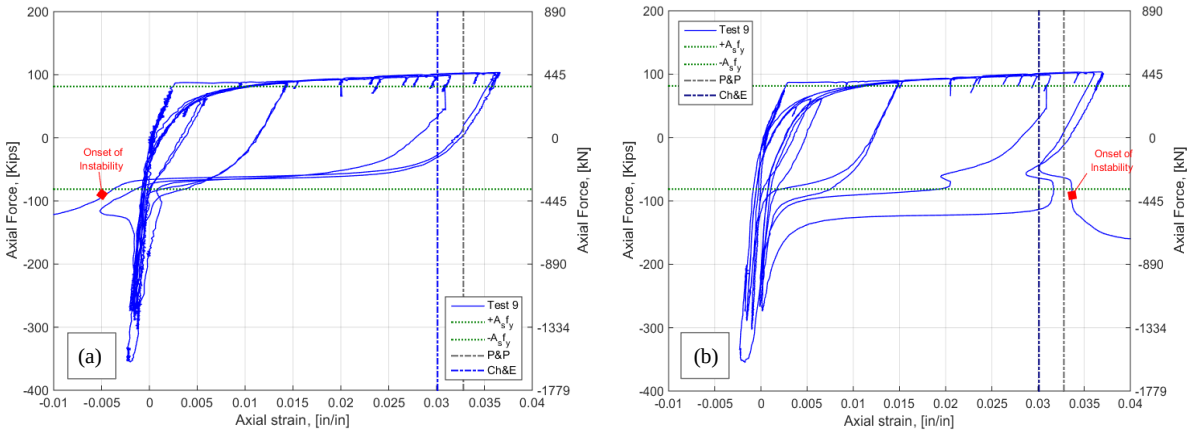

Figure 5-47. Prism 9: Axial Strain vs. Axial Force established 4in. (102mm) below midheight on a) south face and b) north face

Out-of-plane deformations increased upon compressive loading during the cycles associated with the maximum tensile demands. Figure 5-48 shows the evolution of out-of-plane deformations at different stages. The stability criterion from Paulay & Priestley (1993) model calculated as out-of-plane deformation and denoted as stability limit, is included in Figure 5-48 to show that instability was expected beyond this limit. During the final cycle, the maximum out-of-plane deformation was δm = 4.4in. (114mm), located 4in. below midheight, which exceeded 50% of the prism thickness.

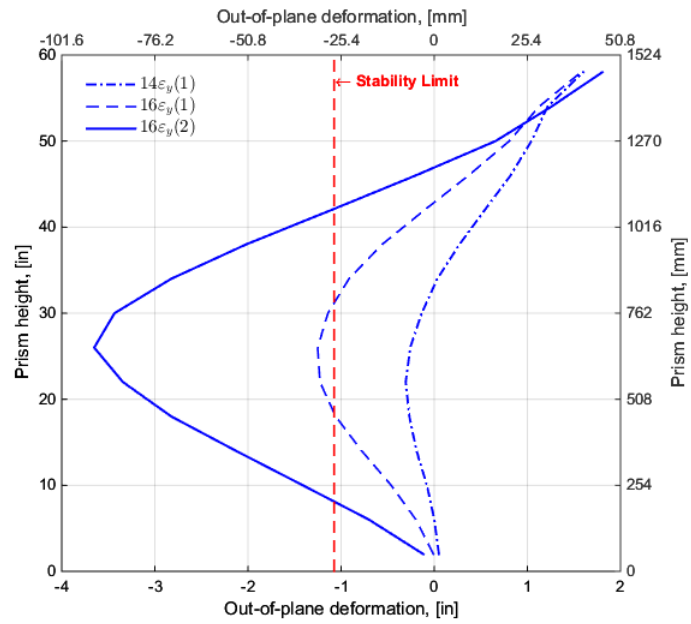

Figure 5-48. Prism 9: Evolution of out-of-plane deformations captured upon compressive loading at different stages

5.1.9.2 Test 9 Conclusions

Prism 9 was tested during five hours where two loading patterns were applied. During the first part, a monotonic out-of-plane displacement was induced until reaching a target of 1.5in. (38mm) equivalent to 2.5% drift. Tensile strains greater than the yielding strain were determined in the bottom north and top south regions. In the second part of the test, seismic axial displacement inputs, based on the 1994 Northridge earthquake (Sylmar station), were applied to the specimen reaching a maximum compression value close to the axial compressive force including P-Δ effects, $P_{2.5\%}$ = -251 kips. Regarding the tensile demands, a maximum axial displacement associated with $16\varepsilon_y$ was applied. Out-of-plane deformations were noticed immediately after $14\varepsilon_y$ and $16\varepsilon_y$ stages when the specimen was subjected to compressive loads. Instability occurred during the last displacement history after a $16\varepsilon_y$ strain was induced. The large buckling deformation led to concrete cover crushing and spalling in the central region of the prism. The axial compressive force at this stage was 62% of the compressive target load. Neither bar buckling nor bar fracture were detected during or after the test. The stirrups remained as originally constructed.

5.1.10 Test 10

Test 10 was conducted at the Constructed Facilities Laboratory on Friday, September 16, 2016, as part of the third phase related to the load path project. An axial compressive load followed by cyclic axial tensile displacements and compressive loads were applied to the specimen to capture its structural performance and to determine additional critical parameters associated with lateral instability of RC walls. Table 5-10 includes the principal properties of Prism 10, where ρ_l is the longitudinal reinforcement ratio, d_{bl} is the diameter of the bar, and s_h is the transverse reinforcement spacing.

Table 5-10. Prism 10: Specifications

Prism	Dimensions as built	Longitudinal Reinforcement Layout	ρ_l	s_h/d_{bl}	ε_y
10	5.5”x12”x60” (140mm x 305mm x 1,524mm)	(6) #3 (9.52mm)	0.010	5.3	0.00217

5.1.10.1 Test 10 Summary

Prism 10 was subjected first to an axial load equivalent to the design axial compression capacity of the prism, *Po* = -294kips (1,308kN). The purpose of this part of the test was to confirm that the boundary element of the wall could sustain this level of compressive load in the absence of lateral displacements. Subsequently, unsymmetrical cycles, which started with an elastic cycle, were applied to the specimen. After yielding, three identical cycles at different axial tensile displacement ductility levels continued until failure was detected. The compressive target load was established from the first part of the experiment. Figure 5-49 shows the axial strain history applied to Prism 10.

At $1\varepsilon_y$ strain, small horizontal cracks appeared all along the prism and slightly extended to the moment connections. Crack widths of about 0.01in. (0.3mm) were captured at midheight. Upon compressive loading cracks uniformly closed as expected. This phenomenon was observed during the following cycles until failure was captured. More cracks formed and the old ones propagated through the $2\varepsilon_y$ cycles. Crack widths close to 0.03in. (0.8mm) and 0.04in. (1.0mm) were measured at midheight during the $4\varepsilon_y$ and $6\varepsilon_y$ cycles, respectively. Vertical cracks were also observed during the $6\varepsilon_y$ first cycle. Through the following cycles the cracks became wider and the number of new cracks decreased. The spacing of the horizontal cracks were governed by the cavities created to include the infrared LEDs from the Optotrak system. During the cycles associated with $8\varepsilon_y$, crack widths close to 0.075in. (1.9mm) were measured at midheight. Signs of concrete spalling were also observed. At $10\varepsilon_y$ first cycle, 0.10in. (2.5mm) crack widths were measured in the interface between the prism and the footing, and close to the cap. Signs of concrete spalling were also captured at this stage. During the $12\varepsilon_y$ cycles,

cracks widths reached 1/8 in. (3.2mm). Concrete cover fell down on the east face of the prism and the transverse reinforcement was exposed within a length of 24in. (610mm). Crack widths close to 3/16in. (4.8mm) were measured during the first cycle at 14ε_y.

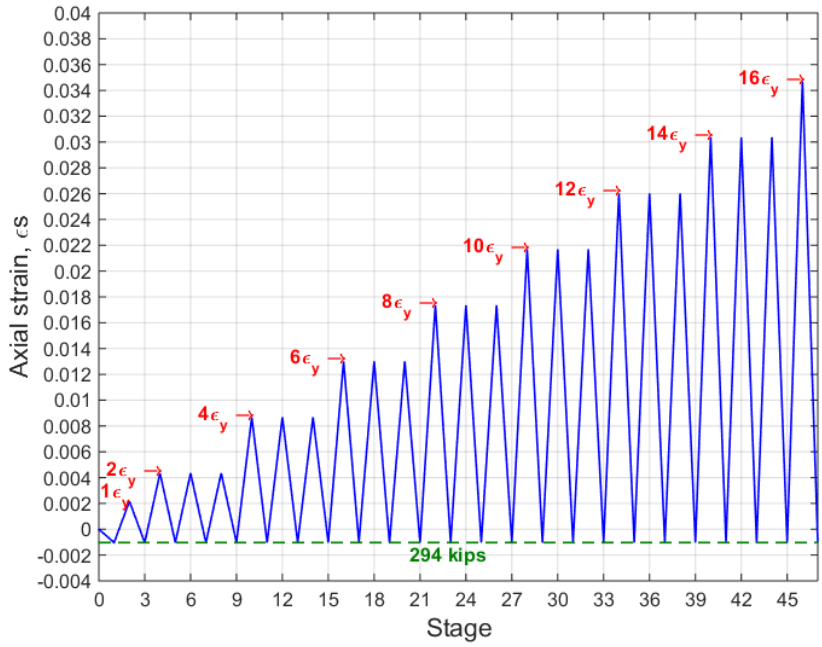

Figure 5-49. Axial Strain History applied to Prism 10

As tensile demands increased during the cycles related to 14ε_y the out-of-plane buckling mechanism was captured upon compressive loading. Since the out-of-plane deformations were relatively small, the compression force developed to resist the overturning moment, was fully reached as cracks close and consequently, the prism returned to a fairly straight and stable position. Figure 5-44 shows the evolution of out-of-plane deformations captured during the last cycle associated with 14ε_y. On the way to 16ε_y, the bar located on the northeast corner fractured at midheight before reaching the tensile target. Subsequently, a last compressive load was applied to the specimen. During this stage, bar buckling was observed in the six longitudinal bars all along the prism. Figure 5-51 presents the final state of Prism 10, where a slight buckled shape is detected. Notice that bar fracture preceded by bar buckling was the cause of the prism failure.

Figure 5-52 shows axial strains plotted against axial loads captured from the gages where bar fracture occurred. Through the 14ε_y cycles, the axial stiffness reduces by the time the axial load approaches the compressive yielding strength. At this stage, the specimen was still extended. These points were associated with the out-of-plane buckling mechanism. In the last cycle, bar fracture was captured and then the maximum applied load at the very end of the test was -272kips (1,210kN), equivalent to 93% of the axial target load, P_o = -294kips (1,308kN).

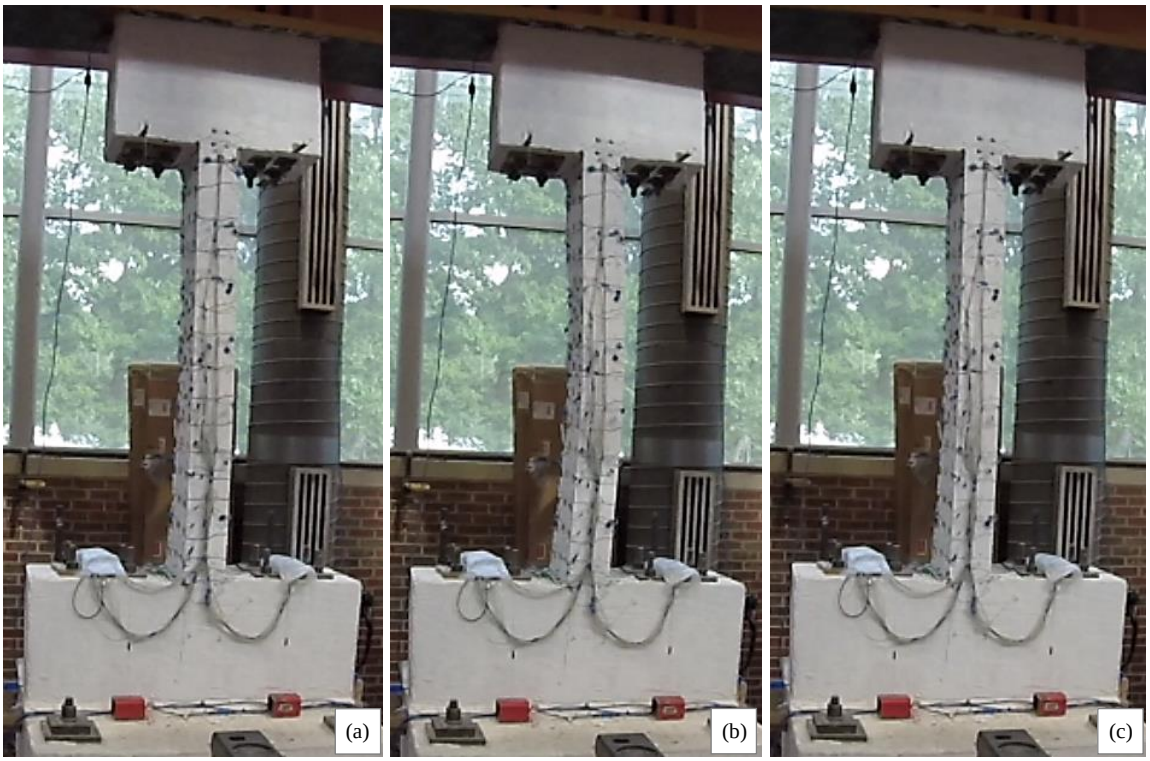

Figure 5-50. Prism 10: Stable out-of-plane buckling mechanism during 14εy(3), third cycle: a) Onset of buckling – cracks opened, b) Stable buckling – cracks partially closed, c) End of buckling - cracks closed.

Figure 5-51. Prism 10: Final state

Figure 5-52 includes the corrected predictions according to Paulay & Priestley (1993) "P&P" and Chai & Elayer (1999) "Ch&E" models once the actual buckled length was determined. In addition, tensile and compressive yielding strengths, *Asfy*, are similarly plotted, where *As* is the area of the longitudinal reinforcement. The responses presented in Figure 5-52 also show that after the first cycle related to $10\varepsilon_y$ the axial tensile force capacity of the prism dropped from 56kips (249kN) to 41kips (182kN), which represents a reduction of about 27%. This variation is attributed to bar buckling that occurred upon compressive loads before applying the second cycle related to $10\varepsilon_y$. In order to verify this statement, the upper and lower gages adjacent to the location where the bar fractured are considered to establish the strain responses during the test. Figure 5-53 shows that during the last nine cycles corresponding to $10\varepsilon_y$, $12\varepsilon_y$, $14\varepsilon_y$ and under compressive loading, the strains reached higher tensile values on the upper gage, and lower compressive values on the lower gage. From this analysis, it is concluded that the bar that fractured, certainly experienced bar buckling at earlier stages that led to a reduction in the tensile capacity of the prism and the subsequent bar rupture.

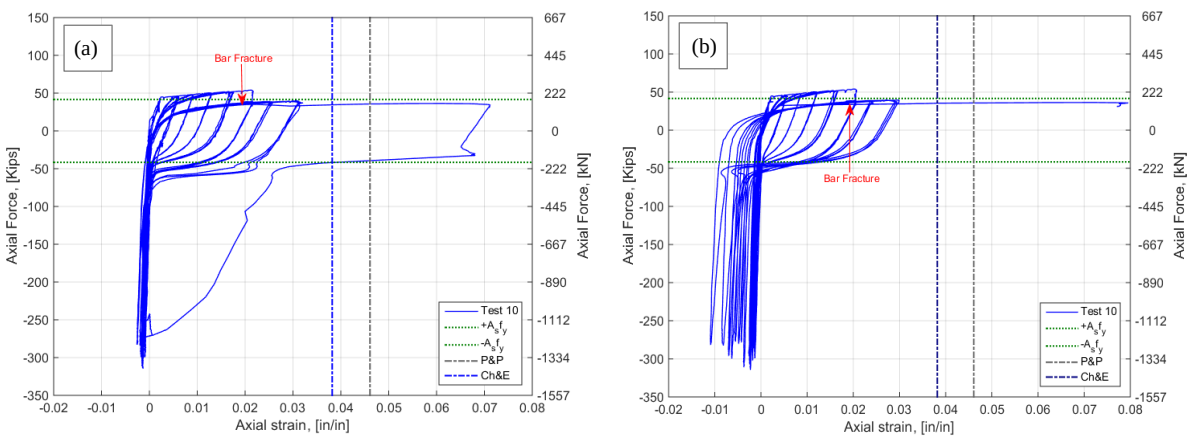

Figure 5-52. Prism 10: Axial Strain vs. Axial Force from established from the region where bar fracture was captured on a) south face and b) north face

Out-of-plane deformations increased upon compressive loading during the cycles associated with $12\varepsilon_y$. Figure 5-53 shows the evolution of out-of-plane deformations at different stages. The stability criterion from Paulay & Priestley (1993) model calculated as out-of-plane deformation and denoted as stability limit, is included in Figure 5-53 to show that instability was expected beyond this limit. During the final cycle, the maximum out-of-plane deformation was δm = 0.9in. (23mm), located 4in. (102mm) below midheight, which is less than 50% of the prism thickness.

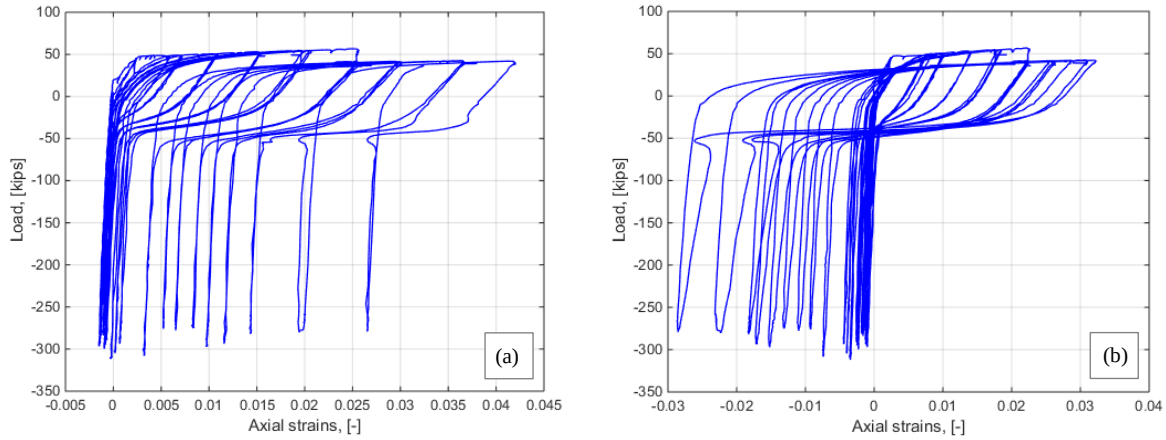

Figure 5-53. Prism 10: Strain history response of two gages adjacent to the location where the bar fractured: (a) upper gage and (b) lower gage

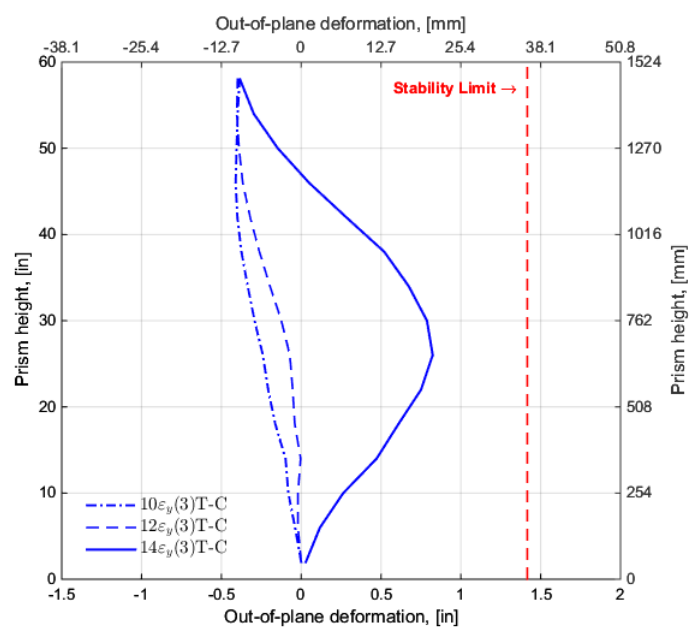

Figure 5-54. Prism 10: Evolution of out-of-plane deformations captured upon compressive loading at different stages

5.1.10.2 Test 10 Conclusions

Prism 10 was tested during four hours where two loading patterns were applied. The first part of the test showed that the prism reached the maximum axial design compressive load with zero loss of capacity. In the second part of the test, progressive cyclic axial loads/strains were applied to the specimen reaching maximum values close to the axial design compressive force, *Po* = -294 kips and $16\varepsilon_y$, in compression and tension, respectively. The specimen presented a stable response at low levels of axial tensile demands. Out-of-plane deformations were not noticed during the cycles before $14\varepsilon_y$. However, the analysis showed a gradual increase in the out-of-plane deformations through the $12\varepsilon_y$

cycles. Bar fracture were observed when the specimen was subjected to tensile demands on the way to $16\varepsilon_y$. This time buckling instability did not occurred because bar buckling failure mode developed at earlier stages, which led to bar fracture. The stirrups and ties remained as originally constructed.

5.1.11 Test 11

Test 11 was conducted at the Constructed Facilities Laboratory on Tuesday, October 4, 2016, as part of the third phase of this research project. Axial cyclic tensile displacements and compressive loads generated from a cyclic loading considering subduction megathrust earthquakes were applied to the specimen to determine additional critical parameters associated with lateral instability of RC walls. Table 5-11 describes the principal properties of Prism 11, where ρ_l is the longitudinal reinforcement ratio, d_{bl} is the diameter of the bar, and s_h is the transverse reinforcement spacing.

Table 5-11. Prism 11: Specifications

Prism	Dimensions as built	Longitudinal Reinforcement Layout	ρ_l	s_h/d_{bl}	ε_y
11	5.5”x12”x60” (140mm x 305mm x 1,524mm)	(6) #3 (9.52mm)	0.010	5.3	0.00217

5.1.11.1 Test 11 Summary

Prism 11 was subjected to axial tensile strains and compressive loads generated from a cyclic protocol created according to Bazaez & Dusicka (2016), where inelastic cycles and cumulative damage demands of subduction megathrust earthquakes were considered to develop more realistic testing protocols to improve seismic assessment of RC bridge columns. Moment-Curvature analyses of four prototype structural walls were conducted using CumbiaWall (Herrick & Kowalsky, 2016). Subsequently, equivalent yielding displacements (δy) were obtained to calculate different inelastic protocols, in accordance with the following equation described already in Chapter 4:

$$f(N) = \left(a \cdot e^{bN} + c \cdot e^{dN}\right)\delta_y$$

where a, b, c, and d, are exponential coefficients associated with different ductility levels and fundamental periods of predefined structural systems established in Bazaez & Dusicka (2016) approach; and N, is the number of inelastic cycles. The ductility and the fundamental period selected to create the loading history were $\mu = 4$ and $T = 1.0s$, respectively. Ductility 4 accounts for typical systems where damage is limited though drift capacity. Period 1.0s considers intermediate fundamental periods for bridges and mid-rise buildings. Consequently, the exponential coefficients to obtain the cycles amplitudes would be: $a = 0.9557$, $b = 0.0439$, $c = 8.91E\text{-}4$, and $d = 0.4853$.

Once the cyclic displacement responses of the walls were determined, strains ratios at each stage were calculated as a function of ε_y. Finally, since upon $16\varepsilon_y$ strain, Prism 10 suffered from bar fracture, the strain ratios were scaled to $16\varepsilon_y$, selected as target to be reached in a previous cycle before the maximum peak equal to $24\varepsilon_y$ is achieved. The unique compressive load was Po = -294 kips

(1,308kN), which is the compressive capacity of the prism. Figure 5-55 shows the axial strain history applied to Prism 11. Notice that instead of considering the maximum peak as 24ε_y, Figure 5-55 displays a value of 22ε_y since this was the actual average strain reached during the test at that stage.

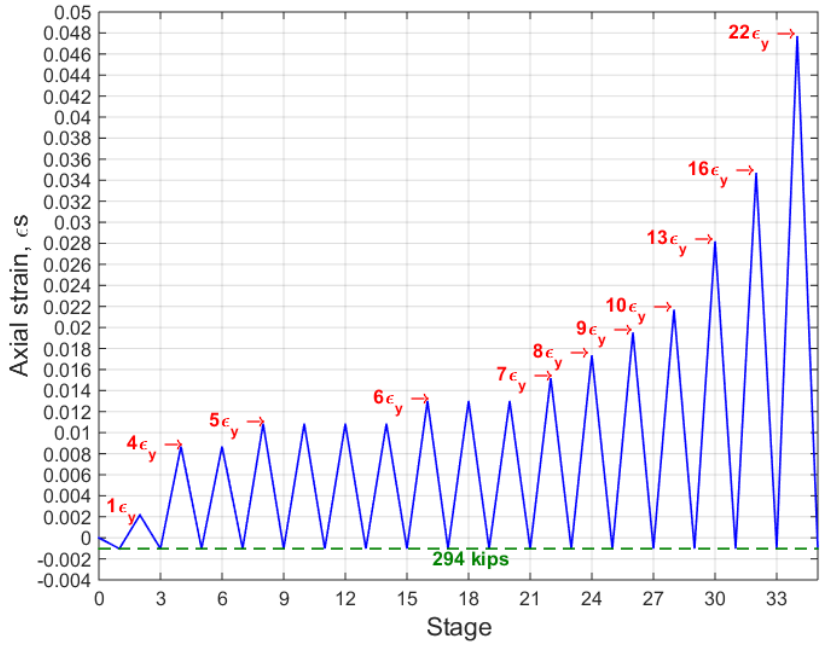

Figure 5-55. Axial Strain History applied to Prism 11

At 1.0ε_y strain demand, small horizontal cracks appeared all along the prism. Upon compressive loading cracks uniformly closed as expected. This phenomenon was observed during the following cycles until failure was captured. Crack widths between 0.05in. (1.3mm) and 0.075in. (1.9mm) were measured at midheight during the 4ε_y, 5ε_y, and 6ε_y cycles. Concrete flacking was captured upon compressive loading during the second cycle associated with 5ε_y. Concrete spalling was observed during the 7ε_y cycle. Crack widths close to 0.10in. (2.5mm) were measured at this stage on the midheight region and small vertical cracks propagated to the foundation. Through the following cycles the cracks became wider and the number of new cracks decreased. The spacing of the horizontal cracks were governed by the cavities created to include the infrared LEDs.

Crack widths close to 0.10in. (2.5mm) were observed during the 8ε_y cycles. Crack widths close to 1/8in. (3.2mm) were measured during the 9ε_y and 10ε_y cycles. Signs of concrete spalling were observed at 10ε_y; and, upon compressive loading, bar buckling was captured on the south face at midheight. Through the 13ε_y cycle, new cracks formed and older cracks became wider. Bar buckling continued propagating. At 16ε_y tensile strain, cracks widths reached 3/8in. (9.5mm). At the time the

target load was achieved in compression, more bars buckled all along the prism. Concrete spalling was also observed. Crack widths close to 1/4in. (6.4mm) were measured when the axial tensile strain reached the peak at $22\varepsilon_y$.

Out-of-plane buckling deformations were observed during the $13\varepsilon_y$ and $16\varepsilon_y$ cycles, which confirmed that as tensile demands increases, the out-of-plane buckling mechanism develops upon compressive loading. Since the out-of-plane deformations were relatively small, the compression force developed to resist the overturning moment, is fully reached as cracks close and consequently, the prism returns to a fairly straight and stable position. Figure 5-56 shows the evolution of out-of-plane deformations captured during the cycle associated with $16\varepsilon_y$. When compressive forces were acting on the specimen after reaching the maximum tensile peak, instability occurred as exposed in Figure 5-57. Substantial damage among concrete cover crushing was observed at midheight.

Figure 5-58 shows axial strains plotted against axial loads captured where the out-of-plane deformation reached a maximum value at the end of the test. During the last three cycles the axial stiffness of the prism reduces at the time the axial load approaches the compressive yielding strength. At this stage, the specimen was still extended. These points were associated with the out-of-plane buckling mechanism. In the last cycle, instability was captured since the prism was not able to recover its strength. The maximum applied load at this stage was -109 kips (485kN), equivalent to 37% of the compressive target load, *Po* = -294 kips (1,308kN).

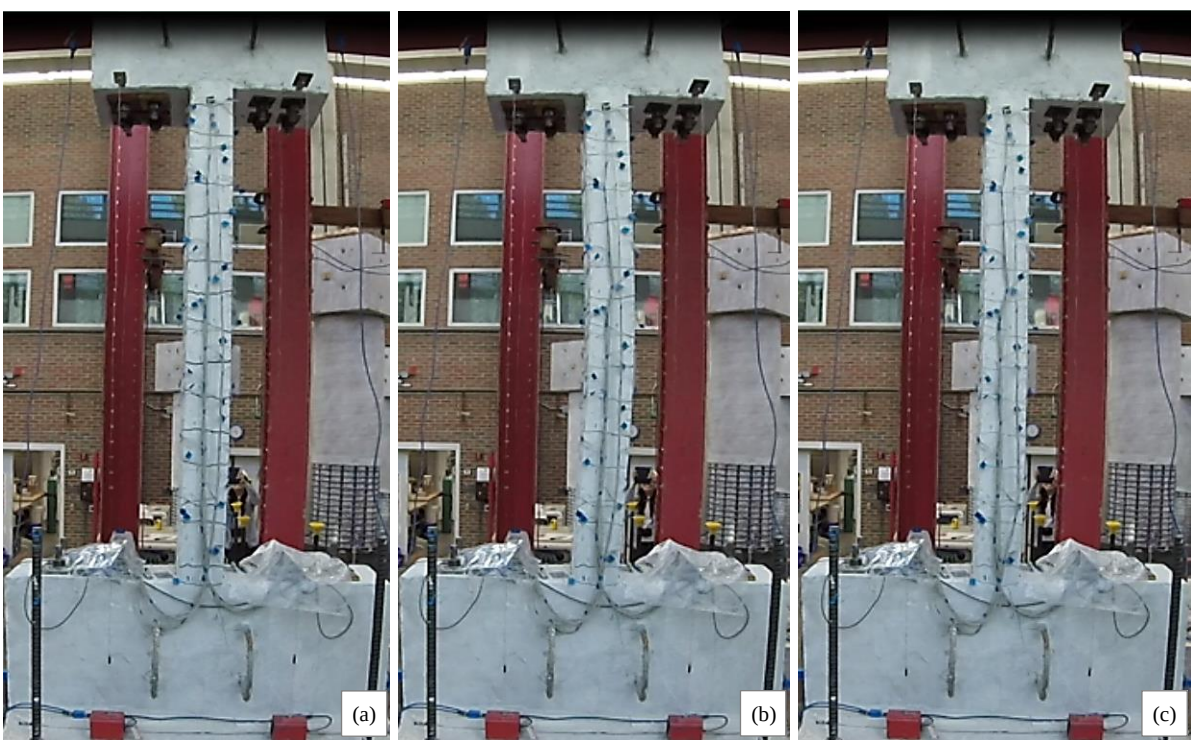

Figure 5-56. Prism 11: Stable out-of-plane buckling mechanism during the 16εy cycle: a) Onset of buckling – cracks opened, b) Stable buckling – cracks partially closed, c) End of buckling - cracks closed.

Figure 5-57. Prism 11: Instable out-of-plane buckling mechanism during the 22εy cycle

Figure 5-58 also shows the corrected predictions according to Paulay & Priestley (1993) "P&P" and Chai & Elayer (1999) "Ch&E" models once the actual buckled length was determined. In addition, tensile and compressive yielding strengths, *Asfy*, are similarly plotted, where *As* is the area of the longitudinal reinforcement.

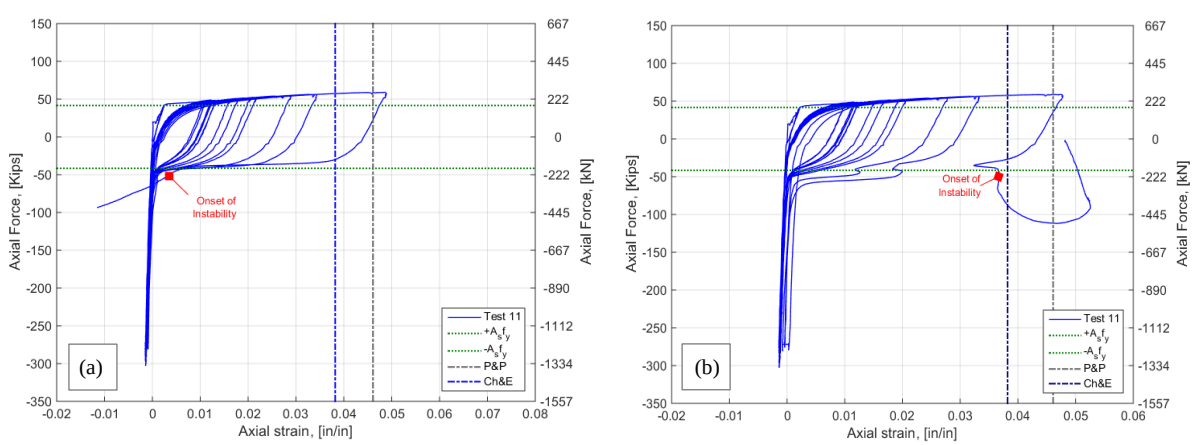

Figure 5-58. Prism 11: Axial Strain vs. Axial Force from established at midheight on a) south face and b) north face

Out-of-plane deformations increased upon compressive loading during the last three cycles. Figure 5-59 shows the evolution of out-of-plane deformations at different stages. The stability criterion from Paulay & Priestley (1993) model calculated as out-of-plane deformation and denoted as stability limit, is included in Figure 5-59 to show that instability was expected beyond this limit. During the final cycle, the maximum out-of-plane deformation was δm = 4.4in. (112mm), located at midheight, which exceeded 50% of the prism thickness.

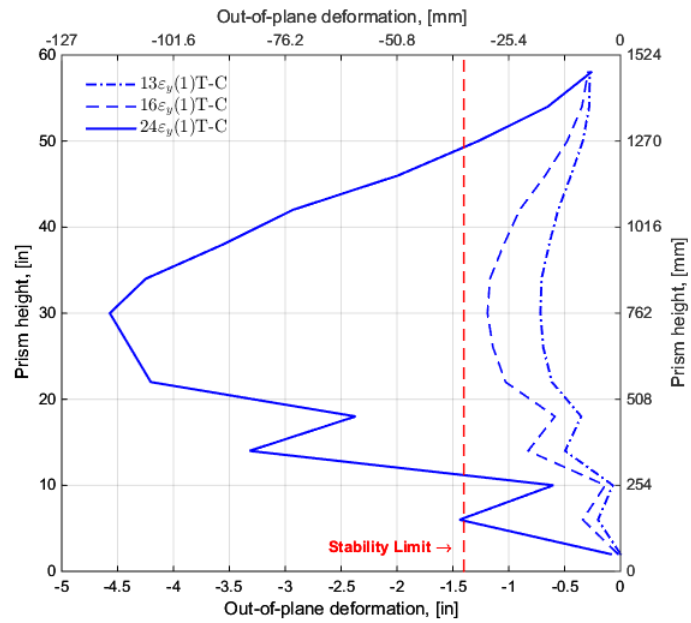

Figure 5-59. Prism 11: Evolution of out-of-plane deformations captured upon compressive loading at different stages

5.1.11.2 Test 11 Conclusions

Prism 11 was tested during four hours where it was subjected to axial cyclic tensile strains and compressive loads generated from a cyclic protocol created to account for inelastic cycle effects and cumulative damage demands from subduction megathrust earthquakes. The loads/strains that were applied to the specimen reached maximum values close to the axial design capacity, *Po* = -294 kips in compression, and 22ε_y in tension. The specimen presented a stable response at low levels of axial tensile demands. First signs of out-of-plane deformations and bar buckling were noticed under compressive loads during the cycle associated with 10ε_y. These mechanisms became more severe in the following cycles until instability was observed during the last cycle associated with 22ε_y. The large out-of-plane buckling deformation led to concrete cover crushing and spalling in the central region of the prism. The axial compressive force at this stage resulted 37% of the compressive force applied in a previous cycle. Bar fracture was not detected during or after the test. The stirrups remained as originally constructed.

5.1.12 Test 12

Test 12 was conducted at the Constructed Facilities Laboratory on Wednesday, October 12th, 2016, as part of the third phase related to this research project. An axial cyclic load generated from a seismic historic record from 1994 Northridge earthquake (Sylmar station) was applied to the specimen to capture its structural performance and to determine additional critical parameters associated with lateral instability of RC walls. Table 5-12 includes the principal properties of Prism 12, where ρ_l is the longitudinal reinforcement ratio, d_{bl} is the diameter of the bar, and s_h is the transverse reinforcement spacing.

Table 5-12. Prism 12: Specifications

Prism	Dimensions as built	Longitudinal Reinforcement Layout	ρ_l	s_h/d_{bl}	ε_y
12	5.5”x12”x60” (140mm x 305mm x 1,524mm)	(6) #3 (9.52mm)	0.010	5.3	0.00217

5.1.12.1 Test 12 Summary

Prism 12 was subjected to an axial seismic axial displacement history based on the structural response of a prototype RC wall exposed to an actual in-plane horizontal earthquake record. The seismic record selected for this analysis was the 1994 Northridge earthquake (Sylmar station). The main purpose of subjecting the specimen to this kind of demand was to consider the effects of near-field records that contain long duration pulses.

The strain response of a bar located at the base of the boundary elements of a the prototype wall was determined through SeismoStruct V7.0 (Seismosoft Ltd., 2014). For the first input data, the maximum tensile strain was scaled to $16\varepsilon_y$ based on Prism 10 response. A second input data scaled to $18\varepsilon_y$ was also created in case the prism survived the first input data, which actually happened during the test. The unique compressive load was, Po = -294 kips (1,308kN), equivalent to the compressive strength capacity of the prism. Figure 5-60 shows the axial strain history applied to Prism 12.

During $16\varepsilon_y$ (1) strain, where (1) implies the first seismic axial strain input, crack widths close to 3/16in. (4.8mm) were captured in the region close to the footing. The out-of-plane buckling mechanism was observed upon compressive loading. Since the out-of-plane deformations were relatively small, the compression force developed to resist the overturning moment, was fully reached as cracks close and consequently, the prism returned to a straight and stable position. Through the next cycle, out-of-plane buckling deformations were slightly notice. At the end of the stage # 7, signs of concrete flacking were observed.

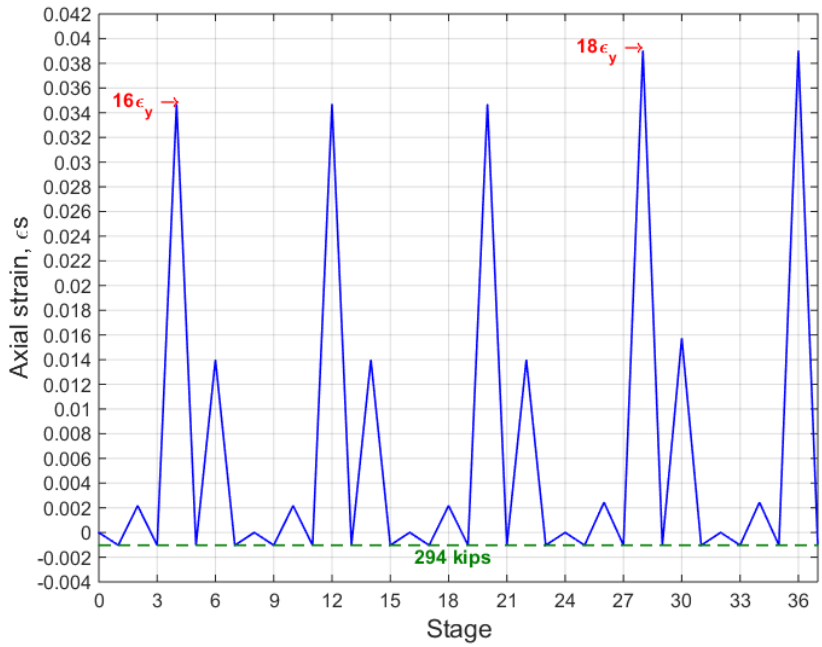

Figure 5-60. Axial Strain History applied to Prism 12

The same response was captured during the next two 16ε_y and the first 18ε_y input signals. However, more damage related to concrete spalling was accumulated during these cycles. Concrete cover fell down on the west face of the prism and the transverse reinforcement was exposed within a length of 40in. (1,106mm). In addition, signs of bar bucking appeared during the 16ε_y (2) input data, where (2) represents the second axial strain input at this level. Figure 5-61 shows the evolution of out-of-plane deformations captured during the cycle associated with 18ε_y (1). Upon tensile displacements and on the way to 18ε_y (2), two longitudinal bars fractured on the central region of the south face before reaching the tensile target. Subsequently, the prism was subjected to a last compressive load and during this stage out-of-plane instability combined with bar buckling were observed. Figure 5-62 presents the final state of Prism 12.

Figure 5-63 shows axial strains plotted against axial loads captured where the out-of-plane deformation reached a maximum value at the end of the test. During the maximum tensile strains cycles, the axial stiffness of the prism reduces at the time the axial load approaches the compressive yielding strength. At this stage, the specimen was still extended. These points were associated with the out-of-plane buckling mechanism. Figure 5-63 also shows that after 18ε_y (1), the axial tensile force capacity of the prism decreased from 59kips (262kN) to 39kips (173kN), which represents a reduction of about 34%. This variation is attributed to accumulated local damage due to bar buckling that occurred upon compressive loading after reaching 18ε_y (1). In the last cycle, instability was captured

since the prism was not able to recover its strength. The maximum applied load at this stage was -95 kips (423kN), equivalent to 32% of the compressive target load, *Po* = -294 kips (1,308kN).

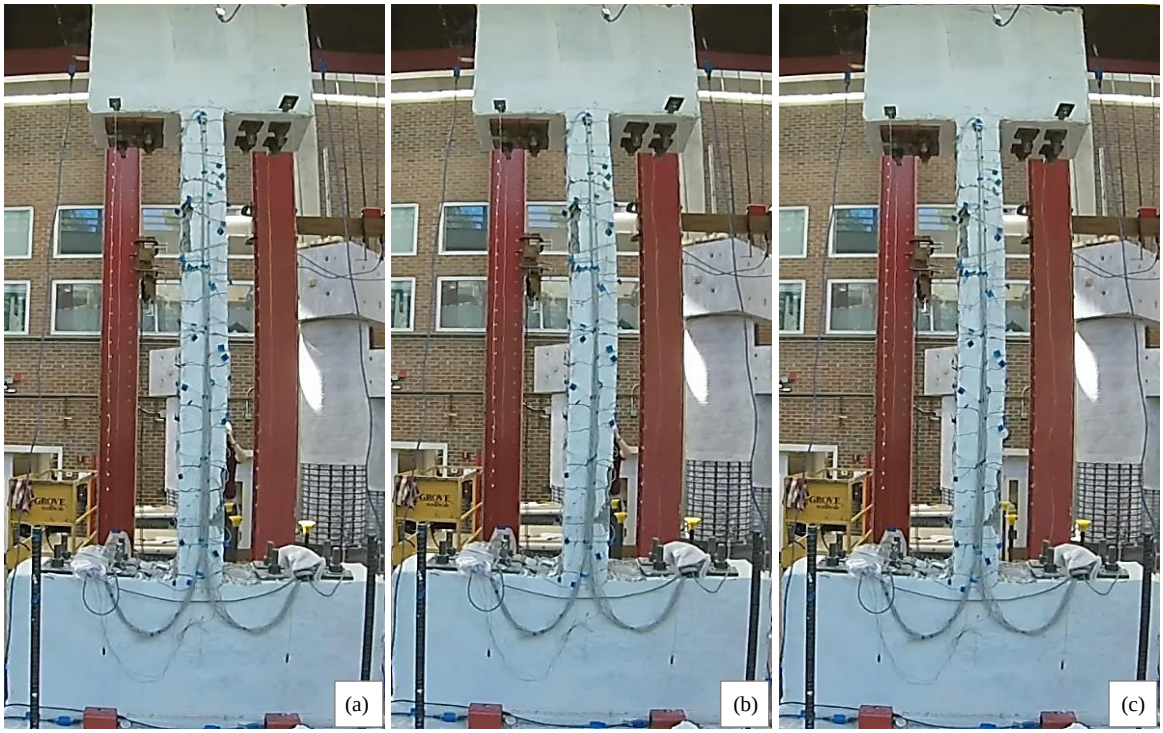

Figure 5-61. Prism 12: Stable out-of-plane buckling mechanism during the 18εy(1) first cycle: a) Onset of buckling – cracks opened, b) Stable buckling – cracks partially closed, c) End of buckling - cracks closed.

Figure 5-62. Prism 12: Instable out-of-plane buckling mechanism during the last cycle

Figure 5-63 also shows the corrected predictions according to Paulay & Priestley (1993) "P&P" and Chai & Elayer (1999) "Ch&E" models once the actual buckled length was determined. In addition, tensile and compressive yielding strengths, *Asfy*, are similarly plotted, where *As* is the area of the longitudinal reinforcement.

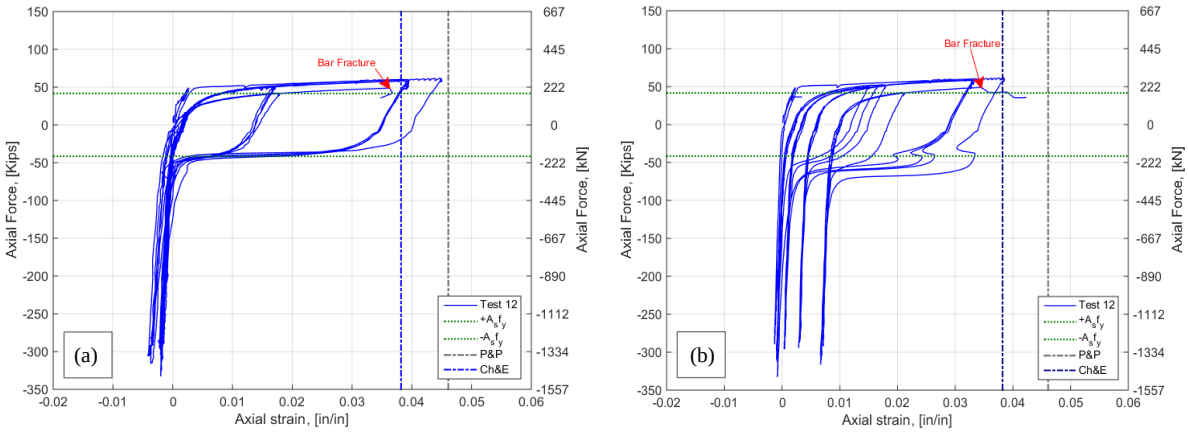

Figure 5-63. Prism 12: Axial Strain vs. Axial Force established 4in. (102mm) above midheight on a) south face and b) north face

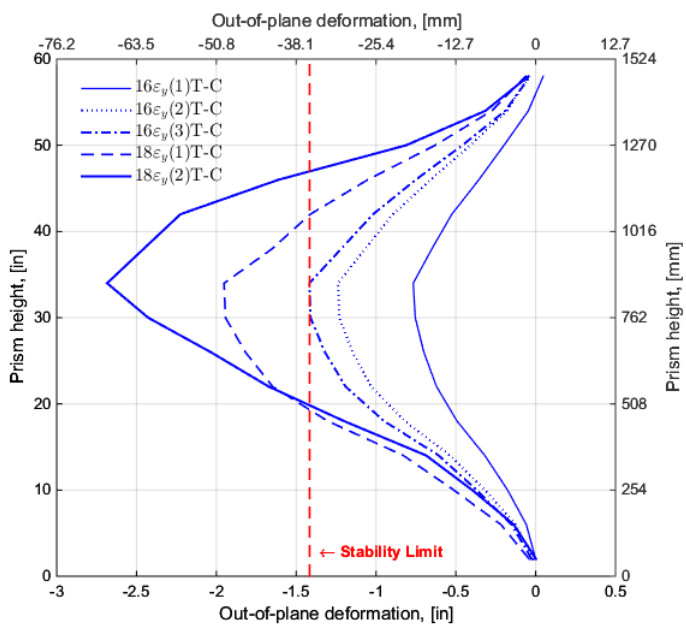

Figure 5-64. Prism 12: Evolution of out-of-plane deformations captured upon compressive loading at different stages

Out-of-plane deformations increased upon compressive loading during the cycles associated with the maximum tensile demands. Figure 5-64 shows the evolution of out-of-plane deformations at

different stages. The stability criterion from Paulay & Priestley (1993) model calculated as out-of-plane deformation and denoted as stability limit, is included in Figure 5-64 to show that instability was expected beyond this limit. During the final cycle, the maximum out-of-plane deformation was δm = 2.7in. (69mm), located 4in. above midheight, which exceeded 50% of the prism thickness.

5.1.12.2 Test 12 Conclusions

Prism 12 was tested during three hours where it was subjected to axial cyclic tensile displacements and compressive loads generated from the 1994 Northridge earthquake (Sylmar station) in order to consider the effects of near-field records that contain long duration pulses. The cyclic axial loads/strains that were applied to the specimen reached maximum values close to the axial design capacity, Po = -294 kips (1,308kN) in compression, and $18\varepsilon_y$ in tension. The specimen presented a stable response at low levels of axial tensile demands. Relevant signs of out-of-plane deformations were noticed under compressive loads during the cycles associated with $16\varepsilon_y$ and $18\varepsilon_y$. The onset of bar buckling was detected during $16\varepsilon_y$ (2) upon compressive demands. The latter mechanism became more severe in the following cycles until bar fracture occurred during the last cycle associated with $18\varepsilon_y$ (2). Subsequently, instability related to inelastic out-of-plane buckling deformations developed upon compressive loads, which also led to concrete cover crushing and spalling in the central region of the prism. The axial compressive force at this stage was 32% of the compressive force applied in a previous cycle. The stirrups remained as originally constructed.

5.2 Trends of the experimental results

This section summarizes the tendencies captured from the experimental data associated with the influence of different parameters on the onset of out-of-plane buckling instability. Trends in the impact of crucial factors like induced out-of-plane displacements, out-of-plane deformations linked to the stability criteria proposed by Paulay & Priestley (1993), longitudinal reinforcement ratio, hysteretic response of the longitudinal reinforcement, curvature distribution, crushing limit state, tensile loading paths, and transverse reinforcement spacing are discussed in this section. The analytical study that includes the parametric study and the validation of a new proposed model, which is detailed in Chapter 6, is based on the key findings explained in this section.

5.2.1 Out-of-plane displacements vs. maximum tensile strains

Peak tensile strains captured at different stages for each prism and their structural response showed that out-of-plane displacements applied to the top of the specimens slightly affect the onset of buckling instability. The following subsections detail what was detected along the three experimental phases.

5.2.1.1 Experimental Phase 1

Figure 5-65 presents the average of the peak tensile strains determined from the gages where maximum out-of-plane deformations were measured at the end of each test, calculated as ratios of the yielding strain ($\varepsilon_y = 0.00239$). The horizontal axis represents four lateral out-of-plane drift percentages considered during Phase 1. The results from Test 1 and Test 5 are excluded from Figure 5-65 since the essence of the axial loading protocols and the lateral out-of-plane displacements varied from the other four tests.

Progressive stable cycles “Stable” and the last elastic cycles “Last EB” are identified in the graph. Notice that the predicted maximum allowed strains, in accordance with Paulay & Priestley (1993) “PP” and Chai & Elayer (1999) “CE” models are close to $10\varepsilon_y$, being the first a little bit more conservative. Inelastic buckling “IB” occurred upon compressive loading after reaching tensile demands around $12\varepsilon_y$. This implies that the CE model was closer to the experimental results. However, both models conservatively predict the onset of instability even when out-of-plane displacements are absent. The CE model considers that the hysteretic contribution of the longitudinal reinforcement is approximately between $3\varepsilon_y$ and $5\varepsilon_y$; nonetheless, the first value is recommended for design purposes and consequently, it is considered in this study for the three phases ($\eta = 3$).

Prism 3 and Prism 6 reported higher peak tensile strains before buckling instability developed. In the case of Prism 3, it could be attributed to the fact that the specimen deformed in the same direction that the out-of-plane lateral displacement was applied, and consequently less damage was accumulated in the buckled region when the specimens were subjected to compressive loads. In the case of Prism 6,

the large lateral drift applied to the specimen delayed the evolution of out-of-plane deformations, and subsequently buckling instability occurred later.

The most important aspect to note is that the onset of instability is slightly affected by the combination of axial cyclic displacements and lateral out-of-plane drifts, as suggested by the models and the structural response of the prisms. The analytical validation of this statement will be discussed in the following section.

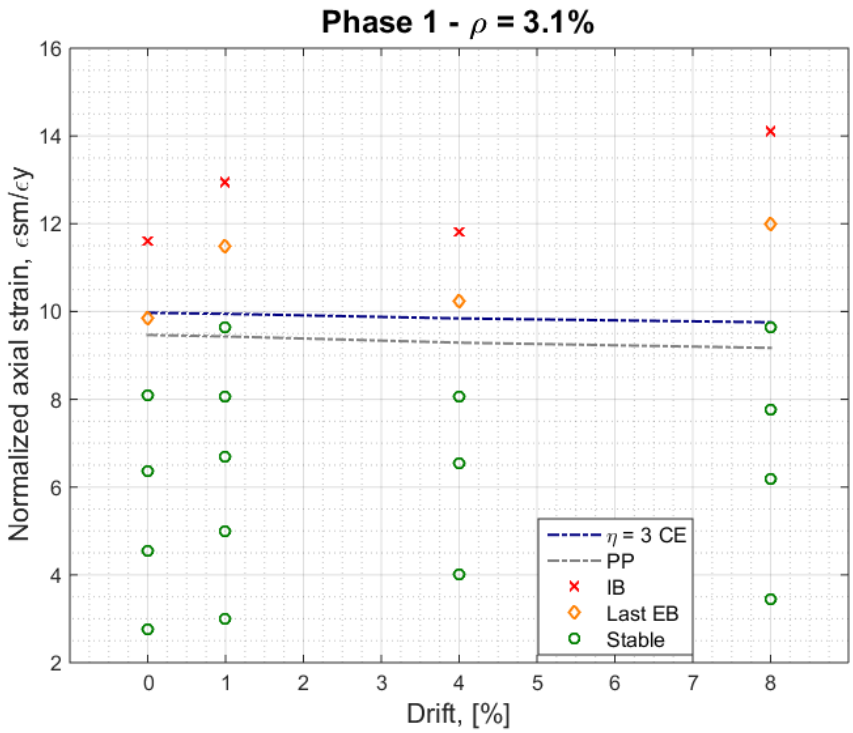

Figure 5-65. Phase 1: Peak tensile strains

5.2.1.2 Experimental Phase 2

Figure 5-66 presents the average of the peak tensile strains determined from the gages where maximum out-of-plane deformations were measured at the end of each test, calculated as ratios of the yielding strain (ε_y = 0.00238). The horizontal axis characterizes the three lateral out-of-plane drift percentages considered during Phase 2.

Progressive stable cycles "Stable" and the last elastic cycles "Last EB" are identified in the graph. Notice that the predicted maximum allowed strains, in accordance with Paulay & Priestley (1993) "PP" and Chai & Elayer (1999) "CE" models, are close to $13\varepsilon_y$, being the later a little bit more conservative. However, inelastic buckling "IB" occurred upon compressive loading after reaching tensile demands close to $14\varepsilon_y$. This implies that the PP model was closer to the experimental results. Once again, note that the onset of instability is slightly affected by the combination of axial cyclic

displacements and lateral out-of-plane drifts, as suggested by the models and the structural response of the prisms.

Prism 9 reported higher peak tensile strains before buckling instability developed under compressive loads, which could be attributed to the axial strain protocol followed during this test. Minor damage was accumulated in the buckled region after the first pulse-type signal was applied and consequently, buckling instability was delayed until reaching higher tensile strains.

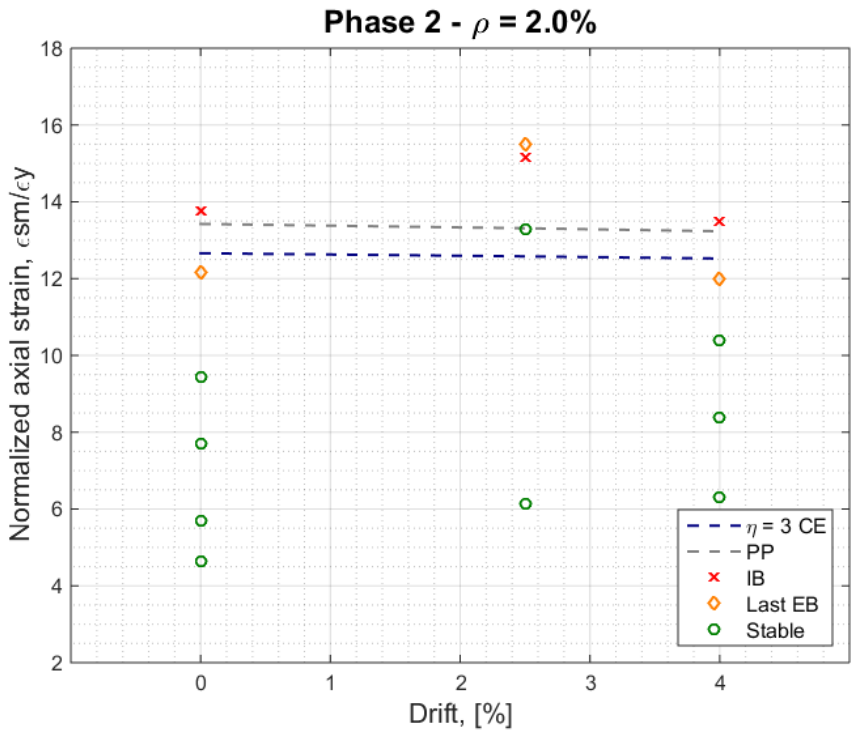

Figure 5-66. Phase 2: Peak tensile strains

5.2.1.3 Experimental Phase 3

Figure 5-67 presents the average of the peak tensile strains determined from the gages where maximum out-of-plane deformations were measured at the end of each test, calculated as ratios of the yielding strain (ε_y = 0.00217). Since the results from Phase 1 and Phase 2 suggested that out-of-plane displacements slightly affect the onset of instability due to out-of-plane buckling, the three prisms contemplated for this third phase were only subjected to axial demands.

Progressive stable cycles "Stable" and the last elastic cycles "Last EB" are identified in the graph. The predicted maximum allowed strains, in accordance with Paulay & Priestley (1993) "PP" and Chai & Elayer (1999) "CE" models, are close to $20\varepsilon_y$ and $18\varepsilon_y$, respectively. Prism 10 experienced bar buckling "BB" through the $10\varepsilon_y$ cycles and bar fracture "BF" before the predicted values from the mentioned models were reached. Prism 11 exhibited bar buckling after the $10\varepsilon_y$ cycle and inelastic buckling "IB" upon compressive loading after the $22\varepsilon_y$ cycle was applied. Prism 11 reported higher

peak tensile strains before buckling instability occurred, which was expected due to the characteristics of the megathrust earthquake type protocol followed during this test. Prism 12 experienced a combination of three failure modes at the end of the test, were inelastic buckling were captured after bar buckling and bar fracture. The results suggest that the PP model overestimates the onset of instability. Clarifications about the additional failure modes that appeared during Phase 3 are discussed in the transverse reinforcement spacing section.

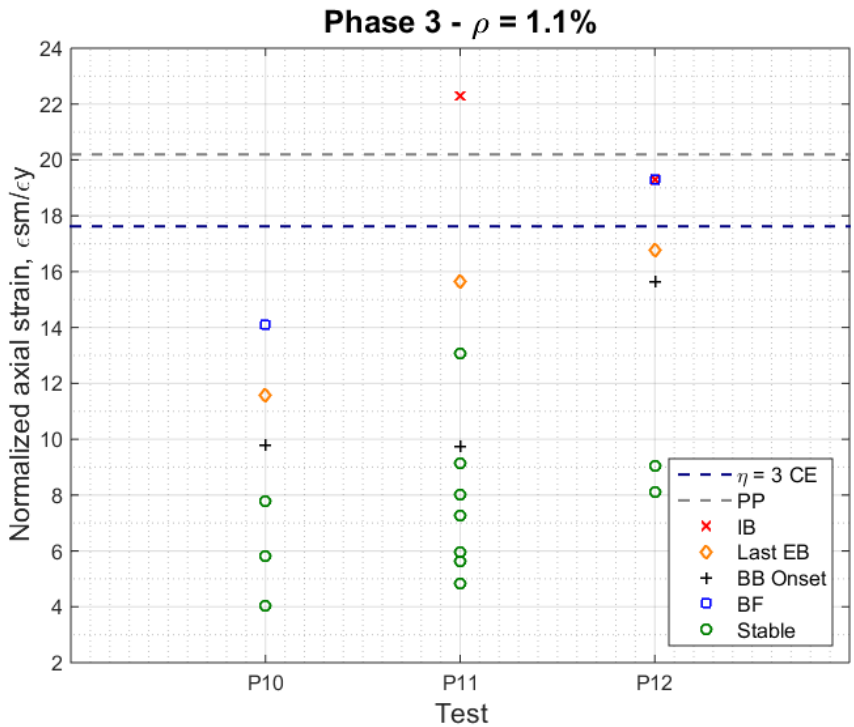

Figure 5-67. Phase 3: Peak tensile strains

5.2.2 Influence of out-of-plane displacement on boundary elements stability

The out-of-plane deformations observed at different stages for each test that are presented in Section 5.1 constitute the base of the analysis developed in this section. Figure 5-68 shows the deformed shape of Prism 2 captured during the third cycle associated with $10\varepsilon_y$ at the time a maximum out-of-plane deformation δ_m was captured under compressive loading. The trend line is also included in the graph, which follows a 4th degree polynomial function:

$$y = a \cdot x^4 + b \cdot x^3 + c \cdot x^2 + d \cdot x + e \tag{5-1}$$

In general, the coefficients in Equation (5-1) can be obtained from the boundary conditions and known parameters like the top out-of-plane displacement δ_t and δ_m developed at $X_m = 0.5L$. In order to determine the points of contraflexure, the curvature of the prism can be stablished from the second derivative of the buckled shape, which is acceptable for small deflections. Since X_1 and X_2 are

calculated equating the curvature function to zero, then the length of the buckled region used in Paulay & Priestley (1993) "PP" and Chai & Elayer (1999) "CE" models is $Lo = X_1 - X_2$. The stability criteria stipulated in Paulay & Priestley (1993) model is comparable to $\xi_c = \delta_m / b_w$, then it can be replaced in the PP and CE models as shown in Equation (5-2) and Equation (5-3), respectively. Finally, through an iterative process that accounts for the variation of X_m, X_1, and X_2, as a function of δ_t, it is demonstrated that out-of-plane displacements slightly influence the limits of maximum tensile strains ε_{sm} to prevent buckling instability. The dashed lines in Figures 5-65, 5-66, and 5-67, which show the tendency of the two models, consider the analysis covered in the current section.

$$\varepsilon_{sm} \leq 8\beta \left(\frac{b_w}{L_o} \right)^2 \left(\frac{\delta_m}{b_w} \right) \tag{5-2}$$

$$\varepsilon_{sm} \leq \frac{\pi^2}{2} \left(\frac{b_w}{L_o} \right)^2 \left(\frac{\delta_m}{b_w} \right) + 3\varepsilon_y \tag{5-3}$$

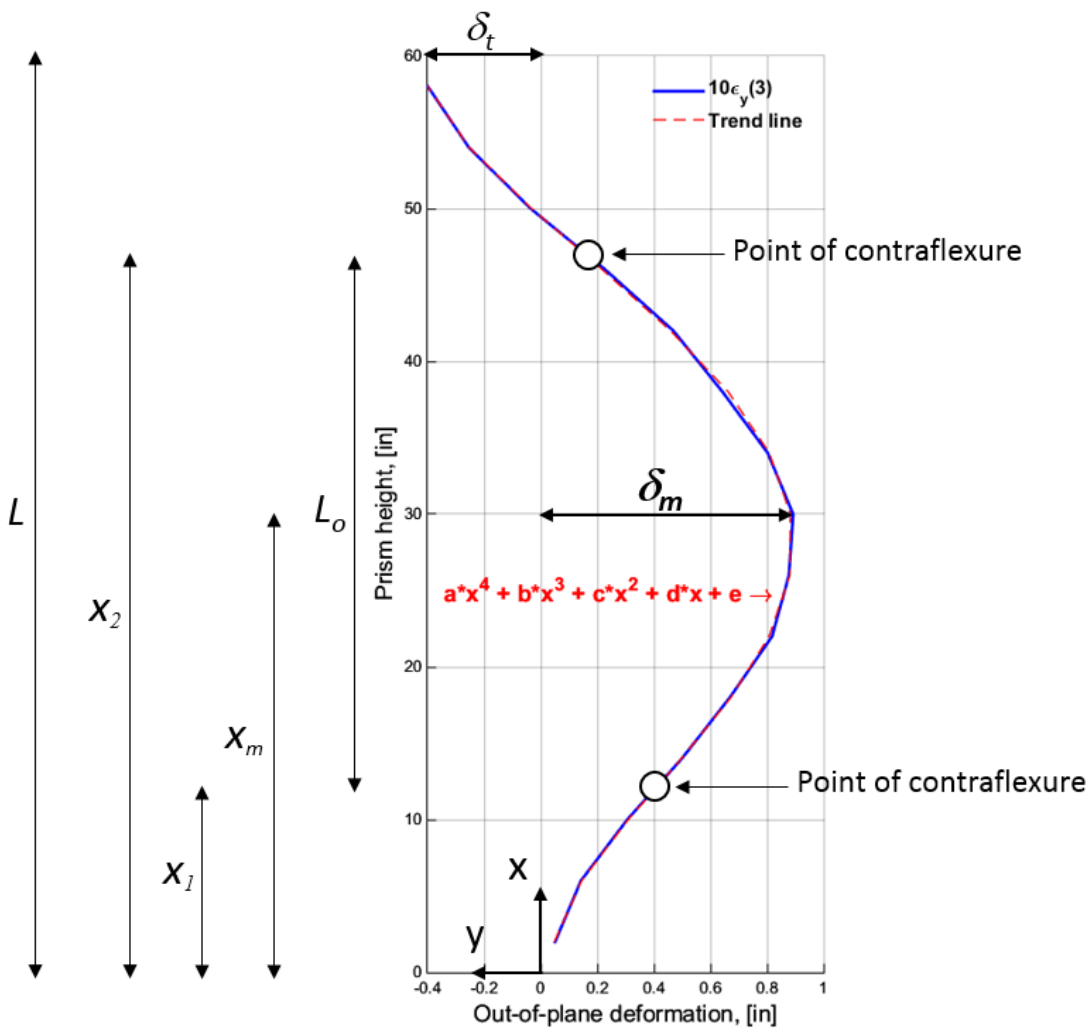

Figure 5-68. Buckled shape of Prism 2 during the $10\varepsilon_y(3)$ third cycle

5.2.3 Out-of-plane deformations vs. stability criteria

Relative out-of-plane deformations captured at midheight during different stages for each prism showed that buckling instability occurred once the stability criteria from Paulay & Priestley (1993) model, denoted as "Stability Limit", was exceeded. The out-of-plane deformations corresponding to the last cycle for each prism mainly depend on the compressive loads that were manually controlled once instability was detected. The following subsections present details about the out-of-plane deformations calculated through the three experimental phases.

5.2.3.1 Experimental Phase 1

Figure 5-69 displays relative out-of-plane deformations normalized to the thickness of the prisms from the six specimens tested during Phase 1. Notice that Prism 2, Prism 3, and Prism 5 started developing out-of-plane deformations at earlier stages compared with Prism 4 and Prism 6. Notice how the out-of-plane deformations continue increasing as more damage is accumulated in the buckled region even for similar demand cycles. All cases showed that buckling instability occurred once the "Stability Limit" and the predicted strain ratios from Paulay & Priestley (1993) "PP" and Chai & Elayer (1999) "CE" models, which were close to $10\varepsilon_y$, were exceeded. In the graph, the larger markers identify the buckling instability stage. The results demonstrated that the "Stability Limit" represents a reliable parameter to prevent out-of-plane instability of RCSW boundary elements with longitudinal reinforcement ratios around 3%.

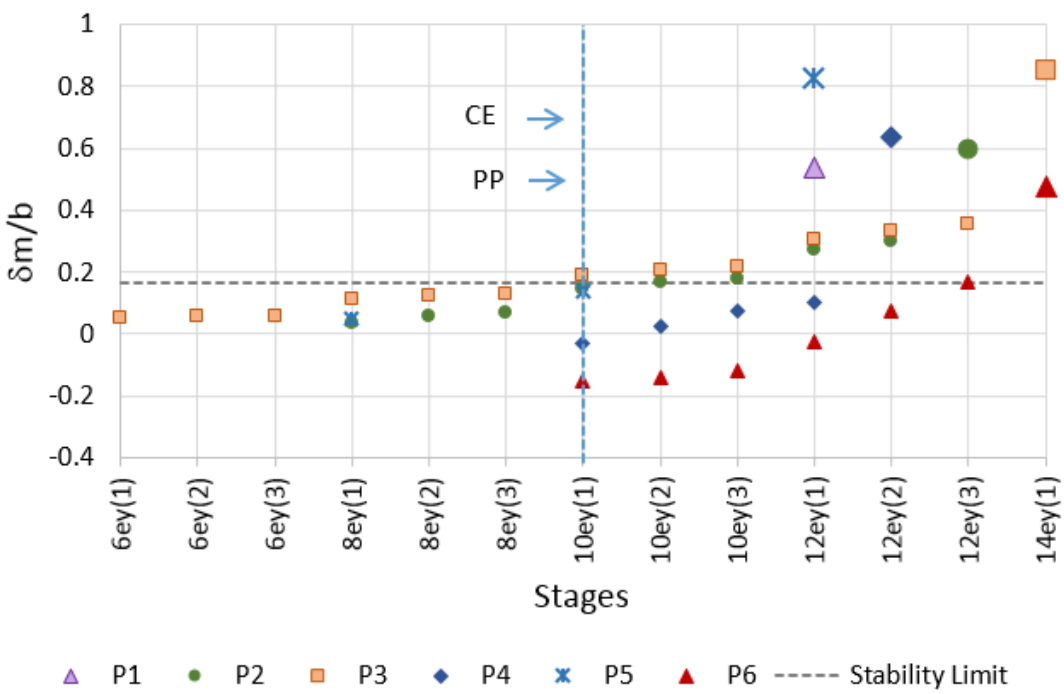

Figure 5-69. Phase 1: Maximum out-of-plane deformations captured at midheight

5.2.3.2 Experimental Phase 2

Figure 5-70 displays relative out-of-plane deformations normalized to the thickness of the prisms from the three specimens tested during Phase 2. Prism 8, which also contemplated an out-of-plane displacement equivalent to 4% drift, exhibited out-of-plane deformations at earlier stages compared with Prism 7, which was only subjected to cyclic axial loading. Out-of-plane deformations keep increasing as more damage is accumulated in the buckled region even for same level cycles. Due to the characteristics of the loading protocol followed by Prism 9, out-of-plane deformations appeared later. The three prisms showed that buckling instability occurred once the "Stability Limit" and the predicted strain ratios from Paulay & Priestley (1993) "PP" and Chai & Elayer (1999) "CE" models, which were close to $13\varepsilon_y$, were exceeded. In the graph, the larger markers identify the buckling instability stage. For longitudinal reinforcement ratios around 2%, the results demonstrated that the "Stability Limit" represents a reliable factor to prevent out-of-plane instability of RCSW boundary elements due to in-plane loading.

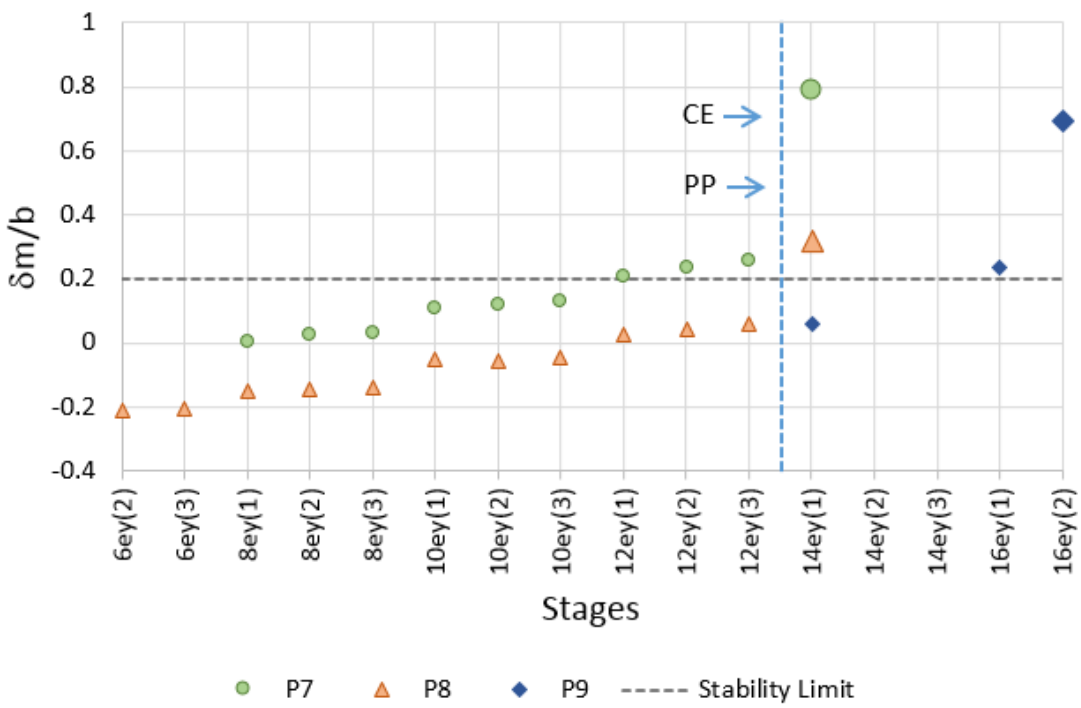

Figure 5-70. Phase 2: Maximum out-of-plane deformations captured at midheight

5.2.3.3 Experimental Phase 3

Figure 5-71 displays relative out-of-plane deformations normalized to the thickness of the prisms from the three specimens tested during Phase 3. Due to the characteristics of the loading protocol followed by Prism 12, out-of-plane deformations appeared at later stages compared with Prism 10 and Prism 11. Notice how out-of-plane deformations continue increasing as the tensile

demands increase. Prism 10 did not experienced buckling instability since bar fractured occurred at earlier stages. Prism 11 showed that buckling instability occurred once the "Stability Limit" and the predicted strain ratio from Paulay & Priestley (1993) "PP" model, which was close to $20\varepsilon_y$, were exceeded. Prism 12 showed that buckling instability occurred once the "Stability Limit" and the predicted strain ratio from Chai & Elayer (1999) "CE" model, which was close to $18\varepsilon_y$, were exceeded. The CE model demonstrated to be more conservative than the PE model. In the graph, the larger markers identify the buckling instability stage. Bar buckling and/or bar fracture could have influenced the onset of instability during Test 12.

The tests results demonstrated that the "Stability Limit" represents a reliable factor to prevent out-of-plane instability of walls boundary elements due to in-plane loading for longitudinal reinforcement ratios around 1%. However, since Phase 3 included three different axial loading protocols, it is noted that the onset of inelastic instability could also be affected by this parameter, which will be discussed in later sections.

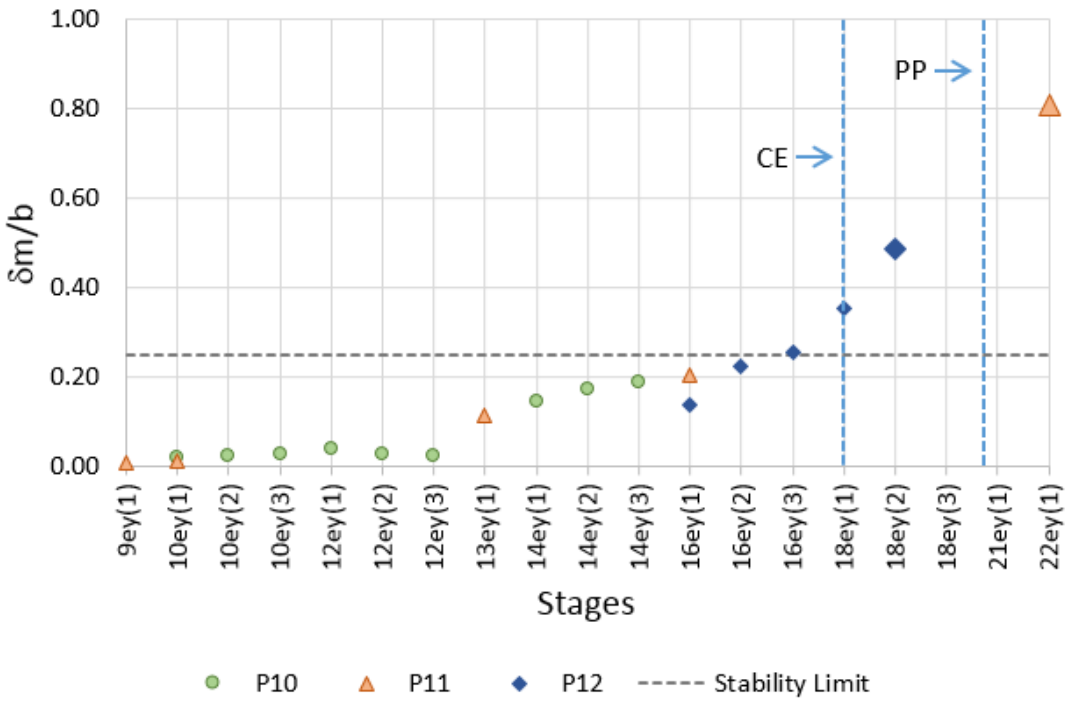

Figure 5-71. Phase 3: Maximum out-of-plane deformations captured at midheight

5.2.4 Longitudinal reinforcement ratio vs. maximum tensile demands

The results of the tests showed that the longitudinal reinforcement ratio ρ constitutes one of the most important parameters regarding the maximum tensile demands that boundary elements of RCSW could reached before instability develops under compressive loading. Figure 5-72 displays two limits for each longitudinal reinforcement ratio considered in the experimental program. The lower

and upper limit represent minimum and maximum tensile strains captured during the cycles when inelastic buckling occurred. Notice that smaller longitudinal reinforcement ratios close to 1.0% lead to higher tensile strains that result from higher in-plane displacements when RCSW are subjected to in-plane loading. This implies that boundary elements of RCSW that consider larger reinforcement ratios are prone to buckle at earlier stages with smaller in-plane displacements. This last statement suggests that strain levels should be limited through displacement or curvature ductility levels.

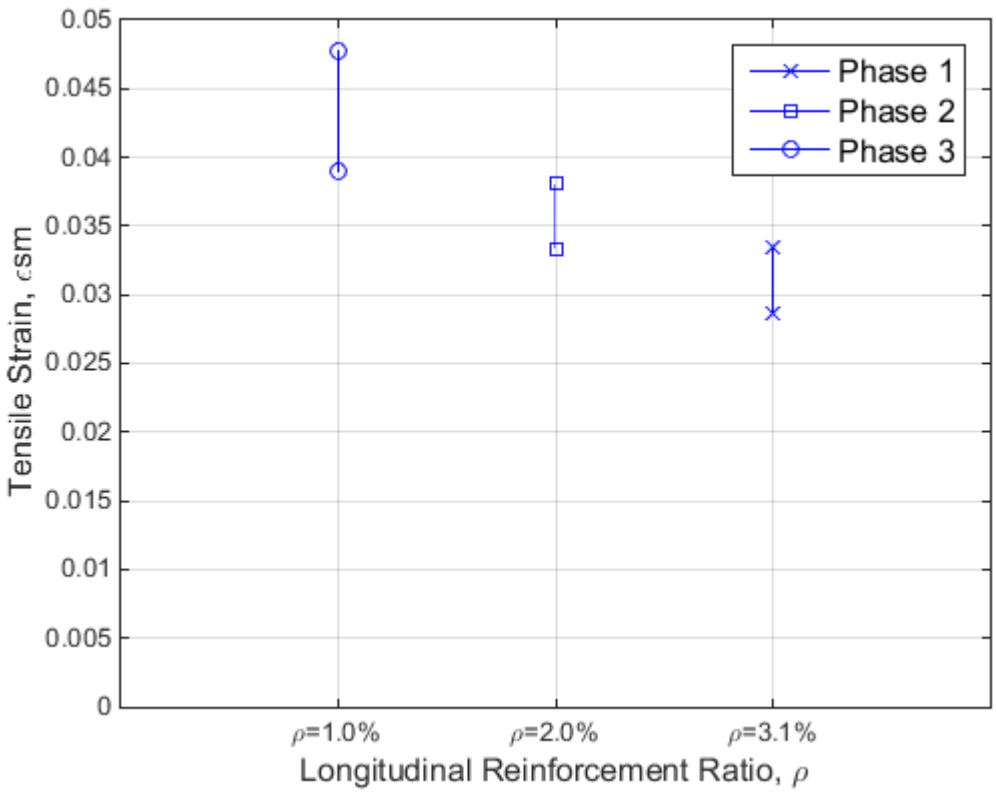

Figure 5-72. Maximum tensile strains influenced by longitudinal reinforcement ratios

5.2.5 Curvature distribution

The analysis covered in Section 5.2.2 constitutes the basis of the analysis conducted in this section. The buckled shape of the prisms follows a 4th degree polynomial function; subsequently, the curvature distribution could be expressed as the second derivative of the buckled shape for small deflections:

$$\phi(x) = \frac{d^2 y}{dx^2} = 12a \cdot x^2 + 6b \cdot x + 2c \tag{5-4}$$

In Section 5.2.2, it was demonstrated that the out-of-plane displacements slightly affect the tensile strain levels that lead to inelastic buckling. Subsequently, the coefficients *a*, *b*, and *c*, can be determined as a function of the maximum out-of-plane deformation δ_m, which is assumed to be located

at midheight for simplification, and the buckled region length L_o that resulted equal to $\left(1/\sqrt{3}\right)L$ when out-of-plane displacements are not included. Solving Equation (5-4) for *a*, *b*, and *c*, the maximum curvature ϕ_{max} can be obtained by Equation (5-8).

$$a = -\frac{\delta_m}{\left(\sqrt{3}/2 \cdot L_o\right)^4} \tag{5-5}$$

$$b = \frac{4\delta_m}{\left(\sqrt{3}/2 \cdot L_o\right)^3} \tag{5-6}$$

$$c = -\frac{4\delta_m}{\left(\sqrt{3}/2 \cdot L_o\right)^2} \tag{5-7}$$

$$\phi_{\max} = \frac{16}{3}\frac{\delta_m}{L_o^2} \tag{5-8}$$

From this last equation, the coefficient $(16/3)^{-1}$ identifies a quadratic curvature distribution, denoted from here on out as *c*, which is different from what Paulay & Priestley (1993) "PP" and Chai & Elayer (1999) "CE" models suggest. As already mentioned in Chapter 2, the PP model considers a constant curvature distribution with $c = 1/8$ and the CE model proposes a sinusoidal curvature distribution with $c = 1/\pi^2$. The coefficient *c* significantly affects the idealized hysteretic response of the longitudinal reinforcement of RCSW boundary elements, as it will be study in the next section.

5.2.6 Hysteretic response of longitudinal reinforcement

The idealized axial response of the prisms tested by Chai & Elayer (1999), was covered in Chapter 2, where three strain components were identified. Recalling these three components, ε_a* is the axial strain at first closure of cracks, ε_r is the strain required to yield the longitudinal reinforcement in compression, and ε_e accounts for the effect of strains elastically recovered during unloading. The current tests results showed that this hypothesis was valid; however, Section 5.2.5 recognized that the actual curvature distribution varies from what Chai & Elayer (1999) suggests. Consequently, the strain components would need to be accordingly adjusted as explained next.

The first strain component that accounts for the average of the axial strains at first closure of cracks, can be expressed in terms of the maximum curvature ϕ_{max}, determined at midheight, and the prism thickness b_w, as follows:

$$\varepsilon_a^* = 0.5 \cdot \phi_{\max} \cdot b_w \tag{5-9}$$

If Equation (5-8) is replaced in Equation (5-9), and the maximum out-of-plane displacement is normalized to the prism thickness ($\xi = \delta_m/b_w$), then ε_a* can be determined by

$$\varepsilon_a^* = \frac{8}{3}\left(\frac{b_w}{L_o}\right)^2 \xi \tag{5-10}$$

The cover crushing limit state identified by Chai & Elayer (1999), which will be recognized and quantified in the next section, suggests that ξ is fairly close to ξ_c, from the stability criteria established by Paulay & Priestley (1993), when the first crack closure occurs, and consequently ε_a* can be expressed as

$$\varepsilon_a^* = \frac{8}{3}\left(\frac{b_w}{L_o}\right)^2 \xi_c \tag{5-11}$$

Comparing this expression with the one suggested by Chai & Elayer (1999), it is noted that the only difference lies on coefficient 8/3, which is significantly less than $\pi^2/2$. This variation will affect the range for ε_r. In order to determine the functions that define the two remaining strain components, it is necessary to capture the axial response of the prisms tested during the current project. Figure 5-73 shows nominal axial strains plotted against axial forces captured at midheight from south and north faces in Prism 2. The maximum strains ε_{sm} and the strains ε_o where elastic recovery occurs for every cycle are identified in the graph through "x" and "o", respectively. Notice the different hysteretic response from the two data points, especially through the last cycle when instability occurred. When the buckling mechanism was rising during the test, the south face and the north face experienced tensile and compressive strains, respectively. Since the response in north face ended in the compression side, only the corresponding average of the three strain components from the last cycle are identified in Figure 5-73(b).

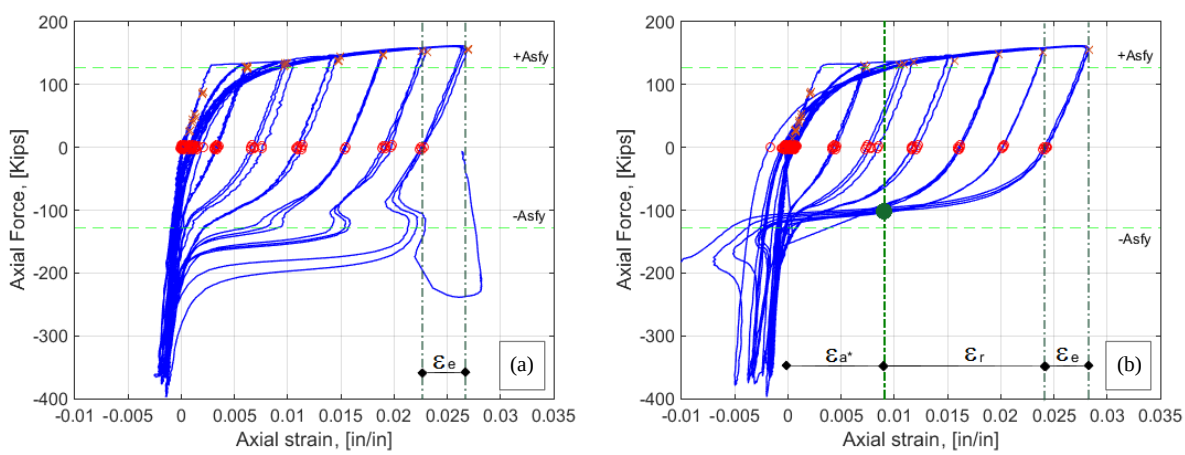

Figure 5-73. Axial Strain vs. Axial Load in Prism 2: a) south face and b) north face

The elastic recovery strain ε_e is obtained from $\varepsilon_e = \varepsilon_{sm} - \varepsilon_o$. Subsequently, the reloading strain ε_r can be determined subtracting the remaining strain components from ε_{sm}, i.e., as $\varepsilon_r = \varepsilon_{sm} - \varepsilon_e - \varepsilon_{a*}$. The rest of the specimens followed a similar procedure. Table 5-13 presents a summary of the average

of the strain components determined for all the prisms captured during the last cycles. Table 5-13 shows that ε_e and ε_r vary in ranges from 1.0 to 2.2 and 5.8 to 12.6, respectively. The data from Prism 10 are not considered to establish the range for ε_r, since it suffered from bar fracture at earlier stages.

Table 5-13. Tensile strain components

Phase	Prism	Face	ε_{sm}	$\varepsilon_{sm}/\varepsilon_y$	ε_o	$\varepsilon_e/\varepsilon_y$	$\varepsilon_a^*/\varepsilon_y$	$\varepsilon_r/\varepsilon_y$
1	1	South	0.02750	12.0	0.02475	1.7	3.8	6.6
		North	0.03051	12.8	0.02585	2.0		7.0
	2	South	0.02699	11.3	0.02283	1.7	3.8	5.8
		North	0.02835	11.9	0.02424	1.7		6.4
	3	South	0.02970	12.4	0.02608	1.5	3.8	7.1
		North	0.03233	13.5	0.02808	1.8		8.0
	4	South	0.02885	12.1	0.02458	1.8	3.8	6.5
		North	0.02754	11.5	0.02376	1.6		6.2
	5	South	0.02740	11.5	0.02470	1.1	3.8	6.6
		North	0.02755	11.5	0.02513	1.0		6.7
	6	South	0.03227	13.5	0.02769	1.9	3.8	7.8
		North	0.03506	14.7	0.03134	1.6		9.3
2	7	South	0.03252	13.6	0.02919	1.4	4.6	7.6
		North	0.03308	13.9	0.02947	1.5		7.8
	8	South	0.03273	13.7	0.02891	1.6	4.6	7.5
		North	0.03168	13.3	0.02821	1.5		7.2
	9	South	0.03666	15.4	0.03255	1.7	4.6	9.1
		North	0.03715	15.6	0.03353	1.5		9.5
3	10	South	0.03160	14.6	0.02790	1.7	7.7	5.2
		North	0.02953	13.6	0.02628	1.5		4.4
	11	South	0.04880	22.5	0.04407	2.2	7.7	12.6
		North	0.04784	15.4	0.04334	2.1		12.3
	12	South	0.04509	20.8	0.04028	2.2	7.7	10.9
		North	0.03861	17.8	0.03421	2.0		8.1

In the case of Chai & Elayer (1999) model, ε_{a*} is higher than ε_r, however Table 5-13 suggests that ε_r is higher than ε_{a*}, which is a fact reflected in the hysteric response depicted in Figure 5-73. The hysteretic response of the prisms suggests that higher longitudinal reinforcement contents require lower reloading strains ε_r, and subsequently it should be defined as a function of the longitudinal reinforcement ratio ρ.

5.2.7 Crushing limit state

According to the experimental study conducted by Chai & Elayer (1999), the onset of inelastic buckling is accompanied by concrete cover crushing and spalling developed in the buckled region

where the maximum out-of-plane deformation is located. This fact was also detected specially during the experimental Phase 1 and Phase 2, when the prisms failed due to pure buckling instability. Since concrete cover crushing corresponds to an additional limit state that can be used through analytical modeling to predict the onset of out-of-plane instability, a more detailed analysis is addressed in this section to determine a performance criteria limit.

Prism 2, Prism 7 and Prism 8 were considered to conduct this analysis. Table 5-14 shows concrete cover strains calculated during the corresponding final cycles, based on the longitudinal reinforcement strains captured at midheight, where the maximum out-of-plane deformations occurred. Notice that the minimum value is slightly larger than 0.004. In accordance with the literature (Paulay & Priestley, 1992), the instant at which unconfined concrete crushing begins would be 0.004, which has been widely accepted by other researchers. This value coincides with the minimum observed from Table 5-14. Consequently, it will be considered during the analytical study as a strain limit associated with cover concrete crushing damage state.

Table 5-14. Concrete cover strain

Prism	Steel Strain 1	Steel Strain 2	Cover strain
2	0.0228	-0.0062	-0.0088
7	0.0290	-0.0019	-0.0055
8	0.0272	-0.0008	-0.0041

5.2.8 Axial loading paths

A total of three axial loading protocols were applied along the experimental program. The cyclic loading and the megathrust-type earthquake protocols led to a similar structural response and the inelastic buckling mechanism occurred when it was expected. The buckled region continued accumulating more damage under compressive loading as tensile strains progressively increased. The out-of-plane deformations also followed the same pattern.

However, the high pulse-type earthquake protocol suggested that higher tensile demands could be reached before a boundary element undergoes buckling instability. An important fact to notice regarding this specific type of protocol applied to actual structural walls is that successive severe strong motions could lead to buckling instability in a long term. Consequently, in the aftermath of a severe earthquake, rapid Direct Displacement-Based Assessment procedures could be required to ensure the stability of a structural wall during a possible subsequent seismic event.

5.2.9 ACI 318-14 transverse reinforcement spacing for boundary elements

The ACI 318-14 (18.10.6.4), specifies that the transverse reinforcement spacing in boundary elements should be limited by the smallest of one-third of the minimum dimension of the boundary element or six times the diameter of the smallest longitudinal bar d_{bl}. The three phases contemplated a spacing equal to 2in. (51mm), which represents one-third of the prism thickness, including the cover. Regarding the recommendation related to d_{bl}, Phase 1 and Phase 2 comprised a transverse reinforcement spacing equal to $3.2d_{bl}$ and $4d_{bl}$, respectively, and Phase 3 involved a spacing equal to $5.3d_{bl}$.

Neither bar buckling not bar fracture were detected during the first two phases. However, through Phase 3, the six longitudinal bars from the three prisms experienced bar buckling all along the height of the prisms. For the cases of Prism 10 and Prism 12, this failure mode led to bar fracture upon higher tensile demands. These results suggest that the transverse reinforcement spacing limits stablished in the ACI 318-14 (18.10.6.4) should be revised in order to prevent bar buckling. In accordance with the current experimental results, the transverse reinforcement spacing limit associated with d_{bl}, should be reduced from $6d_{bl}$ to $4d_{bl}$.

5.2.10 Experimental program: Concluding remarks

Based on the experimental results and the analyses presented in previous sections, the following observations constitute the basis of the parametric study conducted in Chapter 6:

1. The onset of instability is slightly affected by the combination of axial cyclic displacements and lateral out-of-plane displacements.
2. The fixed end conditions implemented within the experimental program revealed that the buckled shape of the prisms follows a 4th degree polynomial function and consequently the curvature would be better characterized by a quadratic distribution.
3. The stability criteria developed by Paulay & Priestley (1993) represent a conservative but reliable condition to prevent out-of-plane instability of wall boundary elements due to in-plane loading.
4. Boundary elements of RCSW that consider larger longitudinal reinforcement ratios are prone to buckle at earlier stages with smaller in-plane displacements. Consequently, tensile strains should be limited through displacement or curvature ductility levels.
5. The functions that define the hysteretic response of boundary elements, which account for tensile strain components, should be adjusted to reflect more precisely the effect of different longitudinal reinforcement ratios.

6. Concrete cover crushing limit state, established at 0.004 strain, accompanies the onset of inelastic buckling originated in the buckled region where the maximum out-of-plane deformation develops.
7. The cyclic loading and the megathrust-type earthquake protocols led to a similar structural response. The high pulse-type earthquake protocol suggests that higher tensile demands could be reached before buckling instability occurs.
8. The possibility of successive severe earthquakes, suggests that rapid Direct Displacement-Based Assessment procedures could be required after the first earthquake strikes to guarantee that a structural wall remains stable during a next seismic event.
9. The ACI 318-14 (18.10.6.4) transverse reinforcement spacing limit associated with the bar diameter of the longitudinal reinforcement d_{bl}, should be reduced from $6d_{bl}$ to $4d_{bl}$ in order to prevent bar buckling.

CHAPTER 6: ANALYTICAL STUDY

This chapter summarizes the calibration and validation of a fiber-based numerical model considering the experimental outcomes. In addition, Chapter 6 describes the results of the parametric study conducted on several RC prisms simulating boundary elements of RCSW.

6.1 Numerical model

Non-linear static time-history analyses are conducted using SeismoStruct 2016, a fiber-based Finite Element (FE) package capable of predicting the structural response of space frames elements, accounting for geometric nonlinearities and material inelasticity (Seismosoft Ltd., 2014). A force-based (FB) formulation was implemented over a more common displacement-based (DB) formulation. Both approaches form part of the distributed plasticity models that allow the spread of inelasticity along the member length throughout different monitoring sections.

In accordance with Almeida et al. (2014) and D'Aniello et al. (2010) the FB formulation has proven to be numerically robust and reliable, as it always provides an exact solution for frame elements since it is independent from material constitutive behavior. This latter feature exposes the feasibility of an FB approach to conduct nonlinear analysis. In addition, only a single FE could be required to represent an entire structural member, and consequently, no meshing is necessary.

SeismoStruct uses an optimized Gauss-Lobatto distribution as numerical integration method, which comprises at least one control point at each end of a member. Figure 6-1 illustrates an example of a typical RC cross-section discretization. The numerical model considered during this study was refined through six FE that represent a fixed-fixed RC boundary element. Since high levels of inelasticity were expected, 200 section fibers and 4 integration sections were adopted.

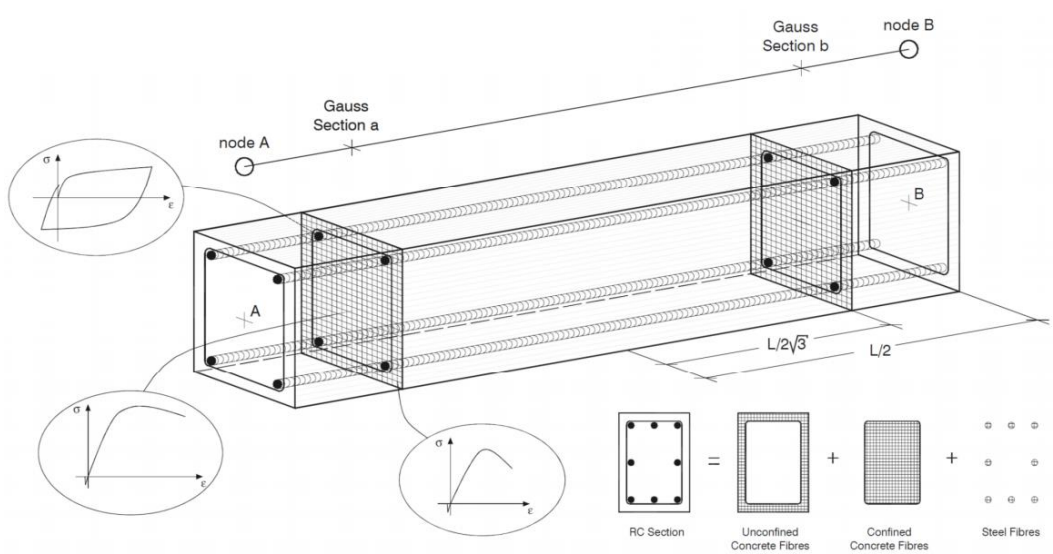

Figure 6-1. Discretization of a typical RC cross-section. (Seismosoft Ltd., 2014)

6.1.1 Reinforcing steel model

SeismoStruct considers four different material models to characterize the cyclic behavior of reinforcing steel. For this study, the Menegotto-Pinto steel model (stl_mp) was adopted, which is based on the stress-strain relationship developed by Menegotto and Pinto (1973) and the isotropic hardening rules proposed by Filippou et al. (1983). Table 6-1 shows the proposed calibration parameters that define the mechanical characteristics of the longitudinal and transverse reinforcement based on the structural response of 12 specimens tested during the experimental phase.

Table 6-1. Reinforcement steel: Material model parameters

Parameter	R_o	a_1	a_2	a_3	a_4
Value	20.0	18.0	0.15	0.025	2.0

The parameter R_o controls the shape of the transition curve between initial and post-yield stiffness. It accounts for Bauschinger effects and pinching of the hysteretic loops. Coefficients a_1 and a_2 calibrate the changes of R_o to capture the updated curvature parameter R_n (Seismosoft Ltd., 2014). Coefficients a_3 and a_4 define the degree to which isotropic hardening is included in the material stress-strain response. Figure 6-2 and Figure 6-3 show the stress-strain cyclic response of the Menegotto-Pinto model and the definition of the curvature parameter $R(\xi)$, respectively.

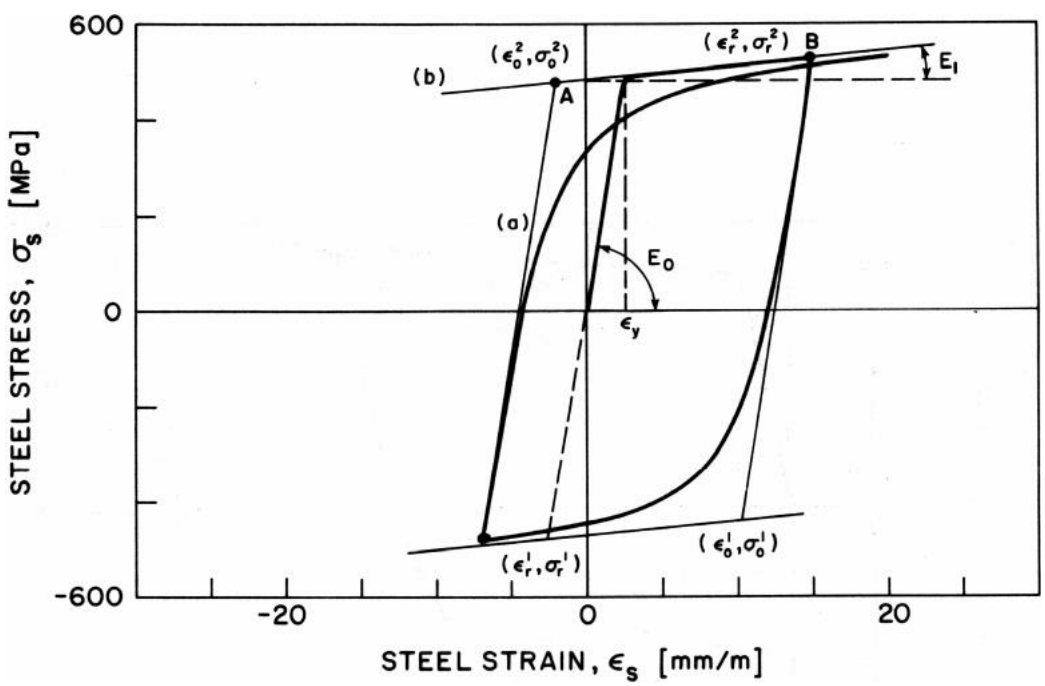

Figure 6-2. Menegotto-Pinto Steel Model. (Yu, 2006)

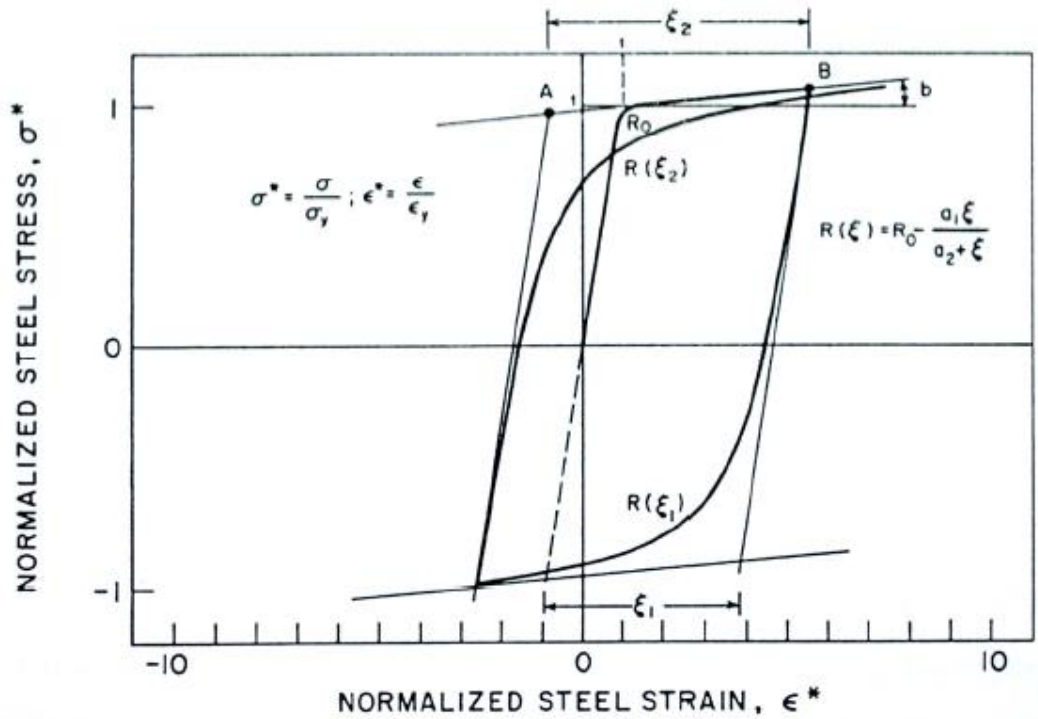

Figure 6-3. Definition of the curvature parameter *R (ξ)* in Menegotto-Pinto Steel Model. (Yu, 2006)

6.1.2 Concrete model

The Mander et al. nonlinear concrete model (*con_ma*) was adopted over three additional models defined in SeismoStruct. This uniaxial nonlinear constant confinement model follows the constitutive rule proposed by Mander et al. (1988), shown in Figure 6-4, and the cyclic laws suggested by Martínez-Rueda & Elnashai (1997). The confinement factors were determined automatically through the section characteristics considering stirrups closed at 135˚.

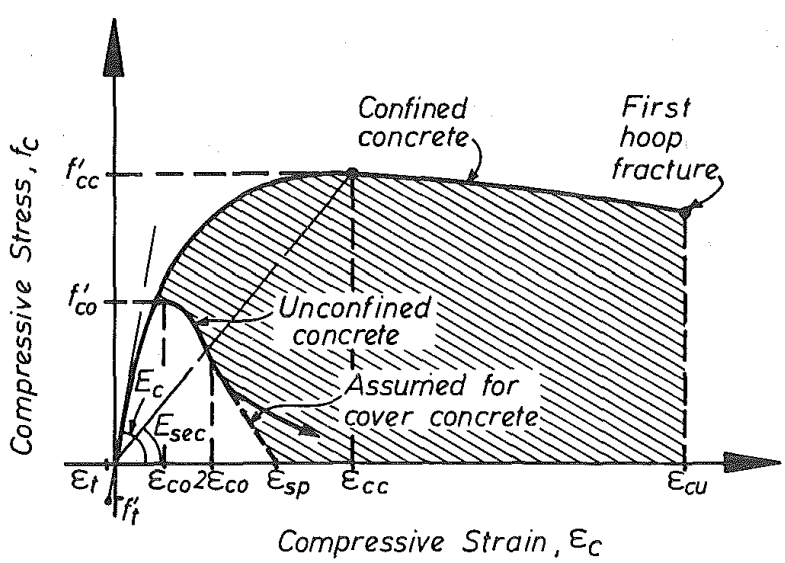

Figure 6-4. Stress-Strain model for monotonic loading of confined and unconfined concrete. (Mander et al., 1988)

6.1.3 Performance criteria

SeismoStruct is capable of monitoring different performance limit states (e.g. yielding of steel, fracture of steel, spalling of concrete). The limit state associated with out-of-plane buckling instability is concrete cover crushing, in accordance with the analysis described in Chapter 5. Consequently, the numerical model considers a value equal to -0.004 as performance criterion, and once this value is recognized in the fibers representing the concrete cover along the buckled region upon compressive loading, the analysis is automatically paused.

6.2 Validation: experimental results vs. numerical model

In order to calibrate and subsequently validate the numerical model, the axial hysteretic response of the 12 specimens tested during the experimental program, is considered as the main monitoring pattern in combination with the buckled shape. Displacements and loads in the axial direction represent the hysteretic curves. The experimental axial displacements of each prism were determined from the 3D coordinates of the first and last LED infrared sensors attached to the reinforcement line located in the southwest corner since the reported data from these sensors proved to be consistent all along the tests. Figure 6-5 illustrates the location of the aforementioned LED infrared sensors.

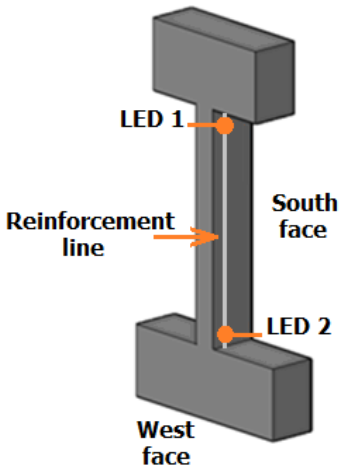

Figure 6-5. Reference data points to calculate axial deformations from the tested prisms

The numerical models simulating the 12 prisms included the same corresponding experimental loading protocols. The compressive targets were controlled through displacements equivalent to the effect of the experimental axial compressive loads. The mechanical material properties adopted for each phase are summarized in Table 6-2. The parameters and criteria described in the preceding section are adopted in the computational model. A thickness cover equal to 1/4in. (6.4mm) was assumed for the 12 prisms in accordance with what was observed in the experimental phase. Figure 6-6 shows a typical cross section captured from the SeismoStruct interface.

Table 6-2. Numerical model: Material mechanical properties

Prisms	Concrete strength		Reinforcement Steel		
	f'_c (compression) ksi (MPa)	f_t (tension) ksi (MPa)	E_s ksi (GPa)	f_y ksi (MPa)	ε_y in/in (mm/mm)
P1, P2, P3, P4, P5, P6	7.10 (49.0)	0.50 (3.4)		69.3 (478.0)	0.00239
P7, P8, P9	7.00 (48.3)	0.50 (3.4)	29,000 (200)	69.1 (476.0)	0.00238
P10, P11, P12	6.30 (43.4)	0.48 (3.3)		62.9 (434.0)	0.00217

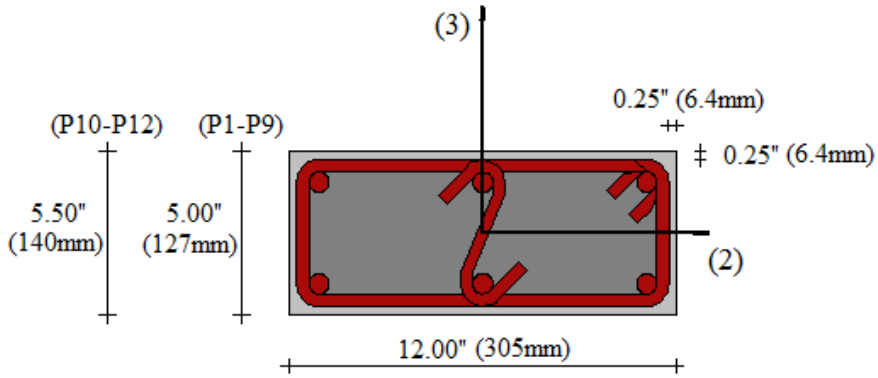

Figure 6-6. Numerical model: Typical cross section

6.2.1 Hysteretic response

Figure 6-7 shows an acceptable agreement between the experimental response and the computed response of the prisms from Phase 1. A slight discrepancy is detected in the compressive side during the cycles associated with higher tensile demands for Prism 2 and Prism 3, where the out-of-plane lateral displacements are small. However, the general response is not affected since the numerical model is capable to accurately capture the maximum tensile strains that the prisms are able to sustain before buckling instability is recognized under compressive loading. Table 6-3 depicts gross experimental and maximum tensile strains from the models normalized to the yielding strain corresponding to Phase 1.

Figure 6-8 also illustrates a satisfactory agreement between the experimental response and the modeling response of the prisms from Phase 2. The response of the Prism 7 model, which considered an insignificant out-of-plane lateral displacement, reported a different performance in the compressive side during the cycles related to higher tensile strains. Nevertheless, in general the numerical models representing the three prisms are capable to accurately predict the maximum tensile strains that cause out-of-plane buckling instability under compressive loading. Table 6-4 compares the gross experimental and the maximum tensile strains from the models normalized to the yielding strain corresponding to Phase 2.

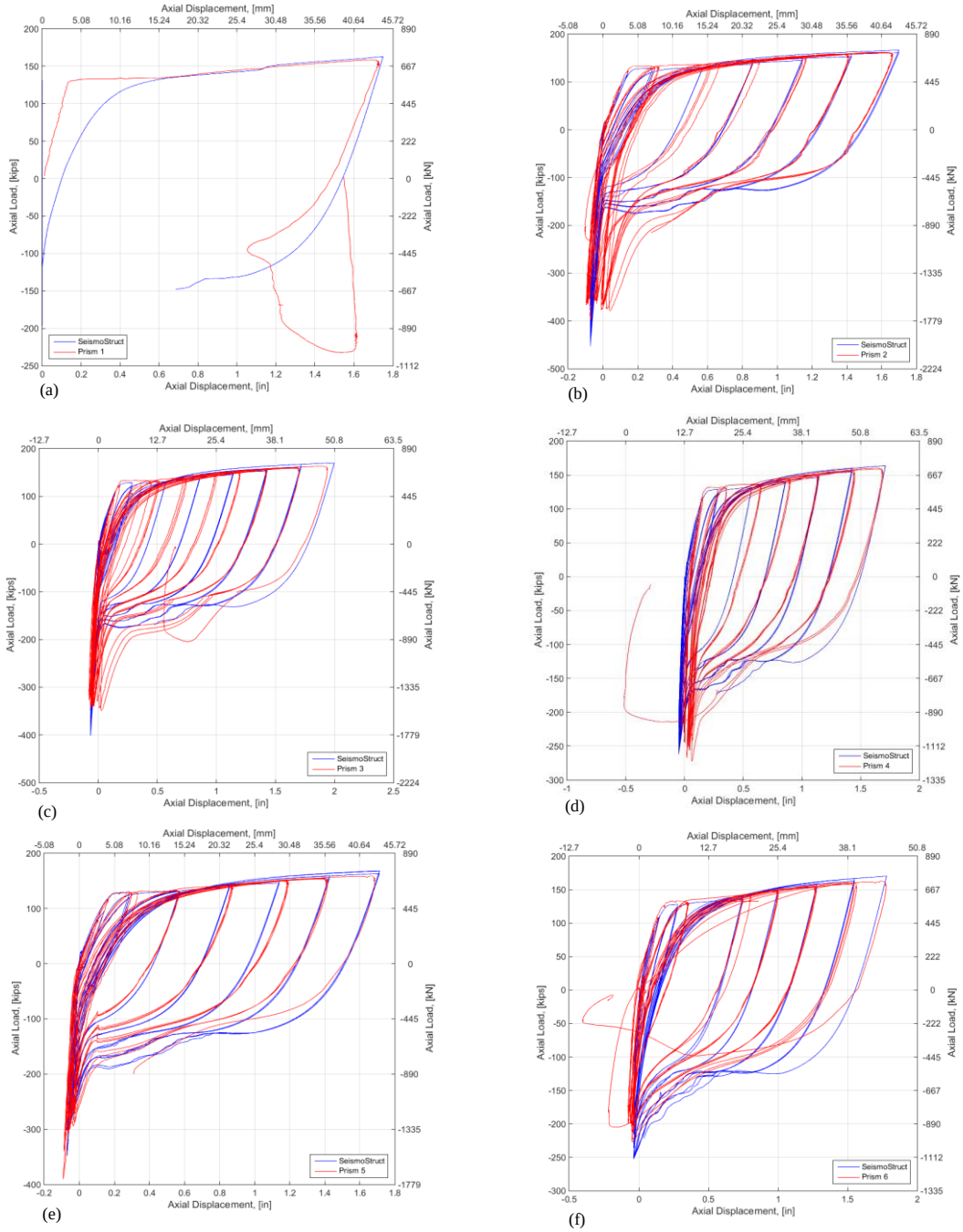

Figure 6-7. Phase 1: Experimental and Numerical Hysteretic Curves

Table 6-3. Phase 1: Maximum normalized tensile strains captured before buckling instability

Prism	$\varepsilon_{smax}/\varepsilon_y$ – Experiment, (1)	$\varepsilon_{smax}/\varepsilon_y$ – Num. model, (2)	(1)/(2)
1	12	12	1
2	12	12	1
3	14	14	1
4	12	12	1
5	12	12	1
6	12	12	1

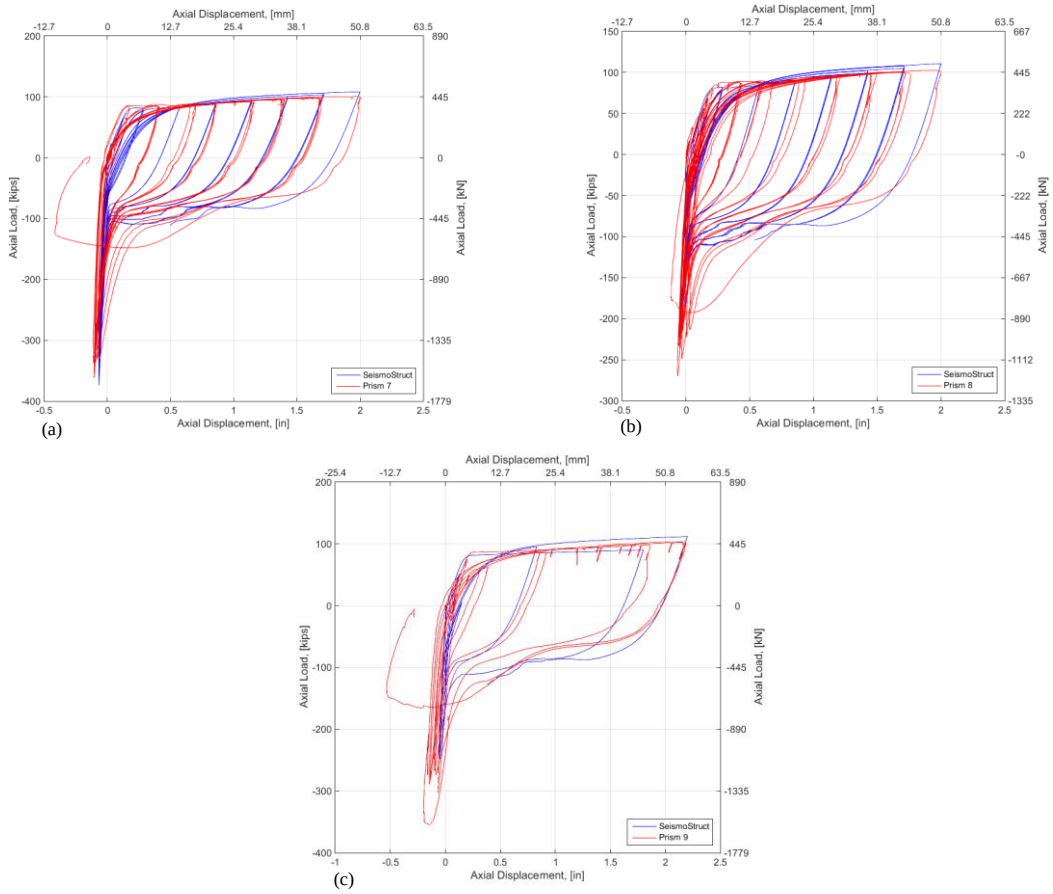

Figure 6-8. Phase 2: Experimental and Numerical Hysteretic Curves

Table 6-4. Phase 3: Maximum normalized tensile strains captured before buckling instability

Prism	$\varepsilon_{smax}/\varepsilon_y$ – Experiment, (1)	$\varepsilon_{smax}/\varepsilon_y$ – Num. model, (2)	(1)/(2)
7	14	14	1
8	14	14	1
9	16	16	1

The experimental response and the numerical response of the prisms from Phase 3 show a relatively acceptable agreement. Prism 10 exhibited bar buckling and bar fracture at early stages during the test before buckling instability was developed, which justifies the difference observed in Figure 6-9(a). Figure 6-9(b) shows that the numerical model that idealizes Prism 11 is capable to capture the maximum tensile strains that lead to out-of-plane buckling instability under compressive loading, even though this specimen experienced bar buckling. During the test, Prism 12 exhibited bar buckling and bar fracture failure modes before developing buckling instability and consequently, the numerical model reports higher tensile strains before buckling instability is captured. Table 6-5 presents gross experimental and numerical maximum tensile strains normalized to the yielding strain corresponding to Phase 3.

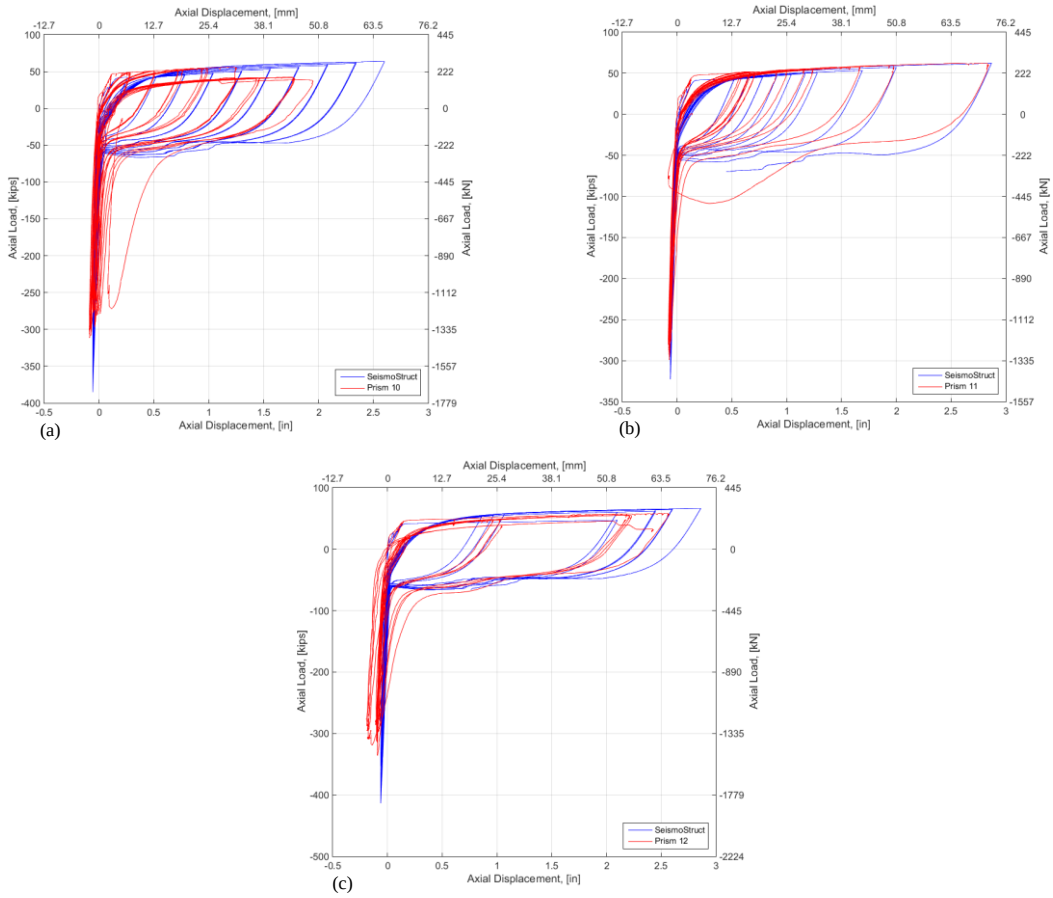

Figure 6-9. Phase 3: Experimental and Numerical Hysteretic Curves

Table 6-5. Phase 3: Maximum normalized tensile strains captured before buckling instability

Prism	$\varepsilon_{smax}/\varepsilon_y$ – Experiment, (1)	$\varepsilon_{smax}/\varepsilon_y$ – Num. model (2)	(1)/(2)
10	-	20	-
11	22	22	1
12	18	22	0.9

6.2.2 Structural performance

Figure 6-10 shows five stages captured from the numerical model simulating Prism 2. The four central elements were selected to monitor three different limit states associated with longitudinal reinforcement tensile strains and concrete cover compressive strains. Figure 6-10(a) represents the stage where steel yielding limit state is recognized upon tensile loading. Figure 6-10(b) shows the first time when the out-of-plane buckling mechanism is exhibited upon compressive loading. Figure 6-10(c) shows the stage when the prism returns from position (b) to a straight position at the time the maximum compressive displacement is applied. Figure 6-10(d) shows the time when the limit state that characterizes the maximum tensile strains predicted from Paulay & Priestley (1993) and Chai & Elayer (1999) models are reached. Figure 6-10(e) illustrates the phase where concrete cover crushing

is recognized. Overall, the generic numerical model proved to be accurate when identifying the strain limit states during the expected stages for the 12 prisms.

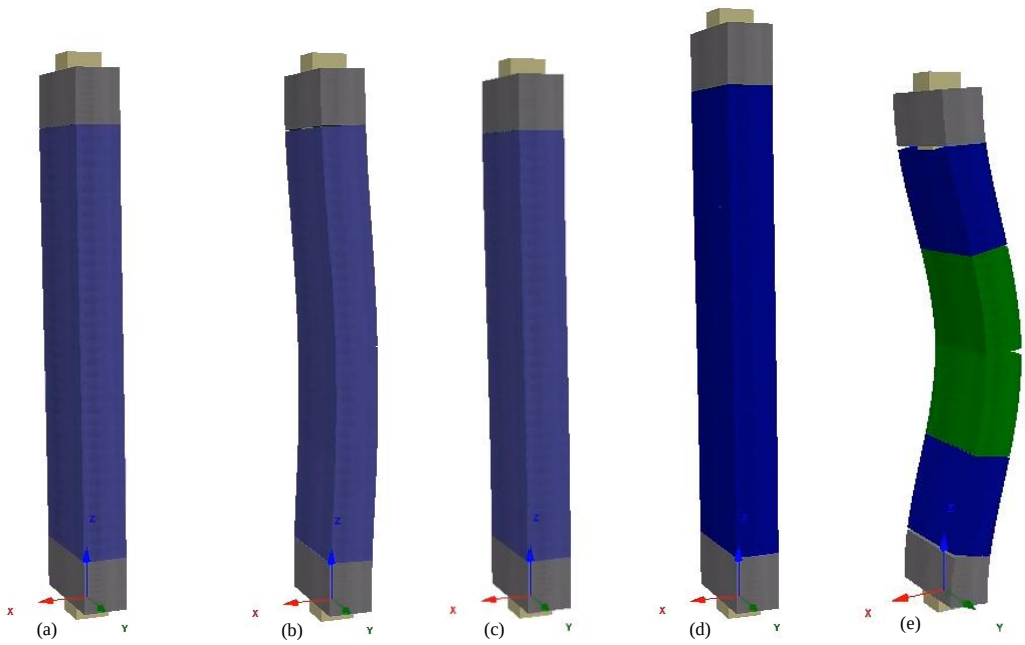

Figure 6-10. Stages captured from the SeismoStruct interface

The experimental results showed that if the axial tensile strains continue increasing or more damage is accumulated through similar tensile demands, out-of-plane deformations continue growing until buckling instability develops upon compressive loading. The increment of flexibility directly related to the tensile demands is also captured through the numerical model. This constitutes an additional parameter that supports the validation of the fiber-based model implemented through SeismoStruct.

6.2.3 Out-of-plane deformations

Stable experimental out-of-plane deformations δm_e normalized to out-of-plane deformations from the numerical model δm_c are presented in Figure 6-11. The horizontal axis represents the target tensile strains at each cycle where a buckled shape formed upon compressive loading. The out-of-plane deformations are captured at midheight on each corresponding prism from Phase 1. Due to the characteristics of the loading protocol induced to Prism 1, where only one axial cycle was applied, its results are excluded from this comparison.

In general, the numerical model overestimates the deformations during the cycles where the out-of-plane buckling mechanism starts to develop. Conversely, the out-of-plane deformations are underestimated in the cycles close to the stage where instability is exhibited. However, this difference

results irrelevant since the onset of inelastic buckling occurs in the expected stages once the numerical model recognizes the concrete cover crushing performance criterion upon compressive loading.

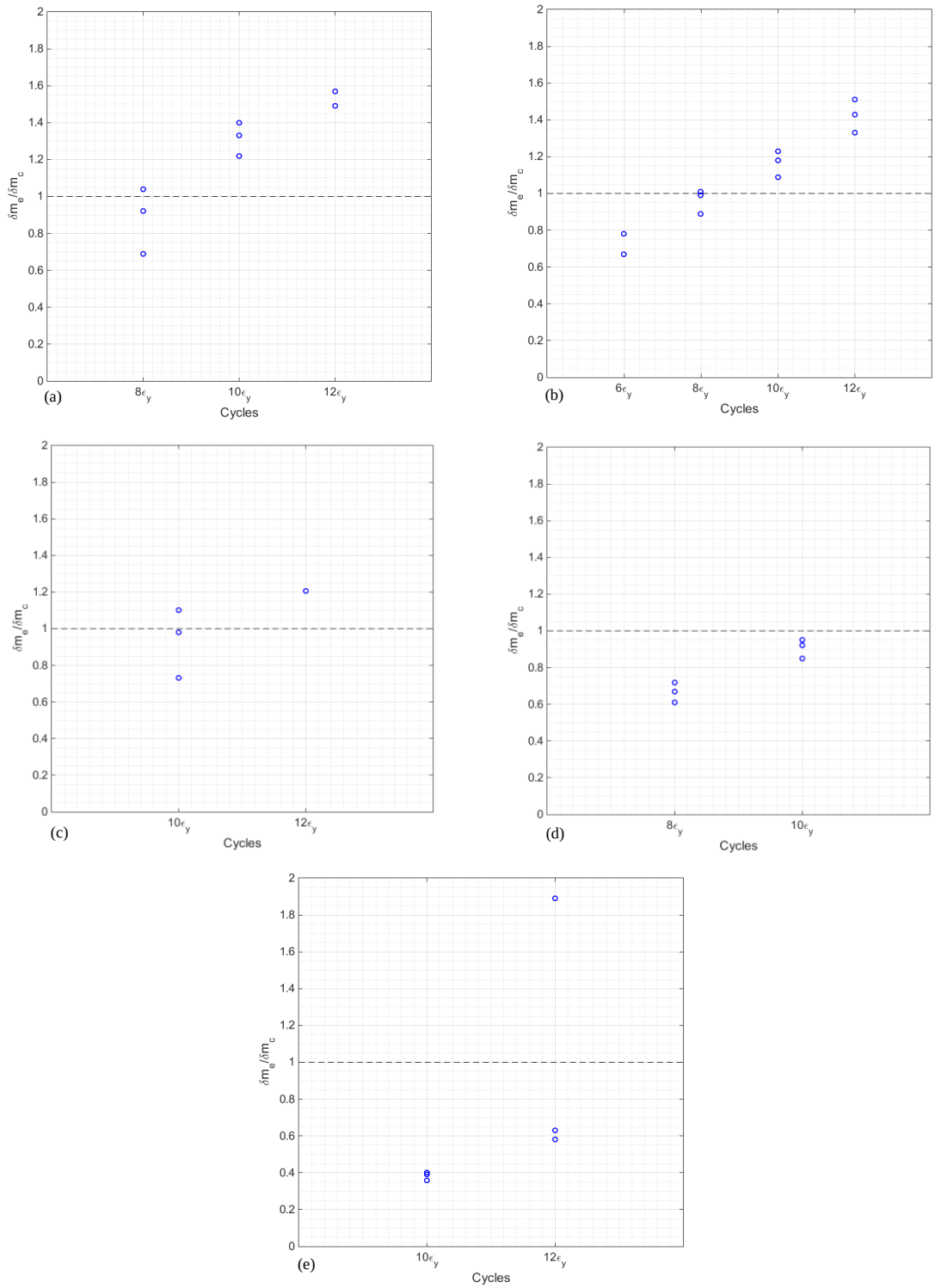

Figure 6-11. Phase 1: Experimental vs. Computed out-of-plane deformations; (a) Prism 2, (b) Prism 3, (c) Prism 4, (d) Prism 5, (e) Prism 6

The observations described for Phase 1 apply to the response from the prisms representing Phase 2 and Phase 3, as shown in Figure 6-12 and Figure 6-13, respectively. Even though Prism 10 did not experience buckling instability, it is possible to compare the out-of-plane deformations during stable cycles. Prism 9 and Prism 12 only exhibit out-of-plane deformations at higher tensile cycles compared to their counterparts due to the characteristics of the loading protocol, which is based on a high-pulse type earthquake.

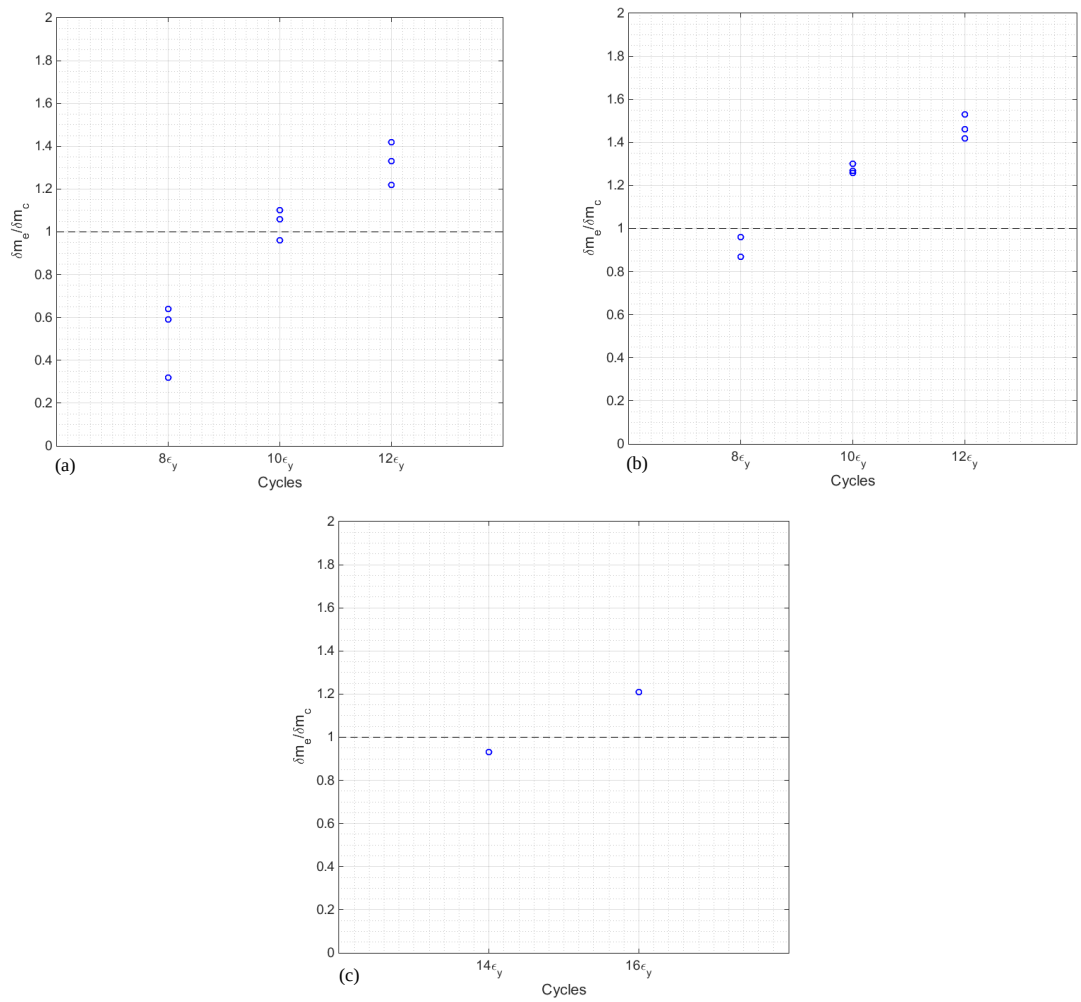

Figure 6-12. Phase 2: Experimental vs. Computed out-of-plane deformations; (a) Prism 7, (b) Prism 8, (c) Prism 9

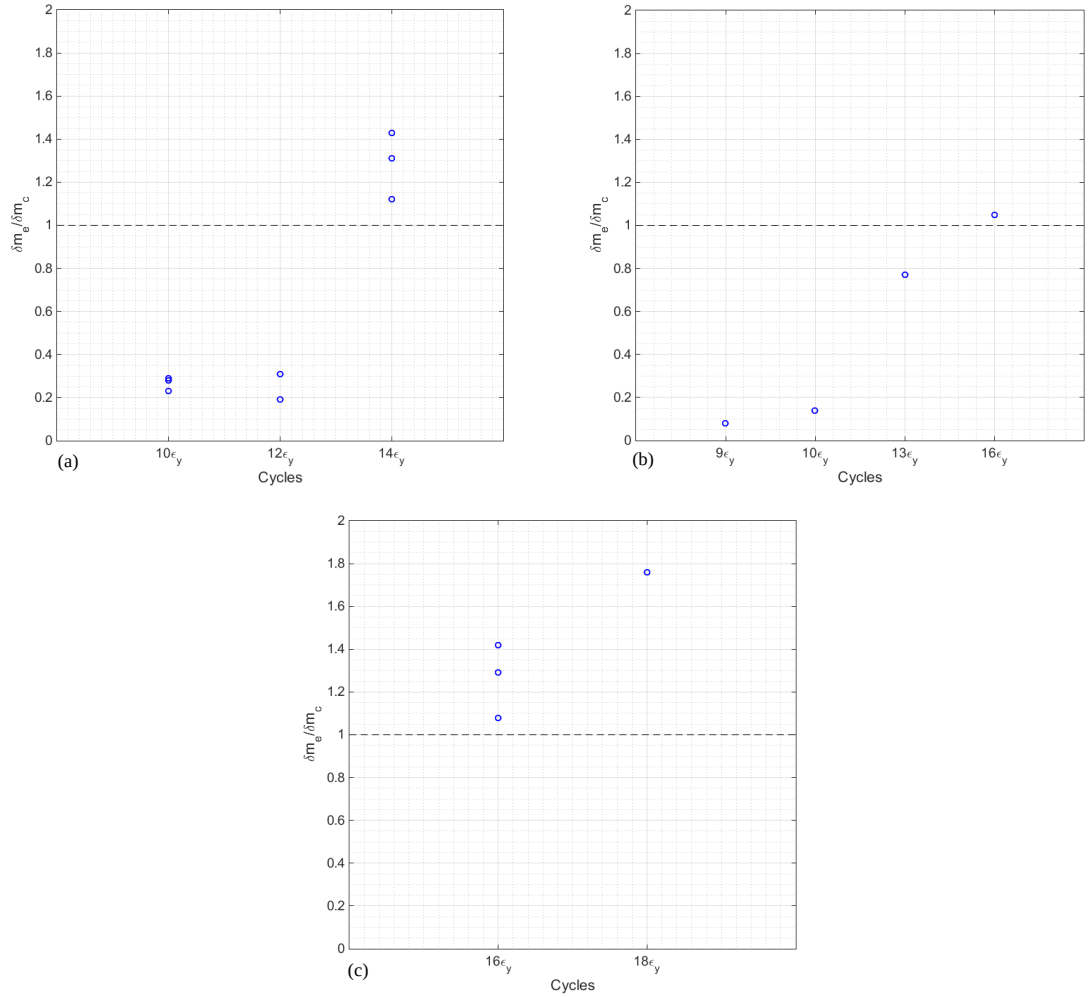

Figure 6-13. Phase 3: Experimental vs. Computed out-of-plane deformations; (a) Prism 10, (b) Prism 11, (c) Prism 12

6.2.4 Numerical model validation: Concluding remarks

The results from the numerical models showed an acceptable agreement with the experimental results. In general, the following observations validate the numerical model implemented through SeismoStruct, which constitutes a powerful tool to develop the parametric study detailed next.

- The maximum experimental tensile strains that caused out-of-plane buckling instability under compressive loading are accurately captured through the numerical model.
- The limit state associated with cover concrete crushing defined through the performance criteria interface from SeismoStruct, detects the onset of out-of-plane buckling instability in the same cycles where this failure mode was detected during the experimental program.
- Even though the comparison of the experimental and numerical out-of-plane deformations showed an important disagreement, the onset of buckling instability is not altered.
- The experimental results showed that as tensile demands increase, the flexural rigidity decreases, which was also captured through the numerical model.

6.3 Parametric study

The parametric study conducted on structural walls by Herrick & Kowalsky (2016) demonstrated that the wall geometry and the longitudinal reinforcement ratio are the most critical parameters that influence the onset of out-of-plane buckling instability of planar reinforced concrete structural walls due to in-plane loading. The results from the experiments carried on the current study corroborated that the longitudinal steel content highly affects the stability of boundary elements in a wall. In addition, both studies proved that the predictions from the Paulay & Priestley (1993) and Chai & Elayer (1999) models approximately capture the maximum tensile strains that cause buckling instability. However, the strain components identified by Chai & Elayer (1999) that describe the hysteric response of wall end regions, showed disagreement regarding the strains at first crack closure based on the current experimental results, as explained in Chapter 5. Adjustments are suggested to account for the identified issue and consequently, the numerical model described and validated in previous sections is used to conduct a parametric study to encompass the hysteretic response of representative cases considering the effect of critical parameters.

Through this section, the structural performance of 180 RC prisms simulating boundary elements of RCSW is analyzed. The parametric study involves the most influential factors corresponding to wall geometry and reinforcement ratio. Out-of-plane displacements are omitted from the study, since in accordance with the experimental results this parameter is inconsequential for the onset of buckling instability. The concrete and steel reinforcement material properties of the 180 prisms are characterized by typically used values. Regarding the axial loading protocol, a three-cycle type was included since the aim is to determine crucial variations through consecutive and close cycles. Even though the parametric study is conducted on boundary elements from RC wall buildings, the key findings perfectly apply to end regions of pier walls.

6.3.1 Material properties

The concrete parameters considered in SeismoStruct through the Mander et al. (1988) model (*con_ma*) are detailed in Table 6-6, where f'_c is the compressive strength, f_t is the tensile strength, E_c is the modulus of elasticity, ε_c is the strain at peak, and γ_c is the specific weight.

Table 6-6. Parametric study: Concrete model parameters

f'_c ksi (MPa)	f_t ksi (MPa)	E_c ksi (MPa)	ε_c in/in (mm/mm)	γ_c kip/in^3 (N/mm^3)
5.0 (34.5)	0.4 (2.8)	4,000 (27,600)	0.002	8.8E-5 (2.4E-5)

Table 6-7 shows the values adopted to define the Menegotto & Pinto (1973) model (*st_mp*) in SeismoStruct. In the table, E_s is the elastic modulus, f_y is the yield strength, μ is the strain hardening parameter, ε_{ult} is the fracture/buckling strain, and γ_s is the specific weight.

Table 6-7. Parametric study: Reinforcement steel parameters

E_s ksi (GPa)	f_y ksi (MPa)	μ	R_o	a_1	a_2	a_3	a_4	ε_{ult} in/in (mm/mm)	γ_s kip/in^3 (N/mm^3)
29,000 (200)	60.0 (414)	0.0086	20.0	18.0	0.15	0.025	2.0	0.11	2.9E-4 (7.8E-5)

6.3.2 Geometric and reinforcement detailing parameters

Typical wall geometries from RC buildings are analyzed to determine different cross sections and longitudinal reinforcement ratios. An axial load ratio ALR of 0.2 was used to calculate the approximate neutral axis depth of the walls under study (Moehle et al., 2012). The walls require boundary elements designed in accordance with ACI 318-14.

Table 6-8. Parametric study: Geometry and longitudinal reinforcement detailing

Variable	U.	Case 1	Case 2	Case 3	Case 4	Case 5	Case 6	Case 7	Case 8
Phase					**1**				
Interstory height, h_s	in m				94.0 2.4				
Buckled region length, $L_o=h_s/\sqrt{3}$	in m				54.3 1.4				
Wall length, l_w	in m	59.0 1.5	79.0 2.0	98.0 2.5	118.0 3.0	138.0 3.5	157.0 4.0	197.0 5.0	236.0 6.0
Boundary element length, l_{be}	in m	11.0 0.27	14.0 0.36	180.0 0.45	21.0 0.54	25.0 0.63	28.0 0.72	35.0 0.90	43.0 1.08
Wall thickness, b_w	in m	6.0, 9.0 0.15, 0.23	6.0 0.15	6.0, 9.0 0.15, 0.23	6.0, 9.0 0.15, 0.23	6.0, 9.0 0.15, 0.23	6.0, 9.0 0.15, 0.23	6.0, 9.0 0.15, 0.23	6.0, 9.0 0.15, 0.23
Longitudinal reinforcement ratio range, ρ_l	%				(0.8-4.5)				
Phase					**2**				
Interstory height, h_s	in m				106.0 2.7				
Buckled region length, $L_o=h_s/\sqrt{3}$	in m				61.2 1.6				
Wall length, l_w	in m	59.0 1.5	79.0 2.0	98.0 2.5	118.0 3.0	138.0 3.5	157.0 4.0	197.0 5.0	236.0 6.0
Boundary element length, l_{be}	in m	11.0 0.27	14.0 0.36	18.0 0.45	21.0 0.54	25.0 0.63	28.0 0.72	35.0 0.90	43.0 1.08
Wall thickness, b_w	in m	7.0, 11.0 0.18, 0.28	7.0 0.18	7.0, 11.0 0.18, 0.28	7.0, 11.0 0.18, 0.28	7.0, 11.0 0.18, 0.28	7.0, 11.0 0.18, 0.28	7.0, 11.0 0.18, 0.28	7.0, 11.0 0.18, 0.28
Longitudinal reinforcement ratio range, ρ_l	%				(0.9-4.7)				
Phase					**3**				
Interstory height, h_s	in m				118.0 3.0				
Buckled region length, $L_o=h_s/\sqrt{3}$	in m				68.1 1.7				
Wall length, l_w	in m	59.0 1.5	79.0 2.0	98.0 2.5	118.0 3.0	138.0 3.5	157.0 4.0	197.0 5.0	236.0 6.0
Boundary element length, l_{be}	in m	11.0 0.27	14.0 0.36	18.0 0.45	21.0 0.54	25.0 0.63	28.0 0.72	35.0 0.90	43.0 1.08
Wall thickness, b_w	in m	7.0, 12.0 0.18, 0.30	7.0 0.18	7.0, 12.0 0.18, 0.30	7.0, 12.0 0.18, 0.30	7.0, 12.0 0.18, 0.30	7.0, 12.0 0.18, 0.30	7.0, 12.0 0.18, 0.30	7.0, 12.0 0.18, 0.30
Longitudinal reinforcement ratio range, ρ_l	%				(0.9-4.7)				

Table 6-8 summarizes the variables considered through the parametric study. Three phases associated with three different interstory heights h_s are established. The wall thickness is determined based on two interstory height-to-thickness aspect ratios, $h_s/b_w=16$ and $h_s/b_w=10$. The longitudinal and transverse reinforcement detailing follows the rules established in ACI 318-14. The longitudinal steel bars account for diameters between #3 (9.525mm) and #10 (32.26mm). The transverse steel bars include a #3 (9.525mm) bar diameter for closed rectangular hooks and consecutive cross ties. The experimental results showed that limiting the spacing of the transverse reinforcement to a maximum value of $6d_b$ could lead to bar buckling, and consequently a $4d_b$ spacing is considered among the additional limits contemplated in ACI 318-14, as suggested in Chapter 5.

6.3.3 Loading protocol

Incremental three-cycle axial displacements at targets selected based on percentages of the reinforcement yielding strain are applied until buckling instability is recognized through the limit state associated with concrete cover crushing in the buckled region upon compressive displacements. The compressive target displacements are determined through values equivalent to the effect of the axial compressive strength P_o of each prism. Figure 6-14 shows a typical axial loading protocol, represented by axial strains, implemented in the parametric study.

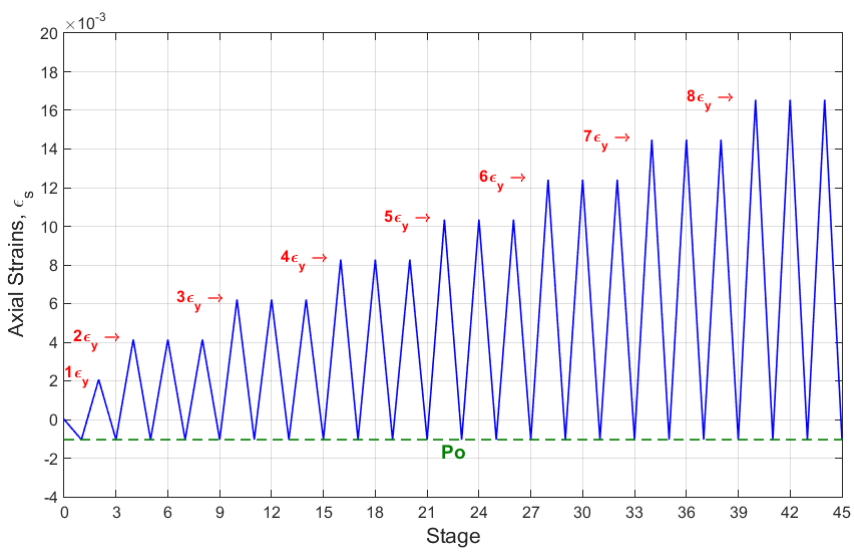

Figure 6-14. Parametric study: Typical axial strain protocol

6.3.4 Results of the parametric study

In general, the numerical model reported to be stable for the cases where the boundary elements have a thickness equivalent to $h_s/16$. Convergence problems appeared for thicker boundary elements associated with $h_s/10$, accompanied by longitudinal reinforcement ratios less than 2.0%. The analysis showed that, this combination leads to higher tensile demands before buckling instability

develops upon compressive demands if convergence issues do not emerge during close earlier stages. Some cases permitted to address convergence problems through incrementing the maximum number of iterations, varying the loop convergence tolerance, and allowing unbalanced forces in case of *fdb_ite* (element loop maximum iteration) error messages. However, in other few cases the numerical model persisted to be unstable.

6.3.4.1 Critical parameters that influence the onset of out-of-plane buckling instability

The effects of two crucial parameters on the onset of buckling instability is displayed in Figure 6-15. Normalized maximum tensile strains from the prisms analyzed in Phase 1 through the parametric study that developed inelastic buckling under compressive loads are plotted against different reinforcement ratios. Higher tensile strains are captured for higher interstory height-to-thickness ratios and vice versa. In addition, the results reveal that boundary elements with large longitudinal reinforcement ratios are prone to experience buckling instability during earlier stages compared with those that account for small longitudinal reinforcement ratios. As described in Chapter 5, the experimental program exposed a similar outcome.

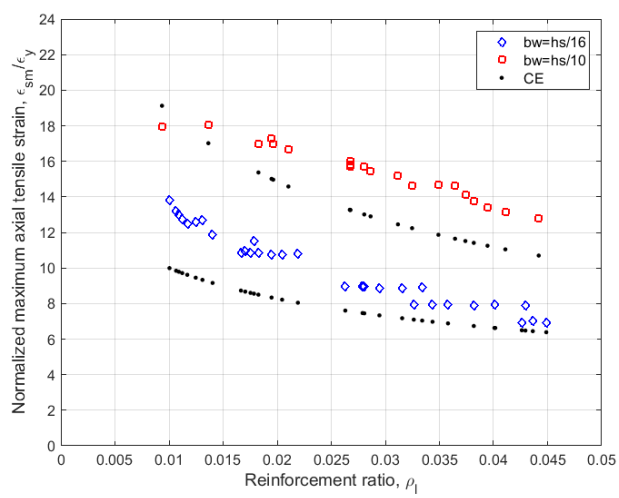

Figure 6-15. Parametric study-Phase 1: Influence of critical parameters

For comparison purposes, the predictions from the Chai & Elayer (1999) model are also plotted in Figure 6-15. This model underestimates the maximum tensile strains when small longitudinal reinforcement ratios and a thickness equivalent to $h_s/16$ are combined. The opposite occurs for a *10* interstory height-to-thickness ratio, as the model tends to overestimate the tensile strains for large longitudinal steel contents. From the parametric study, it is also noticed that the $h_s/16$ case follows a parabolic concave upward distribution, however, the $h_s/10$ case shows a very wide parabola distribution. These key findings suggest additional improvements to be considered in a new model.

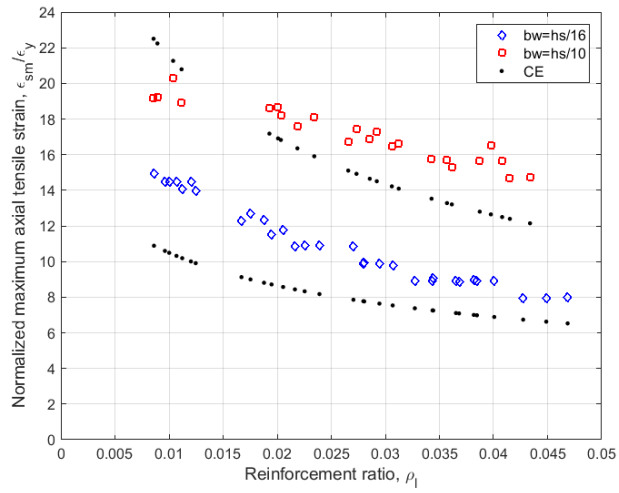

Figure 6-16. Parametric study-Phase 2: Influence of critical parameters

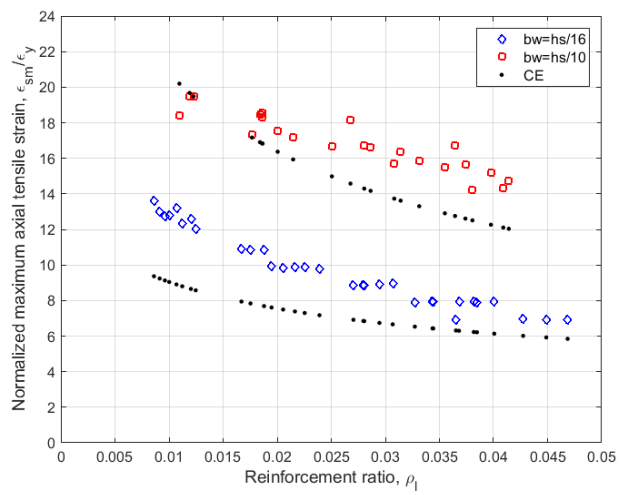

Figure 6-17. Parametric study-Phase 3: Influence of critical parameters

The aforementioned implications related to the influence of longitudinal reinforcement ratios and the interstory height-to-thickness ratios are also noted in the boundary elements contemplated in Phase 2 and Phase 3 from the parametric study, as shown in Figure 6-16 and Figure 6-17, respectively. Similarly, the graphs expose a disagreement between the results from the numerical model and the phenomenological model proposed by Chai & Elayer (1999). In general, the latter model tends to be conservative for interstory height-to-thickness ratios equal to 16. Notice that the phases comprise longitudinal reinforcement ratios close to 4.5%, which are higher than typical values; however, they are included with the only purpose of identifying tendencies beyond reinforcement ratios close to 4.0%.

6.3.4.2 Influence of the boundary element cross section

With the aim of studying the effect of the boundary element length l_{be} on the onset of buckling instability, cross section aspect ratios l_{be}/b_w are plotted against longitudinal reinforcement ratios and normalized maximum tensile strains in Figure 6-18 and Figure 6-19. The graphs show the results from the $h_s/16$ and $h_s/10$ cases considered in Phase 1, respectively. Notice the slight influence of the l_{be} parameter on the inelastic buckling mechanism.

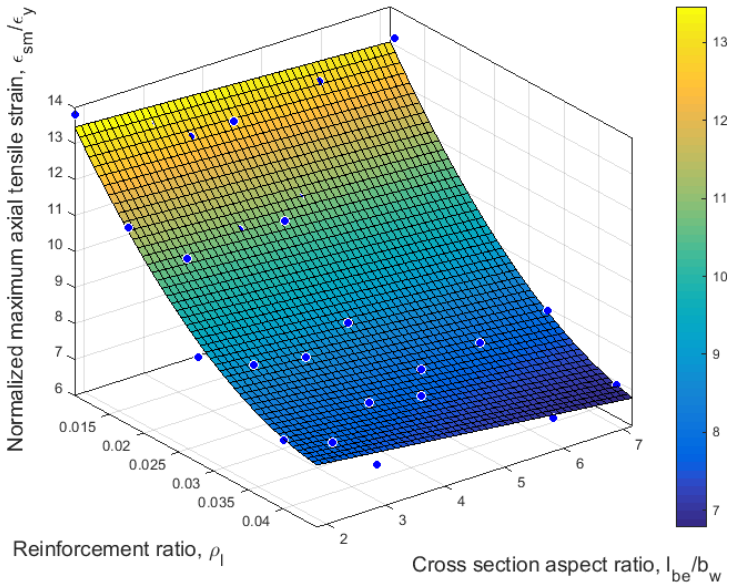

Figure 6-18. Parametric study-Phase 1 ($h_s/16$): Influence of boundary element length, l_{be}

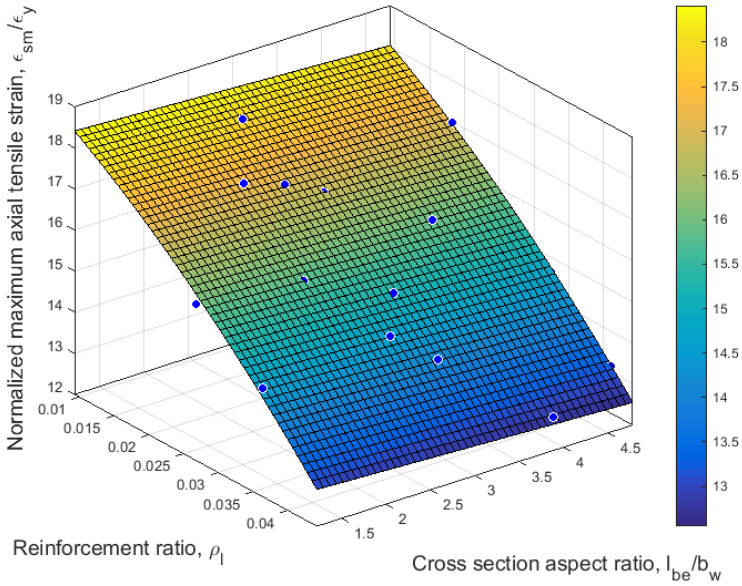

Figure 6-19. Parametric study-Phase 1 ($h_s/10$): Influence of boundary element length, l_{be}

Similar patterns are observed in Phase 2 and Phase 3, through Figure 6-20 to Figure 6-23. According to the Paulay & Priestley (1993) and Chai & Elayer (1999) models, the length of the compression region c_w is only considered in the calculation of the longitudinal reinforcement ratio in that region, and it would slightly affect the onset of instability. This fact is also reflected in the results presented in this subsection, where the importance of the longitudinal steel content on the onset of out-of-plane buckling instability is corroborated.

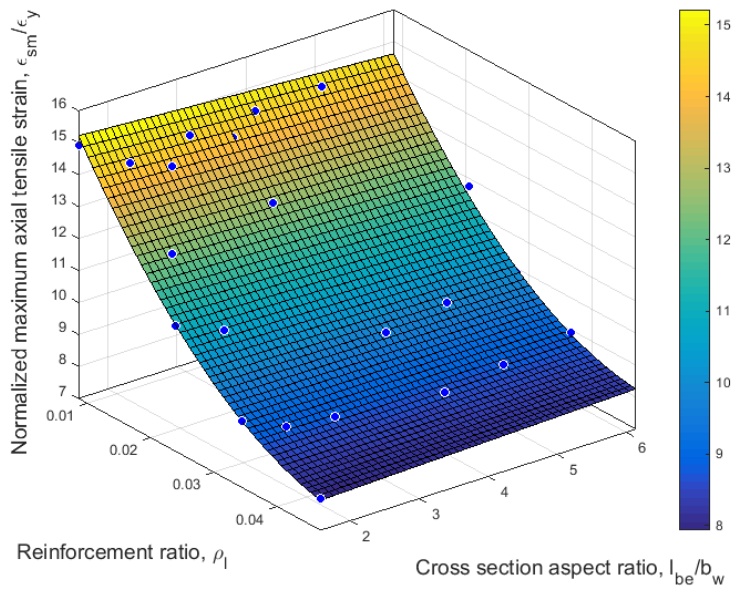

Figure 6-20. Parametric study-Phase 2 (*h_s/16*): Influence of boundary element length, *l_{be}*

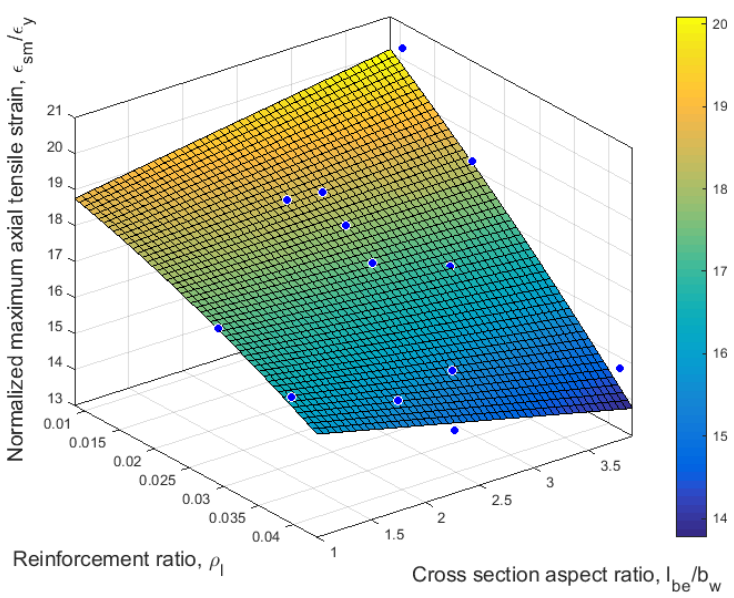

Figure 6-21. Parametric study-Phase 2 (*h_s/10*): Influence of boundary element length, *l_{be}*

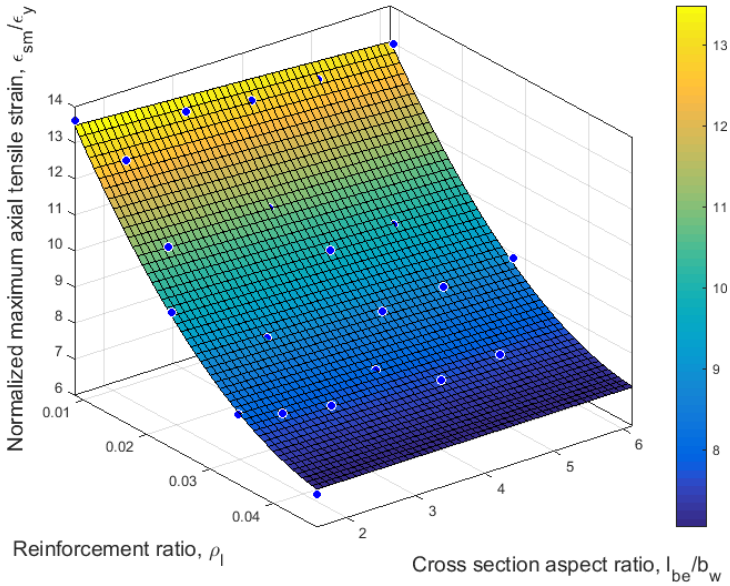

Figure 6-22. Parametric study-Phase 3 (*$h_s/16$*): Influence of boundary element length, *l_{be}*

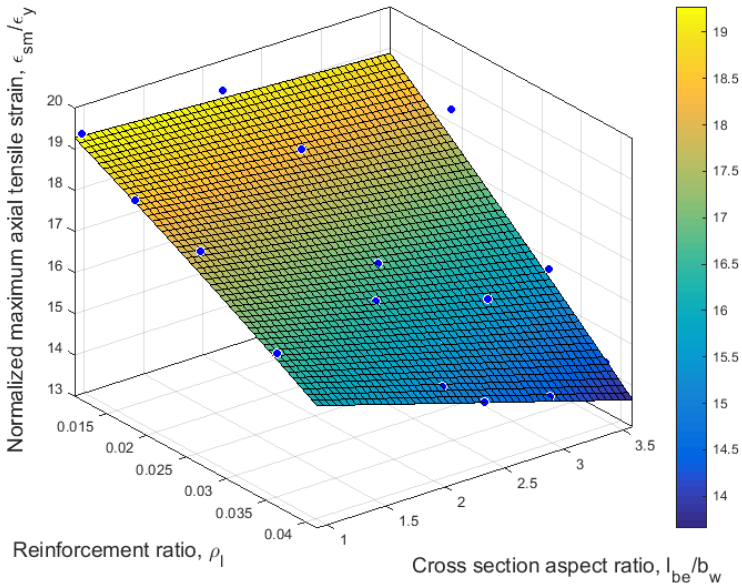

Figure 6-23. Parametric study-Phase 3 (*$h_s/10$*): Influence of boundary element length, *l_{be}*

6.3.4.3 Influence of the interstory height

The onset of buckling instability is slightly affected by the three different interstory heights considered in the parametric study as illustrated in Figure 6-24 and Figure 6-25. Maximum tensile strains from the three phases plotted as a function of longitudinal steel contents for the two aspect ratios, $h_s/b_w=16$ and $h_s/b_w=10$, are presented in the graphs, respectively. Phase 2 reports relatively higher values, which is attributed to the fact that the two actual interstory height-to-thickness ratios

contemplated in this phase are somewhat lower compared to the other phases, proving instead the importance of the interstory height-to-thickness ratio parameter.

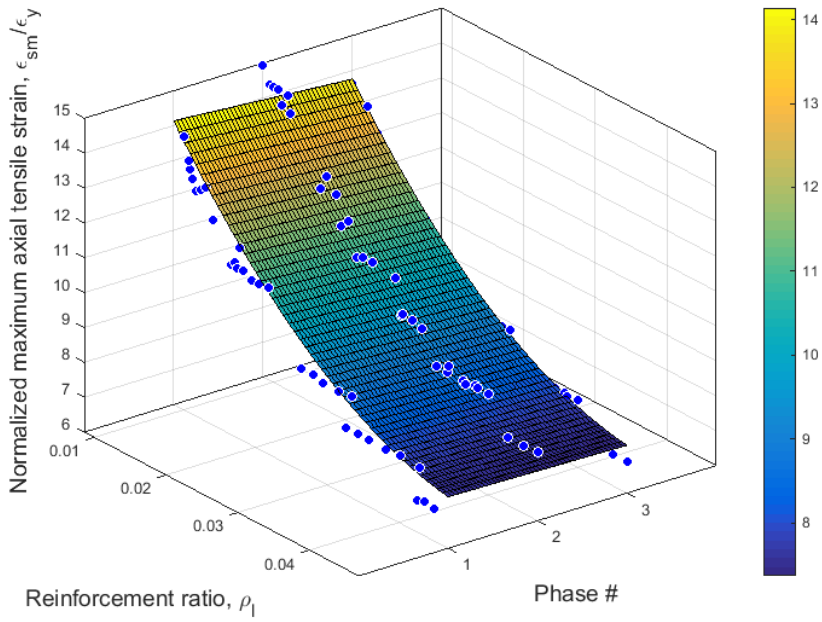

Figure 6-24. Parametric study - *h_s/16*: Influence of interstory height, *h_s*

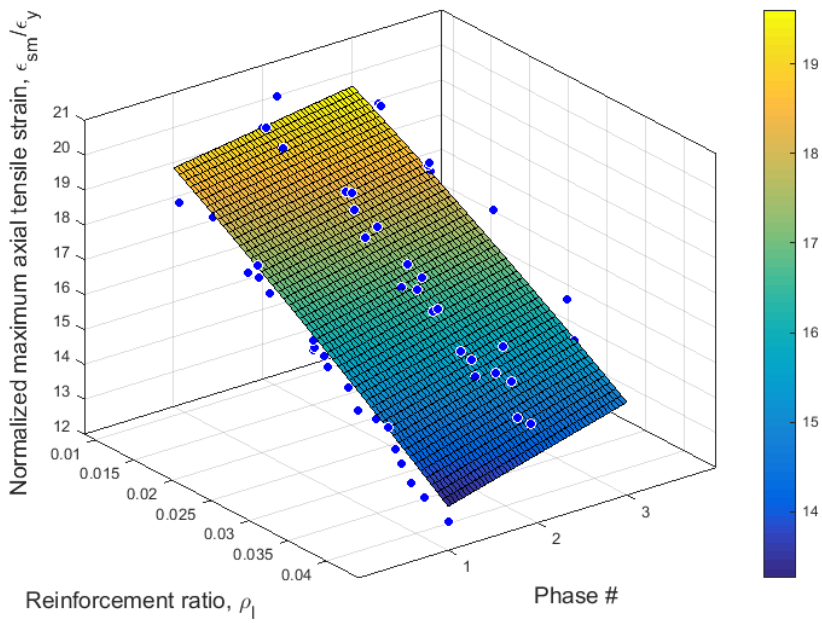

Figure 6-25. Parametric study - *h_s/10*: Influence of interstory height, *h_s*

6.3.4.4 Hysteretic longitudinal reinforcement response

The results from the experimental phase suggested that the strain components associated with the longitudinal reinforcement hysteretic response of the end regions of RCSW need to be adjusted. The axial strain at first closure ε_a* is calculated using Equation (6-1), which was determined from the experimental results. The remaining components are addressed through the parametric study.

$$\varepsilon_a^* = \frac{8}{3}\left(\frac{b_w}{L_o}\right)^2 \xi_c \tag{6-1}$$

The elastic recovery strain ε_e and the reloading strain to cause compression yield ε_r are determined from Figure 6-26 corresponding to Phase 1. Figure 6-26(a) shows strain components of the $h_s/16$ cases and Figure 6-26(b) represents the strain components of the $h_s/10$ cases. The values are normalized to the yielding strain. The elastic recovery strain ε_e is calculated from the difference between the maximum tensile strain ε_{sm} and the corresponding strain at elastic recovery ε_{so}. The difference between ε_{sm}, ε_e, and, ε_a* gives ε_r.

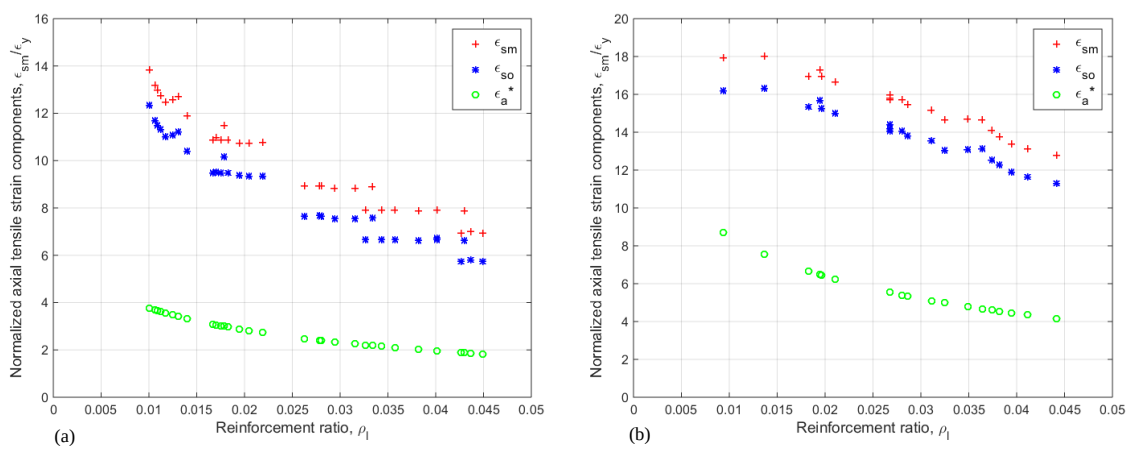

Figure 6-26. Phase 1: Strain components, (a) *$h_s/16$*, (b) *$h_s/10$*

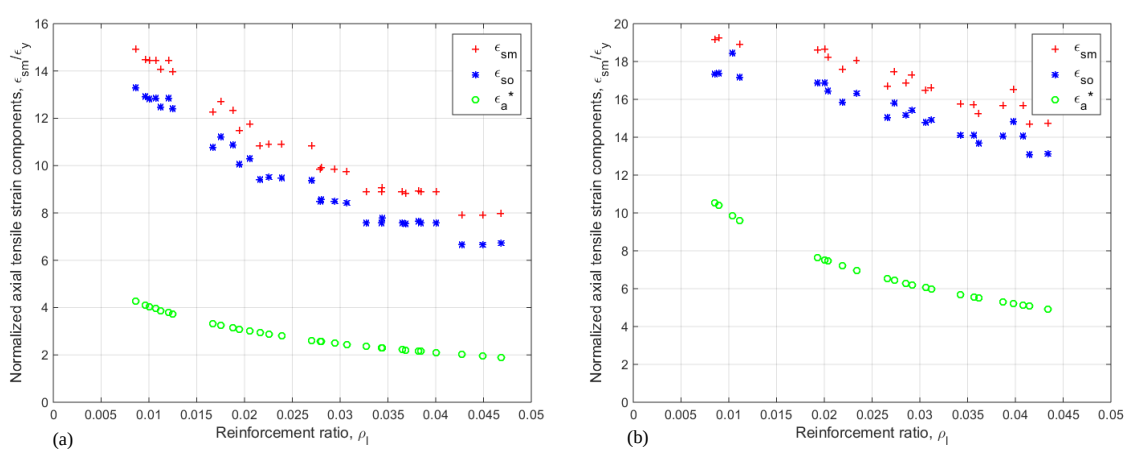

Figure 6-27. Phase 2: Strain components, (a) *$h_s/16$*, (b) *$h_s/10$*

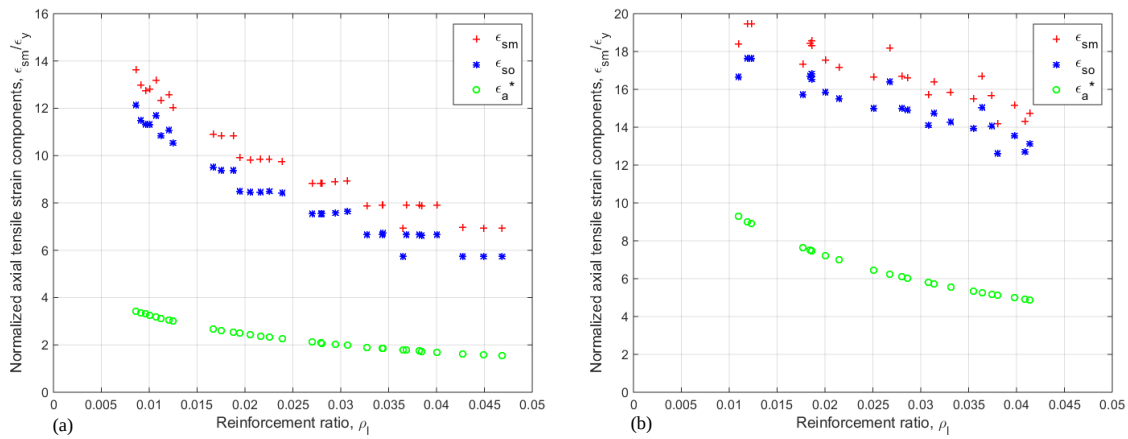

Figure 6-28. Phase 3: Strain components, (a) *h_s/16*, (b) *h_s/10*

Similar calculations are developed for Phase 2 and Phase 3 from Figure 6-27 and Figure 6-28, respectively. Trend polynomial functions that characterize the normalized elastic recovery strain ε_e and the normalized reloading strain to cause compression yield ε_r for the two *h_s/16* and the *h_s/10* cases are summarized in Table 6-9. These functions are determined from a linear regression that fits a polynomial model as expressed in Equation (6-2), which constitutes the basis of a new approach created to prevent out-of-plane buckling instability of RCSW described in Chapter 7. The ranges established for the coefficients *p*00, *p*10 and, *p*01 represent the 95% confidence bounds.

$$fit(x,y) = p00 + p10 * \left(\frac{b_w}{L_o}\right)^2 + p01 * \ln\left(\rho_l\right) \tag{6-2}$$

Table 6-9. Fitting functions for the strain components ε_e and ε_r

Coefficients	ε_e	ε_r	Confidence bounds, ε_e	Confidence bounds, ε_r
		h_s/16		
p00	0.2	-6.7	(0.12,0.33)	(-7.84,-5.63)
p00	27.0	231.8	(19.56,34.45)	(155.7,308.0)
p00	-0.2	-2.7	(-0.23,-0.20)	(-2.85,-2.53)
		h_s/10		
p00	0.6	6.9	(0.36,0.78)	(4.19,9.64)
p00	18.3	79.4	(12.02,24.65)	(-1.66,160.4)
p00	-0.15	0.22	(-0.18,-0.12)	(-0.15,0.59)

Equation (6-2) would require an interpolation or extrapolation procedure to evaluate the out-of-plane buckling instability of walls with interstory height-to-thickness ratios different from 16 and 10. Therefore, a simplified polynomial function that comprises ε_e and ε_r is additionally determined. The application of Equation (6-3) results convenient for design purposes since it can be used directly for any interstory height-to-thickness ratio.

$$\varepsilon_e + \varepsilon_r = \left(-2.4 + 160\left(\frac{b_w}{L_o}\right)^2 - 1.9 \cdot \ln\left(\rho_l\right) \right) \varepsilon_y \tag{6-3}$$

In general, the parametric study reported elastic recovery strains between 1.2 and 1.9 times the yielding strain, and the reloading strains vary from 3.9 to 10.1 times the yielding strain. The prisms tested during the experimental program reported values about the same range, depending primarily on the steel content. If the two strain components are compared with the ranges determined by Chai & Elayer (1999), the results reveal a significant difference specially regarding the reloading strains.

6.3.5 Parametric study: Concluding remarks

Based on the results from the parametric study, the following observations constitute the basis of the new model described in Chapter 7:

1. The onset of out-of-plane buckling instability certainly develops at earlier stages when large longitudinal reinforcement ratios are considered in the boundary elements of RCSW.
2. Interstory height-to-thickness ratios equal to *10* delay the onset of buckling instability with percentages close to 100% compared with interstory height-to-thickness ratios equal to *16*, revealing the importance of considering thicker sections when large in-plane displacements are expected in RCSW.
3. In the three phases contemplated during the parametric study, the curves that relate the tensile strains to cause buckling and the contemplated longitudinal steel ratios present different tendencies directly associated with the two interstory height-to-thickness ratios, which affects also the strain components. The latter fact is not reflected in the Chai & Elayer (1999) model.
4. The boundary element length is a parameter that slightly influence the onset of buckling instability. Length-to-thickness ratios between *1* and *7* were studied, producing similar results for equivalent reinforcement ratios.
5. Variations in the interstory height parameter slightly affect the onset of buckling instability for comparable height-to-thickness ratios.
6. The results from the parametric study also verified that the fundamentals of the existing models covered in this report, are appropriate to be included in a new approach.

7. The ranges of the strain components obtained from the hysteretic response of the longitudinal steel are similar to the ranges determined in the experimental program.
8. Convergence problems arose specially for the cases where low longitudinal steel contents and thicker sections were analyzed, resulting in lack of final solutions for some cases. However, regression equations expressed as a function of identified critical parameters that represent the tendencies found through the results, constitute an important source to develop a new model to prevent out-of-plane buckling failure mode.

CHAPTER 7: NEW MODEL TO PREVENT OUT-OF-PLANE BUCKLING INSTABILITY OF RCSW

The results from the experimental phase and the parametric study in conjunction with the fundamentals of the Paulay & Priestley (1993) and Chai & Elayer (1999) models constitute the basis of the new model, proposed in this chapter, to prevent out-of-plane buckling instability of RCSW that require special boundary elements. Based on the direct displacement based design (DDBD) philosophy, recommendations are suggested and explained trough practical applications covering building structural walls.

7.1 HKC model

The new HKC (Haro, Kowalsky & Chai) model is created based on exiting models (Paulay & Priestley, 1993) (Chai & Elayer, 1999) and the results from the analytical and experimental phases. The effects of out-of-plane lateral displacements demonstrated to be insignificant on the out-of-plane buckling mechanism compared with the effects of in-plane lateral displacements, therefore only the latter are considered to develop the new approach. High inelastic tensile strains derived from in-plane loading imposed on a planar reinforced concrete structural wall, have been recognized as a governing parameter to cause out-of-plane buckling instability in the end regions. According to Chai & Elayer (1999) and the results from the current research, the axial hysteretic behavior of the longitudinal reinforcement located in boundary elements combined with the concrete cover crushing limit state, constitute the fundamentals to limit the tensile strains and subsequently the in-plane displacements to ensure stability in a wall.

7.1.1 Strain components

The hysteretic behavior of boundary elements subjected to axial cyclic loading is represented by three strain components already defined in previous chapters. Figure 7-1 recalls different stages from the axial response of Prism 2 captured during the last cycle where out-of-plane buckling instability occurred. Stage 1 identifies the maximum tensile strains ε_{sm}, where the prism shows wide horizontal cracks. The strains at elastic recovery ε_{so} is defined by stage 2, where $\varepsilon_e = \varepsilon_{sm} - \varepsilon_{so}$. Stage 3 indicates the time when the last out-of-plane deformation starts to develop. Strains at first closure ε_{a*} are noticed through stage 4. Next, the strain to cause compression yield ε_r is determined from $\varepsilon_r = \varepsilon_{sm} - \varepsilon_e - \varepsilon_{a*}$. Finally, concrete cover crushing is recognized in stage 5. Beyond this point, the prism becomes unstable.

Based on the preceding recap and the numerical expressions determined in Chapter 6, the three strain components associated with the hysteretic response of wall boundary elements considering the average of the strains captured in the faces parallel to the length of a wall, can be written as

$$\varepsilon_a^* = \frac{8}{3}\left(\frac{b_w}{L_o}\right)^2 \xi_c \tag{7-1}$$

$$\varepsilon_e = \left[a_1 + a_2 * \left(\frac{b_w}{L_o}\right)^2 + a_3 * \ln\left(\rho_{lbe}\right)\right]\varepsilon_y \tag{7-2}$$

$$\varepsilon_r = \left[b_1 + b_2 * \left(\frac{b_w}{L_o}\right)^2 + b_3 * \ln\left(\rho_{lbe}\right)\right]\varepsilon_y \tag{7-3}$$

where b_w/L_o represents the ratio between the thickness of the end region and the buckled length of the wall L_o, which according to the observations from the experimental and the analytical phases is obtained as

$$L_o = {h_s}/{\sqrt{3}} \tag{7-4}$$

where h_s is the interstory height. The stability criteria ξ_c (Paulay & Priestley, 1993) was already detailed in Chapter 2, however it is repeated here for convenience.

$$\xi_c = 0.5\left(1 + 2.35m - \sqrt{5.53m^2 + 4.70m}\right) \leq 0.5 \tag{7-5}$$

$$m = \rho_{lbe}\frac{f_y}{f_c^{'}} \tag{7-6}$$

where m is the mechanical reinforcement ratio, ρ_{lbe} is the longitudinal reinforcement ratio of the boundary element of the wall, and f'_c is the uniaxial concrete compressive strength.

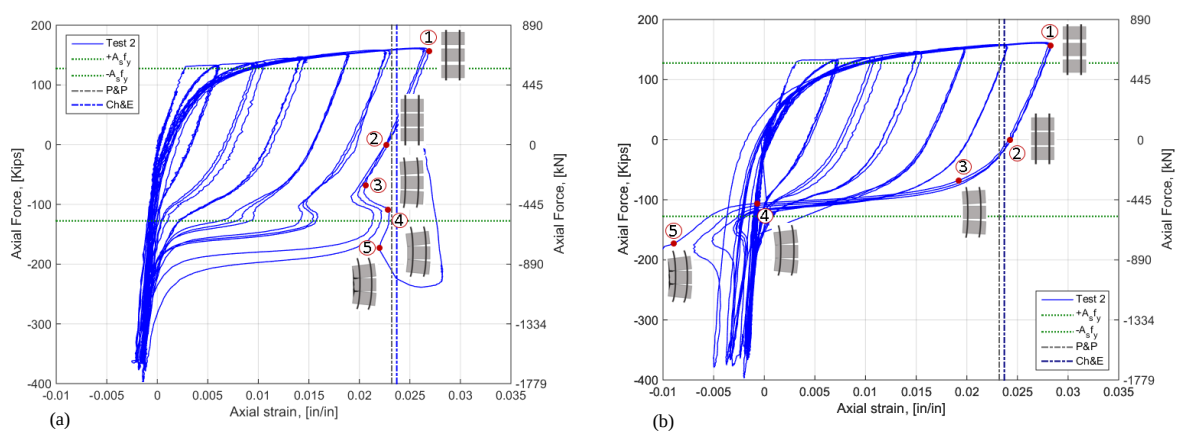

Figure 7-1. Axial Response of Prism 2 - Stages: a) south face and b) north face

For design purposes, coefficients a_1, a_2, and a_3 are correspondingly combined with coefficients b_1, b_2, and b_3. Consequently, the maximum tensile strain may be obtained from Equation (7-8), which constitutes the HKC model to prevent out-of-plane buckling instability of special RCSW that require boundary elements considering the effects of in-plane and out-of-plane loading.

$$\varepsilon_{sm} \leq \varepsilon_a^* + \varepsilon_e + \varepsilon_r \tag{7-7}$$

$$\varepsilon_{sm} \leq \frac{8}{3}\left(\frac{b_w}{L_o}\right)^2 \xi_c + \left[\alpha_1 + \alpha_2\left(\frac{b_w}{L_o}\right)^2 + \alpha_3 * \ln(\rho_{lbe})\right]\varepsilon_y \tag{7-8}$$

where ε_y is the yielding strain of the longitudinal reinforcement. The coefficients α_1, α_2, and α_3 are defined as

$$\alpha_1 = (-5;6) \rightarrow (h_s/16;\ h_s/10)$$

$$\alpha_2 = (200;100) \rightarrow (h_s/16;\ h_s/10)$$

$$\alpha_3 = (-2.5;-0.1) \rightarrow (h_s/16;\ h_s/10)$$

That is, if a wall thickness is $h_s/16$, then $\alpha_1 = -5$, $\alpha_2 = 200$, and $\alpha_3 = -2.5$. On the other hand, if a wall thickness is $h_s/10$, then $\alpha_1 = 6$, $\alpha_2 = 100$, and $\alpha_3 = -0.1$. The ranges contemplated for coefficients α_1, α_2, and α_3 were calibrated from the results of the parametric study as shown in the following section.

Equation (7-8) requires an interpolation or extrapolation procedure to evaluate the out-of-plane buckling instability mechanism of walls with interstory height-to-thickness ratios different from 16 or 10. The simplified version of the HKC model, which is presented in Equation (7-9), results more efficient for design purposes since it can be applied directly for any buckled length-to-thickness ratio.

$$\varepsilon_{sm} \leq \frac{8}{3}\left(\frac{b_w}{L_o}\right)^2 \xi_c + \left[-2.4 + 160\left(\frac{b_w}{L_o}\right)^2 - 1.9 \cdot \ln(\rho_{lbe})\right]\varepsilon_y \tag{7-9}$$

7.1.2 Validation of the HKC model

The HKC model is validated in this section through the results from the experimental and the analytical phases, showing satisfactory results. In general, the HCK model reports to be more accurate compared with the models also presented through this research.

7.1.2.1 Validation: analytical phase

The results from the parametric study showed that the trends on the maximum tensile strains associated with the effect of the reinforcement steel content, are different for the $h_s/16$ and $h_s/10$ cases from a same phase. For this reason, two sets of coefficients were determined in Chapter 6 for each aspect ratio from the 95% confidence bounds that characterize the trend functions of the elastic recovery strain ε_e and the reloading strain ε_r. The ranges of these coefficients are considered to calibrate the HKC model.

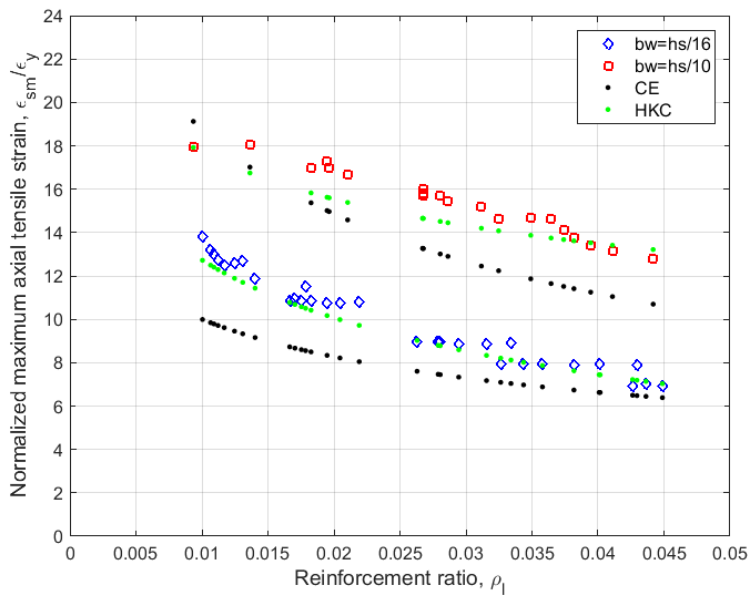

Figure 7-2. Validation of the HKC model: Parametric Study Phase 1

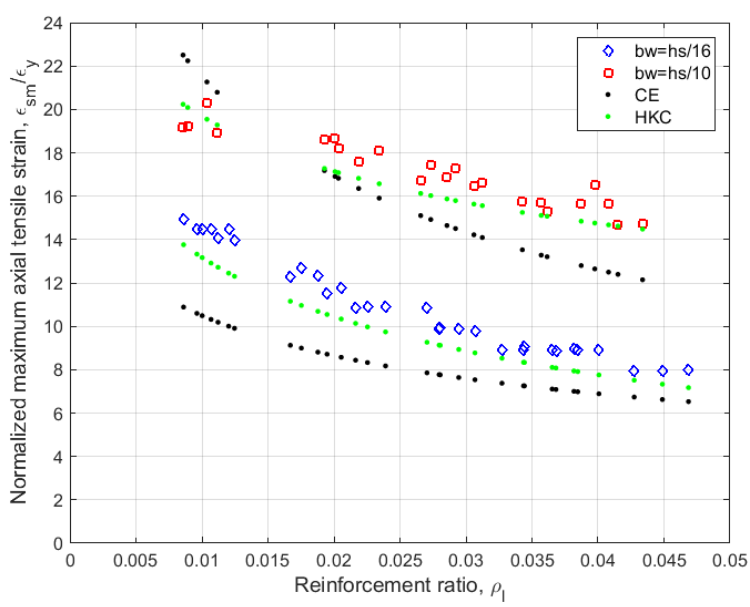

Figure 7-3. Validation of the HKC model: Parametric Study Phase 2

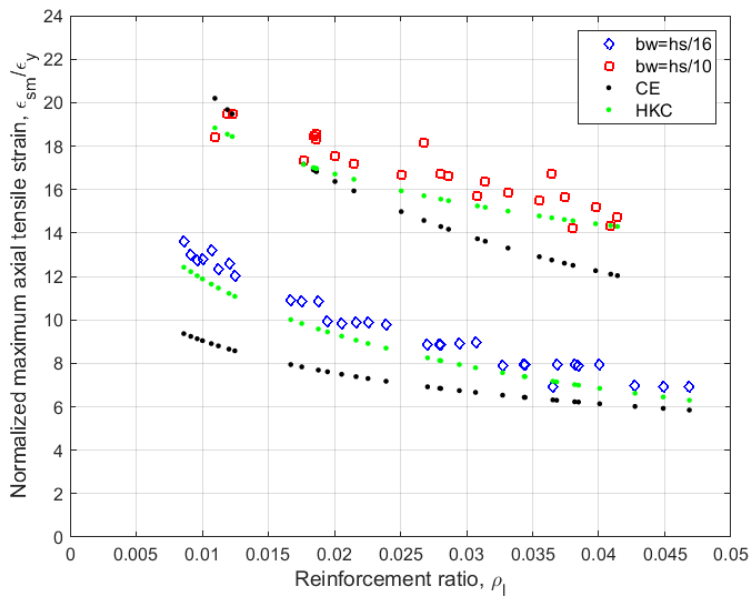

Figure 7-4. Validation of the HKC model: Parametric Study Phase 3

Figure 7-2, Figure 7-3, and Figure 7-4 show the maximum tensile strains that led to out-of-plane instability of the specimens analyzed through the parametric study including the predictions from the CE (Chai & Elayer, 1999) and HKC models. These predictions account for the stability coefficients established for $h_s/16$ and $h_s/10$ in the previous section, reflecting good agreement with the lower values. Notice that the HKC predictions are slightly higher for longitudinal reinforcement ratios greater than 4%, however, these percentages are rarely used in boundary elements.

7.1.2.2 Validation: experimental phase

Figure 7-5, Figure 7-6, and Figure 7-7 now include the predictions from the simplified HKC model associated with the three experimental phases. These figures were already obtained in Chapter 5. Notice that the simplified HKC model is capable to predict the expected values for the case of Phase 1. Moreover, the new approach results less conservative than the studied PP (Paulay & Priestley, 1993) and CE phenomenological models. Phase 2 reports a better agreement between the three models, with less conservative values determined through the HKC model. The results from Phase 3 can be taken as a valuable reference even though bar buckling also occurred through the tests. For this latter case, the predictions from the HKC model, which are close to the values from the CE model, show also an acceptable agreement.

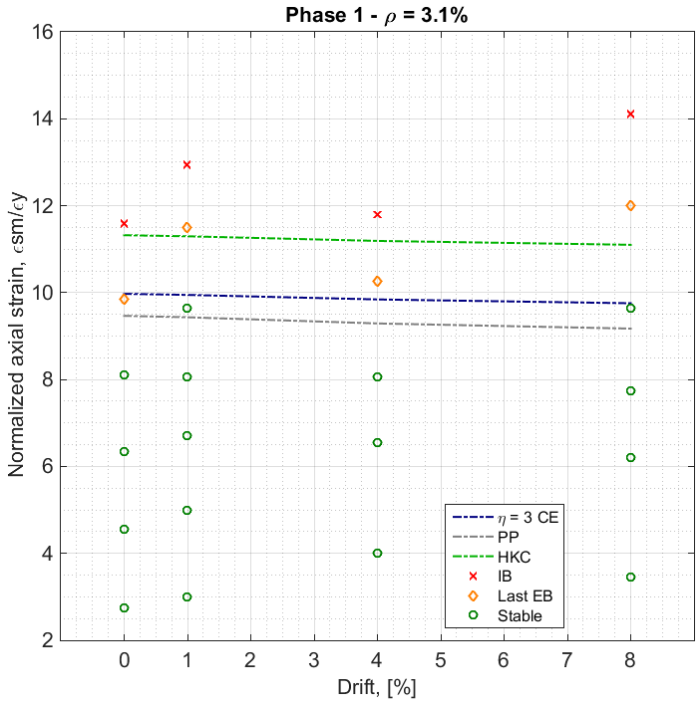

Figure 7-5. Validation of the HKC model: Experimental Phase 1

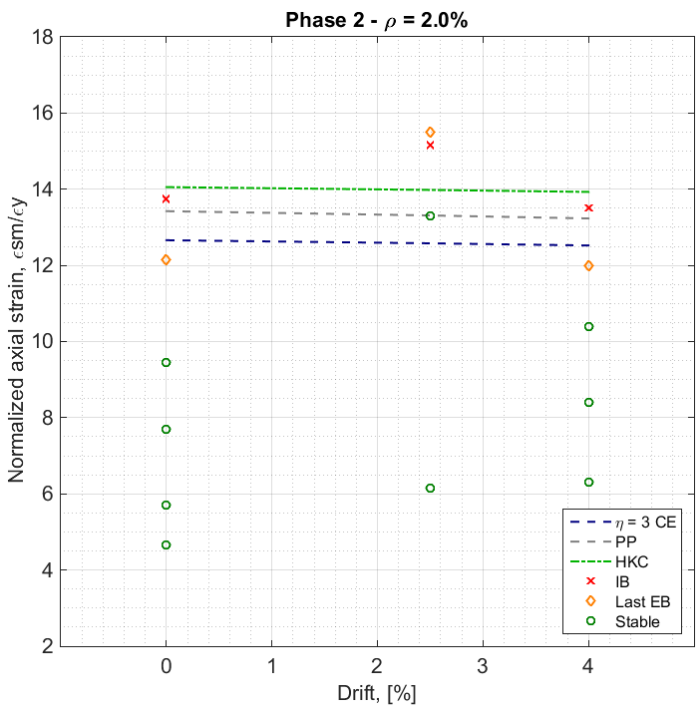

Figure 7-6. Validation of the HKC model: Experimental Phase 2

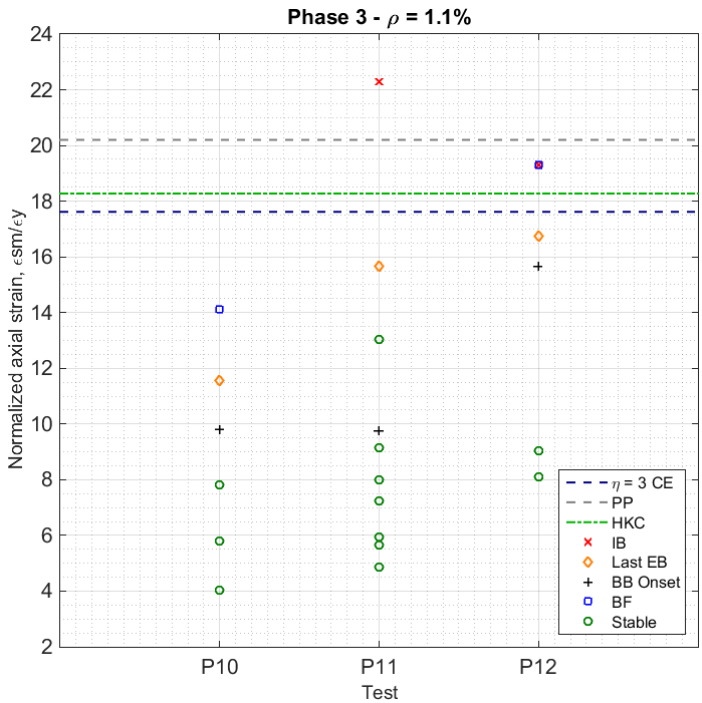

Figure 7-7. Validation of the HKC model: Experimental Phase 3

7.2 Axial strain gradient effects

As stated in Chapter 2, the idealization of wall end regions by RC prisms subjected to axial cyclic and lateral loads results useful to study the effect of critical parameters involved in the out-of-plane buckling mechanism of planar cantilever structural walls of tall buildings. This hypothesis suggests a uniform distribution of tensile strains along the height of the critical story, as shown in Figure 7-8 (Chai & Elayer, 1999). Due to the lateral support provided by the floor system, a wall buckles at the interstory level that experiences wide horizontal cracks accompanied by large inelastic tensile strains, followed by compressive loads.

However, the damage captured in actual walls and previous analytical studies has demonstrated that the end region of a wall exhibits strain gradients not only along the height of the wall but also along the length of the wall, being the first one the most critical on the onset of lateral instability (Parra, 2015). As proved over the current research, in the case of a constant strain gradient, the maximum out-of-plane deformations occur near the mid-height of the free interstory height h_s. This was attributed to the formation of the buckled shape in the mid-zone over a length equivalent to $h_s/\sqrt{3}$ or approximately 60% of h_s. The experimental phase reported that even cyclic axial displacements combined with high out-of-plane lateral drifts led to buckled lengths about $h_s/\sqrt{3}$.

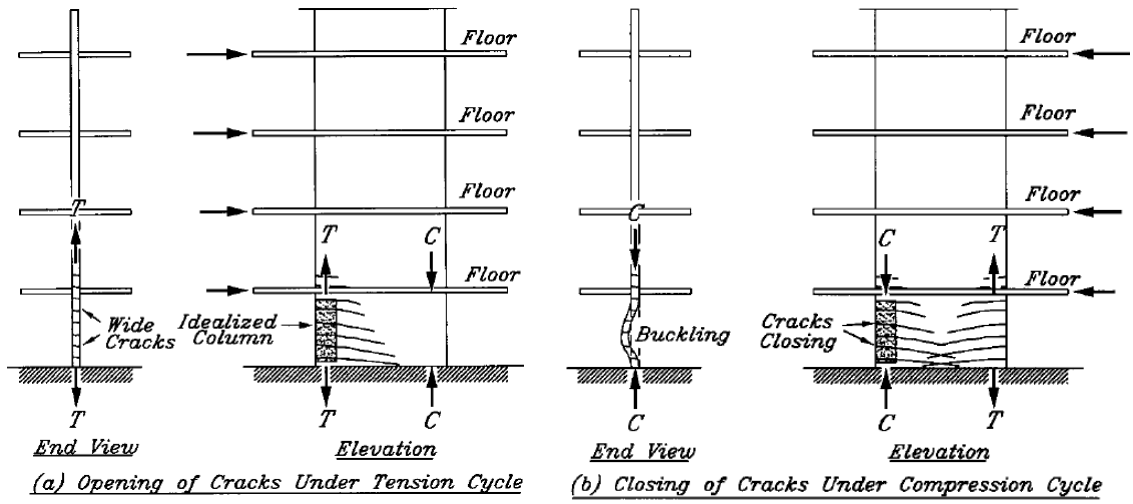

Figure 7-8. End region idealization of a building RC wall (Chai & Elayer, 1999).

In the wall end regions, where the axial strain gradient is important, the buckled shape is displaced to the zone that experiences the maximum tensile strains, consequently the maximum out-of-plane deformation would develop close to the mid-height of the relocated buckled region. The HCK model assumes that the length of the buckled zone remains as established through the experimental and the analytical study, and consequently the axial strain gradient would not affect its suitability. In order to validate this hypothesis, two research programs and a finite element numerical simulation, developed as part of the current research, are analyzed in the following section.

7.2.1 Buckled region length

The analyses described next mainly focus on capturing the length of the buckled region considering the effect of axial strain gradients. Further details about the key findings on each study can be investigated in the corresponding references.

7.2.1.1 Experimental study on thin walls tested by Rosso et al. (2015)

The principal outcomes of the study conducted by Rosso et al. (2015) were already presented in Chapter 2. Figure 7-9 shows the normalized web edge out-of-plane deformations of wall TW1 captured at different stages. The graph shows that the maximum out-of-plane deformation occurs at 750mm, which implies that the buckled length is close to twice this value. Consequently, it would be equivalent to $0.75h_w$ that was also established by Rosso et al. (2015).

The HCK model suggests a value 20% lower, but it still represents a good estimation. The difference could be mainly attributed to the reinforcement distribution adopted in the walls tested by Rosso et al. (2015), which considers only one curtain of vertical and longitudinal steel. This, combined with the fact that these walls have height-to-thickness ratios equal to 25, make them more flexible.

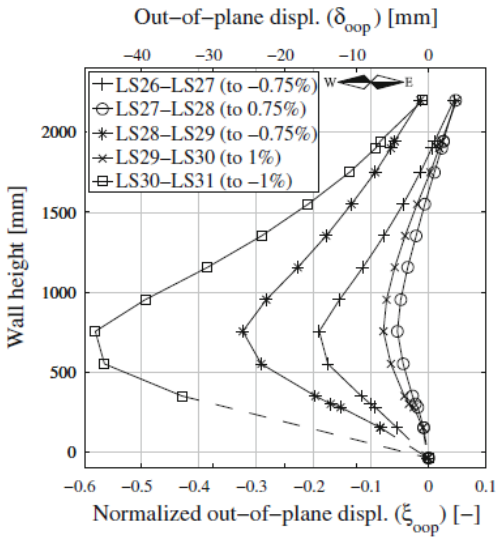

Figure 7-9. Normalized web edge out-of-plane deformations along the height of the of wall TW1 (Rosso et al., 2015).

7.2.1.2 Analytical study on thin walls conducted by Parra (2015)

Parra (2015) developed FE numerical simulations of RC walls and prisms already tested in previous experimental programs. Part of the study focused on identifying the effects of strain gradients along the height of the boundary region and along the length of planar walls on the onset of lateral instability. Figure 7-10 shows the numerical estimation of the out-of-plane deformations captured at two different stages along the height of the end region of wall R2 tested by (Oesterle et al., 1976), which was described in Chapter 2.

The height-to-thickness ratio of wall R2 is equal to 45 and two steel curtains of reinforcement were provided. Notice that the maximum out-of-plane deformations occur about 60in. (1.5m) height. This suggests that the buckled region length is about 120in. (3.0m), which related to the height of the wall is 2/3h_w. The HCK model provides a value 10% lower, representing a good estimation.

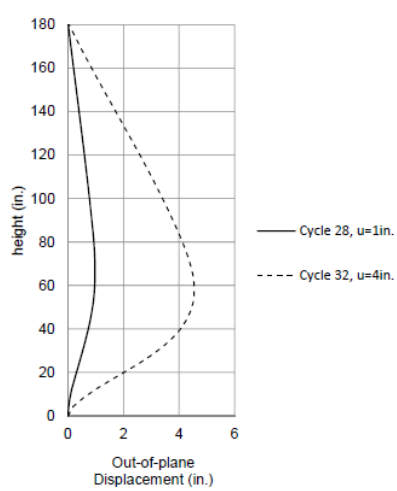

Figure 7-10. Out-of-plane deformations along the edge height of wall R2 (Parra, 2015).

7.2.1.3 Numerical simulation of an RC prism considering axial strain gradient

The end region of a pier wall that requires a special boundary element is idealized through an RC prism simulated in SeismoStruct. In general, the numerical model considers the same material models and the same loading protocol specified in Chapter 6. In order to account for the axial strain gradient, the FE model contemplates grade 60 (420MPa) steel in the inelastic region that expects high tensile strains, which would be the bottom portion. The idealized transition and the top zones include 90ksi (630MPa) and 120ksi (840MPa) steel, respectively. The dimensions of the RC prism are: thickness b_w = 1.0ft (300mm), height h_w = 10.0ft (3,000mm), and length l_{be} = 3.5ft (1,090mm). The height-to-thickness ratio considered for this case represents a typical value used in pier walls. The reinforcement ratio is about 3.0%. Figure 7-11 shows the stage where the concrete cover crushing limit state is captured under compressive loading on the green element. Notice that due to the particularity of the numerical model that considers strain gradient effects, the buckled shape displaced to the bottom region. The prism reached tensile strains close to $16\varepsilon_y$ before inelastic buckling occurred, which was also reported for the counterpart prism, according to the parametric study described in Chapter 6.

Figure 7-12 presents the structural response of the RC prism during the last stage where buckling was detected under compressive loading. Normalized out-of-plane deformations to the prism thickness b_w showed that the maximum deformation is captured at 3ft (910mm) height, suggesting a buckled length of 6ft (1,820mm), which is 60% of h_w. The contraflexure points are considered to determine a more accurate buckled region length, as contemplated by the HKC model. Figure 7-12(a) shows that the first contraflexure point roughly appears at 1ft (300mm) and the second point appears at 7ft (2,100mm). Consequently, the buckled length is still close to $0.60h_w$.

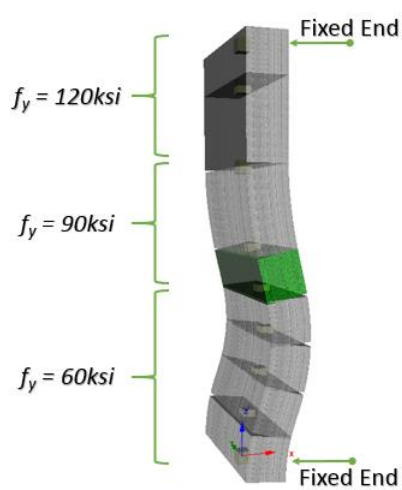

Figure 7-11. Deformed shape of an RC prism that considers strain gradient

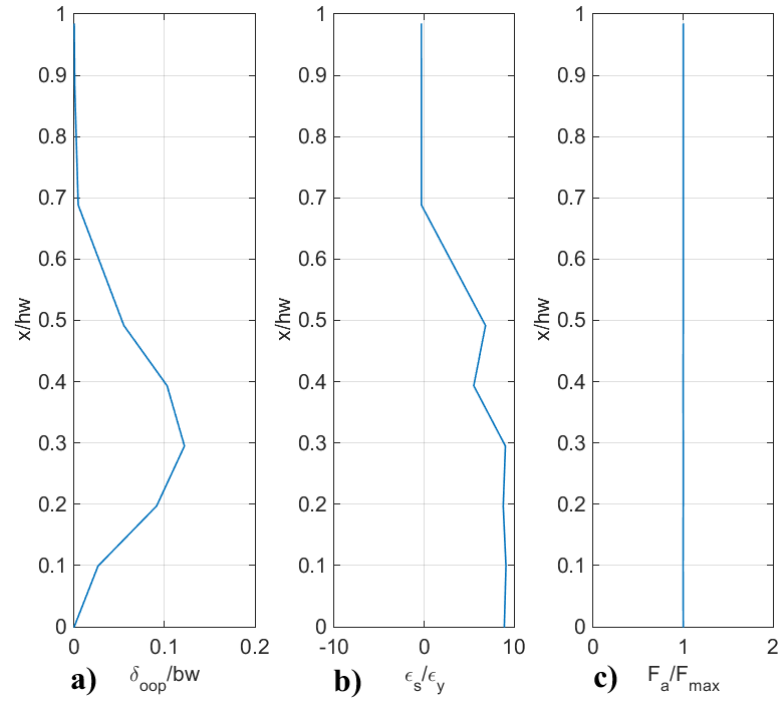

Figure 7-12. Structural response of a boundary element; a) Normalized out-of-plane deformations, b) Axial strain gradient, c) Axial force gradient

Figure 7-12 (b) shows the strain gradient along the height of the prism, where normalized strains are calculated from the average of the strains captured in the two reinforcement curtains at each location. The strains are normalized to the yielding strain ε_y. Significant tensile strains close to $9\varepsilon_y$ are reported in the buckled region and minor compressive strains in the top region. Figure 7-12 (c) depicts the axial force gradient normalized to the maximum compressive force F_{max}, showing that the compressive force is practically uniform along the height of the boundary element. This statement is accepted for boundary elements of walls subjected to loading reversals since the potential buckled zone would experience mainly a uniform compressive axial load.

The analyses presented in this section validate the applicability of the HKC model on structural walls and pier walls with aspect ratios $h_w/l_w \geq 2$ that require special boundary elements. The next section presents different applications addressing assessment and design recommendations considering a direct displacement-based design approach.

7.3 Applications of the HKC model: Direct Displacement-Based Design

7.3.1 Maximum Tensile Strains

Inelastic tensile strain demands imposed by severe earthquakes on vertical bars located in the end regions of cantilever RCSW can be determined through the curvature ductility factor μ_Φ that expressed in terms of the displacement ductility factor μ_Δ is

$$\mu_\phi = 1 + \frac{(\mu_\Delta - 1)\left(1.5 - {h_e}/{2h_w}\right)}{3\frac{L_p}{h_e}\left[1 - \frac{L_p - 2L_{sp}}{2h_e}\right]} \tag{7-10}$$

where L_p is the plastic hinge length, h_e is the effective height assumed equal to $2h_w/3$ for buildings with equal masses and heights, and h_w for bridge pier walls; h_w is the total height of the wall and L_{SP} is the strain penetration length (Priestley et al., 2007). The plastic hinge length, suggested by Priestley et al. (2007), can be determined from Equation (7-11).

$$L_p = k \cdot h_e + 0.1 l_w + L_{SP} \tag{7-11}$$

where $k = 0.2(f_u/f_y - 1) \leq 0.08$ and $L_{SP} = 0.022\, f_{ye}\, d_{bl}$ (f_{ye} in MPa), h_e is the total height of the wall, f_{ye} is the expected longitudinal steel yield strength equal to $1.1f_y$, f_u/f_y is the ratio between the ultimate strength and the yield strength, and d_{bl} is the largest diameter of the longitudinal steel placed in the boundary region.

The curvature ductility factor from Equation (7-10) is obtained replacing the yield displacement $\Delta_{y@he}$ and the plastic displacement $\Delta_{p@he}$, both calculated at the effective height location, into Equation (7-14).

$$\Delta_{y@he} = \frac{\phi_y \cdot h_e^2}{3}\left(1.5 - \frac{h_e}{2h_w}\right) \tag{7-12}$$

$$\Delta_{p@he} = \phi_p \cdot L_p \left(h_e - \left(0.5L_p - L_{SP}\right)\right) \tag{7-13}$$

$$\mu_\Delta = 1 + \frac{\Delta_p}{\Delta_y} \tag{7-14}$$

where ϕ_y is the yield curvature, ϕ_p is the plastic curvature determined as $\phi_p = \phi_m - \phi_y$, and ϕ_m is the maximum curvature calculated as $\phi_m = \mu_\Phi \cdot \phi_y$. According to Priestley et al. (2007), the yield curvature ϕ_y for rectangular concrete walls can be expressed as a function of the vertical steel yielding strain ε_y and the length of the wall as follows

$$\phi_y = {2.0\varepsilon_y}/{l_w} \tag{7-15}$$

For design purposes, the following assumptions are considered for the case of planar walls. Figure 7-13 shows a chart for preliminary estimation of the neutral axis depth c_w as a function of different axial load ratios ($ALR = P_u/A_g f'_c$) (Moehle et al., 2012). In general, c_w can be approximately written as

$$c_w = \left(1.2ALR + 0.04\right) l_w \tag{7-16}$$

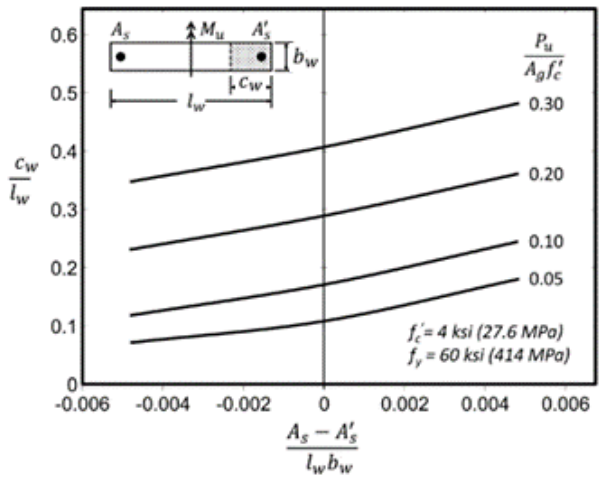

Figure 7-13. Approximate flexural compression depth. (Moehle et al., 2012)

The length of the boundary element l_{be} can be determined from $l_{be} = c_w - 0.1l_w$ or $l_{be} = c_w/2$. Usually, the first expression works for $ALR \leq 0.1$, and the second expression works for $ARL \geq 0.2$. The strain profile of a wall section, shown in Figure 7-14, suggests that the average of the maximum tensile strains ε_{sm} can be calculated as

$$\varepsilon_{sm} = \left(l_w - c_w - {l_{be}}/{2} \right) \phi_m \tag{7-17}$$

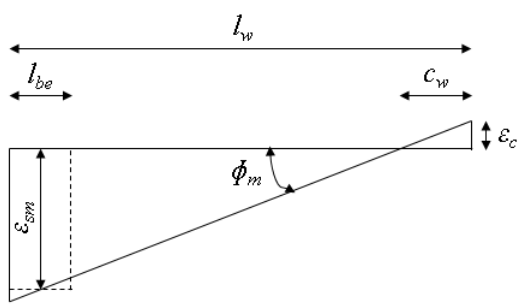

Figure 7-14. Strain profile of an RCSW section

Replacing all the described parameters into Equation (7-17) and considering the average of the expressions to determine l_{be}, the maximum tensile strain can be written as

$$\varepsilon_{sm} = \left(1.95 - 3.60ARL\right) \cdot \varepsilon_y \cdot \mu_\phi \tag{7-18}$$

In order to prevent out-of-plane buckling instability, this maximum tensile strain should be limited by the predictions from the HKC model, which could be easily implemented in a design procedure as shown in the next subsection that exemplify the analysis of a building structural wall.

7.3.1.1 Example: Building Structural Wall

The example presented next is based on the Design Example 6.1 explained in Priestley et al. (2007). The building is to be designed for a damage-control limit state with a drift limit of θ_c = 2% and checked for out-of-plane buckling instability since a wall thickness of 0.25m (0.8ft) is selected. The axial load ratio of the wall is $ARL = 0.2$. The dimensions of the wall are l_w = 8m (26ft) and h_w = 16.8 (55ft). The interstory height of the 6-story building is h_s = 2.8m (9ft). The concrete strength is f'_c = 30MPa (4.4ksi). The yielding and the ultimate strengths of the vertical steel are f_y = 420MPa (61ksi) and f_u = 525MPa (76ksi), respectively. A vertical reinforcement ratio of 1.0% is used in the end regions with the largest bar diameter equal to 20mm (0.79in).

Solution: Out-of-plane buckling instability due to in-plane and out-plane loading is checked following the procedure outlined next considering the DDBD approach.

<u>Step 1:</u> Determine the demand tensile strain from Equation (7-18)

a. Plastic hinge length

   Factor for plastic hinge length: $k = 0.2(f_u/f_y - 1) = 0.2(525/420-1) = 0.05 \leq 0.08$

   Strain penetration length: $L_{SP} = 0.022\, f_{ye}\, d_{bl} = 0.022(1.1*420)*0.020 = 0.203m$

   Plastic hinge length: from Equation (7-4),

   $$L_p = 0.05(0.75*16.8) + 0.1*8 + 0.203 = 1.633m$$

b. Yield strain: $\varepsilon_y = 1.1*420/200000 = 0.00231m/m$

c. Yield curvature: $\phi_y = 2\varepsilon_y/l_w = 2(0.00231)/8 = 0.000578/m$

d. Roof yield displacement: $\Delta_y = \phi_y\,(h_w+L_{SP})^2/3 = 0.000578*(16.8+0.203)^2/3 = 0.0557m$

e. Roof yield drift: $\theta_{yn} = \varepsilon_y\,(h_w+L_{SP})/l_w = 0.00231*(16.8+0.203)/8 = 0.00491\ rad$

f. Plastic rotation: $\theta_p = \theta_c - \theta_{yn} = 0.02 - 0.00491 = 0.0151\ rad$

g. Roof plastic displacement: $\Delta_p = \theta_p\, h_w = 0.0151*16.8 = 0.254m$

h. Displacement ductility: $\mu_\Delta = 1 + \Delta_p/\Delta_y = 1+0.254/0.0557 = 5.56$

i. Curvature ductility:

$$\mu_\phi = 1 + \frac{(5.56-1)*\left(1.5 - \frac{(0.75*16.8)}{(2*16.8)}\right)}{3\frac{1.633}{0.75*16.8}\left[1-\frac{1.633-2*0.203}{2(0.75*16.8)}\right]} = 14.867$$

j. Demand tensile strain: $\varepsilon_{sm} = (1.95-3.60*0.2)*0.00231*14.867 = 0.042m/m$

<u>Step 2:</u> The maximum tensile strain is determined from Equation (7-8) and Equation (7-9) for comparison purposes.

a. Stability criteria

Mechanical reinforcement ratio: $m = \rho_{lbe}(f_y/f'_c) = 0.01(420/30) = 0.14$

Stability criteria: from Equation (7-5),

$$\xi_c = 0.5\left(1 + 2.35*0.14 - \sqrt{5.53*0.14^2 + 4.70*0.14}\right) = 0.227 \le 0.5$$

b. Length of the potential buckled region: $Lo = h_s/\sqrt{3} = 1.617m$

c. Buckled length-to-thickness ratio: $Lo/b_w = 6.5$

d. Stability coefficients: $\alpha_1 = 3.8$, $\alpha_2 = 120$, and $\alpha_3 = -0.58$, for $h_s/b_w = 11.2$

e. Maximum tensile strain from Equation (7-8):

$$\varepsilon_{sm} \le \frac{8}{3}\left(\frac{0.25}{1.617}\right)^2 0.227 + \left[3.8 + 120\left(\frac{0.25}{1.617}\right)^2 - 0.58*\ln(0.01)\right]\cdot 0.00231 = 0.0360$$

f. Maximum tensile strain from Equation (7-9):

$$\varepsilon_{sm} \le \frac{8}{3}\left(\frac{0.25}{1.617}\right)^2 0.227 + \left[-2.4 + 160\left(\frac{0.25}{1.617}\right)^2 - 1.9\cdot\ln\left(0.01\right)\right]\cdot 0.00231 = 0.0380$$

Notice that Equation (7-8) and Equation (7-9) report tensile strains about $16\varepsilon_y$.

Result: The demand tensile strain expected in the wall is larger than the maximum tensile strain limited through the HKC model, suggesting that the wall would experience out-of-plane buckling instability due to combined effects of in-plane and out-of-plane displacements equivalent to drift levels of 2%; consequently, a thicker wall is recommended.

7.3.2 Minimum Wall Thickness

One of the most important critical parameters to prevent out-of-plane buckling instability caused mainly by cyclic in-plane compressive strains preceded by inelastic tensile strains is the thickness of a wall end region. A reliable design to limit the boundary element thickness can be addressed through the simplified version of the HKC model. Substituting Equation (7-18) into Equation (7-9), the minimum thickness is calculated from Equation (7-19).

$$b_{\min} \ge L_o\sqrt{\left(\left(1.95 - 3.60ALR\right)\mu_\phi + 2.4 + 1.9\ln(\rho_{lbe})\right)\varepsilon_y \Big/ \left(\frac{8}{3}\xi_c + 160\varepsilon_y\right)} \qquad (7\text{-}19)$$

Paulay & Priestley (1993) and (Chai & Kunnath, 2005) also established minimum wall thicknesses based on similar contemplations. However, the maximum tensile strains obtained from the two models resulted in some cases extremely conservative according to the experimental observations

and the parametric study. This suggests that the simplified HKC model is more precise to determine the minimum thickness of a wall to ensure out-of-plane buckling stability. Equation (7-19) could be easily applied in a design procedure as demonstrated in the next example.

7.3.2.1 Example: Buildings Structural Wall

The example presented next is based on the case detailed in section 7.3.1.1. This time the problem requires to determine the minimum wall thickness to prevent inelastic out-of-plane buckling.

Solution: Out-of-plane buckling instability due to in-plane and out-plane loading is checked following the procedure outlined next considering the DDBD approach.

Step 1: Determine the curvature ductility from Equation (7-10)

a. Plastic hinge length

Factor for plastic hinge length: $k = 0.2(f_u/f_y - 1) = 0.2(525/420-1) = 0.05 \leq 0.08$

Strain penetration length: $L_{SP} = 0.022\, f_{ye}\, d_{bl} = 0.022(1.1*420)*0.020 = 0.203m$

Plastic hinge length: from Equation (7-4),

$$L_p = 0.05(0.75*16.8) + 0.1*8 + 0.203 = 1.633m$$

b. Yield strain: $\varepsilon_y = 1.1*420/200000 = 0.00231m/m$

c. Yield curvature: $\phi_y = 2\varepsilon_y/l_w = 2(0.00231)/8 = 0.000578/m$

d. Roof yield displacement: $\Delta_y = \phi_y (h_w+L_{SP})^2/3 = 0.000578*(16.8+0.203)^2/3 = 0.0557m$

e. Roof yield drift: $\theta_{yn} = \varepsilon_y (h_w+L_{SP})/l_w = 0.00231*(16.8+0.203)/8 = 0.00491\ rad$

f. Plastic rotation: $\theta_p = \theta_c - \theta_{yn} = 0.02 - 0.00491 = 0.0151\ rad$

g. Roof plastic displacement: $\Delta_p = \theta_p h_w = 0.0151*16.8 = 0.254m$

h. Displacement ductility: $\mu_\Delta = 1 + \Delta_p/\Delta_y = 1+0.254/0.0557 = 5.56$

i. Curvature ductility:

$$\mu_\phi = 1 + \frac{(5.56-1)*\left(1.5 - \frac{(0.75*16.8)}{(2*16.8)}\right)}{3\frac{1.633}{0.75*16.8}\left[1 - \frac{1.633-2*0.203}{2(0.75*16.8)}\right]} = 14.867$$

Step 2: Determine the minimum thickness from Equation (7-19)

a. Stability criteria

Mechanical reinforcement ratio: $m = \rho_{lbe}(f_y/f'_c) = 0.01(420/30) = 0.14$

Stability criteria: from Equation (7-5),

$$\xi_c = 0.5\left(1 + 2.35*0.14 - \sqrt{5.53*0.14^2 + 4.70*0.14}\right) = 0.227 \leq 0.5$$

b. Length of the potential buckled region: $L_o = h_s/\sqrt{3} = 2.8/\sqrt{3} = 1.617m$

c. Minimum end region wall thickness:

$$b_{\min} \geq 1.617\sqrt{\frac{\left(\left(1.95-3.60*0.2\right)*14.867+2.4+1.9\ln(0.01)\right)*0.00231}{\frac{8}{3}(0.227)+160*0.00231}} = 0.272m$$

Result: The minimum boundary region thickness suggested by the simplified HKC model is approximately 0.30m (12.0in.) to prevent instability due to combined effects of in-plane and out-of-plane displacements equivalent to drift levels close to 2%.

7.4 Preliminary estimation of the minimum structural wall thickness

Preliminary estimations of specific design parameters are required usually for rapid controls. In this section, the HKC model including a DDBD procedure is implemented through charts that provide the minimum thickness of structural walls that require special boundary elements considering the influence of ductility levels, reinforcement ratios, and wall heights, as shown in Figure 7-15. The mechanical material properties are f'_c = 30MPa (4.4ksi) and f_y = 420MPa (60ksi).

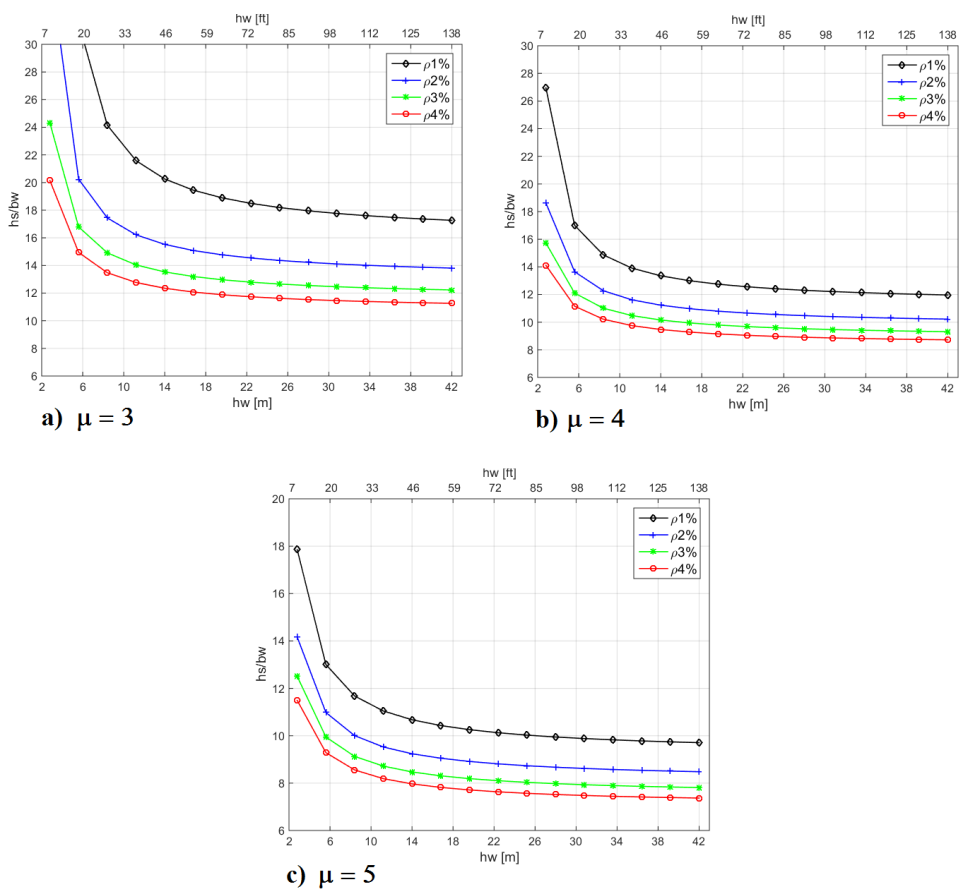

Figure 7-15. Approximate minimum wall thickness for structural walls

The charts are created for an axial load ratio equal to 0.15 and a height-to-length ratio equal to 4, selected as a critical combination. Beyond a height-to-length ratio of 4, the outcomes tend to be similar as demonstrated in Chapter 8 where a case study related to a pier wall is presented. Notice that the minimum thickness of a structural wall tends to be similar for taller walls with similar longitudinal reinforcement ratio. In addition, note the significant effect of the ductility level on the minimum thickness required to prevent out-of-plane buckling instability.

7.4.1 Case Study: 18-story RC building in Santiago, Chile

An 18-story condominium, already described in Chapter 2, reported severe damage after the Chile earthquake on February 27th, 2010. Two walls that were aligned to the very slender transverse direction in one of the towers exhibited buckling instability at the parking level. The total height of the damaged tower is about 56m and the longitudinal reinforcement ratio in the end regions is assumed to be about 1%. The interstory height-to-thickness ratio of these walls was 17.7 and the wall thickness was 175mm, which satisfied the limit of 18 specified by the Chile Concrete Design Standard (NCh 433 1996) (Saatcioglu et al., 2013).

The preliminary estimation chart associated with ductility $\mu=4$ is used to determine the minimum wall thickness that the studied wall would have required to prevent out-of-plane buckling, as shown in Figure 7-16. The HKC model suggests a height-to-thickness ratio of 12, which is less than the limit of 16 prescribed in ACI 318-14. Considering a clear story height of 3.1m, the tower would have required a thickness no less than 260mm in the regions where the plastic hinge is anticipated.

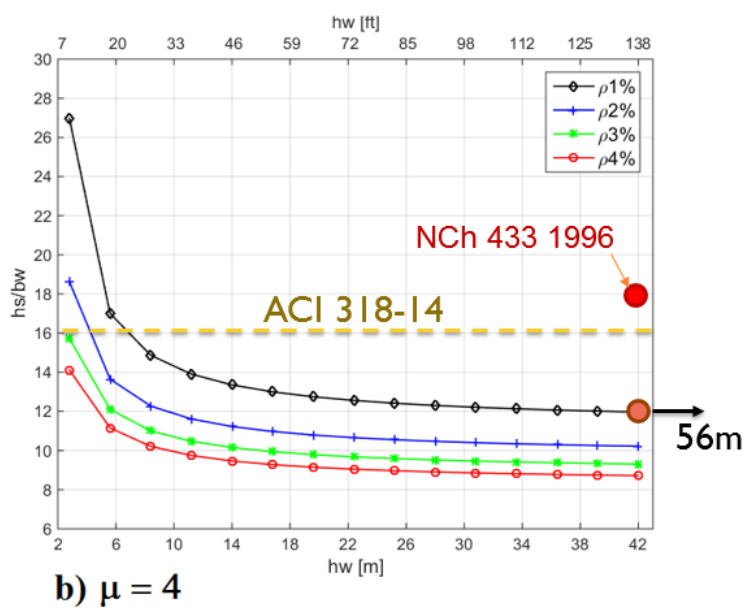

Figure 7-16. Case study: Approximate estimation of the minimum wall thickness

7.5 Summary: HKC model for structural walls

This section summarizes the basic equations already presented through the examples that assess the out-of-plane buckling instability limit state of special reinforced concrete structural walls with aspect ratios $h_w/l_w \geq 2$ that require special boundary elements.

- Maximum tensile strains:
  - Simplified HKC model:

$$\varepsilon_{sm} \leq \frac{8}{3}\left(\frac{b_w}{L_o}\right)^2 \xi_c + \left(-2.4 + 160\left(\frac{b_w}{L_o}\right)^2 - 1.9 \cdot \ln\left(\rho_{lbe}\right)\right)\varepsilon_y$$

- Minimum Wall Thickness:

$$b_{\min} \geq L_o \sqrt{\left(\left(1.95 - 3.60ALR\right)\mu_\phi + 2.4 + 1.9\ln(\rho_{lbe})\right)\varepsilon_y \Big/ \left(\frac{8}{3}\xi_c + 160\varepsilon_y\right)}$$

- Length of the potential buckled region: $L_o = h_s/\sqrt{3}$
- Stability criteria: $\xi_c = 0.5\left(1 + 2.35m - \sqrt{5.53m^2 + 4.70m}\right) \leq 0.5$
- Mechanical reinforcement ratio: $m = \rho_{lbe}(f_y/f'_c)$
- Curvature ductility: $\mu_\phi = 1 + \dfrac{(\mu_\Delta - 1)\left(1.5 - h_e/2h_w\right)}{3\dfrac{L_p}{h_e}\left[1 - \frac{L_p - 2L_{sp}}{2h_e}\right]}$
- Effective height: h_e = *(determined %)*h_w
- Plastic hinge length: $L_p = k \cdot h_e + 0.1l_w + L_{SP}$
- Factor for plastic hinge length: $k = 0.2(f_u/f_y - 1) \leq 0.08$
- Strain penetration length: $L_{SP} = 0.022\, f_{ye}\, d_{bl}$ (f_{ye} *in MPa*)

CHAPTER 8: DESIGN RECOMMENDATIONS FOR PIER WALLS

Pier walls are occasionally employed in bridges because of their in-plane lateral stiffness. These walls are usually thicker than the structural walls contemplated in buildings. However, their clear heights are also larger, giving rise to height-to-thickness ratios that may be larger than those of buildings and consequently, may be prone to buckle.

Experimental tests on reinforced concrete prisms representative of boundary elements of prototype typical planar RC walls were conducted to study the effects on out-of-plane instability due to a combination of selected longitudinal reinforcement ratios and various load paths. As has been observed in past studies, when the buckled deformation was enough to cause instability, loss of vertical load carrying capacity occurred. The experimental results indicated that imposed out-of-plane displacements do not impact stability, however, in-plane loading history does impact the onset of the out-of-plane buckling limit state. In addition, the hysteretic response of the longitudinal reinforcement suggested further analysis to improve the predictions regarding the tensile strain components that lead to instability.

Subsequently, a fiber-based computational model was developed and calibrated based on the response of the tested specimens. A parametric study was conducted, where formerly identified critical parameters were considered in order to establish an out-of-plane buckling stability limit state as a function of longitudinal tensile strains reached at the end regions of RC walls. A new model, identified as the HKC model, that addresses the buckling instability of structural or pier walls has been calibrated and validated considering the fundamentals from previous models and the key findings from the experimental and the analytical studies. Direct displacement-based design recommendations associated with the maximum tensile strains that a wall could sustain before exhibiting out-of-plane instability, and the minimum wall thickness to prevent inelastic buckling were covered in Chapter 7.

This chapter includes practical applications addressing assessment and design procedures considering a direct displacement-based design approach and the HKC model where pier walls with aspect ratios $h_w/l_w \geq 2$ that require special boundary elements are studied.

8.1 Applications of the HKC model: Direct Displacement-Based Design

8.1.1 Example: Bridge Pier Wall

The bridge is to be designed for a displacement ductility level of $\mu_\Delta = 4$ in the transverse and longitudinal directions and checked for out-of-plane buckling instability. The dimensions of the analyzed pier wall are l_w = 4m (13ft) and h_w = 8m (26ft). A wall thickness b_w of 0.3m (1ft) has been selected. The axial load ratio of the pier wall is $ARL = 0.1$. The concrete strength is f'_c = 35MPa (4.4ksi). The yielding and the ultimate strengths of the steel reinforcement are f_y = 420MPa (61ksi)

and f_u = 630MPa (76ksi), respectively. A vertical steel ratio of 2.0% is used along the length of the wall with the largest bar diameter equal to 25.4mm (#8).

Solution: Out-of-plane buckling instability due to in-plane and out-plane loading is checked following the procedure outlined next considering the Direct Displacement-Based Design (DDBD) approach.

<u>Step 1:</u> Determine the maximum tensile strain from Equation (7-18)

a. Plastic hinge length

Factor for plastic hinge length: $k = 0.2(f_u/f_y - 1) = 0.2(630/420-1) = 0.1 \geq 0.08$

Consequently, $k = 0.08$

Strain penetration length: $L_{SP} = 0.022\, f_{ye}\, d_{bl} = 0.022(1.1*420)*0.0254 = 0.258m$

Plastic hinge length: from Equation (7-4), $L_p = 0.08(8) + 0.1*4 + 0.258 = 1.298m$

b. Yield strain: $\varepsilon_y = 1.1*420/200000 = 0.00231m/m$

c. Curvature ductility: since $h_e = h_w$ for pier walls, Equation (7-10) reduces to

$$\mu_\phi = 1 + \frac{(4-1)}{3 \cdot \frac{1.298}{8}\left[1 - \frac{1.298 - 2*0.258}{2(8)}\right]} = 7.479$$

d. Maximum tensile strain: $\varepsilon_{sm} = (1.95-3.60*0.1)*0.00231*7.479 = 0.0275m/m$

<u>Step 2:</u> The maximum tensile strain is determined from Equation (7-9).

a. Stability criteria

Mechanical reinforcement ratio: $m = \rho_{lbe}(f_y/f'_c) = 0.02(420/35) = 0.24$

Stability criteria: from Equation (7-5),

$$\xi_c = 0.5\left(1 + 2.35*0.24 - \sqrt{5.53*0.24^2 + 4.70*0.24}\right) = 0.181 \leq 0.5$$

b. Length of the potential buckled region: $L_o = h_w/\sqrt{3} = 8/\sqrt{3} = 4.619m$

c. Maximum tensile strain from Equation (7-9):

$$\varepsilon_{sm} \leq \frac{8}{3}\left(\frac{0.30}{4.619}\right)^2 0.181 + \left[-2.4 + 160\left(\frac{0.30}{4.619}\right)^2 - 1.9 \cdot \ln(0.02)\right] \cdot 0.00231 = 0.0152$$

Result: The maximum tensile strain expected in the pier wall is greater than the maximum tensile strain limited through the HKC model, suggesting that the pier wall would experience out-of-plane buckling instability due to combined effects of in-plane and out-of-plane displacements equivalent to ductility μ = 4.

8.1.2 Example: Bridge Pier Wall

The example presented next is based on the problem solved above. This time the problem requires to establish the minimum pier wall thickness to prevent inelastic out-of-plane buckling.

Solution: Out-of-plane buckling instability due to in-plane and out-plane loading is checked following the procedure outlined next considering the DDBD approach.

Step 1: Determine the curvature ductility from Equation (7-10)

a. Plastic hinge length

Factor for plastic hinge length: $k = 0.2(f_u/f_y - 1) = 0.2(630/420-1) = 0.1 \geq 0.08$

Consequently, $k = 0.08$

Strain penetration length: $L_{SP} = 0.022\, f_{ye}\, d_{bl} = 0.022(1.1*420)*0.0254 = 0.258m$

Plastic hinge length: from Equation (7-4), $L_p = 0.08(8) + 0.1*4 + 0.258 = 1.298m$

b. Yield strain: $\varepsilon_y = 1.1*420/200000 = 0.00231m/m$

c. Curvature ductility: from Equation (7-10),

$$\mu_\phi = 1 + \frac{(4-1)}{3 \cdot \frac{1.298}{8}\left[1 - \frac{1.298 - 2*0.258}{2(8)}\right]} = 7.479$$

Step 2: Determine the minimum thickness from Equation (7-19)

a. Stability criteria

Mechanical reinforcement ratio: $m = \rho_{lbe}(f_y/f'_c) = 0.02(420/35) = 0.24$

Stability criteria: from Equation (7-5),

$$\xi_c = 0.5\left(1 + 2.35*0.24 - \sqrt{5.53*0.24^2 + 4.70*0.24}\right) = 0.181 \leq 0.5$$

b. Length of the potential buckled region: $L_o = h_w/\sqrt{3} = 8/\sqrt{3} = 4.619m$

c. Minimum end region wall thickness:

$$b_{\min} \geq 4.619\sqrt{\frac{\left((1.95 - 3.60*0.1)*7.479 + 2.4 + 1.9\ln(0.02)\right)*0.00231}{\frac{8}{3}(0.181) + 160*0.00231}} = 0.630m$$

Result: The minimum boundary region thickness suggested by the HKC model would be 0.63m (24.0in.) to prevent lateral instability due to combined effects of in-plane and out-of-plane displacements equivalent to ductility levels up to 4.

8.2 Preliminary estimation of the minimum pier wall thickness

Preliminary estimations of specific design parameters are required usually for rapid controls. In this section, the HKC model and a DDBD procedure are implemented through charts that provide the minimum thickness of pier walls that require special boundary elements considering the influence of ductility levels, reinforcement ratios, and pier wall heights, as shown in Figure 8-1. The mechanical material properties are f'_c = 35MPa (4.4ksi) and f_y = 420MPa (60ksi).

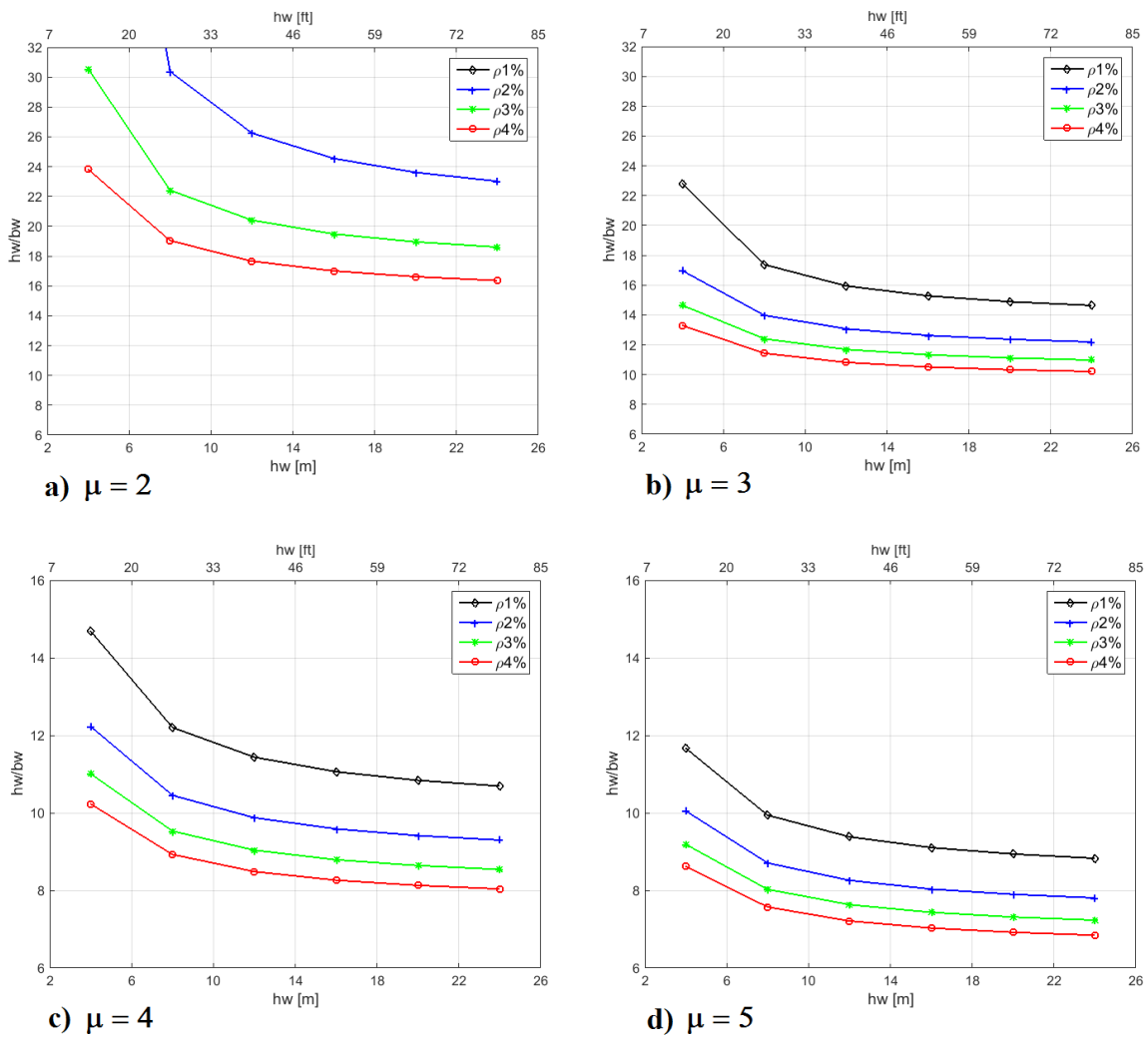

Figure 8-1. Approximate minimum wall thickness for pier walls

The charts from Figure 8-1 are created for an axial load ratio equal to 0.05 and a height-to-length ratio equal to 4, selected as a critical combination. The missing values in the ductility 2 chart imply low demand levels compared with the required tensile strains for 1% steel content. Notice that the minimum thickness of a pier wall tends to be similar for taller walls with high longitudinal reinforcement ratios. In addition, the charts expose the significant effect of ductility levels on the minimum thickness required to prevent out-of-plane buckling instability.

Figure 8-2 presents the HKC model predictions of a 12m (39.4ft) height pier wall in terms of aspect ratio, normalized axial strain, curvature ductility, and in-plane drift percentage. The pier wall requires special boundary elements and has a uniformly distributed longitudinal reinforcement ratio of 2%. Figure 8-2(a) demonstrates that beyond a height-to-length ratio of 4, the outcomes tend to be comparable, supporting the choice of the aforementioned critical combination. Figure 8-2(b) shows the influence of the ductility level on the maximum tensile demands and consequently the minimum required thickness. High curvature ductility levels accompanied by high in-plane drift percentages lead to thicker boundary elements, as exhibited in Figure 8-2(c) and Figure 8-2(d), respectively.

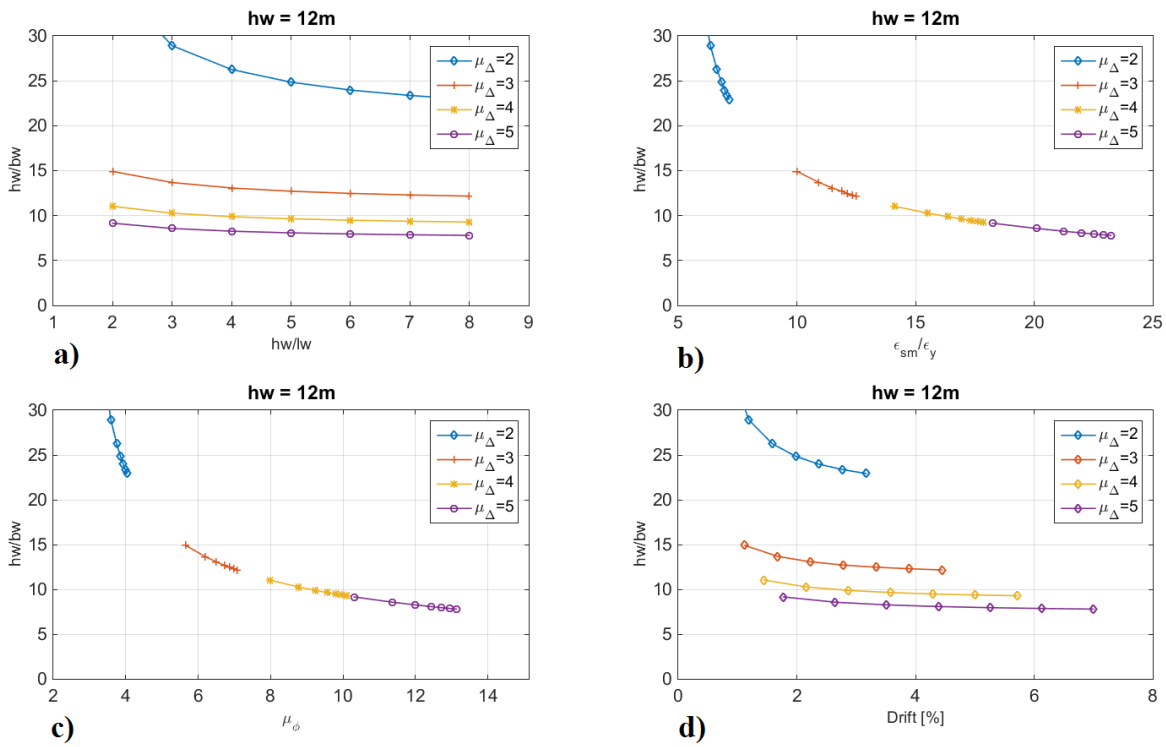

Figure 8-2. HKC model predications of a pier wall with h_w=12m (39.4ft) as a function of: a) aspect ratio, b) normalized maximum tensile strain, c) curvature ductility, d) in-plane drift percentage

8.2.1 Case Study: Alaska DOT Bridge 539

The characteristics of the bridge analyzed in this section is presented in Table 8-1. Note that the height-to-thickness ratio is less than 2, however it is close enough to evaluate the stability of the pier wall through the HKC model. Special boundary elements are assumed to be contemplated in the design. The preliminary estimation chart associated with ductility $\mu=4$ is used to determine the minimum wall thickness that the studied pier would require to prevent out-of-plane buckling, as shown in Figure 8-3. Considering a clear height of 41ft (12.5m), the HKC model suggests a height-to-thickness ratio of 11.5 that implies a thickness no less than 3.5ft (1.1m) in the region where the plastic

hinge is anticipated. The as-built wall thickness is 4.33ft (1.3m), which satisfies the minimum thickness and consequently the wall would not be prone to buckle when subjected to ductility levels up to 4.

Table 8-1. Alaska DOT pier wall

Pier Wall Id.		539
Year		1973
l_w	[ft]	26
h_w	[ft]	41
b_w	[ft]	4.33
reinf. (l)	[-]	14
reinf. (t)	[-]	s#6@12"+4t#4@12"
ρ (l)	[-]	0.0092
h_w/t_w	[ft/ft]	9.5
h_w/l_w	[ft/ft]	1.6
Shape		

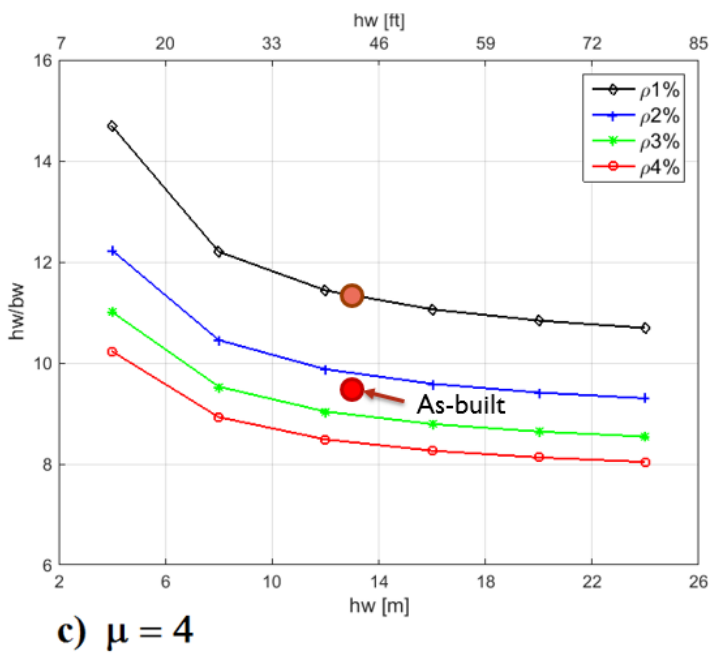

c) $\mu = 4$

Figure 8-3. Case study: Approximate assessment of the minimum pier wall thickness

8.3 Summary: HKC model for pier walls

This section summarizes the basic equations already presented through the examples covered in Chapter 8 to assess the out-of-plane buckling instability limit state of pier walls with aspect ratios $h_w/l_w \geq 2$ that require special boundary elements.

- Maximum tensile strains:
  - Simplified HKC model:

$$\varepsilon_{sm} \leq \frac{8}{3}\left(\frac{b_w}{L_o}\right)^2 \xi_c + \left(-2.4 + 160\left(\frac{b_w}{L_o}\right)^2 - 1.9 \cdot \ln\left(\rho_{lbe}\right)\right)\varepsilon_y$$

- Minimum Wall Thickness:

$$b_{\min} \geq L_o \sqrt{\left(\left(1.95 - 3.60ALR\right)\mu_\phi + 2.4 + 1.9\ln(\rho_{lbe})\right)\varepsilon_y \Big/ \left(\frac{8}{3}\xi_c + 160\varepsilon_y\right)}$$

- Length of the potential buckled region: $L_o = h_w/\sqrt{3}$
- Stability criteria: $\xi_c = 0.5\left(1 + 2.35m - \sqrt{5.53m^2 + 4.70m}\right) \leq 0.5$
- Mechanical reinforcement ratio: $m = \rho_{lbe}(f_y/f'_c)$
- Curvature ductility: $\mu_\phi = 1 + \dfrac{\left(\mu_\Delta - 1\right)}{3\dfrac{L_p}{h_w}\left[1 - \frac{L_p - 2L_{sp}}{2h_w}\right]}$
- Plastic hinge length: $L_p = k \cdot h_w + 0.1l_w + L_{SP}$
- Factor for plastic hinge length: $k = 0.2(f_u/f_y - 1) \leq 0.08$
- Strain penetration length: $L_{SP} = 0.022\, f_{ye}\, d_{bl}$ (f_{ye} in MPa)

CHAPTER 9: DISCUSSION AND FUTURE WORK

9.1 Discussion

Inelastic buckling instability had been only observed in laboratory tests conducted on RC structural walls, however during recent earthquakes this failure mode generated significant damage to buildings that included rectangular or flanged wall geometries. In the first part of this report, the damage associated with the out-of-plane buckling mechanism that was reported after the Chile (2010) and New Zealand (2011) earthquakes was covered. Past experimental programs conducted on thin RC walls where buckling instability was captured or studied were also described. In addition, experimental investigations on RC prisms simulating end regions were detailed. Furthermore, the state-of-the-art of phenomenological models created to prevent this failure mode was studied.

End regions of RC walls accumulate more damage when walls exhibit out-of-plane buckling instability. Past research on RC prisms that represent end regions subjected to axial tensile and compressive cycles, has demonstrated to be efficient and convenient to study the influence of critical parameters affecting the onset of the out-of-plane buckling mechanism. Therefore, twelve RC prisms representative of boundary elements of prototype typical RC walls were tested in the Constructed Facility Laboratory at the North Carolina State University. The effects of three different longitudinal reinforcement ratios in combination with different axial and lateral loading paths were studied.

The experimental results indicated that imposed out-of-plane displacements slightly impact the lateral stability, however, in-plane loading history does impact the onset of the local buckling limit state of walls. In addition, the results showed that boundary elements that consider larger longitudinal steel ratios are prone to buckle at earlier stages with smaller in-plane displacements. This suggests that tensile strains should be limited through displacement or curvature ductility levels. The deformed shape of the prisms and the axial hysteretic response of the steel located in opposite faces also showed to be important to establish the maximum tensile strain components that lead to instability.

A numerical fiber-based model was used to conduct the parametric study that included the analysis of complementary critical factors that influence the out-of-plane stability of walls. The numerical model was first calibrated and validated using the experimental results. The performance criteria associated with concrete cover crushing, recognized in the buckled region under compressive loading, constituted the key factor to capture instability. A total of 180 RC prisms subjected to axial cyclic loading were simulated in SeismoStruct. The results from the experimental phase and the parametric study in conjunction with the fundamentals of the Paulay & Priestley (1993) and Chai & Elayer (1999) models supported the conception of a new model, the HKC model, which demonstrated to be more reliable to prevent out-of-plane buckling instability of RC walls.

The phenomenological models developed through prisms consider a uniform distribution of tensile strains along the height of the end region, with a buckled shape formed at the mid-height zone.

Observed damage on structural walls have proved that axial strain gradients relocate the buckled region close to the slab-wall or the foundation-wall interfaces. However, analyses on the results of previous studies and an additional numerical simulation conducted as part of this research program, validated the suitability of the HCK model for structural walls and pier walls.

Design recommendations, which contemplate the direct displacement-based design method, were established and detailed through four examples. The examples covered the procedure to control the maximum tensile strain limit that a structural wall and a pier wall could sustain before experiencing out-of-plane buckling instability. In addition, a method to determine the minimum thickness of a boundary element to guarantee out-of-plane stability when a structural wall and a pier wall are subjected to combined effects of lateral load reversals was described through the examples. The proposed recommendations could be easily included in existing design procedures because of their convenience.

Preliminary estimations are usually convenient during design phases for rapid control of geometric parameters. The HKC model combined with a DDBD procedure have been implemented through charts that provide the minimum thickness of structural walls and pier walls that require special boundary elements. The charts consider the influence of ductility levels, reinforcement ratios, and wall heights. Two case studies of walls from a building damaged during the Chile 2010 earthquake and a bridge constructed by the Alaska DOT were assessed using the preliminary estimation charts created as part of the outcomes of the current research.

9.2 Future Work

The results of the research conducted through this project have demonstrated the potential of the HKC model to assess the of out-of-plane buckling instability of RC walls. However, some opportunities to expand this work remain. The importance of the topic suggests further investigation by a deep study of the parameters that affect the onset of instability.

Additional experimental and analytical studies on RC prisms would include different interstory height-to-thickness ratios, one to three reinforcement vertical layers, different cover thickness, and earthquake-type loading protocols. The stipulations included in the HCK model would improve based on new findings.

Experimental studies on scaled pier walls are recommended to analyze the effect of axial strain gradients, since bridge pier walls usually exhibit massive geometries compared with structural walls.

Another field of interest is the time-history dynamic analysis of RC walls considering the key findings from the experimental and the parametric study. A finite element model that contemplates strain gradients would result convenient for this purpose.

This research focused on RC structural walls. Reinforced masonry can also exhibit out-of-plane instability due to the combination of in-plane and out-of-plane loads as noticed by few studies. Consequently, additional experiments on reinforced masonry prisms are suggested to further investigate

REFERENCES

Aaleti, S., Brueggen, B. L., Johnson, B., French, C. E., & Sritharan, S. (2013). Cyclic Response of RC Walls with Different Anchorage Details: An Experimental Investigation. *Journal of Structural Engineering*, (July), 1181–1191. http://doi.org/10.1061/(ASCE)ST.1943-541X.0000732

AASHTO. (2010). *AASHTO LRFD Bridge Design Specifications* (Fifth Edit). AASHTO.

AASHTO. (2011). *AASHTO Guide Specifications for LRFD Seismic Bridge Design*. *AASHTO Guide Specifications for LRFD Seismic Bridge Design*. AASHTO.

ACI 318-14. (2014). *Building Code Requirements for Structural Concrete (ACI 318-14) and Commentary (ACI 318R-14)*. *ACI 318-14*.

Alarcón, C. (2013). *Influence of Axial Load in the Seismic Behavior of Reinforced Concrete Walls With Nonseismic*. Pontificia Universidad Católica de Chile.

Almeida, J. P., Tarquini, D., & Beyer, K. (2014). Modelling Approaches for Inelastic Behaviour of RC Walls: Multi-level Assessment and Dependability of Results. *Archives of Computational Methods in Engineering*, *23*(1), 69–100. http://doi.org/10.1007/s11831-014-9131-y

ASTM. (2014). *ASTM A370: Standard Test Methods and Definitions for Mechanical Testing of Steel Products*. *ASTM International*. http://doi.org/10.1520/A0370-14.2

ASTM C39. (2015). *ASTM C39 / C39M - 16b Standard Test Method for Compressive Strength of Cylindrical Concrete Specimens*. West Conshohocken. Retrieved from https://www.astm.org/Standards/C39.htm

Bazaez, R., & Dusicka, P. (2016). Cyclic Loading for RC Bridge Columns Considering Subduction Megathrust Earthquakes. *Journal of Bridge Engineering*, *21*(5), 1–13. http://doi.org/10.1061/(ASCE)BE.1943-5592.0000891

Berg, G. V., Bolt, B. A., Sozen, M. A., & Christopher, R. (1980). *Earthquake in Romania, March 4, 1977: An Engineering Report*. Washington, D.C. Retrieved from https://books.google.com/

Birely, A. C. (2011). *Seismic Performance of Slender Reinforced Structural Concrete Walls*. University of Washington.

Brueggen, B. L. (2009). *Performance of T-shaped reinforced concrete structural walls under multi-directional loading*. *Dissertation Abstracts International*. University of Minnesota. Retrieved from https://nees.org/resources/236

Caltrans. (2013). *Caltrans Seismic Design Criteria* (Version 1.). Sacramento, CA, U.S.: California Department of Transportation.

Canadian Standards Association. (2004). *Design of Concrete Structures CSA A23.3-04*.

Chai, Y. H., & Elayer, D. T. (1999). Lateral stability of reinforced concrete columns under axial reversed cyclic tension and compression. *ACI Structural Journal*, *96*(96), 780–789.

Chai, Y. H., & Kunnath, S. K. (2005). Minimum thickness for ductile RC structural walls. *Engineering*

Structures, *27*, 1052–1063. http://doi.org/10.1016/j.engstruct.2005.02.004

Christensen, D. (2002). The Great Alaska Earthquake of 1964. Retrieved November 11, 2016, from http://www.aeic.alaska.edu/quakes/Alaska_1964_earthquake.html

Chrysanidis, T. A., & Tegos, I. A. (2012a). The influence of ratio of the longitudinal reinforcement of the boundary edges of structural walls to the resistance against lateral instability of earthquake-resistant reinforced concrete structural walls. In *15th World Conference on Earthquake Engineering (15WCEE)* (p. 10). Lisboa.

Chrysanidis, T. A., & Tegos, I. A. (2012b). The influence of tension strain of wall ends to their resistance against lateral instability for low-reinforced concrete walls. In *15th World Conference on Earthquake Engineering (15WCEE)* (p. 10). Lisboa.

Committee on the Alaska Earthquake of the Division of Earth Sciences. National Research Council. (1973). *The Great Alaska Earthquake of 1964 - Engineering. National Academy of Science.* Washington, D.C. Retrieved from https://books.google.com

Creagh, A., Acevedo, C., Moehle, J., Hassan, W., & Tanyeri, A. C. (2010). *Seismic Performance of Concrete Special Boundary Element* (Vol. 1). Austin: University of California Berkeley.

D'Aniello, M., Portioli, F., & Landolfo, R. (2010). Modelling issues of steel braces under extreme cyclic actions. In Mazzolani (Ed.), *Urban Habitat Constructions under Catastrophic Events* (p. 1048). London.

EEFIT. (1986). *The Mexican Earthquake of 19th September 1985*. London.

EEFIT. (1993). *The Loma Prieta Earthquake of 17 October 1989*. London.

EEFIT. (1994). *The Magnitude 6.7 Northridge, California, Earthquake of 17 January 1994*. London.

EEFIT. (1997). *The Hyogo-Ken Nanbu (Kobe) Earthquake of 17 January 1995*. London.

EEFIT. (2003). *The Kocaeli, Turkey Earthquake of 17 August 1999*. London.

Elnashai, A. S., Gencturk, B., Kwon, O.-S., Al-Qadi, I. L., Hashash, Y., Roesler, J. R., … Valdivia, A. (2010). *The Maule (Chile) earthquake of February 27, 2010: Consequence assessment and case studies*. *MAE Center Report No. 10-04*. Retrieved from https://www.ideals.illinois.edu/handle/2142/18212

Filippou, F. C., Popov, E. P., & Bertero, V. V. (1983). Effects of Bond Deterioration on Hysteretic Behaviour of Reinforced Concrete Joints. *Earthquake Engineering Research Center*. Retrieved from http://www.ce.berkeley.edu/~filippou/Research/Publications/Reports/EERC-83-19.pdf

Flintrop, A., Wallace, J. W., & Segura, C. (2013). *Testing of Reinforced Concrete Shear Wall Boundary Elements Designed According to ACI 318-11* (Vol. 1). University of Minnesota.

Goodsir, W. J. (1985). *The design of coupled frame-wall structures for seismic actions*. University of Canterbury.

Herrick, C. K. (2014). *An Analysis of Local Out-of-Plane Buckling of Ductile Reinforced Structural Walls Due to In-Plane Loading*. North Carolina State University.

Herrick, C. K., & Kowalsky, M. J. (2016). Out-of-Plane Buckling of Ductile Reinforced Structural Walls due to In-Plane Loads. *Journal of Structural Engineering*, *1*, 1–15. http://doi.org/10.1061/(ASCE)ST.1943-541X.0001660.

Johnson, B. (2010). *Anchorage detailing effects on lateral deformation components of RC shear walls*. University of Minnesota.

Kam, W. Y., & Pampanin, S. (2011). The seismic performance of RC buildings in the 22 February 2011 Christchurch earthquake. *Structural Concrete*, *12*(4), 223–233. http://doi.org/10.1002/suco.201100044

Lungu, D. (2008). History of earthquake engineering, lessons learnt and outcomes on today practice; Perspective from Romania. In *AFPS 25th birthday*. Nice, France: Association Française du génie Parasismique.

Mander, J. B., Priestley, M. J. N., & Park, R. (1988). Theoretical Stress-Strain Model for Confined Concrete. *Journal of Structural Engineering*, *114*(8), 1804–1826. http://doi.org/10.1061/(ASCE)0733-9445(1988)114:8(1804)

Marihuén, A. (2014). *Comportamiento Sísmico Armado Esbeltos De Hormigón Armado*. Pontificia Universidad Católica de Chile.

Martínez-Rueda, J. E., & Elnashai, A. S. (1997). Confined concrete model under cyclic load. *Materials and Structures*, *30*(3), 139–147. http://doi.org/10.1007/BF02486385

Menegotto, M., & Pinto, P. E. (1973). Method of Analysis for Cyclically Loaded R. C. Plane Frames Including Changes in Geometry and Non-Elastic Behavior of Elements under Combined Normal Force and Bending. In *Symposium on Resistance and Ultimate Deformability of Structures Acted on by Well Defined Loads* (pp. 15–22). Zurich, Switzerland: International Association for Bridge and Structural Engineering. http://doi.org/http://dx.doi.org/10.5169/seals-13741

Moehle, J. P., Ghodsi, T., Hooper, J. D., Fields, D. C., & Gedhada, R. (2012). Seismic Design of Cast-in-Place Concrete Special Structural Walls and Coupling Beams A Guide for Practicing Engineers. *NEHRP Seismic Design Technical Brief*, (6).

Moroni M. O. (2002). Concrete shear wall construction. Santiago: University of Chile. Retrieved from http://www.world-housing.net/wp-content/uploads/2011/08/Type_RC_Wall.pdf

Oesterle, R. G., Fiorato, A. E., Johal, L. S., Carpenter, J. E., Russell, H. G., & Corley, W. G. (1976). Earthquake resistant structural walls - Tests of isolated walls.

Parra, P. (2015). *Stability of Reinforced Concrete Wall Boundaries*. University of California, Berkeley.

Parra, P. F., & Moehle, J. P. (2014). Lateral Buckling in Reinforced. *10th National Conference on Earthquake Engineering*. http://doi.org/10.4231/D3V40K05Q

Paulay, T., & Priestley, M. J. N. (1992). *Seismic design of reinforced concrete and masonry buildings. 1992. Wiley, New York.*

PEER. (2000). *Structural Engineering Reconnaissance of the August 17, 1999 Earthquake: Kocaeli*

(Izmit), Turkey. Berkeley.

Priestley, M. J. N., Calvi, G. M., & Kowalsky, M. J. (2007). *Displacement-Based Seismic Design of Structures*. Pavia: IUSS PRESS.

Rosso, A., Almeida, J. P., & Beyer, K. (2015). Stability of thin reinforced concrete walls under cyclic loads: state-of-the-art and new experimental findings. *Bulletin of Earthquake Engineering*, 30. http://doi.org/10.1007/s10518-015-9827-x

Rutenberg, A., Jennings, P. C., & Housner, G. W. (1980). *The Response of the Veterans Hospital Building 41 in the San Fernando Earthquake*. Pasadena, California.

Saatcioglu, M., Palermo, D., Ghobarah, A., Mitchell, D., Simpson, R., Adebar, P., … Hong, H. (2013). Performance of reinforced concrete buildings during the 27 February 2010 Maule (Chile) earthquake. *Canadian Journal of Civil Engineering*, *40*(July), 693–710. http://doi.org/10.1139/cjce-2012-0243

Seismosoft Ltd. (2014). *SeismoStruct User Manual*. Pavia.

Shea, M., Wallace, J. W., & Segura, C. (2013). *Seismic performance of thin reinforced concrete shear wall boundaries*. University of Massachusetts Amherst.

Sritharan, S. (2011). The M6 . 3 Christchurch Earthquake : Performance of Buildings in CBD Sri Sritharan Command Center. Buffalo: NEES.

Sritharan, S., Beyer, K., Henry, R. S., Chai, Y. H., Kowalsky, H., & Bull, D. (2014). Understanding poor seismic performance of concrete walls and design implications. *Earthquake Spectra*, *30*(1), 307–334. http://doi.org/10.1193/021713EQS036M

Strong Motion Center. (2014). San Fernando Earthquake of 09 Feb 1971. Retrieved November 11, 2016.

Su, N. (2001). Structural Evaluations of Reinforced Concrete Buildings Damaged by Chi-Chi Earthquake in Taiwan. *Practice Periodical on Structural Design and Construction*, (August), 119–128.

T. Paulay and M. J. N. Priestley. (1993). Stability of Ductile Structural walls. *ACI Structural Journal*, *90*, 385–392.

Thiele, K., Wenk, T., & Bachmann, H. (2000). *Versuche an Stahlbetontragwänden unter pseudodynamischer Einwirkung*. Zürich.

Thomsen, J. H., & Wallace, J. W. (2004). Displacement-Based Design of Slender Reinforced Concrete Structural Walls—Experimental Verification. *Journal of Structural Engineering*, *130*(4), 618–630. http://doi.org/10.1061/(ASCE)0733-9445(2004)130:4(618)

U. S. Geological Survey. (1985). *Preliminary Report of Investigations of the Central Chile Earthquake of March 3, 1985*. Denver, Colorado.

Vallenas, J. M., Bertero, V. V., & Popov, E. P. (1979). *Hysteretic Behavior of Reinforced Concrete Structural Walls*. Berkeley: University of California.

Wallace, J. W., & Moehle, J. (2012). Behavior and Design of Structural Walls–Lessons From Recent Laboratory Tests & Earthquakes. *Proceedings of the International Symposium on Engineering Lessons Learned from the 2011 Great East Japan Earthquake*, (2010), 1132–1144.

Welt, T. S. (2015). *Detailing for Compression in Reinforced Concrete Wall Boundary Elements: Experiments, Simulations, and Design Recommendations*. University of Illinois at Urbana-Champaign.

Yu, W. (2006). *Inelastic Modeling of Reinforcing Bars and Blind Analysis of the Benchmarks Tests on Beam-Column Joints under Cyclic Loading*. *Rose School–European School for Advanced Studies …*. European School for Advanced Studies in Reduction of Seismic Risk.